Chemical Modifications and Passivation Approaches in Metal Halide Perovskite Solar Cells

Mojtaba Abdi Jalebi

Churchill College

University of Cambridge

This dissertation is submitted for the degree of

Doctor of Philosophy

April 2018

To my parents, brothers and friends.

به دانش بود نیک فرجام تو

به مینو دهد چرخ آرام تو

Ferdowsi "Persian poet"

"Success is the result of perfection, hard work, learning from failure, loyalty and persistence."

Colin Powell

Chemical Modifications and Passivation Approaches in Metal Halide Perovskite Solar Cells

Mojtaba Abdi Jalebi

Churchill College, University of Cambridge

This dissertation describes our study on different physical properties of passivated and chemically modified hybrid metal halide perovskite materials and development of highly efficient charge transport layers for perovskite solar cells. We first developed an efficient electron transport layer via modification of titanium dioxide nanostructure followed by a unique chemical treatment in order to have clean interface with fast electron injection form the absorber layer in the perovskite solar cells. We then explored monovalent cation doping of lead halide perovskites using sodium, copper and silver with similar ionic radii to lead to enhance structural and optoelectronic properties leading to higher photovoltaic performance of the resulting perovskite solar cells. We also performed thorough experimental characterizations together with modeling to further understand the chemical distribution and local structure of perovskite films upon monovalent cation doping. Then, we demonstrate a novel passivation approach in alloyed perovskite films to inhibit the ion segregation and parasitic non-radiative losses, which are key barriers against the continuous bandgap tunability and potential for high-performance of metal halide perovskites in device applications, by decorating the surfaces and grain boundaries with potassium halides. This leads to luminescence quantum yields approaching unity while maintaining high charge mobilities along with the inhibition of transient photo-induced ion migration processes even in mixed halide perovskites that otherwise show bandgap instabilities. We demonstrate a wide range of bandgaps stabilized against photo-induced ion migration, leading to solar cell power conversion efficiencies of 21.6% for a 1.56 eV absorber and 18.3% for a 1.78 eV absorber ideally suited for tandem solar cells. We then systematically compare the optoelectronic properties and moisture stability of the two developed passivation routes for alloyed perovskites with rubidium and potassium where the latter passivation route showed higher stability and loading capacity leading to achieve substantially higher photoluminescence quantum yield. Finally, we explored the

possibility of singlet exciton fission between low bandgap perovskites and tetracene as the triplet sensitizer finding no significant energy transfer between the two. We then used tetracene as an efficient dopant-free hole transport layer providing clean interfaces with perovskite layer leading to high photoluminescence yield (e.g. ~18%). To enhance the poor ohmic contact between tetracene and the metal electrode, we added capping layer of a second hole transport layer which is extrinsically doped leading to 21.5% power conversion efficiency for the subsequent solar cells and stabilised power output over 550 hours continuous illumination.

Declaration

I hereby declare that except where specific reference is made to the work of others, the contents of this dissertation are original and have not been submitted in whole or in part for consideration for any other degree or qualification in this, or any other University. This dissertation is the result of my own work and includes nothing, which is the outcome of work done in collaboration, except where specifically indicated in the text. In the following chapters, the use of first person plural is strictly a matter of style. This dissertation does not exceed 60,000 words in length.

Mojtaba Abdi Jalebi

Cambridge

April 2018

Acknowledgements

The results presented in this dissertation would not have been possible without the help and support from the group of brilliant scientists I have had the good fortune to work with. Whilst the work presented is my own, unless explicitly stated, I have received valuable guidance and tutorage during my three and a half years for which I am extremely thankful.

To start with, I thank my supervisor, Prof. Sir Richard Friend, for his visionary supervision and helping me progress in the right direction and always making me feel excited and happy about my work. His personal excitement about science is a viral feeling, which will stay with me throughout my life. I will always be thankful that I got a chance to work alongside such a brilliant mentor.

Second, I would also like to express sincere gratitude to Dr. Aditya Sadhanala who patiently demonstrated the working principles of photothermal deflection spectroscopy and trained me on this setup as well as many scientific discussions for different projects and being such a fantastic friend for me with loads of kind support.

I extend my gratitude to Dr Sam Stranks, who has been a fantastic collaborator and provided me with consistently wise and extremely clever thoughts and support on my work from the time that we first met in late 2016.

I am greatly indebted to the immense scientific discussion with my lab collaborators including Dr. Akshay Rao, Dr. Luis Pazos, Zahra Andaji Garmaroudi, Dr. Reza Saberi Moghaddam, Dr Johannes M Richter, Mejd Alsari, Edward P Booker, Dr Andrew J Pearson, Dr. Maxim Tabachnyk and Dr. Felix Deschler. I want to thank the rest of the optoelectronic (OE) group for creating such a nice atmosphere to work.

Additional thanks go to the staff members of OE who make the group a fantastic place to work. To Prof. Neil Greenham and to Prof. Henning Sirringhaus for making me feel welcomed in OE as well as for their invaluable perspective. I would like to thank the OE support team particularly Richard Gymer and Alex Crook for keeping the office ticking and supplied with enough materials.

I would like to thank my collaborator at École Polytechnique Fédérale de Lausanne, Prof. Michael Grätzel, Dr. Ibrahim Dar, Dr Neha Arora, Dr. Fabrizio Giordano and Dr. Shaik Mohammed Zakeeruddin for their valuable collaboration and scientific discussions. Special thanks to my collaborator at materials science and metallurgy department in Cambridge, Dr Stefania Cacovich, Dr Giorgio Divitini and Dr Caterina Ducati. Further thanks to Dr Bertrand Philippe, Dr Meysam Pazoki and Prof. Håkan Rensmo from Uppsala University. Particular thanks to Dr. Eline M Hutter and Prof.Tom J Savenije from Delf University.

Last but not the least; I would like to thank my family: my parents, for giving birth to me at the first place and supporting me spiritually throughout my life. I would like to thank my brothers who are always supportive and encourage me to move forward. Special and endless thanks to Nafise, for her love and support through all the challenging moments and for the adventures we embark on together.

Contents

List of Figures

Chapter 2

Chapter 3

Chapter 4

Chapter 5

Chapter 6

Chapter 7

Chapter 8

Chapter 1

Introduction

This chapter would give a brief overview of the structure and contents of this PhD thesis.

1. Introduction

The development and implementation of low-cost, clean, and scalable energy solutions is imperative to not only securing a peaceful and sustainable future, but to also improving the livelihood of the 1.3 billion people worldwide who lack access to electricity. It is clear that providing energy access for all, in a way that does not damage the environment and the people within it, is one of the central challenges of the modern age. The technology needed to achieve these aims already exist, but implementation remains inadequate due to a combination of political, economic and cultural barriers.

Semiconductor photovoltaics (PV) are the main part of the solution to address the energy challenges. Solar panels have the potential to provide a large proportion of our renewable energy needs in the near future[1], and to bring energy and development to the world's bottom billion. In the last 50 years, semiconductor and solar cell research have focused on silicon as the active material. The fabrication of silicon solar cells has been optimized extensively and their usage skyrocketed in the last decade, while the cost dropped by an order of magnitude[2]. However, there remain a number of disadvantages to crystalline silicon solar cell panels, namely their complex manufacture – leading to higher costs, their heaviness and their inflexibility. Furthermore, it takes several years until a silicon solar cell produced as much energy from the sun as spent for its production.

Solution-processable semiconductors can overcome these limitations. They offer the tantalizing possibility of flexible, ultra-cheap, roll-to-roll processing giving low upfront device costs, which is especially crucial for customers in the developing world. The key challenges for these new materials technologies is achieving comparable conversion efficiency and long-term operational stability. Organic photovoltaic, dye-sensitized solar cells and hybrid PV research offered steady progress in the last decade, both in enhancement to our fundamental materials understanding and in device efficiencies.

Solar cells based on metal-halide perovskite absorbers, and in particular organic–inorganic hybrid compounds, have sprung to the forefront of photovoltaic research activity, over the past few years, and become promising candidates for cheap, solution-processed, highly efficient solar cells with a short energy payback time[3,4]. The power conversion efficiency of perovskite solar cells has risen in just five years from about 3% to over 22% (these values were independently certified), with significant improvements occurring after 2012[5–8]. This efficiency is already comparable to commercially-available thin-film PV technologies but still lower than record crystalline-Silicon devices. This is a paradigm shift in semiconductor

technology that has opened up new opportunities. In order to realize their commercial potentials, the stability of perovskite devices must be addressed as well as optimisation of materials synthesis and fabrication methods for large-area production.

In this dissertation, we present our study on different aspects of passivated and chemically modified hybrid metal halide perovskite materials and development of highly efficient charge transport layers for perovskite solar cells. We use photothermal deflection optical absorption spectroscopy and photoluminescence characterizations as our central experimental probe of materials properties. Chapter 2 describes the theoretical framework and relevant background necessary to understand the evolution of perovskite field and the physics described in the following chapters. In Chapter 3, we summarise the experimental techniques and protocols for materials synthesis and characterisations used to acquire our results.

Chapter 4 focuses on the optimisation of the interfacial properties of titanium dioxide as the electron transport layer in mesoscopic perovskite solar cells. We show modification of the mesoporous-TiO_2 by $TiCl_4$ treatment substantially reduces the surface traps and energetic disorder and lead to an order of magnitude enhancement in the bulk electron mobility and corresponding decrease in the electron transport activation energy. We also demonstrate the optimization on particle size and porosity of the mesoporous-TiO_2 to enhance the charge collection efficiency leading to decreased recombination at the interface with perovskite via a compact formation of the capping $CH_3NH_3PbI_3$ layer.

In Chapter 5, we investigate the possibility of doping in perovskite with monovalent cation additives having similar ionic radii to lead including sodium, copper and silver, and their impact on the structural and optoelectronic properties of $CH_3NH_3PbI_3$ perovskite. We observed significant reduction of sub-bandgap optical absorption and lower energetic disorder along with a shift in the Fermi level of the perovskite in the presence of these cations. The bulk hole mobility of the additive based perovskites as estimated using the space charge limited current method exhibited an increase of up to an order of magnitude compared to the pristine perovskites with a significant decrease in the charge transport activation energy. The enhanced properties of additive-based perovskite reflected in the performance of the subsequent solar cells originating from the formation of uniform and continuous perovskite film, better conversion and loading of perovskite as well as the enhancement in the bulk charge transport along with a minimization of disorder via additive pointing towards possible surface passivation. We then show the chemical distribution and electronic structure of solution

processed $CH_3NH_3PbI_3$ perovskite structures upon doping with these cations. A shift in the main perovskite X-ray diffraction peaks for the monovalent cation-based films suggests incorporation of these cations into the perovskite lattice. We also find a significant change in the valence band position for Cu- and Ag-doped films although the perovskite bandgap remains the same, indicating a shift in the Fermi level position towards the middle of the bandgap. Such a shift infers that incorporation of these monovalent cations de-dope the n-type perovskite films when formed without added cations. This de-doping effect leads to cleaner bandgaps as reflected by the lower energetic disorder in the monovalent cation doped perovskite thin films as compared to pristine films. Density functional theory (DFT) calculations show that the formation energies favour interstitial doping over substitutional doping. We model a significant change in the local structure, chemical bonding of metal-halide and the electronic structure in the doped perovskites.

In Chapter 6, we demonstrate a novel passivation approach in alloyed perovskite films to inhibit the ion segregation and parasitic non-radiative losses, which are key barriers against the continuous bandgap tunability and potential for high-performance of metal halide perovskites in device applications, by decorating the surfaces and grain boundaries with potassium halides. This leads to luminescence quantum yields approaching unity while maintaining high mobilities exceeding 40 $cm^2V^{-1}s^{-1}$, along with the inhibition of transient photo-induced ion migration processes even in mixed halide perovskites that otherwise show bandgap instabilities. We propose that potassium iodide additives minimize halide vacancies, which are responsible for charge carrier trapping, while also immobilizing the surplus halides into benign products. We demonstrate a wide range of bandgaps stabilized against photo-induced ion migration, leading to solar cell power conversion efficiencies of 21.6% for a 1.56 eV absorber and 18.3% for a 1.78 eV absorber ideally suited for tandem solar cells.

We then summarize our study on the optoelectronic properties of multiple cation perovskite films focusing on the passivated triple-cation lead mixed halide perovskite with potassium and rubidium species in Chapter 7. The optoelectronic and chemical studies reveal that the alloyed perovskites are tolerant towards higher loadings of potassium than rubidium. Whereas potassium complexes with bromide from the perovskite precursor solution to form thin passivation layers that decorate perovskite grain boundaries and interfaces, rubidium additives, at similar concentrations, favour the formation of phase-segregated micron-sized rubidium-halide crystals. This tolerance by the mixed-cation lead mixed-halide perovskite to higher

loadings of potassium allows us to achieve superior luminescent properties with potassium passivation.

In Chapter 8, we first explore the possibility of singlet exciton fission from tetracene as the triplet sensitizer and synthesised low-bandgap perovskite films based on mixture of lead (Pb) and tin (Sn) as the divalent cation ($CH_3NH_3Sn_xPb_{1-x}I_3$). We show no significant energy transfer from tetracene to perovskite based on the collected negative feature from tetracene in the excitation scan of perovskite as well as no magnetic field photoluminescence response for perovskite peak when it is interfaced with tetracene. In the second part of this chapter, we introduce tetracene as a dopant free and efficient hole-extraction layer in the rubidium passivated perovskite solar cells. We demonstrate that tetracene provide clean interfaces with perovskite layer leading to high photoluminescence yield (e.g. ~18%) while it shows poor ohmic contact with the metal electrode. We then show using a capping layer of another hole-extraction layer (e.g. doped Spiro-OMeTAD) provides a graded hole-injection interface with superior ohmic contacts. For complete solar cell devices containing tetracene and a capping layer of doped Spiro-OMeTAD as the graded hole transport layers, we demonstrate PCEs of up to 21.5% and stabilised power output over 550 hours continuous illumination, validating our approach.

Lastly, in Chapter 9, we review the chief results that are presented in this thesis, and suggest some possible directions for future research.

1. Introduction

Chapter 2

Background

This chapter would briefly introduce the photovoltaic devices and plausible ways to go beyond efficiency limits in solar cells. It also introduces to the emerging field of metal halide perovskite semiconductors explaining the evolution of perovskite solar cells, versatile forms and the relevant properties of them that will be discussed in the thesis.

2.1 Solar Energy

Currently, the dominant portion of the world's energy requirement (*i.e.*, 85%) is being supplied by the combustion of oil, coal, and natural gas, which facilitates global warming and has deleterious effects on our environment[9]. Therefore, the development of CO_2-neutral sources of renewable energy is of paramount interest. Among all renewable energy resources, solar energy is by far the largest exploitable one. About $8.9\times1o^4$ TW of solar radiation reaches the surface of our planet, and even if only a fraction of this energy can be harvested, it has an immense potential of providing carbon-neutral electricity. According to the World Energy Outlook of the International Energy Agency (EIA), individuals' access to electricity is one of the most clear undistorted indications of a country's energy poverty status. However, to date about 1.3 billion people worldwide, near 20% of the world's population, are still deprived of access to electricity[10]. Since the sun shines all over the planet and is abundantly available in most developing countries, exploiting solar energy could be a major driving force for economic development or at least for an improvement of living-conditions.

Despite of these promising facts, only about 1.3% of the world's power capacity is covered so far by photovoltaics (PV). Although PV capacity has experienced an exponential growth in the past 5 years and has reached a total installed capacity exceeding 400 GW_p in 2017[11], more efforts are needed from politicians and scientists to reach a sizeable share of PV in total energy consumption. Furthermore, cost and efficiency, as the main obstacles to the extensive adoption of PV technologies, must be tackled.

In recent years, the decreasing price of PV systems has levelized the cost of PV produced electricity to the point that it can now compete with the variable portion of consumer electricity prices in many countries worldwide. Substantial further cost reduction is required, however, to allow PV to compete in more electricity markets and to enter the multi-terawatt regime. To date, the PV market is mainly dominated by crystalline silicon modules relying on the use of large quantities of expensive and energy-intensive, high purity crystalline or polycrystalline silicon. In order to reduce material usage and cost, much effort has been devoted to thin-film technologies, such as CdTe, $CuInSe_2$ (CIS), Cu (In, Ga) Se_2 (CIGS) and amorphous Si (a-Si: H). Emerging PV thin-film technologies based on new materials, such as organic PV (OPV), dye-sensitized solar cells (DSCs) and, particularly the most recent one, perovskite solar cells (PSCs) have the combination of lower cost and comparable efficiency[12]. These emerging PV

technologies hold the promises for significantly reduced fabrication cost and environmental impact through solution-based, scalable roll-to-roll processing and short energy payback times[13,14].

2.2 Solar Cells; definition, history and efficiency limit

Solar cells are devices for directly converting the sun's energy into electricity via producing voltage upon illumination. The active material is typically a semiconductor, which absorbs photons and excites electrons. The photo-excited electrons are then extracted via the n-type electrode (anode), and a hole is injected into the p-type contact (cathode). The most common architecture of a solar cell contains a semiconducting material sandwiched between n- and p-type electrodes. To generate photocurrent, separation of electrons (e^-) and holes (h^+) need to be followed by their movement towards the respective electrodes. The power conversion efficiency (PCE) of a solar cell is defined as the ratio between the electrical power output and the optical power input.

The photovoltaic effect was first demonstrated by Becquerel in the early 19th century, most likely around 1839-1841[15]. By far the most widely known and studied solar cells is the crystalline silicon which is based on the p–n junction (formed when n-type semiconductors (semiconductors doped with impurities leading to an excess of electrons) and p-type semiconductors (doped to give an excess of holes) are brought into intimate contact). The first practical silicon p-n junction solar cell was invented in 1953 at Bell Labs[16]. Silicon photovoltaics increased their PCE in the 20th century from 1% to 6%[16]. The power conversion efficiency of silicon photovoltaics has increased steadily since then until the end of the 20th century when it reached 25%[17], and it has shown only minimal improvement in the past 20 years reaching 26.7%[18,19].

The fundamental efficiency limit of a solar cell is determined by several factors as shown in Figure 2.1. Photons with energies below the optical band gap of the semiconductor are not absorbed, whereas photons with energies above the band gap are not completely converted to electrical output because of thermalization of charge carriers (Figure 2.1a, inset). Based on these two factors, ~45% of the incident spectrum integrated solar power remains for semiconductors with a band gap of 1.1 to 1.4 eV[20]. This is the highest PCE that would be generated if the solar cell were operated at a voltage corresponding to the band gap energy and

a current corresponding to full capture of all photons with energy above the band gap, followed by full collection of all generated carriers[21].

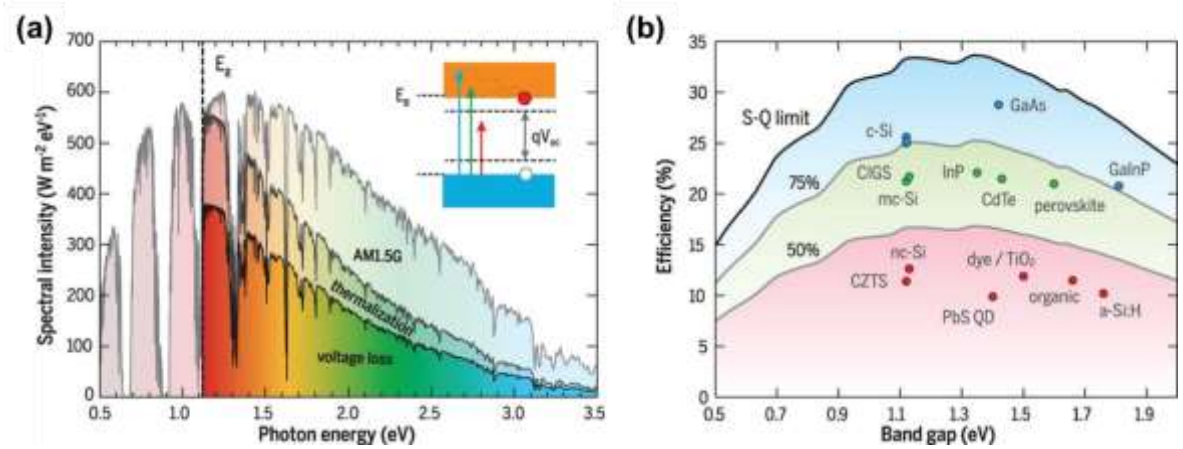

Figure 2.1. Origin of efficiency limits in solar cell and relative records for a variety of PV technologies. (a) The solar spectrum at AM1.5 with distinct dips due to molecular absorption in Earth's atmosphere. Photons with energies below the band gap (E_g, dashed black line corresponds to the band gap of Si) are not absorbed, whereas photons with energies above the band gap are not fully converted to electrical energy because of thermalization of charge carriers. The maximum power generated by the solar cell is limited by voltage loss relative to the band gap voltage. Inset: Electronic band structure with the separation of the quasi-Fermi levels determining the open-circuit voltage Voc. (b) Theoretical Shockley-Queisser detailed-balance efficiency limit as a function of band gap (black line) and 75% and 50%of the limit (gray lines).The record efficiencies for different materials are plotted for the corresponding band gaps. Figure from Polman and colleagues[9].

However, the open-circuit voltage (V_{oc}) even in an ideal solar cell is always lower than the band gap energy of the semiconductor because thermodynamic detailed balance requires the cell to be in equilibrium with its environment, which implies that there is spontaneous light emission from the cell. The corresponding radiative carrier recombination represents a dark current that causes V_{oc} to be considerably below the band gap voltage V_g (Figure 2.2b). Furthermore, under maximum-power operation (at maximum $J \times V$), the voltage V_{mp} is lower than V_{oc} and the current density J_{mp} is lower than the maximum (short circuit) current density J_{sc} (Figure 2.2a,

inset). The efficiency limit considering these factors was first derived by Shockley and Queisser (S-Q) in 1961[21]. In Figure 2.1b, we see this limiting efficiency for a single-junction solar cell under "one-sun" illumination (100 $mW.cm^{-2}$) with the standard AM1.5 solar spectrum as a function of band gap; the maximum efficiency occurs for a semiconductor with a band gap of 1.34 eV and is 33.7%[9].

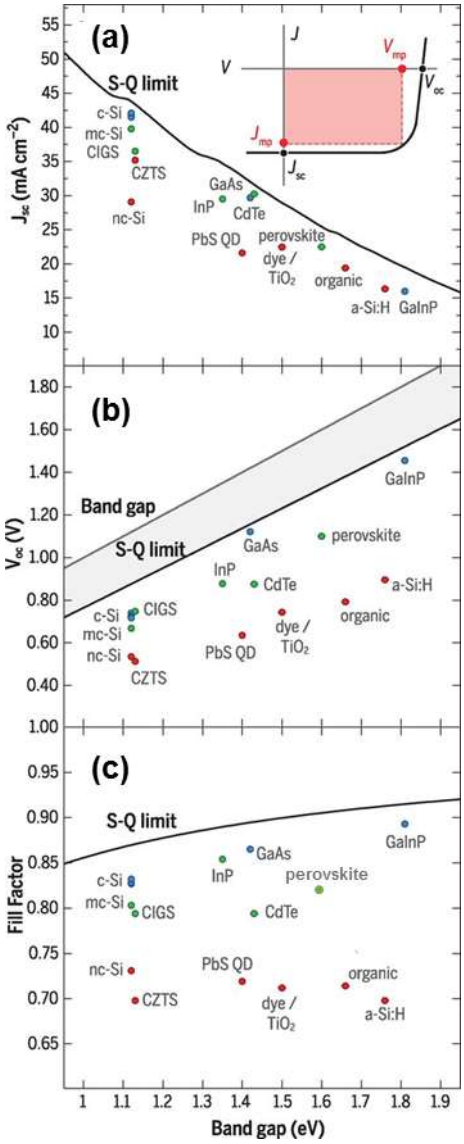

Figure 2.2. A comparison between the detailed-balance S-Q limit and the photovoltaic parameters of the record device in different solar cell technologies. Single-junction solar cell parameters are shown as a function of band gap energy according to the Shockley-Queisser limit (solid lines) and reported experimental values for record-efficiency cells. (a) Short-circuit current J_{sc}. Inset: A typical current-voltage curve, with V_{oc}, J_{sc}, V_{mp}, and J_{mp} indicated. The

product of current and voltage is highest at the maximum power point ($J_{mp}V_{mp}$). (b) Open-circuit voltage V_{oc}. The voltage corresponding to the band gap is shown for reference, with the voltage gap V_g-V_{SQ} indicated by the gray shaded region. (c) Fill factor FF = $(J_{mp}V_{mp})/(V_{oc}J_{sc})$. All the photovoltaic parameters are measured at standard AM1.5 illumination at one-sun (100 mW/cm^{-2}). Figure from Polman and colleagues[9].

In operating solar cells, not all incident light is absorbed in the active layer(s) and not all generated carriers are collected; hence, J_{sc} is below the maximum value that can be achieved for a given band gap, E_g (Figure 2.2a). The achievable V_{oc} is also reduced below the S-Q value by such phenomena as Auger recombination, band tail recombination, and recombination at bulk, interface, and surface defects (Figure 2.2b)[22–24]. Furthermore, resistance and contact losses and other non-idealities reduce the fill factor (Figure 2.2c), defined as $FF = (J_{mp}V_{mp})/(V_{oc}\ J_{sc})$[25]. Combined, these factors lead to practical efficiencies that are often substantially lower than the S-Q limit for a given band gap.

2.3 Beyond the Shockley-Queisser limit

As stated in the previous section, the S-Q detailed-balance model describes the efficiency limit for a single-junction solar cell under one-sun illumination. It is plausible to suppress the S-Q limit for a single junction solar cell via using the process of multiple exciton generation (converting a single photon to multiple excitons, e.g., in quantum dots), by up- or down-conversion of incident light (to make the incident spectral range better match the semiconductor absorption spectrum), or by limiting the range of radiative emission angles (raising the cell voltage)[26,27]. For instance, singlet exciton fission (SF) is process where the energy from one highly energetic spin-singlet exciton can be rapidly re-distributed into two triplet excitons with half of the initial singlet energy. Singlet exciton fission is spin-conserving process since the initial combined spin-state of the two triplet excitons has spin 0, as illustrated in Figure 2.3[28]. This process is shown to occur on sub-100 femtosecond timescales with yield of 200%[29,30]. The energy re-distribution in SF allows for doubling the photocurrent from blue light. When combining such a high-bandgap SF material with a low-bandgap semiconductor, the analogue to the Shockley-Queisser limit rises from 33.7% to 46 %. Figure 2.3b highlights the potential photocurrent contribution of an organic fission layer combined with a low bandgap acceptor such as silicon.

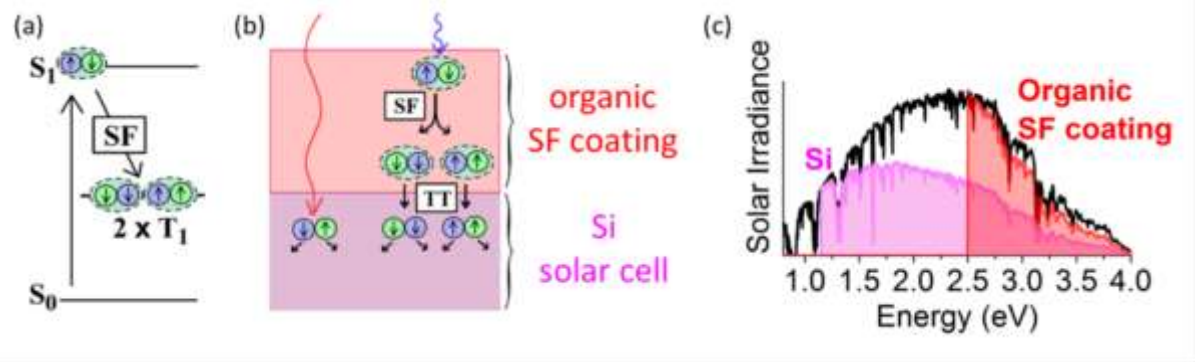

Figure 2.3. Mechanism for singlet exciton fission (SF) process in organic materials. (a) One photogenerated singlet exciton (S1) undergoes fission into two triplet excitons (T1). (b) An illustration of how any type of solar cell, e.g. from silicon (Si), can be SF sensitized using triplet transfer (TT) from a thin organic SF coating. The organic layer absorbs high-energy photons, which generate singlet excitons and undergo singlet fission to form triplet excitons. The triplet excitons are then transferred into the inorganic layer where charges can easily be separated and extracted at electrodes. Simultaneously the inorganic harvests low-energy photons. (c) Illustration that the SF process can lower heat loss from blue sunlight in Si solar cells. Figure used with permission from reference[31].

Another way of going beyond the S-Q limit in solar cells is to utilize multi-junction concept[32] where multiple p-n junctions made of semiconductor materials with different bandgap are implemented in the device architecture to absorb a broader range of wavelengths (Figure 2.4). Theoretically, an infinite number of junctions would have a limiting efficiency of 86.8% under highly concentrated sunlight[33]. The highest reported efficiency under one-sun illumination is 38.8% for a GaInAs/GaInP/GaAs/AlGaInAs/AlGaInP five-junction tandem geometry[19]. However, the manufacturing of multi-junction devices architecture is complex and expensive as ultrahigh-vacuum crystal-growth techniques are required to epitaxially grow the single-crystalline semiconductor layers as well as the intermediate tunnel barrier buffer layers. Moreover, in the series-connected architecture current-matching among the subcells is required, meaning that the subcell generating the lowest current limits the overall multi-junction cell current. Furthermore, the lattice-matched crystal-growth process limits the semiconductor materials composition. Furthermore, the optically series-connected configuration dictates that each subcell is subject to the same light-concentration factor, an additional constraint reducing power-generation efficiency.

An alternative approach is shown in Figure 2.4b; a design for a multi-junction photovoltaic architecture featuring an optically-in-parallel array of high-efficiency single-junction cells that form the receiver of a spectrum-splitting photonic structure[34]. In this architecture, the spectrum-splitting structure directs light of different wavelengths to individual subcells that are optimized for the corresponding spectral bands and concentration factor, with no limitations due to current matching, and with full flexibility in the choice of semiconductor material for the different subcells. Furthermore, although conventional multi-junction cells have employed three or four subcells, and the overall thermalization loss is still substantial, the alternative depicted in Figure 2.4b can easily accommodate a larger number of subcells. If narrow (<300 meV) spectral bands from a spectrum-splitting photonic structure can be efficiently directed to an array with 8–10 types of subcell, thermalization can be limited to approximately 10%[35].

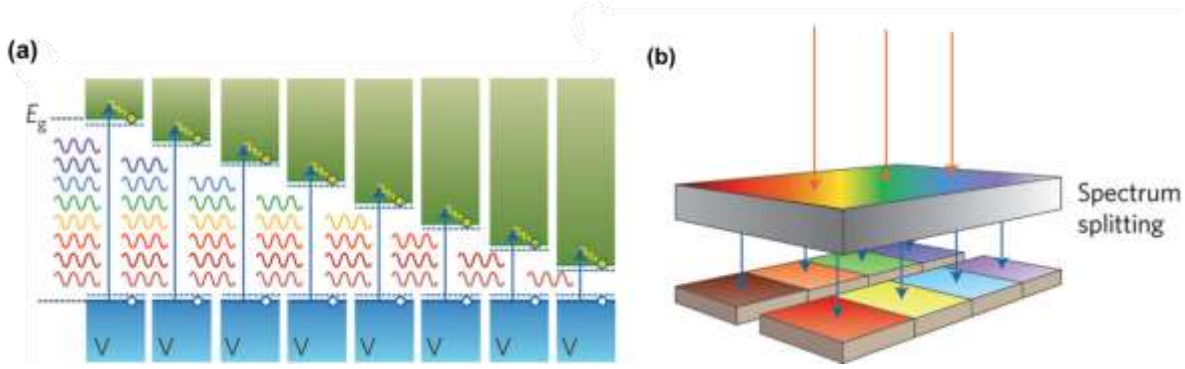

Figure 2.4. Multi-bandgap energy diagrams. In (a) the chemical potentials defining the open circuit voltages are illustrated with blue dashed lines, and the energy of the incoming photons with a gradient of colors, where the blue are those with higher energies and red the lowest. In (b) a potential implementation of such system using spectrum splitting is illustrated. Figure from Polman and coulleages[35].

Furthermore, concentrating PV, that is, increasing the solar flux by focusing light on a solar cell, can (linearly) increase J_{sc} and (logarithmically) increase V_{oc}, leading to a higher efficiency[36]. This concept has been applied in PV systems using macroscale lenses or parabolic mirrors in combination with ultrahigh-efficiency tandem cells[37]. A record cell efficiency of 46.0% was measured using a GaInP/ GaAs/GaInAsP/GaInAs tandem cell under 508×

concentrated light[19]. Concentrating PV requires a tracking system to follow the Sun and requires direct (rather than diffuse) sunlight[38].

2.4 Perovskite Semiconductors

Perovskites originate from the discovery of $CaTiO_3$ by the Russian mineralogist Lev Perovski. Later, many materials with the same crystal structure were discovered and more generally, perovskite represent AMX_3 crystals, where A is a monovalent cation, M a divalent metal cation and X an oxide or a halide anion. Perovskites extend as a three-dimensional network formed by an MX_6 corner-sharing octahedron arrangements where M occupies the center of an octahedra surrounded by X located at the corners (Figure 2.5). Species A represents a monovalent cation, which fills the hole formed by the eight adjacent octahedra in the three-dimensional structure and balances the charge of the whole network. The large monovalent metal cation A can be Ca, K, Na, Pb, Sr, or various rare metals. In case of organic–inorganic hybrid perovskite, A is replaced by an organic cation, which is enclosed by twelve nearest X anions. The prerequisite for a closed-packed perovskite structure is that the organic cation must fit in the hole formed by the eight adjacent octahedra connected through the shared X corners. Too bulky organic cations cannot be embedded into the 3D perovskite. The size of organic cation and metal ion is an important parameter to modulate the optical and electronic properties of perovskite material. Ideally, perovskites have cubic geometry but in fact, they are pseudo-cubic or distorted cubic in nature[39]. Any kind of distortion will influence physical properties of perovskite materials, such as electronic, optical, magnetic and dielectric properties.

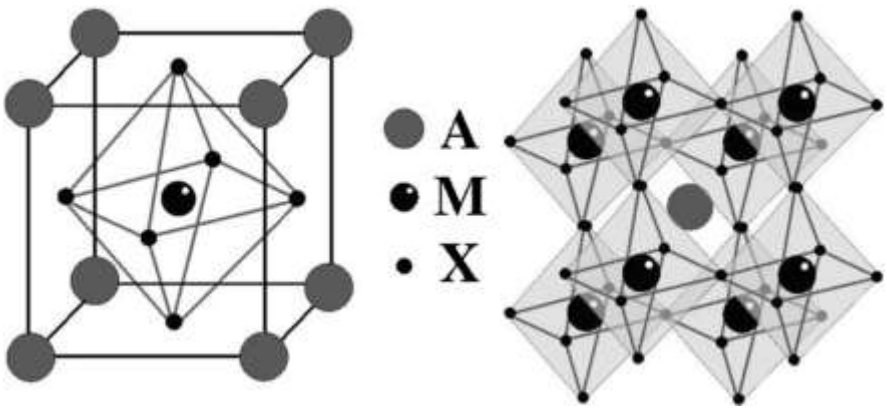

Figure 2.5. Ball-and-stick model of the basic perovskite structure (Left). Right: Extended 3D perovskite network structure connected through corner-shared octahedra[39].

The other typical structure of organic–inorganic perovskite materials is two-dimensional layered perovskite, which are formed by alternating the organic and inorganic layer in the structure. The concept of two-dimensional layered organic–inorganic perovskite structure was derived from the three-dimensional AMX_3 structure by cutting 3D-perovskite into one layer thick slice along <100> direction. A is replaced by suitable cationic organic molecule, which can be aliphatic or aromatic ammonium cations. The inorganic layer, denoted as "perovskite sheet", consists of corner-sharing metal halide (MX_6) octahedral which are then sandwiched by these cationic organic molecules to form two-dimensional organic–inorganic layered perovskite[40]. The perovskite structures are illustrated in Figure 2.6 and can be denoted by general formula $(RNH_3)_2MX_4$ or $(NH_3^+\text{-}R\text{-}NH_3^+)MX_4$, where X is a halogen, M is a divalent metal ion such as Cu^{2+}, Ni^{2+}, Co^{2+}, Fe^{2+}, Mn^{2+}, Pd^{2+}, Cd^{2+}, Ge^{2+}, Sn^{2+}, Pb^{2+}, Eu^{2+} etc. or trivalent Bi^{3+} and Sb^{3+}[41]. The organic layer consists of either a bilayer or a single layer of cationic organic molecules between the inorganic perovskite sheets for $(RNH_3)_2MX_4$ or $(NH_3^+\text{-}R\text{-}NH_3^+)MX_4$ structure, respectively, where R is organic radical group. By taking the example of bilayer (monoammonium cation, RNH_3^+), the NH_3^+ head of the cationic organic molecule is tethered to the halogens in one inorganic layer through hydrogen/ionic bonding, and the R group is located in a tail-to-tail conformation through van der Waals interactions into the gap between the inorganic layers.

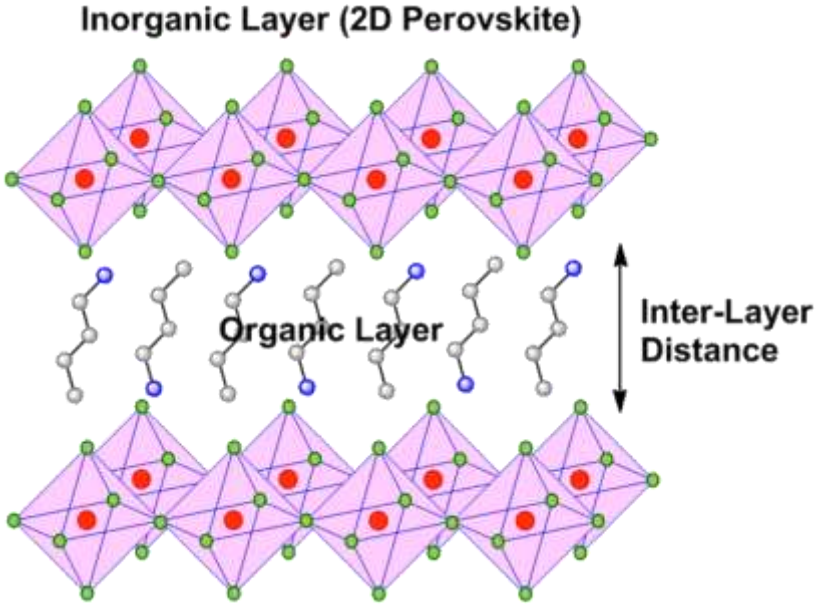

Figure 2.6. The schematic for two-dimensional (2D) organic-inorganic perovskite crystal structure. Adapted form reference[40].

2.5 Metal Halide Perovskite in photovoltaic devices

Research on metal halide perovskites has started over a century[12], although present results benefit from recent investigations of implemented perovskite thin-film in transistors and light-emitting diodes (LEDs) by Mitzi and co-workers[40,42]. Although these LEDs doubtless exhibited photovoltaic properties and their use in solar cells was anticipated[40], this was not studied at the time, partly because of Pb toxicity and the fact that more benign Sn materials were not considered to be sufficiently robust[12].

Miyasaka and co-workers reported the first implementation of perovskite materials in photovoltaic devices in 2009[5]. This work employed $CH_3NH_3PbX_3$ (X = Br, I) perovskite nanocrystals to replace the conventional dye sensitizer, in liquid electrolyte-based dye sensitized solar cells. They measured a relatively low power conversion efficiency (PCE) of 3.8% and 3.1 % in $CH_3NH_3PbI_3$- and $CH_3NH_3PbBr_3$-based cells, respectively. Soon after, the PCE was raised to 6.5% via surface treatment of titania, as reported in the work by Park and colleagues in 2011[43]. However, these cells suffered from a major drawback, as they were decomposing very rapidly, typically 80% degradation after 10 min of illumination, due to the dissolution of the perovskite in the liquid electrolyte[44].

The interest in the perovskite system has soared with its introduction in the solid-state counterpart of the dye-sensitized solar cell, using Spiro-OMeTAD (2,2',7,7'-tetrakis(N,N-di-p-methoxyphenylamine)-9,9'-spirobifluorene) as the hole transport layer[7,45], which was first developed for organic LEDs[46] but was also found to be effective in solid-state dye cells[47]. Record efficiencies of 9.7% were obtained for $CH_3NH_3PbI_3$ deposited on TiO_2 mesoporous framework (Figure 2.7a)[33], while in the same period Lee et al. reported PCE of 10.9% for a supposedly mixed halide $CH_3NH_3PbI_2Cl$ deposited on Al_2O_3 framework[34], where no extraction of the charges in the mesoporous oxide is possible. Due to the high short-circuit currents and photo-voltages (respectively close to 20 mA cm^{-2} and 1 V), these two works with four additional developments broaden the field significantly.

One of these developments was the use of the mixed-halide $CH_3NH_3PbI_{3-x}Cl_x$, which exhibited better stability and carrier transport than its pure iodide equivalent[7,48]. A second involved going beyond earlier nanoparticle structures by coating mesoporous TiO_2 surfaces with a thin perovskite capping layer and thereby forming relatively thin absorber cells (Figure 2.7b)[49]. A third was replacing conducting mesoporous TiO_2 by a similar but non-conducting Al_2O_3

network. This improved the open-circuit voltage (V_{oc}), boosting the reported efficiency to 10.9%; it also demonstrated that perovskites have a broader potential than just being used as sensitizers, as they are able to transport both electrons and holes between cell terminals[34]. The fourth development exploited such ambipolar transport by demonstrating simple planar cells with the scaffolding (Figure 2.7c, d) completely eliminated[50].

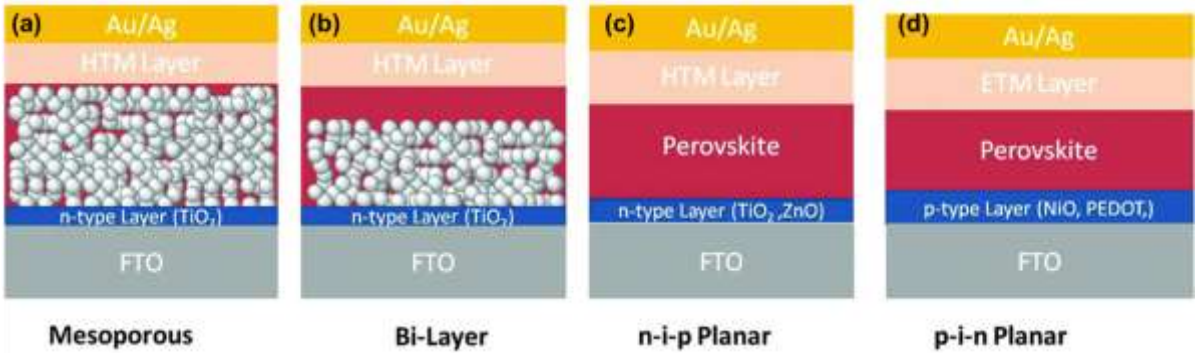

Figure 2.7. Evolution of perovskite device structures. Schematic illustration for (a) mesoscopic, (b) bilayer, planar (c) n-i-p and (d) p-i-n architectures in perovskite solar cells. HTM and ETM represent the hole-transporting material and electron-transporting material, respectively[51].

Further progress in PCE of halide perovskite solar cells was achieved by using a modified perovskite processing method so-called sequential deposition for the fabrication of perovskite on mesoporous titania film leading to a PCE of 15% and a certified value of 14.1% with high reproducibility[49]. At the end of 2013, the efficiency of perovskite devices were further improved to 16.2% by using the mixed-halide $CH_3NH_3PbI_{3-x}Br_x$ (10–15% Br) and a poly-triarylamine HTM. Rapid progress in efficiency from 17.9% in early 2014 to the certified value of 20.1% in November 2014 was achieved by Seok and colleagues at KRICT. This enhancement in efficiency was achieved via chemical modification of perovskite (e.g. introduction of $MAPbBr_3$ into the $FAPBI_3$, MA= CH_3NH_3 and FA= $CH(NH_2)_2$)[52] and developing a new processing method based on a solvent treatment[53]. Although devices based on both $FAPbI_3$ and $FAPbBr_3$ had been earlier reported[54,55], one problem with the iodide is the existence of an isomorphous room-temperature hexagonal phase with much poorer photovoltaic properties. Techniques for stabilizing the desired perovskite phase include high-

temperature annealing post deposition; sequential deposition of PbI_2 followed by FAI reducing the required annealing temperature; intramolecular exchange during sequential deposition; or forming solid solutions $FA_{1-x}MA_xPb(I_{1-y}Br_y)_3$ with both mixed cations and anions,[56] where x is typically 10% and y ranges from 0 to 20%.

An efficiency of 21% was confirmed in late 2015 for a small-area cell that used poly(methyl methacrylate) (PMMA) as a template to control nucleation and crystal growth to prepare perovskite films of high electronic quality in conjunction with $[(FAI)_{0.81}(PbI_2)_{0.85}(MAPbBr_3)_{0.15}]$ precursor solution[57]. This efficiency was further enhanced to 21.6% in late 2016 via addition of rubidium monovalent cation to the triple cation lead mixed halide perovskite containing $(CsFAMA)Pb(I_xBr_{1-x})_3$[58,59]. Furthermore, perovskite solar cells exhibited a certified PCE of 22.1% in June 2017 via managing the halide ratios in formamidinium-lead-halide–based perovskite by Seok and colleagues[60]. They recently surpassed their previous certified efficiency record to 22.7%, which the basic of such work has not yet been published. Based on their recent publication[61], the role of a mediator "to retard the rapid crystallization between organic cations and PbI_2" is stressed as is the role of manipulating "the chemical composition of the perovskites via solvent engineering and intramolecular exchange process" . Importantly, to go beyond 22%, the luminescent properties of the perovskite materials need to be better understood to improve open-circuit voltage (V_{oc}), " because J_{sc} and FF have already attained realistic values". In the Chapter 6 of this thesis, we developed a new passivation approach that boost the luminance efficiency of perovskite in device architectues[62].

2.6 Different forms of metal halide perovskites

A remarkable aspect of metal halide perovskites, compared with other common semiconductors such as crystalline Si and GaAs, is their high crystallinity despite low-temperature processing (sub-200 °C). This enables processing on a range of substrates, and allows facile fabrication of various forms of perovskite materials ranging from nanocrystals to macroscopic single crystals. In the below sub-sections, different forms of perovskites and their fundamental properties are described.

2.6.1 Perovskite nanocrystals

There has been a considerable number of reports on synthesis of monodisperse colloidal nanocrystals based on fully inorganic caesium lead halide perovskites ($CsPbX_3$, X = Cl, Br, I or a mixture thereof) by reacting Cs-oleate with a Pb(II) halide in octadecene[63–65]. Intersnitgly, these perovskite nanocrystals show remarkably high (up to 90%) photoluminescence quantum efficiency (PLQE), narrow emission linewidths (12–42 nm) and spectral tunability across the full visible spectrum (410–700 nm) through compositional modulations and quantum confinement (Figure 2.8a)[63]. Compared with metal chalcogenide-based quantum dots, perovskite nanocrystals have a simpler chemical synthetic route and do not seem to require complex core–shell structures, which have been a prerequisite for high PLQE from CdSe quantum dots[64]. The importance of achieving 90% PLQE is comparable to the sudden surge in power conversion efficiency of perovskite solar cells that the PV field has witnessed.

Furthermore, a novel process route based on a catalyst-free solution-phase synthesis for $CsPbBr_3$ (Figure 2.8b) and $CsPbI_3$ nanowires (Figure 2.8c) has developed[66]. Surprisingly, $CsPbX_3$ nanocrystals crystallize into a cubic phase at room temperature, while the $CsPbX_3$ nanowires show an orthorhombic phase, highlighting the importance of the synthetic conditions and the size and shape of the nanostructures for crystal phase transitions[66]. In the bulk, these materials are not stable in the cubic perovskite structure at room temperature in ambient conditions, and convert into a non-perovskite orthorhombic phase less interesting for light emission and photovoltaic applications[67]. Notably, a similar strategy has been adopted for the synthesis of $MAPbX_3$ nanocrystals and $MAPbX_3$ nanorod arrays[68] (Figure 2.8d).

Moreover, other forms of perovskites including platelets[69] (Figure 2.8e) and microspheres[70] (Figure 2.8f), have also been fabricated to exploit their novel structure–function properties for light-emitting applications. It is expected that the activity in perovskite-based colloidal crystals and crystal control on the nano- and microscale to emerge into a field in its own right over the next few years; it is especially relevant to low-power light-emitting technologies[64].

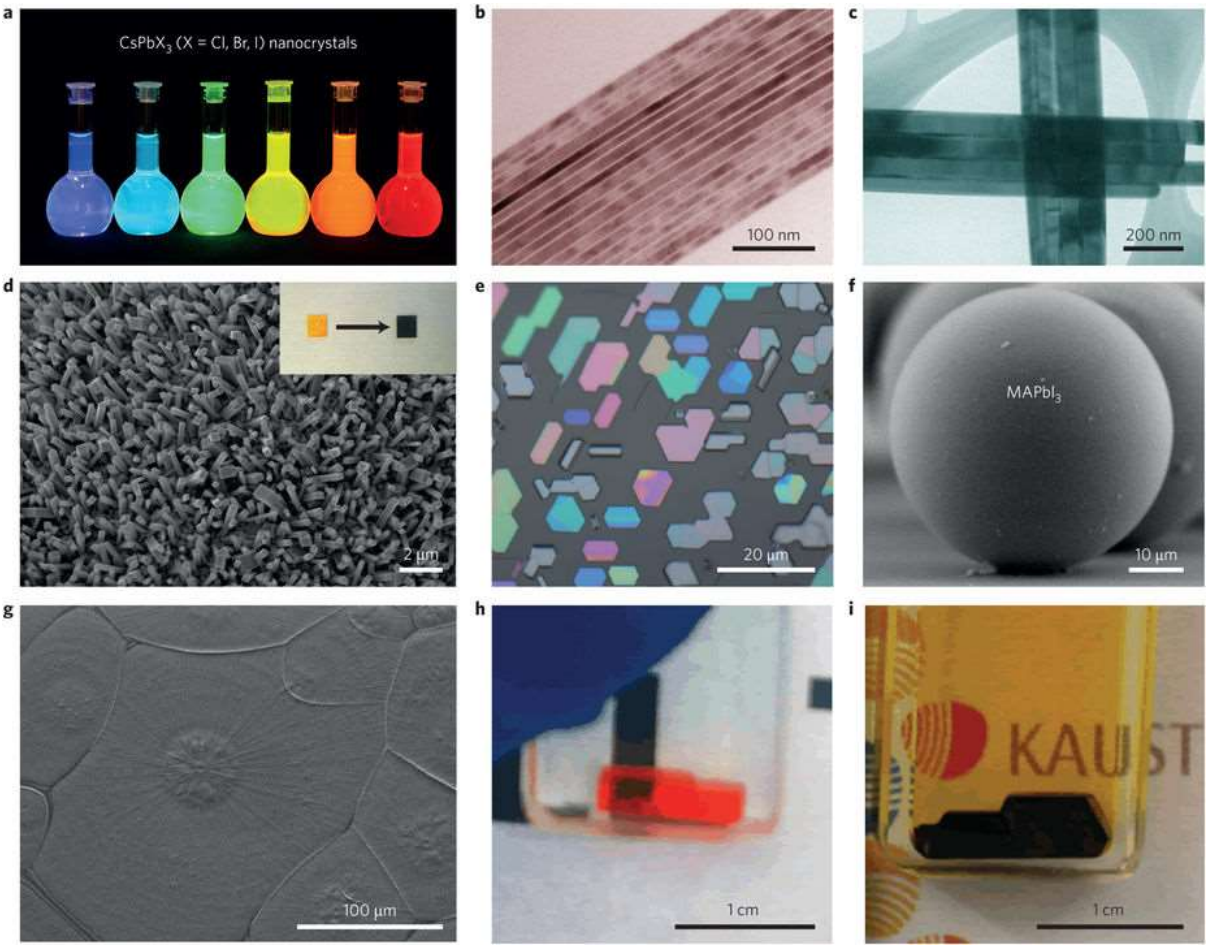

Figure 2.8. **Different forms of metal halide perovskite semiconductors.** (a) Colloidal solutions of $CsPbX_3$ (X = Cl, Br, I) nanocrystals in toluene under an ultraviolet lamp (λ = 365 nm)[63]. (b), (c) Scanning electron microscopy (SEM) images of $CsPbBr_3$ (b) and $CsPbI_3$ (c) nanowires grown by solution-phase synthesis[66]. (d) A $CH_3NH_3PbI_3$ nanorod array formed by vapour phase anion exchange of a $CH_3NH_3PbBr_3$ nanorod array. The inset shows a photograph of a converted chip[71]. (e) An optical image of $CH_3NH_3PbI_3$ platelets prepared by vapour phase synthesis[69]. (f) SEM image of a SiO_2 microsphere coated with $CH_3NH_3PbI_3$ via atomic layer deposition[70]. (g) A SEM image of a $CH_3NH_3PbI_3$ thin film with large polycrystalline domains prepared by doctor-blade coating on a large area[72]. (h), (i) Shape-controlled single crystals of $MAPbBr_3$ (h) and $MAPbI_3$ (i) formed by inverse temperature crystallization[73].

2.6.2 Polycrystalline thin films

The dominant form of metal halide perovskites particularly for photovoltaic applications is polycrystalline based thin film. Unlike other common semiconductors used for thin-film solar

cells, perovskite thin films can be fabricated with similar properties via various deposition procedures, including solution processing[7,45,49], physical vapour phase[50] deposition and combinations of both[74]. Solution processing has advantages over vapour phase deposition in terms of relying on inexpensive deposition equipment, while vapour phase deposition avoids the use of toxic solvents and allows the deposition of homogenous thin films with precisely tunable thickness on arbitrary substrates[75].

Notably, the semiconductor quality of the perovskite thin films, which is highly dependent on the material purity and fabrication method, is of paramount importance for device performance and reproducibility[76]. To date, tremendous efforts have been devoted to optimizing the perovskite crystallization and film formation to obtain highly crystalline and pinhole-free perovskite thin films[77]. Recently, perovskite thin films with full surface coverage and large polycrystalline domains (Figure 2.8g) have been achieved on a large area by doctor-blade coating the precursor inks on hot substrates, resulting in impressive device efficiencies[72].

Observations of non-radiative recombination at grain boundaries in polycrystalline thin films[78] and remarkably high radiative efficiency in perovskite nanocrystals, lead to contradictory interoperations in the feild[64]. Non-radiative recombination at grain boundaries motivates evolving the perovskite thin films towards single-crystal domains, whereas high radiative efficiency indicates that perovskite crystal surfaces are not inherently defective[79]. This indicates the alternative possibility of developing polycrystalline thin films with negligible non-radiative recombination losses, which may require passivation techniques to inhibit grain to grain interactions[62].

2.6.3 Perovskite single crystals

For growth $MAPbX_3$ single crystals, anti-solvent vapour-assisted crystallization method[80] is replacing the classical lengthy cooling-induced crystallization[81]. This enables the preparation of high-quality single crystals at room temperature. The high quality is reflected by low trap-state densities on the order of 10^9 to 10^{10} cm^{-3}, comparable to crystalline silicon grown at high temperature (10^8–10^{15} cm^{-3}), and charge carrier diffusion lengths exceeding 10 μm have been estimated, compared with ~1 μm in a polycrystalline film[48].

This novel crystallization approach rely on the decreased solubility of the perovskite precursor salts in the growth medium. There has recently been an unexpected discovery of an apparent

'inverse solubility' behaviour for $MAPbX_3$ precursor[73,82]. As the temperature of the solution is increased, large crystals are observed to precipitate from the solution. On subsequent cooling, the crystals re-dissolve. Despite lack of understanding of the mechanism, however, this process has been capitalized on to enable the rapid synthesis of various large perovskite crystals (Figure 2.8h, i), providing a good platform for a range of optical and electrical characterizations[73], and broad optoelectronic applications such as photodetectors[83] and radiation energy harvesting[84]. One of the greatest benefit of the single crystal research is an added learning and understanding of crystallization, which will be beneficial for reaching the optimum properties in polycrystalline thin films[85].

2.7 Properties of Metal Halide Perovskite Semiconductors

2.7.1 Optical absorption and Urbach energy

Strong optical absorption is the key to the outstanding performance of perovskite solar cells, reducing both the required thickness and the challenges in collecting photo-generated carriers. Absorption measurements (Figure 2.9a) are consistent with calculations showing direct-bandgap properties for perovskites of interest[86,87]. Two strong, spin–orbit split, excitonic absorption thresholds are apparent, as in direct-bandgap III–V semiconductors[88]. However, reverse ordering of band-edge states (specifically a p-like conduction band)[89] results in splitting in the conduction band, rather than in the valence band. Interestingly, reverse band-edge ordering also gives a bandgap that increases with increasing temperature for any given phase[90,91].

The strong excitonic absorption edge also means there is no basis for the common practice of determining bandgaps using Tauc plots[92]. The absorption edge is determined by a broadened exciton impulse response, as is the case for direct III–V semiconductors, with the unbroadened response described by Elliott's theory[88,93]. The relatively high exciton binding energy compared to those of III–V semiconductors with a similar bandgap (37–50 meV has been reported for iodide in the low-temperature phase[94] and 35–75 meV for the mixed chloride at room temperature[91]), not only lowers the absorption threshold, but also increases the strength of the above-bandgap absorption that generates unbound electron–hole pairs. Correspondingly, above-bandgap absorption is comparable to or stronger than that in many direct-bandgap III–

V semiconductors, such as GaAs, although it is lower than that of some inorganic chalcogenides (see Figure 2.9a).

In addition to general interband transitions, an important piece of information that can be garnered from linear absorption spectra is the general degree of structural disorder and distribution of subgap states. Fluctuations in electrostatic potential at the band edge caused by disorder or impurities gives rise to an exponentially increasing density of states approaching the unperturbed continuum. This phenomenological relationship near the onset of optical absorption is known as the Urbach tail and can be described by $d(\ln \alpha)/ d(hv) = (kBT)^{-1}$ [95,96]. If, for example, we assume interband transitions occur from a parabolic VB into exponentially distributed tail states of the CB, we can arrive at the familiar expression for the Urbach energy (E_u or E_0):

$$E_u = [d (\ln \alpha) / d(h\omega)]^{-1} \quad (2\text{-}1)$$

with the density of subgap states in the tail at a given energy proportional to $e^{(E/Eu)}$ [81]. A smaller E_u (i.e., steeper slope on a semi-log plot) indicates less disorder and a narrower distribution of states near the band edge. Several studies have utilized a sensitive technique known as photothermal deflection spectroscopy (PDS), which probes heating caused by nonradiative recombination of photogenerated carriers, to examine α in the range of the Urbach tail[97,98]. Notably, through the compositional range of the mixed halide compound $CH_3NH_3Pb(I_{1-x}Br_x)_3$, E_u is the lowest for x = 0, increases monotonically to a peak value of ~90 meV at x = 0.8, and then again decreases to ~25 meV at x = 1. Such behavior highlights the variable degrees of disorder in I:Br solid solutions, which primarily stems from phase instability due to a tetragonal → cubic transition with increasing Br content[99].

With knowledge of the Urbach energy characteristic of $CH_3NH_3PbI_3$, it is useful to examine how it compares with other semiconductors. De Wolf and collogues have noted a linear empirical relationship between a material's lowest reported room temperature E_u and ($E_g - qV_{oc}$), where q is the elementary charge and V_{oc} represents the largest reported open-circuit voltage for a given compound when serving as the active layer in a PV device (Figure 2.9b)[98]. While V_{oc} is sensitive to device architecture and processing techniques, its thermodynamic limit for a given material occurs when all recombination is radiative, otherwise known as the "radiative limit" [100,101]. In this case, a material's intrinsic propensity for efficient energy

conversion can be expressed as $qV_{oc} = E_g - T\Delta S - k_BT|\ln iPLQY|$, where S is the entropy and iPLQY is the internal photoluminescence quantum yield. Because subgap states act as prominent nonradiative recombination channels, particularly at the relatively low carrier densities in PV operation, the general trend between E_u and $(E_g - qV_{oc})$ is rather intuitive. Despite low-temperature processing, the fact that perovskite materials have Urbach energies comparable to c-Si (11 meV) and lower than that of CIGS is a testament to their high semiconducting quality and relative resilience to formation of deep electronic defects[97].

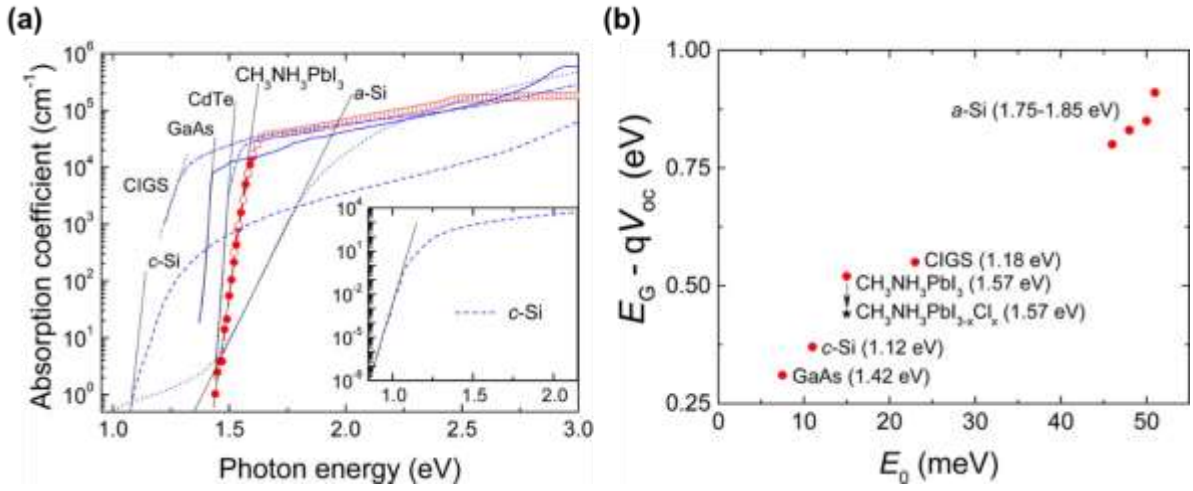

Figure 2.9. Absorption coefficient and Urbach energy for different semiconductors. (a) Effective absorption coefficient of a $CH_3NH_3PbI_3$ perovskite thin film compared with other typical photovoltaic materials, including amorphous silicon (a-Si), GaAs, CIGS, CdTe, and crystalline silicon (c-Si), all measured at room temperature. For each material, the slope of the Urbach tail is shown. For clarity, the inset shows the data for c-Si down to low absorption values. (b) $(E_g/q) - V_{OC}$ versus Urbach energy for typical photovoltaic absorber materials at room temperature. For each material, the value of E_g is also indicated in the legend. Figure from De Wolf and colleagues[98].

2.7.2 Mobilities, carrier lifetimes and diffusion lengths

Semiconductor's electrical properties, such as charge carrier mobilities, diffusion lengths, and lifetimes, are prominent for fabricating optoelectronic devices as well as for developing robust models for device simulations. The electrical mobility, μ, describes the ability of a charge

carrier (either electrons, μ_e, or holes, μ_h) to move within a semiconductor under an applied field. Mobility is important particularly for applications such as field effect transistors (FETs) and photodetectors, where a drift electrical transport mechanism is desirable in order to obtain a fast response time[102].

Furthermore, the diffusion length in a semiconductor is an important quality describing charge transport behaviour in the material. Notably, the diffusion length figure distinguishes between electrons (L_e) and holes (L_h). This quantity describes the motion of charges by diffusion from regions of high carrier population in the semiconductor to areas with lower populations. The diffusion lengths are crucial performance factors in optoelectronics where light excitation produces local excesses of charge. The diffusion length is one of the fundamental parameters governing the operation of diodes and solar cells. It is worthwhile to mention that mobility and diffusion length are intimately connected to each other by the Einstein relation, $D = \mu k_B T$ where $D = L^2 t^{-1}$ is the diffusivity (and t is the carrier lifetime). Additionally, diffusion and drift, most of the time, occur concurrently, as has been shown in the past, for example, by Sze and Ghione[103]. Finally, the carrier lifetime *(t)* describes the time that the charges take to recombine under non-thermodynamic equilibrium situations, such as under photoexcitation. Carrier lifetime is related to the diffusion length and to the number of traps within the semiconductor (traps reduce t).

In Figure 2.10a, the improvement of the diffusion length through recent years of research is plotted. Remarkably, the diffusion length increased from values well below 1 μm to exceeding 10 μm in about 3 years[48,99,104–106]. This improvement reflects the progress that has been recently made in producing solids with better structural order and morphology. As can be seen in Figure 2.10b, the diffusion length has a strong dependence on the grain size of the film. Diffusion lengths well above 1 μm have been achieved by realizing films with an average grain size exceeding 2 μm. The highest measured diffusion lengths are found in perovskite single crystals where values above 10 μm are reported[80,107–109].

The carrier mobility has also been improved over the years and exhibits dependence on the morphology. Mobilities exceeding 10 $cm^2V^{-1}s^{-1}$ have been measured in perovskite films[99,110,111] (particularly Cl–I mixed halide lead perovskite) and above 100 $cm^2V^{-1}s^{-1}$ (using transit time of photocarriers (ToF) measurements) in perovskite single crystals[112,113]. As can be seen in Figure 2.10c, the mobility (as also the diffusion length) does not exhibit a strong dependence on the material composition. The mobility of thin films has been also measured

using FETs and assessed to be ≈1 $cm^2V^{-1}s^{-1}$ [111,114]. It is important to note that FET mobility can be easily over- or underestimated as a result of effects related to the semiconductor/ oxide interface[114].

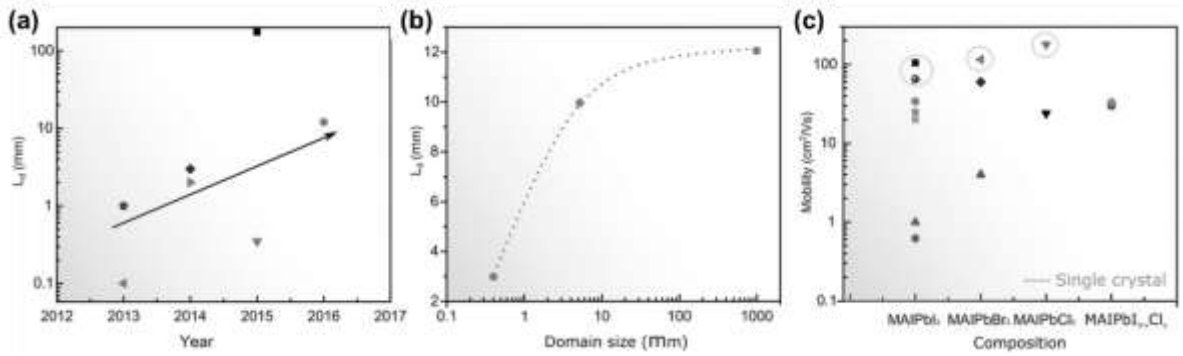

Figure 2.10. Diffusion length and carrier mobility in perovskite semiconductors. (a) Measured diffusion length in lead halide perovskites as a function of the year reported. Increases are attributed to advances in materials processing and fabrication. (b) Diffusion length as a function of the average grain (domain) size. (c) Mobility for different perovskite compositions following the iodine to chlorine progression, and the special mixed iodine–chlorine case. Figure form Adinolfi and colleagues[115].

Charge carrier lifetime used to characterize perovskite solids; although carrier lifetime gives a measure of the quality of the film (t directly has a dependence on the defects), we stress that a proper characterization of a material involves the extraction of mobility and/or diffusion length[116]. Carrier lifetimes in excess of 1 μs have been measured from PL decay[48]. Much longer decays have been shown using different techniques involving electrical measurements (e.g., photovoltage decay)[108]. In such measurements, it is important to discern the recombination decay from the decay that is due to capacitive effects, which are usually convoluted with one another.

Notably, the remarkable enhancement of perovskite-based devices, particularly solar cells, has been narrowly correlated with the development of the deposition techniques used to obtain high-quality (with regard to both crystallinity and morphology) perovskite thin films, since the intrinsic electronic properties of hybrid perovskites in the thin films mainly depends on these

factors. The crystallinity of a film directly determines the defect densities and their distributions, which are crucial parameters influencing the electronic properties. To be more specific, the density of grain boundaries (and so grain sizes), one important aspect used to evaluate the crystallinity and morphology of a thin film, will strongly influence the charge transport in the films because the transport among crystalline grains is, in general cases, strongly deteriorated by the charge localization, scattering and intensive trapping at the boundaries[112].

2.7.3 Luminescence in Metal Halide Perovskite

The luminescence can be described as the photon emission in the UV-Vis-NIR region of radiation due to electronic excitation, either optical or electrical of a material. Hybrid metal halide perovskites have been found to exhibit an intense and broad band luminescence centered very near its absorption edge with a full width at half-maximum of approximately 100 meV (depending on the perovskite composition) at room temperature. The characteristic luminescence width has been generally found to be almost twice as broad as the spectral width of the absorption edge (i.e. 56 meV in $CH_3NH_3PbI_3$ hybrid perovskite)[117]. Moreover, photoluminescence maximum has been described slightly red shifted in energy (~ 30 meV), with respect to the band gap, this small shift being one of the main characteristics in their emission spectra. Figure 2.11a presents as an example normalized absorption and emission spectra for a mixed $CH_3NH_3Pb(Cl_{1-x}I_x)_3$ perovskite

The dominant mechanisms for the luminescence in metal halide perovskites have been extensively studied, confirming that the emission spectra are independent of the excitation energy[118]. Therefore, the luminescence in these materials is homogeneous and fully broadened at every excitation wavelength. Different hypothesis have been proposed in order to explain the luminescence characteristics in hybrid metal halide perovskites. Among them the existence of additional intermediate states in the radiative recombination process with an extremely short lifetime (fs) has been proposed[118]. However, in these cases the emission broadening follows a Lorentzian distribution, while in the case of hybrid perovskites this distribution has been found to be Gaussian[119]. Thus, it seems to be improbable that intermediate states could be responsible for the homogeneous and broad emission. Another explanation, and the most widely accepted, has attributed to phonons present in the radiative recombination process as the cause of the broadband emission. In this case the emission spectra would consist of the band-edge emission peak combined with a number of side bands due to phonons[118]. The changes in the absorption

edge and emission spectra at temperatures between 297 K and 77 K (specifically, evolution of two excitonic peaks was found at 160 K, where a transition from the tetragonal to orthorhombic phase has been described) support this theory, where the overall emission spectral width decreases with temperature consistent with a smaller available phonon population[120]. Figure 2.11b illustrates the photon and phonon emission mechanism.

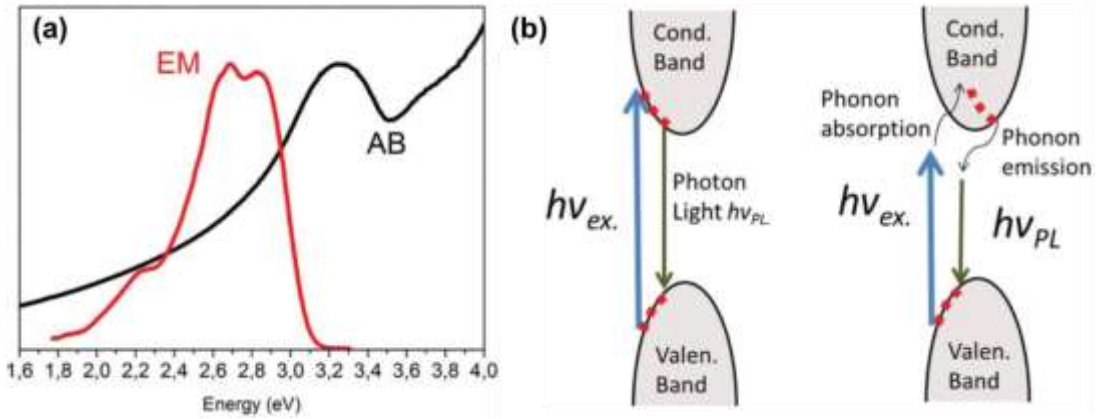

Figure 2.11. Photon and phonon emission mechanism. (a) Normalized UV-Vis absorption (AB, black) and emission spectra (EM, red) of a mixed $CH_3NH_3Pb(Cl_{1-x}I_x)_3$ hybrid perovskite. (b) Schematic band diagrams for photon emission (left) and phonon emission (right) processes, respectively. Figure from Albero and collouges[121].

Despite all these, the rational design of the hybrid perovskite composition has given rise to modulation of their luminescence properties[122]. This is not surprising since composition tuning and design have been widely exploited in photovoltaics in order to control the spectral response, band alignment as well as other characteristics affecting the photovoltaic device performance[123]. In a similar way, accurate compositional design of the hybrid perovskites is able to fine-tune their luminescence quantum yield, emission spectrum and lifetime, among other properties, and therefore, besides the phenomenon of luminescence high control of the light-emitting device characteristics in lighting and lasing applications has been demonstrated[124–126]. Even more, the compositional flexibility in the case of photo- or electroluminescent devices has demonstrated to be wider than in the case of photovoltaics[127]. This is due to the possibility of obtaining suitable light emitting devices employing hybrid perovskites with 2D structures while in photovoltaics, the perovskite structure is restricted to

3D to achieve efficient light harvesting and improve charge transport issues[128–131]. Therefore, broader possibilities in composition are possible to alter light emission.

2.7.4 Trap States in Metal Halide Perovskite

A detrimental factor for charge transport in a semiconductor is the density of trap states, particularly those located deeply in the forbidden bandgap. Deep trap states can act as nonradiative recombination centers, thereby reducing charge carrier lifetimes; whereas shallow trap states may act as scattering centers, which also have negative impacts on charge transport[132]. Defect-assisted recombination is a mechanism competing with radiative recombination and is thus detrimental for light-emitting devices[133]. Additionally, defect-assisted recombination reduces the open-circuit voltage in photovoltaic devices[132]. Therefore, materials with a low trap density are highly desirable. At the same time, a thorough investigation of the properties of the traps is crucial for designing efficient devices.

The exact origin of defect states in perovskite thin films is still unknown but the grain boundaries is one of the most probable option[134]. In general, defect states will accumulate at the surface of crystalline grains due to enriched dangling bonds and unsatisfied stoichiometry. Interestingly, calculations predicted the benignity of the grain boundaries by revealing the shallow energetic levels of the defect states[135], which were also confirmed experimentally[136,137]. Yet, this proposed mechanism was challenged recently by the observation of relatively weaker local PL emission from the grain boundaries than from the grain interior, indicating stronger nonradiative recombination at the boundaries. Furthermore, the areas with weak PL can be improved through passivation[116]. Therefore, it seems that the trap states in the hybrid perovskite films are not negligible as previously expected, and that passivation which targets nonradiative recombination paths is an effective route toward pushing the performance of perovskite solar cells toward their Shockley– Queisser limit[125,138]. In addition, it is rescannable to expect that increasing the grain sizes reducing the density of grain boundaries would also be an efficient way to minimize the overall defect densities in the thin films, and further improve the charge carrier lifetime, mobility, diffusion length, and, ultimately, device performance (Figure 2.12). This notion has been supported by several experimental works[139,140].

The interfaces formed between perovskites and the other layers of a device are another crucial factor. Specifically, this is important when considering defects, since the defects at the

interfaces may not only form intrinsically during the growth of perovskite thin films (i.e., defects at the grain boundaries), but also may be generated or suppressed from the interaction with other device components. For example, Huang and coworkers found that perovskite thin films deposited on c-OTPD (cross-linked *N*4,*N*4′-bis(4-(6-((3-ethyloxetan-3-yl)methoxy) hexyl)phenyl)-*N*4,*N*4′-diphenylbiphenyl-4,4′-diamine) had less bottom surface traps compared to those on poly(3,4-ethylenedioxythiophene) polystyrene sulfonate[141]. 4-tert-butylpyridine, a commonly used dopant in the hole-transporting materials of perovskite solar cells, was reported to be corrosive for perovskites and thus produces additional defects[142]. In addition, the interfacial traps in perovskite solar cells are especially interesting for their suspected roles in the well-known hysteresis problem of *I*–*V* measurements[143,144]. Extensive works have looked at choosing appropriate interface layers to improve the efficiency of charge extraction from the perovskites[145]. It is worth noting that this improvement of charge extraction through interface layers has been sometimes explained by side effects such as the higher mobilities and energy level tailoring of the interface layers[146,147]. Despite this, their potential passivation effects should also be considered.

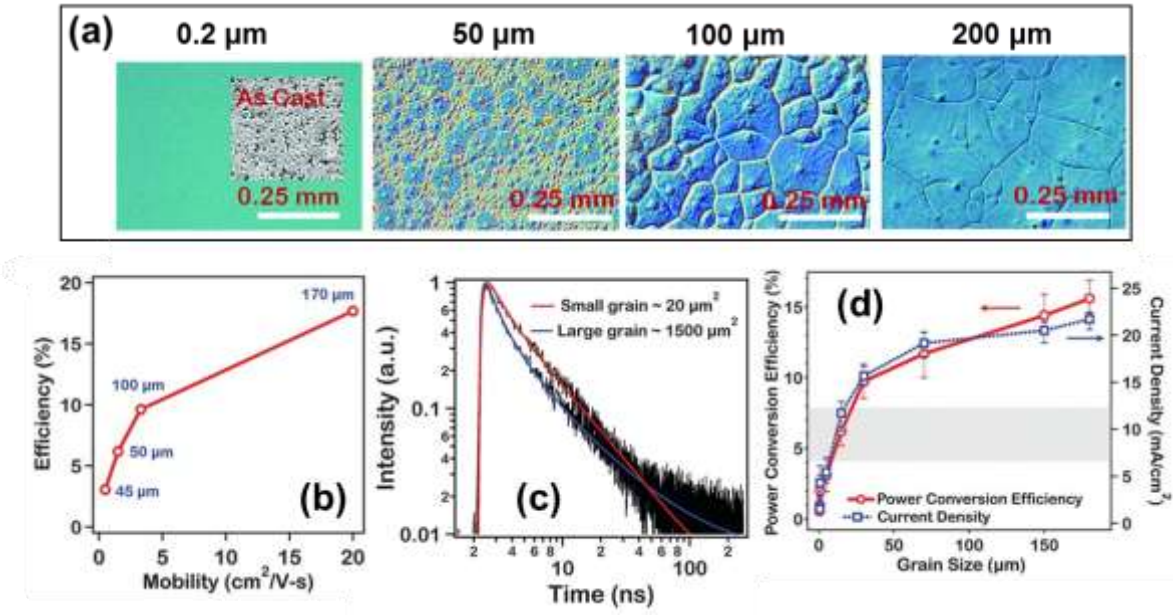

Figure 2.12. Impact of grain-size on the optoelectronic properties of perovskite thin-films and PV parameters. (a) Scanning electron microcopy images of perovskite thin-films prepared via hot-casting method. (b) With all other parameters characterized and/or obtained from the literature, the PCE values appear to be correlated to the bulk mobility of the absorber

(labels correspond to the average grain size). (c) Normalized, microscopically resolved time-correlated single-photon histograms of both a large and a small grain (black). The red and blue lines are fits to the intensity decay considering interband relaxation, radiative bimolecular recombination, and nonradiative decay into states below the gap. (d) Average overall PCE (left) and J_{SC} (right) of perovskite solar cells as a function of crystalline grain size. The figure is reproduced from reference[148].

2.7.5 Non-radiative recombination in Metal Halide Perovskite

Perovskite semiconductors are still far from their full potential in optoelectronic devices, although they showed remarkable rapid rise in the past few years. The emission quantum efficiencies in state-of-the-art materials interfaced with device contacts are far from unity under solar conditions[149,150], particularly in wide-band-gap mixed halide perovskites[151,152]. This suggests that defects are still not entirely benign. Devices also show poor luminescence, indicating that there is further nonradiative recombination at the contacts[153]. Any nonradiative recombination impairs charge density buildup and limits open circuit voltage. Thus, an essential condition for PV and LED devices to reach their efficiency limits is the elimination of all nonradiative recombination[154].

To understand the famous concept of 'an excellent solar cell should also be an excellent LED'[100], we can consider recombination of charge carriers at open-circuit in a solar cell[12]. To build up a large open-circuit voltage, we need to maintain a high photoexcited charge carrier density. Photoexcited electrons and holes in an ideal semiconductor will eventually recombine (radiatively) by emitting a photon. However, any nonradiative recombination will result in additional parasitic recombination pathways of carriers to lower energy states, leading to lower quasi-Fermi levels and effective charge densities and, ultimately, lower open-circuit voltages[155].

In Figure 2.13, the measured open-circuit voltages for different PV technologies are shown along with the components of nonradiative loss (red) from the thermodynamic limits obtained from the Shockley−Quiesser formulation. These nonradiative losses arise from, among others, defects (charge carrier traps) either in the bulk materials or introduced when the material is interfaced with device contacts, poor external light outcoupling, many-body effects such as

Auger processes, and, in the case of silicon, recombination via an indirect band gap[155]. The most efficient single-junction PV devices to date are made from GaAs (power conversion efficiency of 28.8%), which has been shown to have internal luminescence quantum efficiencies > 99%, and less than ~40 mV of nonradiative loss[155]. On the other extreme, organic photovoltaics (OPVs) have poor external radiative efficiencies (~10−5%) owing in part to high defect densities and losses at exciton dissociation heterojunctions and thus suffer from substantial nonradiative losses (~400 mV)[155]. A clear pathway to improving many of the technologies is by eliminating all nonradiative losses.

Interestingly, perovskite devices have shown remarkably low voltage losses, which is consistent with reasonable external EL quantum efficiencies[101,156]. Saliba et al. recently reported devices with quadruple cation perovskites (MA, FA, Cs, and Rb), yielding an impressive voltage of 1.24 V, which is only ~120 mV shy of the radiative limit[58]. This high voltage is in line with the measured external electroluminescent efficiency of 3.8%. However, the logarithmic relationship between voltage and luminescence efficiency means that removing even this small final voltage loss will require an increase in the luminescence by at least a factor of 25[58,153]. These losses are even more substantial in the wider-band-gap perovskites achieved with larger fractions of bromide[151,152] (~260 mV). Despite remarkable progress, there is still work to be done to ameliorate all nonradiative losses to push them to their limits.

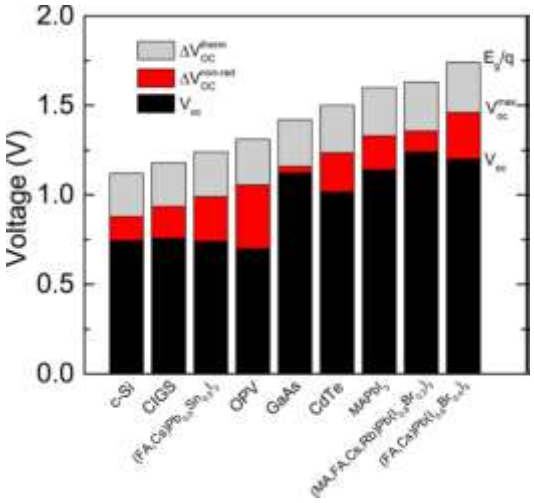

Figure 2.13. Open-circuit voltages and losses of the record solar cells for different PV technologies. The measured V_{oc} is in black, the nonradiative loss from the maximum possible V_{oc} max is in red, and the unavoidable thermodynamic loss from the band gap (E_g) is in gray[79].

Chapter 3

Experimental Methods

In this chapter, we present the experimental techniques and protocols used in this thesis for synthesizing various perovskite materials. We also briefly describe the procedures on fabrication of the perovskite thin films and the complete solar cells. Details about experimental characterizations are also presented.

3.1 Materials and Film Preparations

3.1.1 Materials

All the organic cation salts and titanium dioxide (TiO_2) paste were purchased form Dyesol; the Pb compounds (e.g. PbI_2, $PbBr_2$) from TCI and cesium iodide (CsI), potassium iodide (KI) and rubidium iodide (RbI) from Alfa Aesar. Spiro-OMeTAD was purchased from Borun Chemicals and used as received. Unless otherwise stated, all other materials were purchased from Sigma-Aldrich.

3.1.2 Perovskite film preparations

3.1.2.1 Synthesis and deposition of pristine and monovalent cation doped $CH_3NH_3PbI_3$

PbI_2 was dissolved in N,N-dimethylformamide (DMF) at a concentration of 1.2M under constant stirring at 80 ^oC. The halide salts including NaI, CuBr, CuI and AgI were then added to the lead halide solution at a concentration of 0.02M. All the solution were prepared inside an argon glove box under moisture- and oxygen-controlled conditions (H_2O level: <1 ppm and O_2 level: <10 ppm). The $CH_3NH_3PbI_3$ films were prepared using two-step deposition method[49]. In the first step, the mesoporous TiO_2 was infiltrated with pure or additive based PbI_2 solution by spin coating at 6500 rpm for 30 s and dried at 80 ^oC for 30 min., To form perovskite resulting PbI_2 films were dipped in a solution of CH_3NH_3I in 2-propanol (8 mg mL^{-1}) for 30 s, and were dried at 80 °C for 30 min after cooling to room temperature. The schematic for preparation of pristine and doped perovskite is shown in Figure 3.1. Note that these perovskite compositions were used in chapter 4 and chapter 5.

3.1.2.2 Synthesis and deposition of passivated mixed cation lead mixed halides

The double-cation-based perovskite $FA_{0.84}MA_{0.16}Pb(I_{0.85}Br_{0.15})_3$ was prepared by dissolving PbI_2 (1.2 M), FAI (1.11 M), MABr (0.21 M) and $PbBr_2$ (0.21 M) in a mixture of anhydrous DMF:DMSO (4:1, volume ratios). We then prepared the triple-cation-based perovskite $Cs_{0.06}FA_{0.79}MA_{0.15}Pb(I_{0.85}Br_{0.15})_3$ by addition of 5 volume percent from CsI stock solution (1.5 M in DMSO) to the double cation perovskite solution. The potassium iodide and rubidium

iodide powders were first dissolved in a mixed solution of DMF/DMSO 4:1 (v:v) to make a stock solution of 1.5 M. We then added the resulting KI and RbI solutions into the triple cation perovskite solution in different volume ratios to achieve the desired additive ratios. We then spin-coated the perovskite solutions using a two-step program at 2000 and 6000 rpm for 10 and 30 seconds, respectively, and dripping 150 µL of chlorobenzene 30 seconds the start of the spinning process. We then annealed the films at 100ºC for 1 hour. We prepared all solutions and films in a nitrogen-filled glove box.

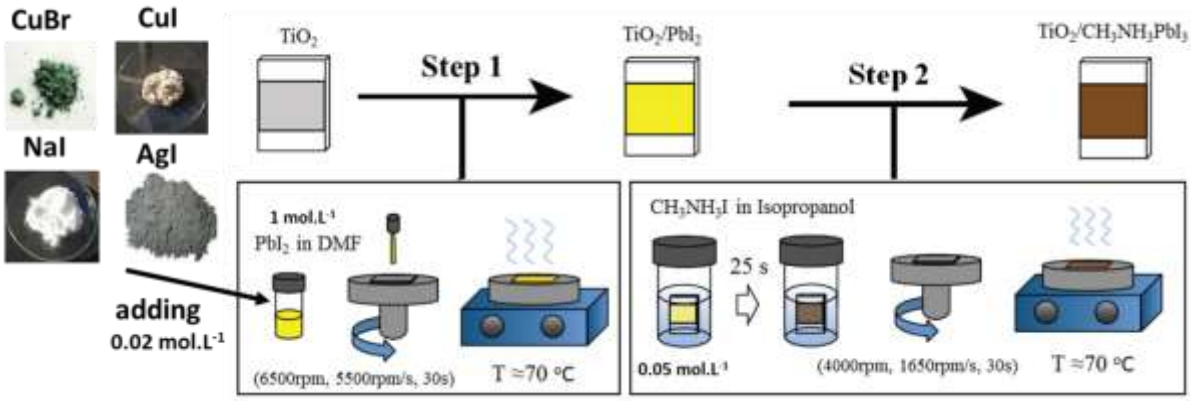

Figure 3.1. Schematic of synthesis and sequential deposition of pristine and monovalent cation doped perovskite.

3.1.2.3 Synthesis and deposition of low bandgap mixture of lead and tin based perovskite

A bright yellow solution of pure lead ($CH_3NH_3PbI_3$) and tin ($CH_3NH_3SnI_3$) perovskite were prepared by dissolving stoichiometric amounts of CH_3NH_3I and MX_2, (M = Sn, Pb) in DMF at one mol.L^{-1} concentration. In order to make mixture of lead and tin based perovskite compounds ($CH_3NH_3Sn_{1-x}PbxI_3$), the pure solution of them were mixed in different ratio as it is demonstrated in Figure 3.2. These solution were spin coated on either a spin coated TiO_2 on a FTO-coated glass or quartz substrates at 4000 rpm for 60 s and dried at 100 ^{0}C for 15 min to remove the solvent (Figure 3.2).

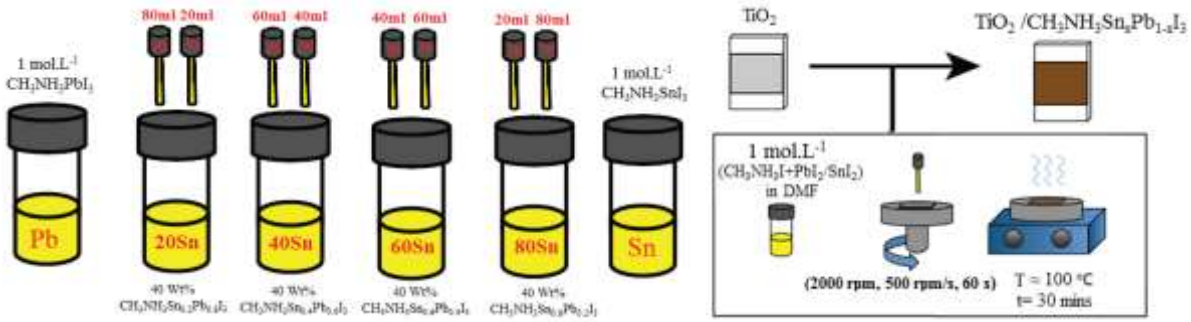

Figure 3.2. Schematic of $CH_3NH_3Sn_{1-x}Pb_xI_3$ solutions (left) and thin-films (right) preparation.

3.2 Perovskite device fabrications

3.2.1 Photoanode (n-type contact) preparation

Photoanodes were fabricated on laser patterned FTO-coated glass (NSG 10, Nippon sheet glass, Japan). Initially, FTO substrates were cleaned sequentially in 2% Hellmanex detergent, 2-propanol and ethanol, and then treated with an ultraviolet/O_3 cleaner for 15 min. A hole-blocking layer of compact TiO_2 was deposited by spray pyrolysis using a precursor solution of titanium di-isopropoxide bis(acetylacetonate; 0.6 ml titanium acetylacetonate in 8ml ethanol) on a hot plate at 450 ^oC. The titanium acetylacetonate was prepared by pouring acetylacetone (Wako Pure Chemical Industries, Ltd.) into titanium isopropoxide (Kanto Chemical Co., Inc.) with a mole ratio of 2:1. For the preparation of mesoporous TiO_2 scaffold, a commercial TiO_2 paste (Dyesol, 18NRT) and two synthetized TiO_2 pastes (NP36 and NP50) were used for chapter three and for the rest of the thesis, we used another commercial TiO_2 paste (Dyesol, 30NRD). All of these TiO_2 pastes were diluted with ethanol (2:7, weight ratio) and was then deposited by spin coating at 5,000 r.p.m. for 30 s. After drying at 125 ^oC, the TiO_2 films were gradually heated to 500 ^oC and annealed at this temperature for 20 min. A schematic of the step by step preparation of titania films is shown in Figure 3.3a. For $TiCl_4$ treatment, 2 M aqueous solutions of $TiCl_4$ were prepared by adding $TiCl_4$ to distilled water in a precooled ice bath. Then the TiO_2 films were dipped in the diluted 40mM aqueous $TiCl_4$ solutions at 70 ^oC for 30 min. After washing with distilled water and ethanol, the samples were annealed at 475 ^oC for 30 min (Figure 3.3b). Lithium-doping of mesoporous titania (mp-TiO_2) was accomplished by spin coating a 0.1 M solution of Li-TFSI in acetonitrile. The solution was prepared freshly before the application in nitrogen atmosphere and 120 µL of that were poured on 1.4 × 1.4 cm^2 substrate coated with mp-TiO_2. After 5 seconds of loading time, the spinning programme

started with an acceleration of 1,000 r.p.m. s^{-1} to a final speed of 3,000 r.p.m., the substrate was left spinning for 30 s. Li^+-doped electrodes were completed with a second annealing step at 450 °C for 30 min. After cooling down to 150 °C, the substrates were immediately transferred in a nitrogen atmosphere glove box for the deposition of the perovskite films. Note that the $TiCL_4$ treatment were only used in Chapter 4 and in the rest of the thesis, we used Li treatment which is easier to use though in both method we improved the interface between mesoporous-TiO_2 and perovskite significantly[157,158].

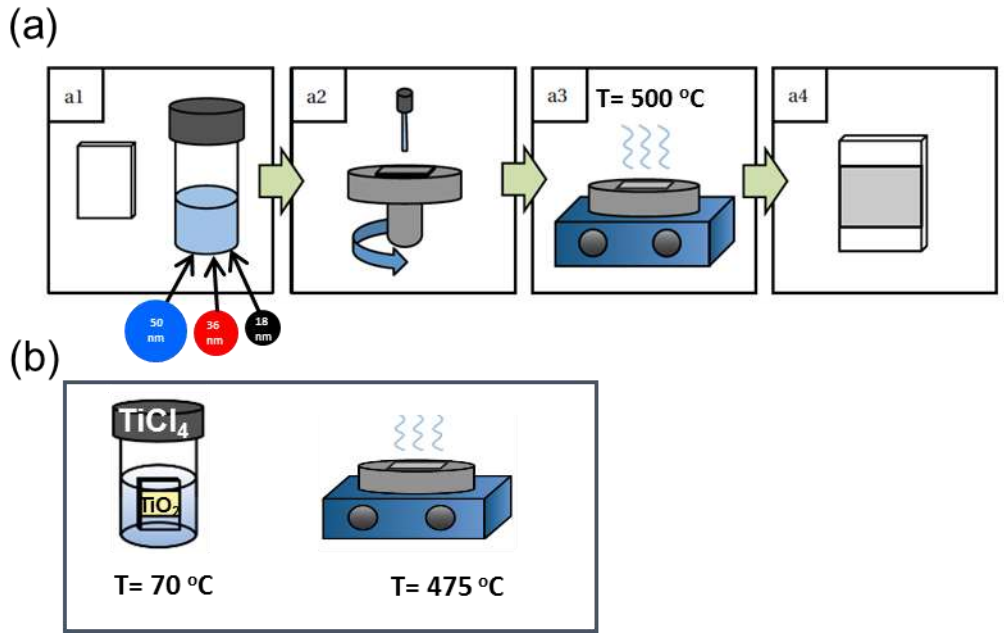

Figure 3.3. Schematic for (a) preparation of photoanodes (n-type contact) for perovskite devices and (b) $TiCl_4$ treatment of photoanodes**.**

3.2.2 Solar cell fabrication

In chapter 3 and chapter 4, we infiltrated the TiO_2 scaffolds with pristine and monovalent cation-doped $CH_3NH_3PbI_3$ using the sequential deposition technique as explained in the perovskite preparation section (Figure 3.1). However, for the rest of the chapters, we used single step deposition technique as per the previous section. After deposition of perovskite on the photoanodes, the hole transport material (HTM) as the p-type contact was deposited by spin coating at 4,000 rpm for 30 s. The spin coating formulation of HTM was prepared by dissolving

72.3 mg 2,2′7,7′-tetrakis-(N,N-di-p-methoxyphenyl amine)-9,9′-spirobifluorene known as spiro-OMeTAD, 28.8 ml 4-tert-butylpyridine, 17.5 ml of a stock solution of 520 $mgml^{-1}$ lithium bis(trifluoromethylsulphonyl) imide in acetonitrile and 29 ml of a stock solution of 300 $mgml^{-1}$ tris(2-(1H-pyrazol-1-yl)-4-tert butylpyridine)cobalt(III) bis(trifluoromethylsulphonyl)imide in acetonitrile in 1 ml chlorobenzene. The tetracene hole transporting layer was deposited via thermal evaporation on the perovskite layer with the evaporation rate of 0.2 $nm.s^{-1}$ and chamber pressure of 10^{-7} mbar. The schematic for deposition of different hole transporting layers is shown in Figure 3.4. Finally, 70nm of gold was thermally evaporated with a rate of 0.1 $nm.s^{-1}$ and chamber pressure of 10^{-6} mbar on top of the device to form the back contact. The schematic and a macroscopic image of compete perovskite solar cells is shown in Figure 3.5. The device fabrication was carried out under controlled atmospheric conditions with a humidity of <1%. The detailed protocol for fabrication of a standard perovskite solar cell used in this thesis is summarized below. We also published a video article of the perovskite solar cell fabrication processes in the Journal of Visualized Experiments[159].

(a) Substrate preparation

a. Pattern fluorine-doped tin oxide (FTO)-coated glass.

i. Cover the active area of the FTO glass with semitransparent adhesive tape.

ii. Pour the zinc (Zn) powder on the uncovered areas of the FTO substrates.

iii. Prepare 2 M of hydrochloric acid (HCl) in distilled water.

iv. Pour the HCl solution onto the part of the FTO glass that is covered with Zn powder.

v. Wash the FTO with water and remove the tape.

b. Cleaning the substrates

i. Wash the FTO glass using 2% (w/v) detergent.

ii. Sonicate the etched FTO substrates in acetone and isopropanol (IPA) for 10 min.

iii. Treat the FTO substrates with an ultraviolet/O3 cleaner for 15 min.

(b) Deposition of a hole blocking layer

a. Add 0.6 mL of titanium diisopropoxide bis(acetylacetonate) (TAA) in 7 mL of IPA.

b. Put the cleaned and patterned FTO substrates on a hotplate at 450 °C and cover the contact area before heating.

c. Spray pyrolysis the TAA solution onto the uncovered area using O_2 as the carrier gas.

d. Leave the samples at 450 °C for 30 min.

(c) Deposition of an electron transport layer

a. Dilute the commercial TiO_2 paste (30-nm particle size) with ethanol (2:7, weight ratio).

b. Homogenize the TiO_2 dilution by sonicating for 30 min.

c. Spin-coat the titania dilution onto the prepared samples with compact TiO_2 layers for 30 s at 5,000 rpm with a ramp of 2,000 rpm.

d. Anneal the titania films at 500 °C for 30 min.

e. Treat the resulting mesoporous TiO_2 films in a 40 mM solution of $TiCl_4$ in distilled water at 70 °C for 20 min.

f. Anneal the $TiCl_4$-treated films at 450 °C for 30 min.

(d) Deposition of the perovskite layer

NOTE: The FTO substrates with titania layers were transferred to a nitrogen glovebox with a humidity of <1% for the rest of the fabrication process.

a. Spin-coat the prepared perovskite solutions using the abovementioned methods (e.g. single step with anti-solvent dripping or sequential deposition) onto the mesoporous TiO_2.

b. Anneal the spin-coated perovskite films on a hotplate at 100 °C for 60 minutes.

(e) Deposition of the hole transport layer

a. Add 72.3 mg of spiro-OMeTAD to 1 mL of chlorobenzene and shake until the solution becomes transparent.

b. Make a stock solution of bis(trifluoromethylsulphonyl)imide (LiTFSI) by adding 520 mg of LiTFSI in acetonitrile.

c. Add 17.5 µL of the LiTFSI stock solution and 28.8 µL of 4-tert-butylpyridine (TBP) to the spiro-OMeTAD solution.

d. Spin-coat the above solution for 30 s at 4,000 rpm with a ramp of 2,000 rpm.

(f) Thermal evaporation of the top contact

a. Mask the samples and put them in the vacuum chamber of the evaporator.

b. Evaporate 80 nm of gold at a rate of 0.1 $nm.s^{-1}$.

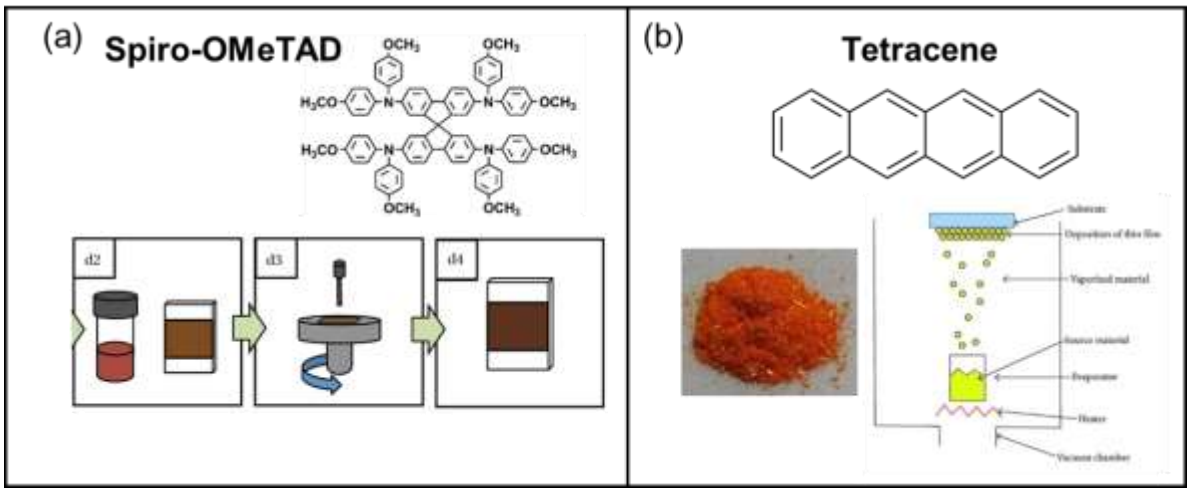

Figure 3.4. Schematic of deposition methods and chemical formula for (a) Spiro-OMeTAD and (b) tetracene hole transporting layers for perovskite solar cell fabrication.

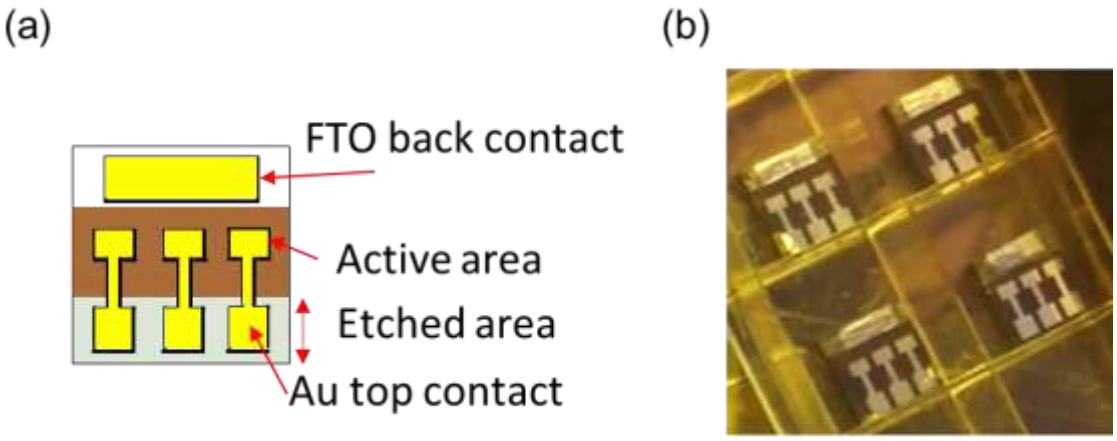

Figure 3.5. (a) Schematic and (b) macroscopic image of complete perovskite solar cells.

3.3 Material characterizations

3.3.1 Scanning Electron Microscopy

The surface morphology of the films was examined using an FESEM (Merlin). An electron beam accelerated to 3 kV was used with an in-lens detector. EDX was carried out on a FEI

Nova NanoSEM at 10kV acceleration voltage using a Bruker XFlash 6 detector. The maps were processed within Esprit 2.1 and Hyperspy.

3.3.2 Scanning Transmission Electron Microscopy-Energy Dispersive X-ray Spectroscopy (STEM-EDX)

A FEI Helios Nanolab dual beam Focus Ion Beam/ Field Emission Gun - Scanning Electron Microscope (FIB/FEGSEM) was employed to prepare a lamella for STEM imaging and analysis. To preserve the perovskite film during specimen preparation, capping layers of Spiro-OMeTAD and platinum were deposited. All imaging was carried out in STEM-HAADF (High Angle Annular Dark Field) mode. STEM/EDX data were acquired in FEI Tecnai Osiris TEM equipped with a high brightness Schottky X-FEG gun and a Super-X EDX system composed by four silicon drift detectors, each approximately 30 mm^2 in area and placed symmetrically around the optic axis to achieve a collection solid angle of 0.9 sr. Spectrum images were acquired with a probe current of 0.7 nA, an acceleration voltage of 200 kV, a spatial sampling of 10 nm/pixel and 100 ms/pixel dwell time. Data were acquired with Tecnai Imaging and Analysis (TIA) and analysed with Hyperspy. *All the STEM-EDX measurements were performed by Dr Stefania Cacovich and Dr Giorgio Divitini.*

3.3.3 Atomic force microscope

The atomic force microscope (AFM) images were obtained using a Thermo Microscope M5 in non-contact mode and scanning over a range of 15 μm by 15μm at a resolution of 256×256 data points. The surface roughness was measured as the root mean-squared roughness over the scanning area.

3.3.4 Kelvin probe force microcopy (KPFM) measurement

Our KPFM apparatus is a Veeco Dimension 3100 system operated in ambient atmosphere. This system was selected due to its ability of scanning over a length of 80 μm. The PtIr tip (Bruker, SCM-PIT, 60-100k Hz), which has a work function of about 4.85 eV was used for this measurement. The oscillation of the tip is controlled in an amplitude-modulation (AM) mode. *The KPFM measurements were performed by Dr. Yuanyuan Hu.*

3.3.5 X-ray diffraction

XRD was performed using a Bruker X-ray D8 Advance diffractometer with Cu $K\alpha_{1,2}$ radiation (λ = 1.541 Å). Spectra were collected with an angular range of $5 < 2\theta < 60$ ° and $\Delta\theta = 0.01227$ ° over 10 minutes. Measurements were made on as prepared films on glass. A Le Bail analysis was carried out on film measurements using the Bruker Topas software. Chebyshev polynomials were used to fit the background and the peak shape modelled with a pseudo-Voigt function. *The XRD measurements in chapter 6 and chapter 7 were done by Edward P Booker and Dr. Andrew J Pearson.*

3.3.6 Grazing Incidence Wide Angle X-Ray Scattering (GIWAXS)

GIWAXS measurements were performed on the XMaS Facility at the ESRF synchrotron. A fixed-exit, water-cooled, double crystal Si(111) monochromator, placed at 25 m from the source was used to monochromatize the X-ray beam coming from a bending magnet (E_c = 9.8 keV). The X-ray energy was tuned to 10 keV (1.2398 Å) and a Rh-coated toroidal mirror was used to focus the monochromatic beam horizontally and vertically. The beam flux was ~5×10^{10} photons s^{-1} at the sample position. The original beam spot size was 500 (horizontal) × 400 (vertical) μm^2 at the sample position. We employed a set of motorized slits (Huber, Germany) immediately before the sample to have a better-defined footprint in the vertical direction. The final beam spot size with slits was 300 (horizontal) × 115 (vertical) μm^2. The beam footprint extended 300 µm horizontally and throughout the perovskite films. The samples were scanned at an out-of-plane incident angle of ~0.3°. *All the GIWAXS measurements were performed by Mejd Alsari and Dr Samuele Lilliu.*

3.3.7 Hard X-ray Photoelectron Spectroscopy (HAXPES)

Photoelectron spectroscopy measurements were performed at the Diamond light Source using the beamline I09 (Oxfordshire, UK). Both soft (758 eV) and hard X-rays (2200 and 6600 eV) were used to illuminate our sample providing information from different probing depth. The soft X-ray energy was selected through a plane grating monochromator while a double-crystal monochromator (DCM) was used in the hard X-ray section. 2200 and 6600 eV correspond to the 1st and 3rd order light when the DCM is set at 2200 eV using a Si(111) crystal. A EW4000 photoelectron analyzer (VG Scienta, Uppsala, Sweden) was used to record the spectra with an analyzer slit open to 0.2 mm. No charge neutralization was used and the binding energy scale

was calibrated by setting the Au 4f core level of a gold reference sample to 84.0 eV. The quantification tables and intensity ratios were calculated from the experimental results after correction by the photoionization cross-section for each element at their specific photon energy, using database values. Note that soft in-house XPS measurements were carried out with a Scienta ESCA 300 instrument, using monochromatized AlKα radiation (hν=1486.6 eV). *All the HAXPES measurements were performed by Dr. Bertrand Philippe.*

3.3.8 Ultraviolet Photoelectron Spectroscopy (UPS)

The UPS system operates by emitting photons of a fixed energy of 21.2 eV (58.4 nm) via a helium gas-discharge lamp. On the basis of Einstein's photoelectric law, photoelectrons are able to escape from the surface of a sample if their kinetic energy is sufficient to overcome the sum of the binding energy of their initial level (taken with reference to E_F) and the material's work function $\Phi = E_{VAC} - E_F$. Here, the secondary electron cutoff represents electrons without any kinetic energy. Consequently, a material's Fermi-level position with respect to the vacuum level (its work function) can be computed by determining the secondary electron cutoff from a UPS spectrum and subtracting it from the incident photon energy adjusted for any external potential applied during the measurement. *All the UPS measurements were performed by Dr. Bertrand Philippe.*

3.4 Optical characterizations

3.4.1 Ultraviolet-visible (UV-Vis) absorption spectroscopy

Ultraviolet-visible (UV-Vis) absorption is one of the most standard measurements for the investigation of optical and electronic properties of semiconductors. The schematic of a typical UV-vis set-up is illustrated in Figure 3.6. Absorption spectra were recorded with a Perkin-Elmer Lambda 1050 spectrophotometer equipped with an integrating sphere to account for reflected and transmitted light within the spectral range of 190-1100 nm. The absorbance data is normally in the form of optical density (OD) or absorbance, which is defined as:

$$OD(\lambda) = \log [I_0(\lambda) / I(\lambda)] = -\log T(\lambda) \quad (3.1)$$

where I_0 is the incident light intensity, and I is the intensity of transmitted light. Transmission (T) is the ratio of transmitted intensity (I) versus the incoming intensity (I_0). The absorption

coefficient of a thin-film sample can be found from the following equation, which describes the attenuation of light intensity due to the absorption of the material.

$$I(\lambda) = I_0(\lambda) \exp(-\alpha t) \quad (3.2)$$

where α is the absorption coefficient (typical units is cm^{-1} for a semiconductor thin film), and t is the thickness of the film.

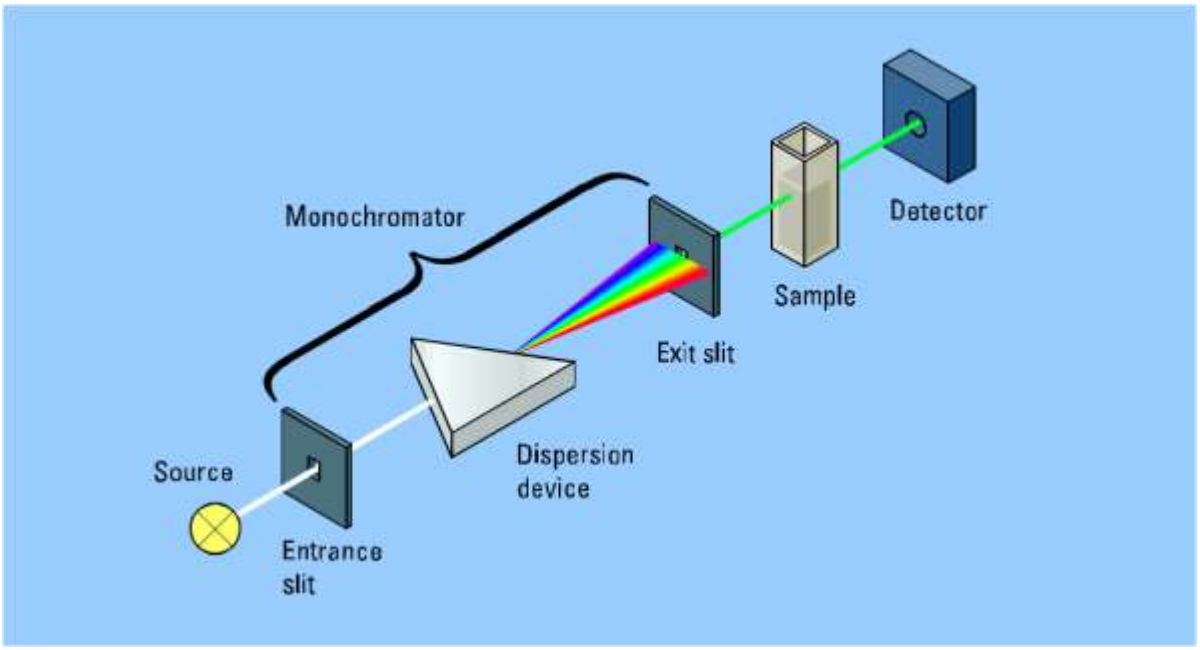

Figure 3.6. Schematic of a typical UV-Vis absorption setup.

3.4.2 Photothermal Deflection Spectroscopy (PDS)

Photothermal Deflection Spectroscopy (PDS) technique is a highly sensitive absorption measurement technique first developed in 1981 by Jackson[160]. PDS is an optical absorption technique, which measures absorption directly by probing the heating effect in the samples upon absorption of light resulting in its capability to measure an absorption, which is 5 - 6 orders of magnitude weaker than the band-edge absorption. Whereas, the standard absorption measurement techniques like UV-Vis spectrometers measure absorption in the transmission mode involving errors due to various optical effects like light scattering, reflection and interference limiting the sensitivity of these techniques. This technique works on absorption

induced heating effect in the sample, due to non-radiative relaxation of the excited species. The PDS setup used in this thesis can measure absorption in the wavelength range of 380 – 2100 nm. In Figure 3.7, we show the comparison between UV-Vis and PDS technique where a $CH_3NH_3PbI_3$ perovskite thin-film is measured using these two techniques. Optical effects such as scattering and reflection affect the UV-Vis measurements while, the PDS is capable of measuring the band-edge down to absorbance of 10^{-5} i.e. five orders of magnitude more weaker absorption than the UV-Vis.

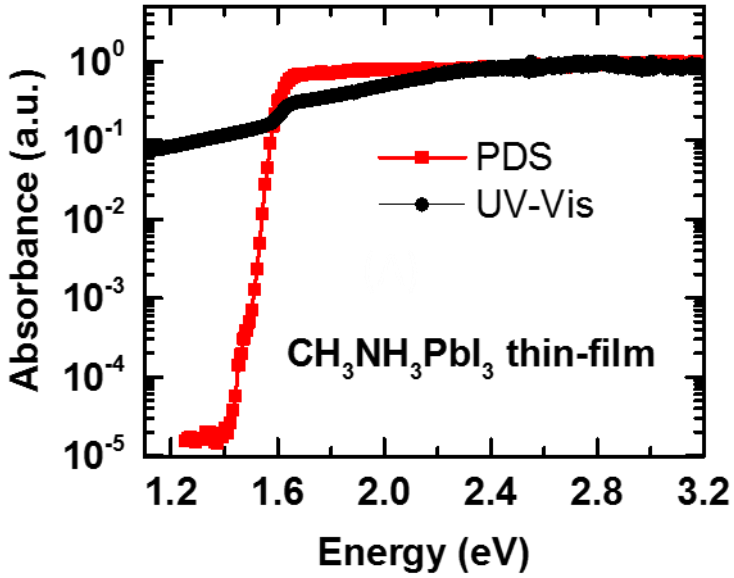

Figure 3.7. Comparison between the UV-Vis and PDS technique. The absorption spectra of a rough $CH_3NH_3PbI_3$ thin-film measured by PDS and UV-Vis.

The samples used for the PDS measurements were prepared in an identical fashion to the solar cell preparation and spun onto water free quartz substrates (which were cleaned with acetone, isopropanol, and deionized water followed by a 10 min oxygen plasma etch). For this particular measurement, we made use of quartz rather than the FTO-coated glass to minimize light absorption because of the substrate. During the measurement, we kept the samples in a hermetically sealed quartz cuvette filled with an inert liquid, Fluorinert FC-72 from 3M Corporation, which acts as the deflection medium with high temperature dependent refractive index. We excited the perovskite films with a modulated monochromated light beam

perpendicular to the plane of the sample. A modulated monochromated light beam was produced by a combination of a Light Support MKII 100W Xenon arc source and a CVI DK240 monochromator. The transverse probe beam was produced with Qioptiq 670-nm fibre-coupled diode laser and passed as close as possible to the sample surface. Beam deflection was measured using a differentially amplified quadrant photodiode and a Stanford Research SR830 lock-in amplifier, which is proportional to the absorption in the sample. In Figure 3.8, we show the schematic for working principle of PDS measurement.

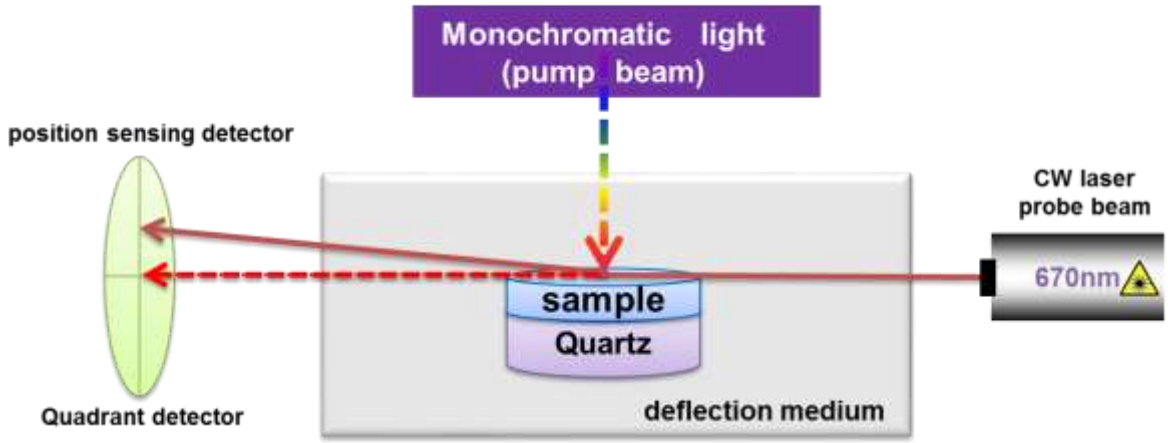

Figure 3.8. Schematic for working principle of photothermal deflection optical absorption spectroscopy (PDS). The absorption spectra of the sample is collected by measurement of the continuous wavelength (CW) laser beam deflection upon excitation with a modulated monochromated light beam perpendicular to the plane of the sample.

Furthermore, PDS technique is a powerful technique to measure the sub-bandgap tail states in a semiconductor up to an absorption coefficients of 1 cm^{-1}. This enables us to probe precisely the Urbach tail states which is a convolution of the absorption contributions from the defects, dopants and thermal potential fluctuations in a semiconductor as represented in Figure 3.9a. Therefore, a parameter known as Urbach energy (E_u) can be extracted from PDS technique, which gives information about the structural order in the material and is defined as:

$$\alpha = \alpha_0 \exp[(E-E_g) / E_u] \qquad \text{for } E < E_g \qquad (3.3)$$

The Urbach energy can be calculated from the inverse of the slope of a linear fit to the Urbach tail (or Urbach front) in the absorption spectra plotted on a natural logarithmic scale. It has a unit of energy (eV) per decade but generally, only energy unit (eV) is explicitly specified. The absorption spectra of hydrogenated amorphous silicon (a-Si:H) is shown in Figure 3.9b along with the Urbach tail (or Urbach front) and defect states. The calculated Urbach energy for a-Si:H is ~ 50 meV[161].

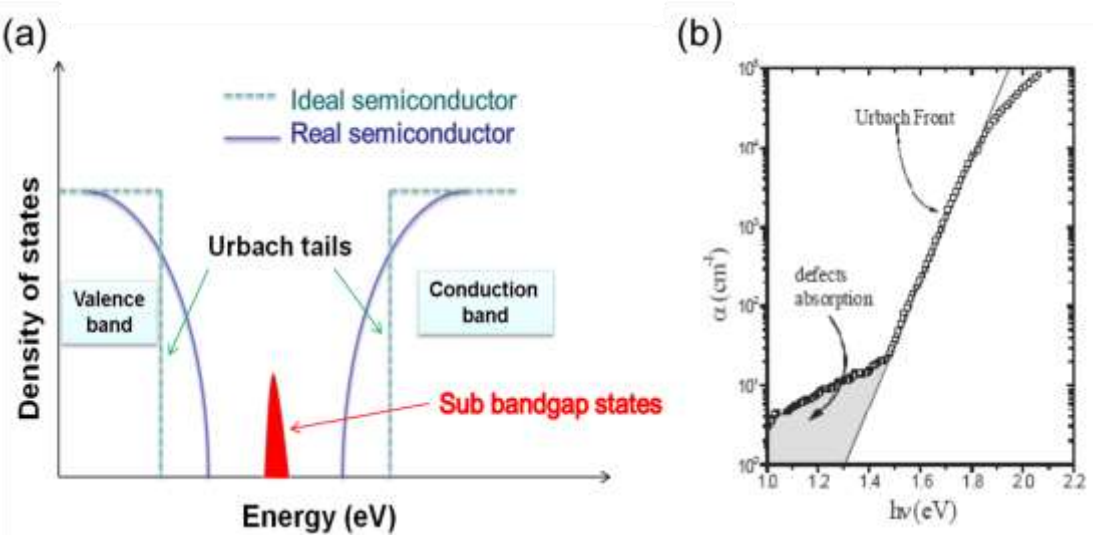

Figure 3.9. (a) Shows the difference between the density of states (DOS) of the valence and conduction bands of an ideal and real semiconductor. In a real semiconductor, sub-bandgap states are present. (b) Shows the absorption spectra of a-Si:H with its Urbach front (or Urbach tail) and defects[162].

Hence, we can use the PDS data to extract the Urbach energy values and get important information about the energetic disorder for the given material. Urbach energy is influenced by the nature of Urbach tail – steeper the Urbach tail less the Urbach energy and vice versa. Similar to the Urbach tail, Urbach energy is an energetic disorder parameter that is a convolution of the contributions from defects, doping, impurities and thermal potential fluctuations. Urbach energy thus provides a simple means to measure energetic disorder and thus opening up new avenues for the use of PDS technique in the field of material characterization.

3.4.3 Photoluminescence quantum yield characterization

Photoluminescence quantum efficiency (PLQE) measurements were taken by mounting perovskite films or encapsulated device stacks in an integrating sphere and photoexciting with a 532-nm continuous-wave laser at the given intensity. The laser and the emission signals were measured and quantified using a calibrated Andor iDus DU490A InGaAs detector for the determination of PL quantum efficiency. The external PLQE was calculated as per de Mello et al[163].

3.4.4 Photoluminescence and Lifetime Measurements

A home-built setup was used to measure the time integrated PL spectra. A 500 mm SpectraPro2500i spectrograph (Princeton Instruments) and a thermoelectrically cooled PIXIS 100-F CCD camera (Princeton Instruments) used as a detector. Diode lasers 407 nm and 470 nm are used as an excitation source. They are driven using DH400, PicoQuant laser controller. The lasers generate pulses with 80 ps full width at half maximum (FWHM) with available repetition rates over 2.5 to 40 MHz. The same setup can also be used to measure PL decay time using a 'time correlated single photon counting' setup (TCSPC). This setup comprises of a monochromator coupled with a micro channel plate photomultiplier tube (MCP-PMT from Hamamatsu - R3809U-50) and TCSPC electronics (Lifespec-pc and VTC900 PC card from Edinburgh Instruments).

3.4.5 Time-resolved photoluminescence

Time-resolved photoluminescence (TRPL) measurements were acquired with a gated intensified CCD camera system (Andor iStar DH740 CCI-010) connected to a grating spectrometer (Andor SR303i). Excitation was performed with femtosecond laser pulses which were generated in a homebuilt setup by second harmonic generation (SHG) in a BBO crystal from the fundamental output (pulse energy 1.55 eV, pulse length 80 fs) of a Ti:Sapphire laser system (Spectra Physics Solstice). Temporal resolution of the PL emission was obtained by measuring the PL from the sample by stepping the iCCD gate delay relative to the pump pulse. The gate width was 20 ns. *The TRPL measurements in chapter 6 were performed by Dr. Johannes M Richter.*

3.4.6 Confocal photoluminescence maps

PL maps were collected using a WITec alpha 300 s setup. The excitation source was 405 nm cw laser (Coherent CUBE), chopped using a Stanford Research SR 540 chopping unit at frequency of 840 Hz. The light was coupled though an optical fiber to the microscope and focused using 100x Nikon lens (NA = 0.7). The sample was positioned on a X-Y piezo stage of the microscope. The PL signal was collected in reflection mode with the same 100x objective and detected using a spectrometer fitted with a CCD detector. A low-pass filter with a cut-off wavelength of 435 nm was fitted before the CCD detector to block the excitation component of transmitted light (405nm). *All the confocal PL measurements were performed by Zahra Andaji Garmaroudi and Mejd Alsari.*

3.5 Charge transport characterizations

3.5.1 Diode for SCLC measurement

Diode for SCLC measurement. Devices were fabricated on pre-cleaned ITO substrates (15 ohm.Sq^{-1}), obtained from XINYAN Technology Ltd. For hole only devices (ITO/PEDOT:PSS/Perovskite/Au), PEDOT:PSS was spin coated at 2000 rpm and annealed at 1800C for 1 hour in air. Perovskite films were obtained by a two-step deposition process as described earlier. Similarly electron only devices (ITO/Perovskite/PCBM/Al) were fabricated. Thin PCBM layer of around 20- 30 nm was utilized to prevent the degradation of the Al electrode due to the perovskite. It was ensured that the presence of a thin layer of PCBM does not significantly degrade the electron transport of the perovskite. Metal electrodes were coated by thermal evaporation (10-6 mbar, 0.1 A0/s, 60 nm thick). The devices were characterized using Keithley 4200 SCS and temperature was varied using a RF probe station from Cryogenic Technologies. *All the SCLC charge tranport measurements were performed by Dr. Satyaprasad P Senanayak.*

3.5.2 Intensity modulated photovoltage spectroscopy (IMVS)

For intensity modulated photocurrent/photovoltage spectroscopy measurements, a white light emitting diode (LED) array driven by a Yokogawa 7651 low-noise DC power supply (Yokogawa, Sugar Land, TA, USA) was used to provide the constant background illumination.

A red light (l ¼ 625 nm) LED ring was used to provide the sinusoidal optical perturbation signal, whose intensity was modulated by the output of a Stanford SR780 dynamic signal analyzer (Stanford Research Systems, Inc. Sunnyvale, CA, USA). The transfer function module of SR780 was used to detect the IMPS/VS signals. The intensity of the modulation light was less than 10% of the white light intensity, and the frequency range was set from 100 KHz to 0.1 Hz for both IMPS and IMVS measurements. *The IMVS measurement was performed by Dr. Fabrizio Giordano.*

3.5.3 Electrochemical impedance spectroscopy (EIS)

EIS of the solar cells was carried out using a precision impedance analyzer HP4294A while the device was illuminated using a home built light source with close to 1 Sun intensity. The device was driven by a small AC frequency and obtained impedance parameters were fitted with a standard circuit to estimate the physical parameters. *All the EIS measurements were performed by Dr. Satyaprasad P Senanayak.*

3.5.4 Time-resolved microwave conductivity (TRMC) measurements

The TRMC technique monitors the change in reflected microwave power by the loaded microwave cavity upon pulsed laser excitation. The photo-conductance (ΔG) of the perovskite films was deduced from the collected laser-induced change in normalized microwave power ($\Delta P/P$) by $-K\Delta(t)=\Delta P(t)/P$, where K is the sensitivity factor. The yield of generated free charges φ and mobility $\Sigma\mu=(\mu_e+\mu_h)$ were obtained by: $\varphi\Sigma\mu=\Delta G/(I_0\beta eF_A)$, where, I_0 is the number of photons per pulse per unit area, β is a geometry constant of the microwave cell, e is the elementary charge, and F_A is the fraction of light absorbed by the sample at the excitation wavelength of 600 nm. *The TRMC measurement was performed by Dr. Eline M Hutter.*

3.6 Solar cell characterizations

Current–voltage characteristics were recorded by applying an external potential bias to the cell while recording the generated photocurrent with a digital source meter (Keithley Model 2400). The light source was a 450 - W xenon lamp (Oriel) equipped with a Schott-K113 Tempax sunlight filter (Praezisions Glas & OptikGmbH) to match the emission spectrum of the lamp to the AM1.5G standard. Before each measurement, the exact light intensity was determined using a calibrated Si reference diode equipped with an infrared cut-off filter (KG-3, Schott).

EQE spectra were recorded as a function of wavelength under a constant white light bias of approximately 5mW.cm^{-2} supplied by an array of white light emitting diodes. The excitation beam coming from a 300 W xenon lamp (ILCTechnology) was focused through a Gemini-180 double monochromator (Jobin Yvon Ltd) and chopped at approximately 2 Hz. The signal was recorded using a Model SR830 DSP Lock-In Amplifier (Stanford Research Systems). All measurements were conducted using a non-reflective metal aperture of 0.105 cm^2 to define the active area of the device and avoid light scattering through the sides.

For stability measurements, the solar cells were transferred to a sealable device holder under nitrogen-glovebox conditions. During testing the device holder was continuously purged with dry nitrogen, pre-filtered (SGT Super Clean) to minimize residual oxygen, moisture and hydrocarbon content. A Newport solar simulator with equivalent AM 1.5 G 1-sun output was used to illuminate the entire device substrate; short wavelengths were filtered using a 435 nm long pass filter (Thor Labs FGL435). Ageing under these conditions resulted in a chamber ambient temperature of approximately 40˚C, as measured by a thermistor next to the solar cell device, which was reached within 30 minutes of the experiment commencing. Photocurrent characteristics were recorded by holding close to the maximum power point voltage (as ascertained from an initial J-V curve) using a Keithley 2636 SMU and a custom-written LabView VI code. Devices were stored in a nitrogen-filled glove box in the dark between shelf-life measurements.

3.7 Density functional theory (DFT) calculations

The crystal DFT calculations were performed following the previously published procedure[164]. The generalized gradient approximation (GGA) for exchange correlation using the Perdew-Burke-Ernzerhof (PBE) functional was applied and simulations used pseudopotential[165] as implemented within the Quantum Espresso package[166]. The Silver 5*d*10/6*s1*,Copper 4*d*10/*5s1, Sodium 2p6/3s1,* lead 5*d*10/6*s*2/6*p*2, the nitrogen 2*s*2/2*p*3, the iodide 5*s*2/5*p*5, and the carbon 2*s*2/2*p*2 electrons were considered as valence electrons. The super cells consisted of 384 atoms in a 2x2x2 tetragonal Bravais lattice, and the initial cell parameters were set to a = 16.*42* °A and c = 24.*92*A° for $CH_3NH_3PbI_3$. The tetragonal unit cell can be described as composed of four slightly distorted cubic unit cells with a cell parameter of around 6.31 A°. Substitution of one lead with Ag, Cu or Na within the lattice corresponds to the ~3% doping. For the interstitial doping , the unit cell has 385 atoms and the dopant has been placed close to an estimated energetically favorable cite within the lattice. The unit cell volume and all coordinates of the atoms have been optimized to have a total force lower than 0.04 Ry/Boh. Cutoff energies for the plane wave function and the charge density were set to 40 and 450 Rydberg, respectively. Brillouin zone samplings were carried out by a 2×2×2 Monkhorst-Pack grid .The

orientation of the different methyl ammonium ions ($CH_3NH_3^+$) was chosen in a way where neighboring dipoles were perpendicular to each other[167]. This configuration of the methyl ammonium ions has been reported to constitute, based on DFT calculations, to be the most stable phase at room temperature for the lead perovskite $CH_3NH_3PbI_3$[167]. Neglecting the Entropy contributions to the energy, the formation energy (E_F) of the doped and pristine lead perovskites was estimated by calculating the difference of their total lattice energy and the relevant precursors. For example:

$100MAI + 99PbI_2 + YI + (1/2)I_2 (Y = Na, Ag \text{ or } Cu) \rightarrow 100MAPb_{1.01}YI_3$

$E_F = E(100MAPb_{1.01}YI_3) - (1/2)E(I_2) - E(YI) - 99E(PbI_2) - 100E(MAI)$

Estimation of the work function forthe corresponding perovskite materials could in principle be done using a slab approach by comparing the bare+Hartree potentials (calculated in QUANTUM ESPRESSO) within slab to value in the vacuum region. However the high dipolar nature of the material with positively charged octahedrons and negatively charged MA cations together with different dipolar orientations of the MA cations inside the lattice makes these calculation difficult to converge and therefore it is difficult to find a stable absolute reference for the vacuum level[164]. Partial Density of states (PDOS) band structure and charge density plots have been calculated by post processing the ground state charge density of the perovskite lattices obtained by Quantum Espresso package. The charge carrier effective masses were calculated using the below equations.

$$(m_h^*)^{-1} = \frac{1}{\hbar^2}\frac{d^2}{dk^2}E_{VB\,max}(k) \tag{3.4}$$

$$(m_e^*)^{-1} = \frac{1}{\hbar^2}\frac{d^2}{dk^2}E_{CB\,min}(k) \tag{3.5}$$

The DFT calculations were performed by Roghayeh Imani and Dr. Meysam Pazoki.

Chapter 4

Modification and chemical passivation of titanium (IV) dioxide nanostructure in mesoscopic perovskite solar cells

We report on the optimization of the interfacial properties of titania in mesoscopic $CH_3NH_3PbI_3$ solar cells. Modification of the mesoporous-TiO_2 film by $TiCl_4$ passivation substantially reduced the surface traps, as evident from sharpness of the absorption edge with a significant reduction in Urbach energy (320 meV to 140 meV) determined from photothermal deflection spectroscopy and lead to an order of magnitude enhancement in the bulk electron mobility and corresponding decrease in the transport activation energy (170 meV to 90 meV) within a device. After optimization of the photoanode-perovskite interface using various sizes of TiO_2 nanoparticles, the best photovoltaic efficiency of 16.3% was achieved with the mesoporous-TiO_2 composed of 36 nm sized nanoparticles. The improvement in device performance can be attributed to the enhanced charge collection efficiency that is driven by improved charge transport in the mesoporous TiO_2 layer. Also, the decreased recombination at the TiO_2-perovskite interface and better perovskite coverage play an important role. A detailed explanation of all these results is presented below and can also be found in the published article - ref. [157].

Contributions. This work was the result of collaborative research with the following contributions: I conceived and planned the experiments with additional input from prof. Richard Friend, prof. Michael Graetzel, Dr Ibrahim Dar and Dr Aditya Sadhanala. I fabricated all samples and devices, performed, and analysed the SEM, XRD, UV-Vis, PDS, PL, TRPL, JV and EQE measurements. Dr Satyaprasad P. Senanayak performed and analysed the EIS and SCLC charge transport measurements (Figure 4.2d, Figure 4.6d, e, Figure 4.10b, Figure 4.11). Dr Fabrizio Giordano performed the IMVS measurement and analysed the data (Figure 4.10a).

4.1 Introduction

A typical mesoscopic perovskite solar cell (PSC) contains a hole blocking TiO_2 (bl-TiO_2) layer, mesoporous TiO_2 (mp-TiO_2), hybrid organic-inorganic perovskite sensitizers, hole transporting material (HTM) and counter electrode (e.g. Au) as the key components. The mp-TiO_2 layer in a typical dye-sensitized solar cell (DSSC) plays three major roles; provides a scaffold to increase the surface area of the absorber layer, act as a hole blocker, and transports photogenerated electron from the sensitized surface to the front contact[168]. Therefore, the active surface area which has a direct link with particle size of mesoporous material is a key parameter in DSSC[169]. However, Lee et al. have shown that hybrid organic-inorganic perovskite absorber can transport photogenerated electron to the conductive substrate itself[170]. On the other hand, it is reported that employing the mesoporous TiO_2 layer substantially reduces the hysteresis behaviour of PSC[171]. In addition, it is widely recognized that the interface between the absorber layer and the carrier transport layers, as well as the inherent carrier transporting properties of the layers are also important. An ideal carrier transport material is expected to possess a suitable energy level, high conductivity, and low surface recombination rate. Several materials have been investigated as electron transport layers (ETL) such as TiO_2, ZnO and phenyl-C_{61}-butyric acid methyl ester (PCBM)[172–175]. Among all of them, TiO_2 arguably is the most commonly used ETL has delivered the best photovoltaic performance in PSC thus far[176]. To improve the performance of mesoscopic solar cells, further investigation is needed to engineer the mp-TiO_2-perovskite interface[177,178].

In this chapter, we explored the effect of $TiCl_4$ post-treatment of mp-TiO_2 on the optical behaviour and the level of electronic disorder using space charge limited current (SCLC) technique and photothermal deflection absorption spectroscopy (PDS) and correlated our findings with the photovoltaic behaviour of the fabricated PSC (Figure 4.1, left section). We further extended the study by investigating the effect of the titania nanoparticle size on the charge transport, recombination properties, optical behaviour and the photovoltaic performance of PSC (Figure 4.1, right section). For a comparative analysis, we synthesized two alkaline TiO_2 pastes (NP36 and NP50) and compared them with commercial 18NRT dyesol TiO_2 nanoparticles. Finally, based on our new findings, we suggest the main criteria for the mp-TiO_2 in acting as an ideal electron transport layer for achieving the high efficiency in PSCs.

4.2 $TiCl_4$ post treatment of mesoporous TiO_2 film

In DSSC, $TiCl_4$-treatment of mp-TiO_2 electrode prior to the device fabrication improves the performance of the photovoltaic devices[179], because of several phenomena, such as an increase in the electron injection rate, a retardation of the electron–hole recombination and/or an increase in the dye loading. However, the exact mechanism of the improvement is not clearly understood[180].

Herein, we investigated the effect of $TiCl_4$-treatment on the morphology and absorption of 36 nm sized mp-TiO_2 as well as on the device performance (Table 4.1). We used a typical structure of perovskite solar cells which consists of spray coated titania compact layer on fluorine-doped tin oxide (FTO) coated glass, spin-coated mp-TiO_2, sequential two-step spin-coated $CH_3NH_3PbI_3$ perovskite, Spiro OMeTAD as a hole transport layer and back contact of thermally evaporated gold layer. It is notable a capping layer of perovskite is formed on top of the mp-TiO_2 layer (Figure 4.1). SEM images of the pristine and treated mp-TiO_2 showed that a very thin layer of compact titania covered the surface of TiO_2 nanoparticles (Figure 4.2a, b). Upon $TiCl_4$ treatment, the photovoltaic devices exhibit an increase in the open circuit voltage (V_{oc}) by 50 mV, in addition to the marginal improvement in the short circuit current (J_{sc}) and fill factor (FF) which gets reflected in the overall efficiencies of the PSC (16.1%). It is notable that the coverage and morphology of perovskite capping layer has not altered upon this treatment (Figure 4.2e, f).

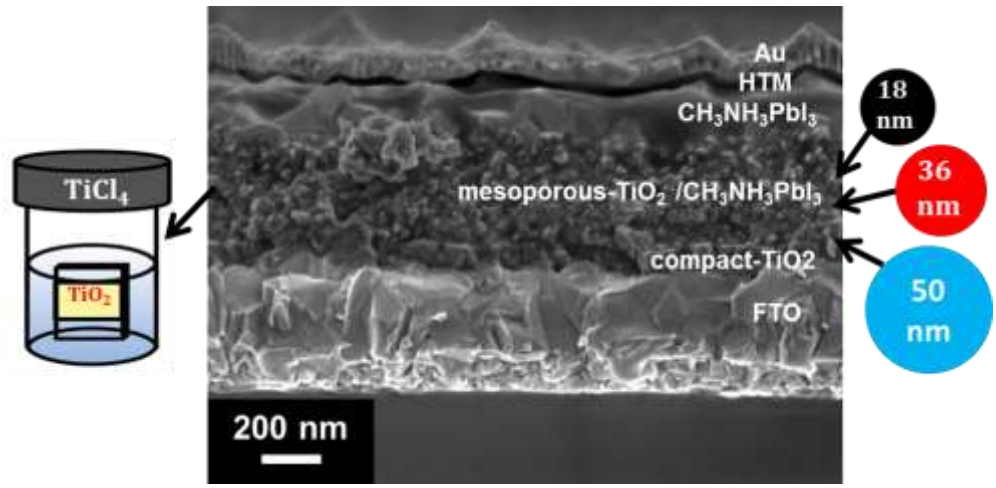

Figure 4.1. SEM cross sectional micrograph of a complete device having the structure of: FTO/compact TiO_2/mesoporous-TiO_2/ $CH_3NH_3PbI_3$/Spiro-OMeTAD/Au.

Table 4.1. Summary of the photovoltaic parameters extracted from J–V measurements under simulated AM1.5G irradiation and electron mobility along with activation energy and the corresponding errors for devices (batch of 20 devices) based on 300nm thick mp-TiO_2 without (pristine) and with $TiCl_4$ post-treatment.

Type of device	J_{SC} (mA cm^{-2})	V_{OC} (mV)	FF	PCE (%)	μ_e (cm^2/Vs)	E_A^e (meV)
Pristine	21.36±0.3	970±12	0.70±0.02	15.2±0.3	0.002±0.001	170±15
$TiCl_4$ post-treated	22.12±0.1	1020±10	0.71±0.01	16.1±0.2	0.03±0.006	95±9

Based on the PDS measurements (Figure 4.2c), $TiCl_4$ treatment significantly reduced the sub-bandgap absorption and increased the density of states near the titania band-edge that has been shown to improve the mobility in metal oxides and could potentially improve the charge transport within the mp-layer in a solar cell configuration[181,182]. In a PDS spectra, the slope of the absorption at the band edge defines the Urbach energy (E_u), and provides a measure for the degree of energetic disorder of a material[183,184]. The estimated Urbach energy for the pristine and $TiCl_4$ post treated titania, along with the respective fitting errors, are 320 and 140 meV, respectively (inset of Figure 4.2c).

Furthermore, a direct estimation of the disorder is obtained from a measure of the activation energy (E_A^e) acquired from the temperature-dependent bulk transport measurements. Based on this measurement on electron-only devices FTO/TiO_2 (treated or untreated)/Perovskite/Al, we estimated the electron mobility (μ_{SCL}^e) ~ 0.002 $cm^2.V^{-1}.s^{-1}$ for pristine devices which increases to around 0.03 $cm^2.V^{-1}.s^{-1}$ upon the treatment (Table 4.1). Correspondingly, the E_A^e decreases from 170 meV to 95 meV for $TiCl_4$-treated mp-TiO_2 based PSC (Figure 4.2d). This enhancement in the electron mobility in addition to passivation of trap states at the perovskite–titania interface which considerably minimizes the recombination of the charge carriers and enhances charge transport can then be correlated to the enhanced V_{oc}, J_{sc} and the overall PCE of devices[185].

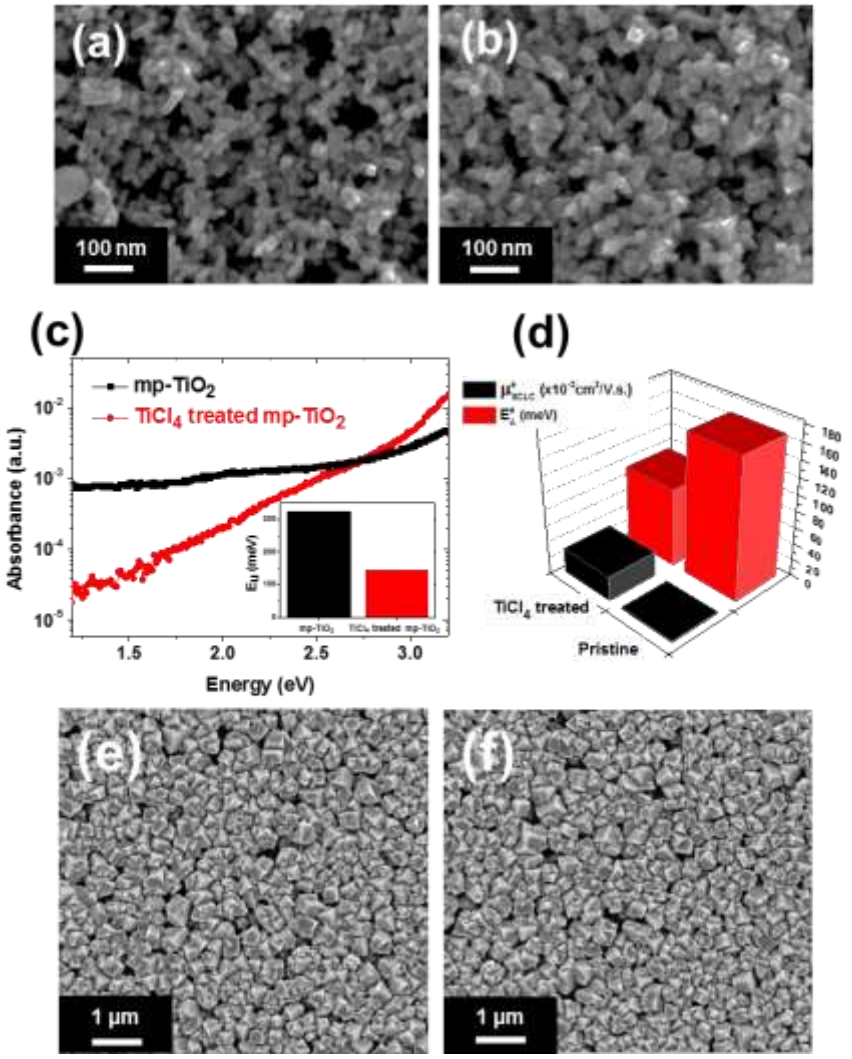

Figure 4.2. (a) Top view SEM images of pristine mp-TiO_2 film and (b) with $TiCl_4$ post-treatment. (c) The PDS absorbance spectra of mp-TiO_2 films, pristine and $TiCl_4$ post-treated. The inset shows the corresponding Urbach energies. (d) Effect of $TiCl_4$ treatment on Electron mobility and activation energy in the fabricated device. Top view SEM images of perovskite capping layer formed on top of (e) pristine (f) $TiCl_4$ treated mp-TiO_2.

4.3 Modification of particle size in mp-TiO_2 nanostructure

To further understand the role of the titania interlayer on the photovoltaic performance, we investigated three different particle sizes of mp-TiO_2 using two synthesised titania with 36 nm (NP36) and 50 nm (NP50) sized nanoparticles based on the reported procedure[186] and the commercial 18NRT dyesol titania paste. In Table 4.2, we summarize the aspects of these titania films. It is evident that NP50 has the maximum pore size of 70 nm compared to 45 nm and 25

nm pore diameter for NP36 and 18NRT, respectively. In addition, the porosity of 18NRT and NP36 films are similar (≈67%) compare to a lower porosity for NP50 (60%). Furthermore, the Brunauer, Emmett and Teller (BET) surface area of these TiO_2 films is diminished significantly from 84.91 $m^2.g^{-1}$ to 29.54 $m^2.g^{-1}$ when the particle size increases from 18 nm to 50 nm. All TiO_2 dispersions were diluted in ethanol using an optimum weight ratio (1:4).

Table 4.2. Characterization of 18NRT dyesol and synthesised TiO_2 nanoparticles.

Type of TiO_2 nanoparticles	Average Particle size (nm)	Average pore diameter (nm)	Porosity (%)	BET Surface area ($m^2.g^{-1}$)
18NRT	18	25	68	84.91
NP36	36	45	66	44.02
NP50	50	70	60	29.54

It is evident from macroscopic images that 18NRT mp-TiO_2 film is transparent while NP36 and NP50 are relatively scattering (Figure 4.3a). It is possible to directly correlate the transparency of the TiO_2 film with the particle size. Films coated with larger nanoparticles were relatively less transparent than those coated with smaller nanoparticles. This behaviour can be attributed to the increase of light scattering with particle size. The scattering behaviour of the titania films with different particle size is also evident from the diffuse reflectance spectra as shown in Figure 4.3b.

Further characterization of the titania nanoparticle size was obtained from both X-ray diffraction patterns (XRD), SEM and TEM measurements. XRD of different titania films were investigated to obtain information regarding the crystal structure, phase composition and the nano-particle size. The XRD patterns for mp-TiO_2 films having different particle sizes confirm the anatase crystal phase of titanium dioxide (Figure 4.4a). In addition, the average particle size for 18NRT, NP36 and NP50 is calculated using the Scherrer equation according to the full width at half maximum (FWHM) of the strongest (101) diffraction peak in XRD pattern. Expectedly, the XRD peaks broaden with decreasing particle size (Figure 4.4b). These values

are consistent with the top-view SEM and TEM images of the titania nanoparticles (Figure 4.5).

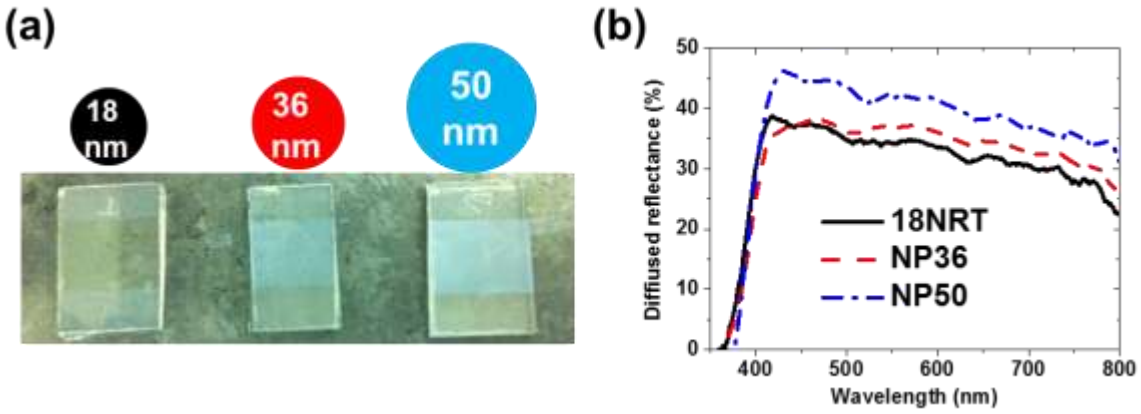

Figure 4.3. (a) The mesoporous TiO_2 films for 18NRT, NP36 and NP50 deposited on FTO coated glass after annealing process. (b) Diffuse reflectance spectra of mesoporous TiO_2 films having different particle size.

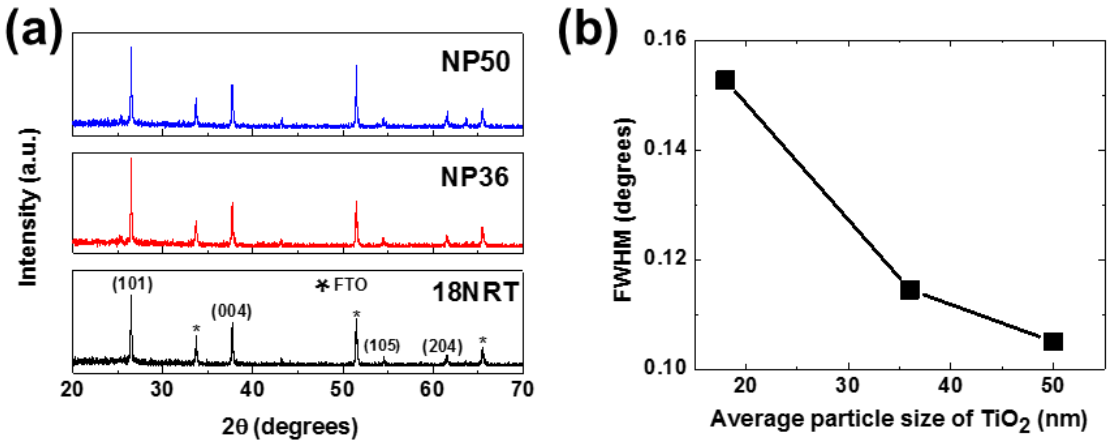

Figure 4.4. (a) X-ray diffraction spectra (b) Full width half maximum (FWHM) of the (101) peak for mesoporous TiO_2 films having different particle size. All the peaks could be indexed to the anatase crystal phase of titanium dioxide (standard JCPD file number (21-1272)).

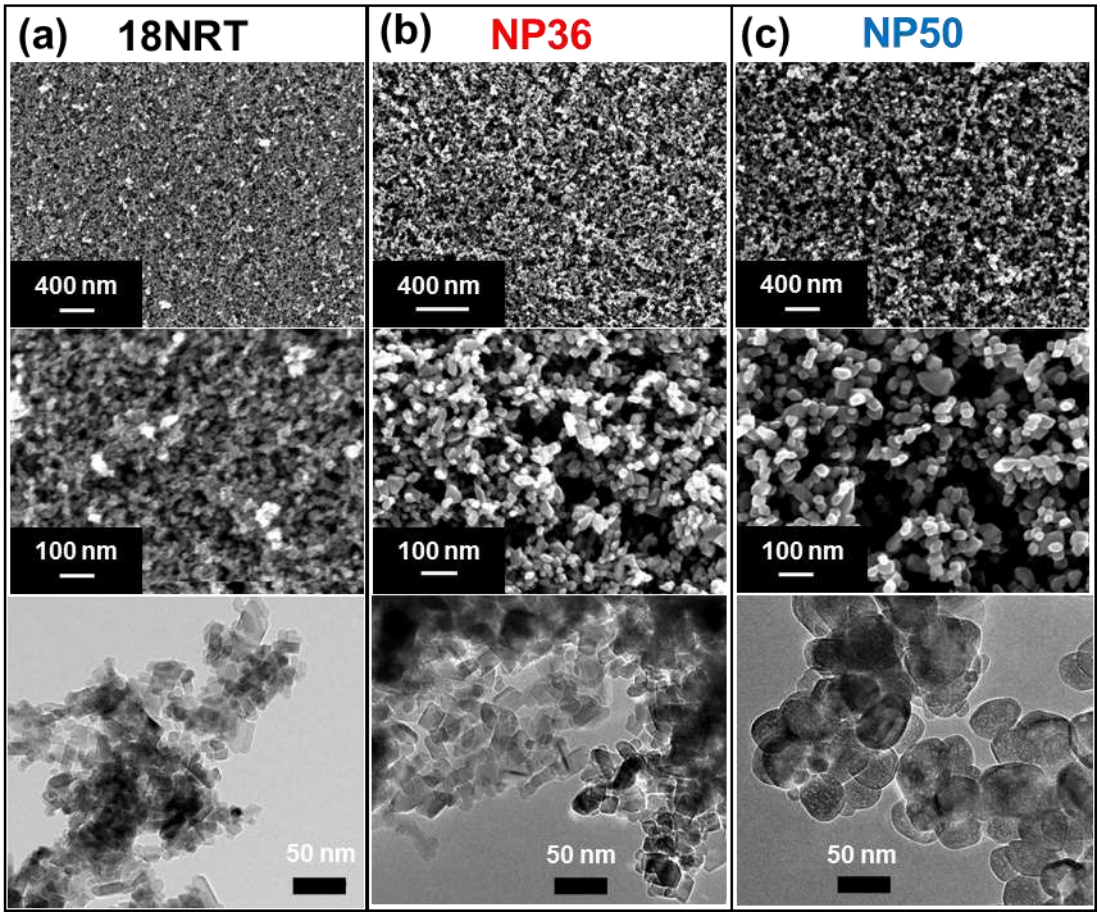

Figure 4.5. Top-view SEM micrographs (top two images) of different mesoporous TiO_2 films and TEM micrographs (bottom images) of (a) 18NRT, (b) NP36 and (c) NP50.

PDS of different sized mp-TiO_2 films shows that the sub-bandgap absorption is lower for both NP36 and NP50 compare to 18NRT and the estimated E_u is the lowest for NP36 (140 meV) representative of the lowest level of electronic disorder (Figure 4.6a). To extract further information on the light-induced charge injection/separation, we performed time-resolved photoluminescence (PL) decay measurements on the $CH_3NH_3PbI_3$ deposited on different mp-TiO_2 films (Figure 4.6c). Using standard biexponential fits, the PL decay of the infiltrated perovskite in 18NRT, NP36 and NP50 films exhibits a time-constant of τ_1= 1.06 ns, 4.49 ns and 6.76 ns, respectively. It is evident that the temporal decay of PL intensity become faster, as the nanoparticle size of the TiO_2 reduces.

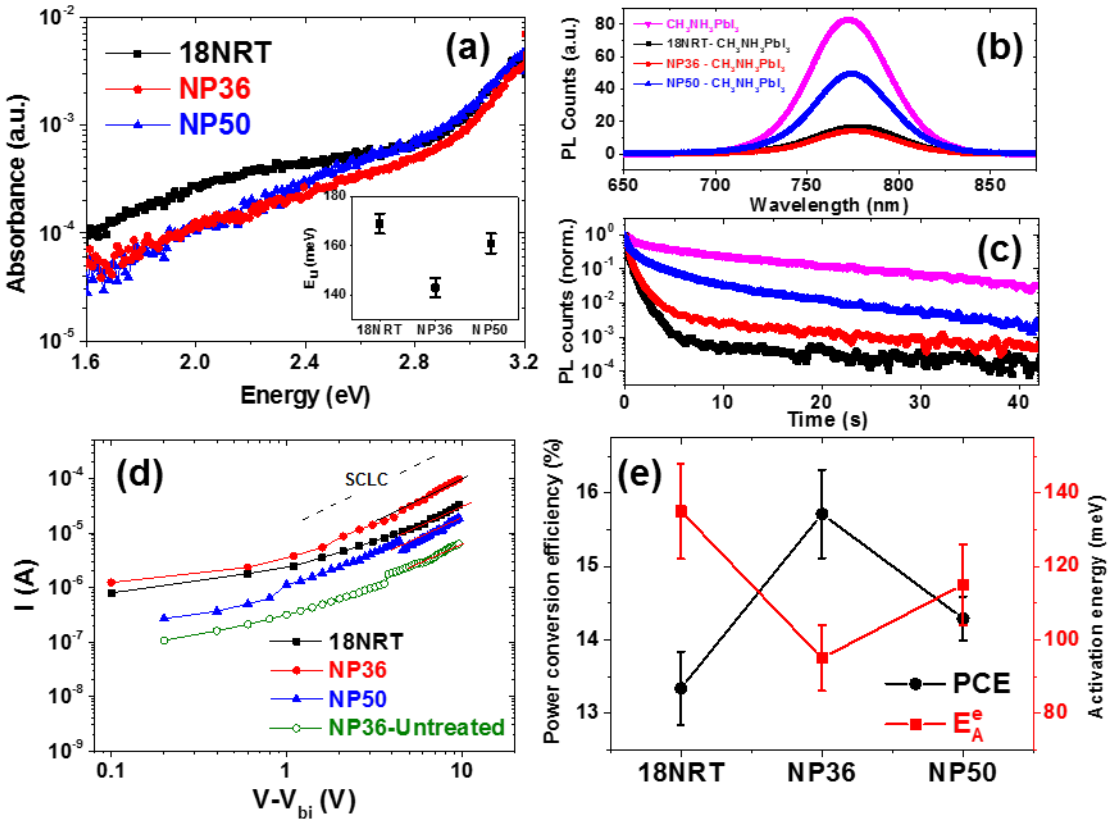

Figure 4.6. (a) The PDS absorption spectra of different mp-TiO_2 films. The inset shows the corresponding Urbach energies for all the titania films. The error bar is defined by the s.d in fitting the Urbach tail. (b) Photoluminescence counts of bare and infiltrated $CH_3NH_3PbI_3$ to different sized mesoporous TiO_2 films. (c) Fluorescence decay kinetics measured at 780 nm upon excitation at 407 nm with fluence of 0.7 nJ.cm^{-2} for perovskite films deposited on different mp-TiO_2 layers. (d) I–V characteristics of electron only devices (FTO/TiO_2/Perovskite/AL), utilized for estimating the SCLC electron mobility. (e) The trends in the PCE and E_A^e for PSC based on different sized mp-titania layers.

The PL decay of the aforementioned films arises from quenching of the PL intensity (Figure 4.6b) because of the following two reasons; first, radiative relaxation of excited electrons back to the ground state of perovskite, second, electron injection from the conduction band of perovskite into the conduction band of titania. Because the radiative relaxation back to the ground state of perovskite occurs at a certain inherent rate that corresponds to the PL decay rate of the bare $CH_3NH_3PbI_3$ shown in Figure 4.6c, the acceleration of the PL decay rate with the reduction of the titania nanoparticle size in the TiO_2/$CH_3NH_3PbI_3$ films indicates more

efficient injection of electrons from the perovskite to TiO_2. Therefore, we can infer that, as the size of TiO_2 nanoparticles become smaller, the electron injection from perovskite to TiO_2 becomes more efficient.

It is well established that not only the precursor compositions of perovskite[187,188] but also the substrate can influence the growth and formation of perovskite films[189,190]. Top-view SEM images of perovskite capping layer on mp-TiO_2 shows that NP36 has the best coverage as the titania layer is fully covered by perovskite crystals while in both 18NRT and NP50, we observe some pinholes in between the perovskite grains (Figure 4.7).

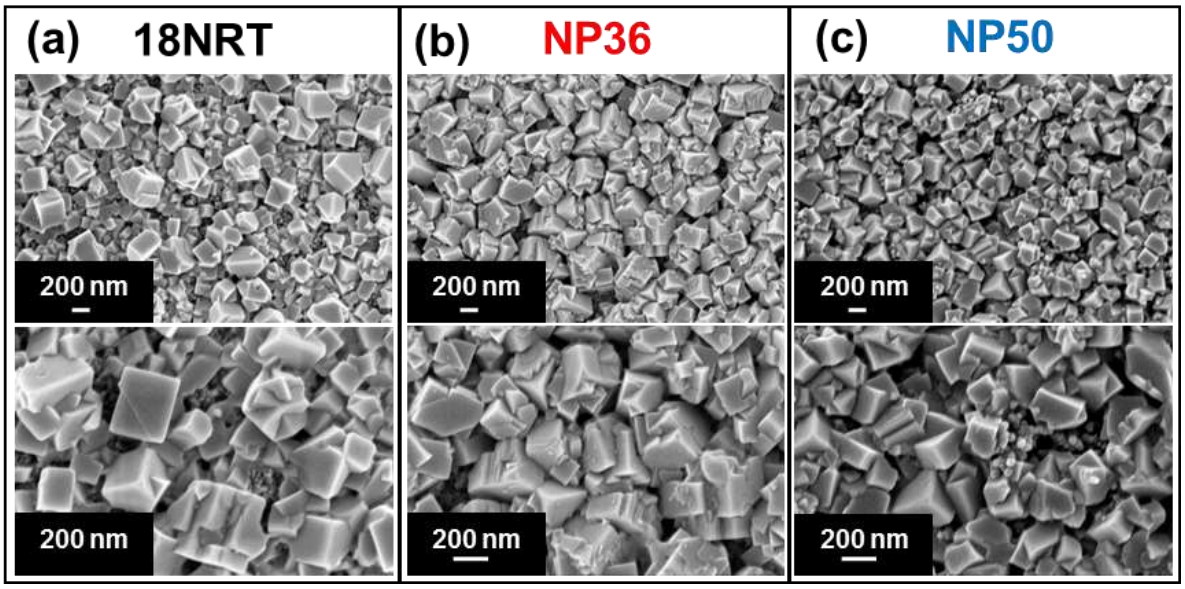

Figure 4.7. Top-view SEM images of sequentially deposited perovskite on top of different mp-TiO_2 (a) 18NRT, (b) NP36 and (c) NP50.

In order to investigate the effect of modification of TiO_2 layer on the electron transport behavior, we fabricated electron only (FTO/TiO_2/Perovskite/Al) devices for SCLC measurement (see details in Experimental methods Chapter)[191]. Remarkably, our transport measurements indicate a clear trend where the μ^e_{SCL} and E^e_A were altered upon modification of mp-TiO_2 (Table 4.3, Figure 4.6d, e). Electron mobility as high as (μ^e_{SCL}) 0.03 $cm^2.V^{-1}.s^{-1}$ and the lowest activation energy of 95 meV was obtained for NP36 based devices. Therefore, the disorder in the perovskite is strongly affected by the layer on which it is deposited[192]. The

observed enhancement in the μ_{SCL}^{e} and the decrease in E_A^e is expected to improve the J_{sc} and decrease the recombination which could enhance the V_{oc} resulting in an overall improvement in the PCE.

Table 4.3. Summary of the photovoltaic parameters derived from J-V measurements and charge mobilities along with activation energies for the perovskite solar cells based on different sized mp-TiO_2 (showing the best performance).

Type of device	J_{SC} (mA cm^{-2})	V_{OC} (mV)	FF	PCE (%)	μ^e ($cm^2.V^{-1}.s^{-1}$)	E_A^e (meV)
18NRT	21.3	965	0.67	13.8	0.01± 0.008	135± 13
NP36	22.2	1029	0.71	16.3	0.03±0.005	95± 9
NP50	21.6	948	0.71	14.6	0.008±0.003	115±11

Hence, as a next step, photoanodes based on different sized mp-TiO_2 were used to explore particle size effect on the photovoltaic performance of PSC (Table 4.3 and Figure 4.8a). The statistics of the photovoltaic parameters follow the same trend as the best performing devices (Figure 4.8c-f). As the diameter of the particles increases from 18 nm to 36 nm, the average J_{sc} rises from 21.1 mA.cm^{-2} to 22.3 mA.cm^{-2}. This trend in J_{sc} can be attributed to the narrow tunnels in the 18 nm TiO_2 mesoscopic framework in which the perovskite cannot infiltrate till the bottom of the TiO_2 layer easily. However, in the NP36, the improved pore filling caused by a larger pore size leads to an enhancement of the J_{sc}. This is consistent with UV-Vis absorption spectra, which shows a higher absorption above the band edge for the perovskite deposited on NP36 compare to 18NRT (Figure 4.9). Further increase of the TiO_2 particle size to 50 nm causes a slight decline in the photocurrent density which may be ascribed to the pronounced scattering properties of larger titania nanoparticles (Figure 4.3) as well as the reduction of the porosity which minimizes the amount of perovskite in the mesoscopic TiO_2 framework. The enhancement in current densities of PSC based on different size of mp-TiO_2 nanoparticles are supported by the improvement in the external quantum efficiency (EQE) spectra shown in Figure 4.8b.

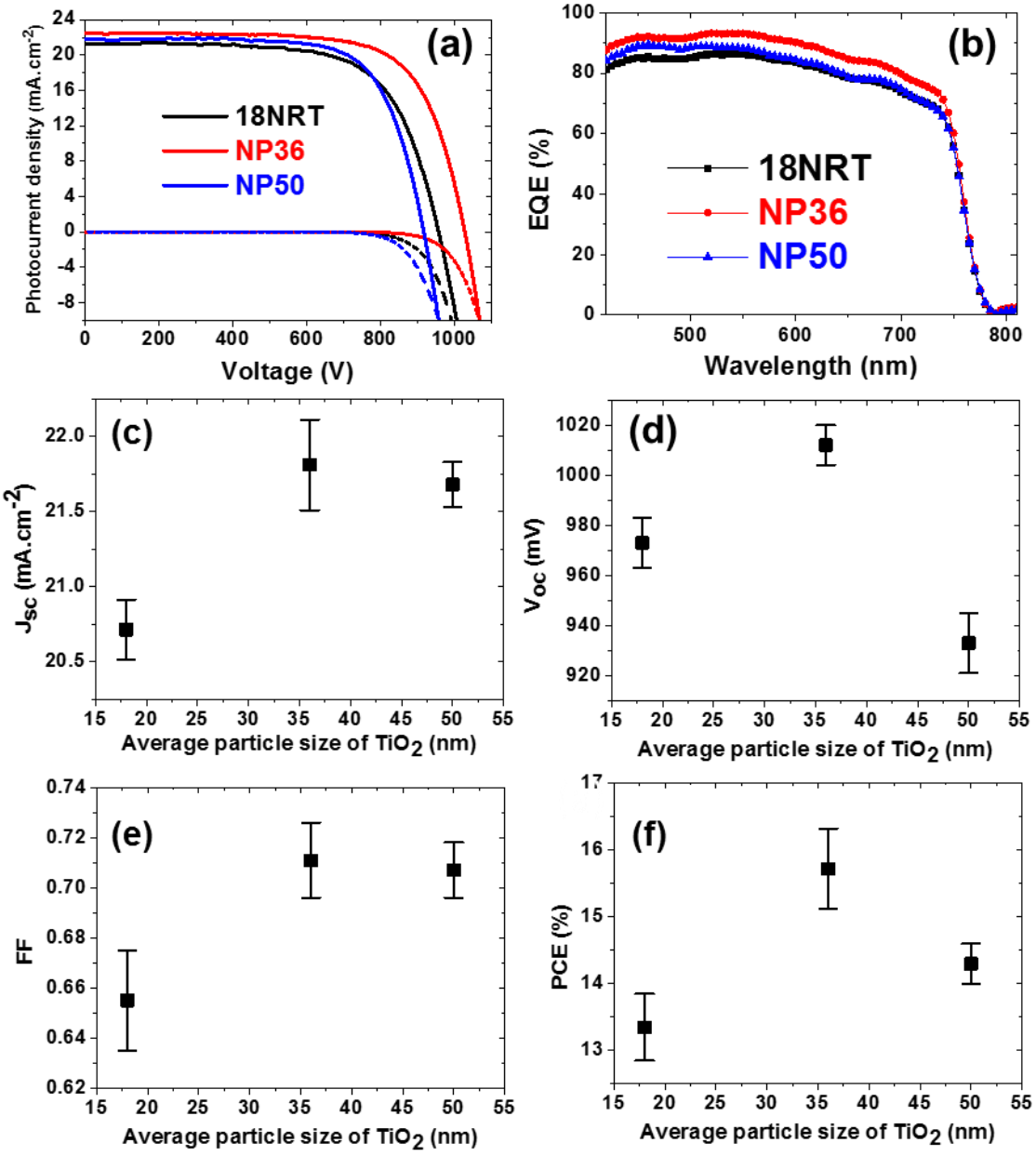

Figure 4.8. (a) Current-voltage characteristics measured under standard 1 sun conditions (AM 1.5 G, 100 mW.cm-^{2}) (solid lines) and dark conditions (dashed lines). (b) External quantum efficiency (EQE) spectra as a function of the wavelength of monochromatic light for the perovskite solar cells obtained from different mp-TiO_2 nanoparticles. Photovoltaic parameters (c) J_{sc}, (d) V_{oc}, (e) FF and (f) PCE extracted from J–V measurements under 100 mWcm^{-2} simulated AM1.5G irradiation for devices based on TiO_2 films of different particle sizes. The error bars represent the standard deviation from the mean value of photovoltaic parameters for ten solar cells per each condition.

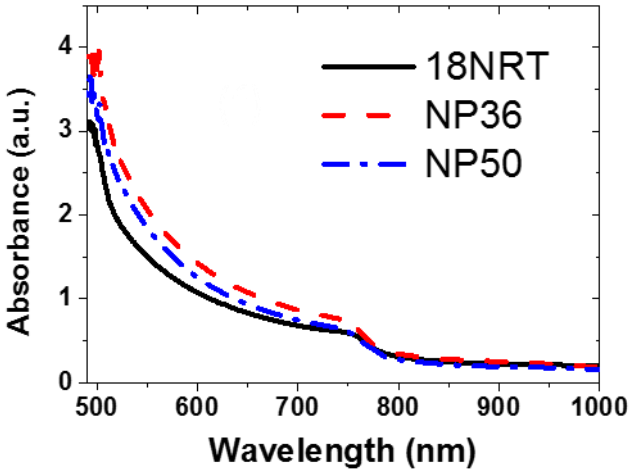

Figure 4.9. UV-Vis absorption spectra of sequentially deposited perovskite on top of mp-TiO_2 having different nanoparticle sizes.

As shown in Table 4.3, the FF increases from 0.67 to 0.71 when the size of TiO_2 nanoparticles increases from 18 nm to 36 nm and remains the same for NP50, which might be attributed to the reduction in the electron transport resistance of the TiO_2 mesoscopic structure and better filling of the perovskite. In addition, the average value of V_{oc} climbed from 970 mV to 1029 mV by changing the TiO_2 average particle size from 18 nm to 36 nm. Our observations indicate that NP36 exhibit the optimum pore size for efficient infiltration of the perovskite into the mp-TiO_2 (Figure 4.7), the highest electron mobility and the lowest disorder in the interface with perovskite resulting in the enhancement of V_{oc}, J_{sc} and a maximum PCE of 16.3%.

Based on the J-V characteristic of the devices under dark, the dark current onset begins at around 600 mV for the NP50 while it shifts to ~650 and ~750 mV for 18NRT and NP36, respectively (Figure 4.8a). On forward biasing, the recombination of the photogenerated electrons at the interfaces between FTO or TiO_2 and HTM is a potential source of dark current. Here, the recombination at the TiO_2-HTM interface for NP50 might be due to the weak coverage of the pores with perovskite that dominates and leads to lower V_{oc} while the effect of recombination from the FTO-HTM interface is negligible due to the complete coverage of FTO by a compact TiO_2 layer.

To study the charge transfer and recombination processes in a PSC based on various sized mp-TiO_2, we performed intensity modulated photovoltage spectroscopy (IMVS) shown in Figure

4.10a. The electron recombination time constant (τ_r) as a function of titania particle size, which is calculated using $\tau_r = 1/2\pi f_r$, where f_r is the characteristic frequency minimum of an IMVS curve. The increased τ_r from 18NRT to NP36 suggests a reduction of the electron recombination process in the PSC. This could be attributed to two factors; firstly, the lowest electronic disorder at the TiO_2-perovskite interface, secondly, the improved blocking effect of perovskite overlayer for NP36, which showed the best perovskite coverage, and potentially helps in reducing the electron-hole recombination between TiO_2 and HTM. However, when the size of TiO_2 nanoparticles is further increased (NP50), higher disorder in the titania layer increases the number of trap sites in the device structure eventually leading to a possibility of electron-hole recombination and hence τ_r decreases [193].

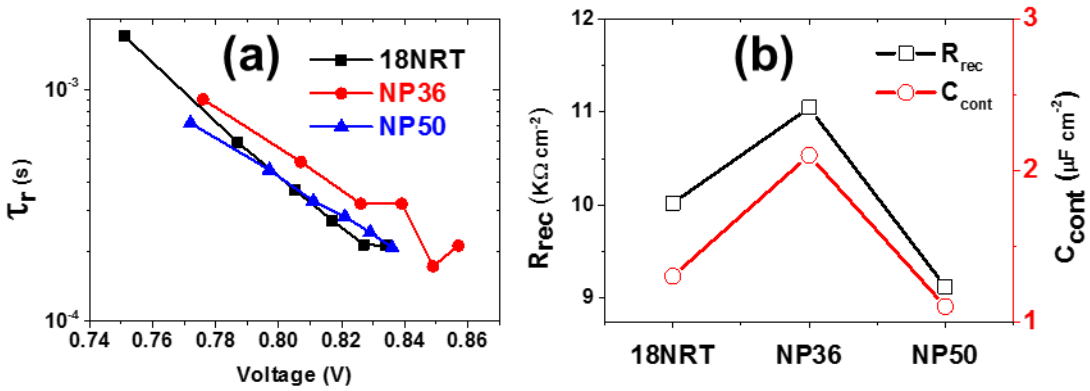

Figure 4.10. (a) Comparison of τ_r for the PSC based on different sized mp-titania layers. (b) The trends in the R_{rec} and Ccont for PSCs based on various mp-TiO_2 layers.

To further understand the transport mechanism, we utilize electrochemical impedance spectroscopy (EIS) on PSC fabricated with different mp-TiO_2 layers. The EIS measurement was performed on the complete photovoltaic devices operating under illumination and open circuit conditions (Figure 4.11). The EIS spectra were fitted with an appropriate equivalent circuit to estimate parameters related to the charge recombination and polarization relaxation of the perovskite layers (Figure 4.11a). Based on the fitting of the equivalent circuit to the EIS data, we obtain the recombination resistance to be maximum for NP36, which is consistent with the trend of higher J_{sc} magnitude (Figure 4.10b). Correspondingly, the large area in the

EIS of the NP50 can be correlated to higher series resistance, which is in agreement with the lower J_{sc} magnitude. Differences in the trend of V_{oc}, J_{sc} and FF of the PSC with the parameters of the EIS spectra arises due to the preliminary level of the equivalent circuit utilized for the fitting.

In general, the observation of higher value of J_{sc} in a photovoltaic device can be related to a range of factors. This includes enhanced transport in the active layer, which supports lower recombination and enhanced charge collection at the adjacent contacts. Since we compare photovoltaic devices with identical active layer fabricated under the same conditions, the differences originating from the charge transport in the active layer can be completely ignored. Hence, the variation in the R_{rec} can be attributed to the collection efficiency of the interface. Similarly, the enhancement of the C_{cont} for a particular photovoltaic cell based on NP36 directly correlates with the enhancement of the V_{oc}.

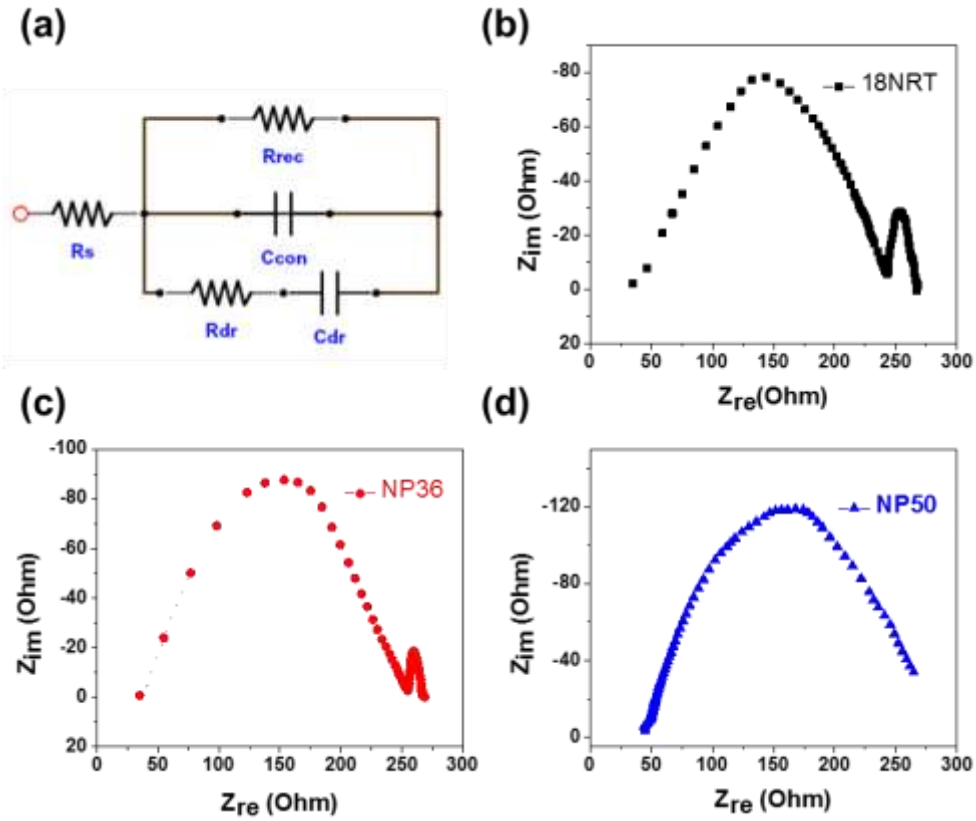

Figure 4.11. (a) Equivalent circuit for electrochemical impedance spectroscopy (EIS) measurements. Typical EIS spectra measured on the perovskite solar cells with different mp-TiO_2 nanoparticle size (b) 18NRT, (c) NP36, (d) NP50.

4.4 Conclusions

In summary, we have systematically studied the different parameters to explore the influence of TiO_2-perovskite interface for mesoscopic perovskite solar cells. We showed that the $TiCl_4$ post treatment of the mp-TiO_2 film prior to device fabrication passivate the titania surfaces, increases the density of states and reduces the disorder level which significantly enhances the open circuit voltage (~ 50mV) and the device performance. Furthermore, different sized TiO_2 nanoparticles were applied as electron acceptors in the mesoscopic PSC. The particle size effect of TiO_2 nanoparticles on the photovoltaic performance of PSC was investigated which not only influences the contact between the perovskite crystal-TiO_2, but also significantly affects the charge transfer kinetics at the TiO_2-perovskite interface and the overall disorder of the perovskite layer for charge transport. We observe that the particle size of 36 nm is optimum for obtaining the best performance solar cells with consistent and reproducible PSC of 16.3%. Based on transport, spectroscopic and photovoltaic measurements, we conclude that the mp-TiO_2 interlayer should have the least energetic disorder, optimum particle and pore size in order to enhance the homogeneous growth of perovskite over-layer and optimum charge transport properties to realise high efficiency in mesoscopic perovskite solar cells.

Chapter 5

Monovalent Cation (Na, Cu and Ag) Doping of $CH_3NH_3PbI_3$ Perovskite; Chemical distribution and enhancing optoelectronic and structural properties for Efficient Solar Cells

Here, we explore the possibility of doping in perovskite with monovalent cation additives having similar ionic radii to lead including sodium, copper and silver, and their impact on the structural and optoelectronic properties of $CH_3NH_3PbI_3$ perovskite. The enhanced properties of additive-based perovskite reflected in the performance of the subsequent solar cells originating from the formation of uniform and continuous perovskite film, better conversion and loading of perovskite as well as the enhancement in the bulk charge transport along with a minimization of disorder via additive pointing towards possible surface passivation. In the second part of this chapter, we investigate the chemical distribution and electronic structure of solution processed $CH_3NH_3PbI_3$ perovskite structures upon doping with these cations both experimentally and using Density functional theory (DFT) calculations. A detailed explanation of the results from first section of this chapter can also be found in the published article - ref. [194].

Contributions. This work was the result of collaborative research with the following contributions: I conceived and planned the experiments with additional input from prof. Richard Friend, prof. Michael Graetzel, Dr Ibrahim Dar and Dr Aditya Sadhanala. I fabricated all samples and devices, performed, and analysed the SEM, AFM, XRD, UV-Vis, PDS, PL, TRPL, JV and EQE measurements. Dr Satyaprasad P. Senanayak performed and analysed the EIS and SCLC charge transport measurements (Figure 5.7, Table 5.2). Dr Yuanyuan Hu performed the KPFM measurement and analysed the data (Figure 5.6). Mejd Alsari and Dr Samuele Lilliu performed the GIWAXS experiments and analysed the data (Figure 5.11, Figure 5.12, Figure 5.13). Dr Stefania Cacovichp and Dr Giorgio Divitini performed and analysed the STEM–EDX and SEM-EDX measurements. Dr Bertrand Philippe performed and analysed HAXPES measurements. Dr Meysam Pazoki and Rghayeh Imani performed and analysed the DFT calculations.

5.1 Introduction

The four common methods for deposition of metal halide perovskites includes one step spin deposition[195], vacuum vapor deposition[50], two-step deposition technique[49,196], and patterning thin film[197] to prepare the hybrid organic-inorganic perovskite film. So far, solution processed PSC show the highest efficiency and stability[52,140]. However, achieving good quality solution processed $CH_3NH_3PbI_3$ films on top of mesoporous TiO_2 (mp-TiO_2) with high uniformity and smoothness is important as in non-continuous perovskite, pinholes can introduce shunting pathways limiting the device performance. Recent studies show that by upon addition of excess organic component (methyl ammonium iodide) much larger crystalline domains can be created[7], and smoother films can be formed than those processed from a stoichiometric mixture of CH_3NH_3I and PbI_2[198].

Compositional engineering of perovskite is key for customising the electronic properties of perovskite materials[52]. Recent calculations have shown that the electronic band structure is mainly affected by the exterior orbitals of the divalent cation and halide, and hence the monovalent cation does not affect the bonding directly[167,199,200] although it can create indirect steric effects[201] and interact with defects[202]. As a result, a complete or partial substitution of the divalent metal can be used for engineering the light absorption coefficient, the band gap, and the charge carrier diffusion length[106,203]. It has been shown that tuning the optoelectronic properties of perovskites is possible by inclusion or partially substituting Pb with another divalent cation (e.g. Sn, Sr, Cd and Ca)[204,205], a monovalent cation (e.g. Na, Cu, Ag)[194,206], or a trivalent cation (e.g. Bi, In, Au)[207]. This has led to further improvements in solar cell efficiency by adding K[62], Na[208–210,138], Cu[211] or Ag[212,213] into different perovskite systems.

In this work, we explore the effect of adding small amount of monovalent cation halide based salts including NaI, CuBr, CuI and AgI into the perovskite precursor solution on morphology, charge transport, excitonic and optical properties of $CH_3NH_3PbI_3$ perovskite. To the best of our knowledge, the incorporation of $CH_3NH_3PbI_3$ with aforementioned salts has not been reported so far. Morphological characterization based on field emission scanning electron microscopy (FE-SEM) determined that shape and coverage of the $CH_3NH_3PbI_3$ structures prepared in the presence of additives is considerably different from an additive-free reference. In addition, samples were characterized using X-ray diffraction (XRD) to study crystalline phases present in the samples and the extent of lead halide conversion into perovskite in presence of additives.

Comprehensive studies on optical properties of additive based perovskite were carried out using photothermal deflection spectroscopy (PDS), UV-visible absorption and photoluminescence (PL). In addition, kelvin probe force microscopy (KPFM) and space charge limited current (SCLC) technique were used to characterise influence of aforementioned additives on electrical properties of $CH_3NH_3PbI_3$ perovskite. Finally, fabrication of solar cells based on the incorporated monovalent cation in perovskite structure reveals an improvement in power conversion efficiency (PCE) reaching 15.6%, which can be ascribed to the improvement in the conversion reaction, optical, excitonic and electrical properties of $CH_3NH_3PbI_3$.

5.2 Impact of monovalent cation halide additives on the structural and optoelectronic properties of $CH_3NH_3PbI_3$

In this study, $CH_3NH_3PbI_3$ perovskite samples were synthesized using sequential two-steps deposition process[49] in which 0.02 mol.L^{-1} of different additives including NaI, CuBr, CuI and AgI were added into the 1.2 mol.L^{-1} PbI_2 solution in N, N-dimethylformamide (DMF). In this procedure, the $CH_3NH_3PbI_3$ is formed onto ~250 nm thick TiO_2 photoanode films by spin coating DMF solution of PbI_2 followed by dip coating in a solution of isopropyl alcohol containing methylamonium iodide (MAI) under optimized conditions.

5.2.1 Morphological characterization

To understand the impact of these additives on the surface morphology of the PbI_2 and $CH_3NH_3PbI_3$ deposited on mesoporous TiO_2 photoanode, field emission scanning electron microscopy (FESEM) was employed. The top view SEM image confirms that the mesoporous TiO_2 is covered by an overlayer of PbI_2 (Figure 5.1, left-side). It is noteworthy that a significant change in the morphology of PbI_2 overlayer is observed while adding NaI to its solution (Figure 5.1d) and a rough and highly porous overlayer of PbI_2 containing branched large crystals was formed. This morphological difference was also evident from the macroscopic image as the respective PbI_2 film including NaI is relatively more scattering compared to pristine lead iodide film (Figure 5.1f).

In addition, the presence of CuBr does not make any significant difference in the morphology of PbI_2 (Figure 5.1b) whereas, in case of CuI and AgI based samples, we, obtain a uniform and pinhole free overlayer (Figure 5.1c, e). The right side of Figure 5.1 displays top-view SEM

images of $CH_3NH_3PbI_3$ films obtained after the conversion of pristine and additive based PbI_2 films. Comparative SEM analysis brought out variations in perovskite morphology. Pristine samples revealed the formation of large tetragonal-shaped perovskite crystals on top of the mp-TiO_2 film while relatively better surface coverage of mesoporous-TiO_2 with perovskite crystal is observed for CuBr based sample (Figure 5.1b). Moreover, considerable improvement in the surface coverage of titania scaffold with uniform and continuous perovskite structure is observed in the presence of CuI and AgI additives (Figure 5.1c, e). Particularly, in the case of $CH_3NH_3PbI_3$ incorporated with AgI, the perovskite crystals are better-connected. In Figure 5.1d, large crystals of NaI based perovskite sample with asymmetric shape are observed which infers that the nature of PbI_2 film can define the morphological properties of resulting perovskite films.

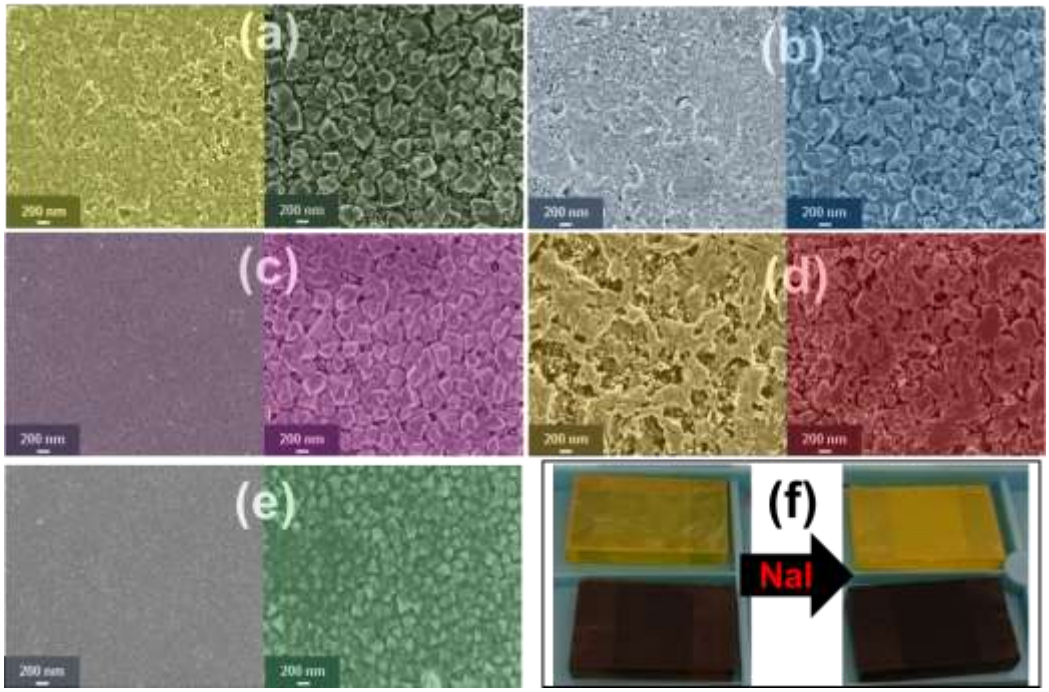

Figure 5.1. Top-view SEM images of PbI_2 (left side) and $CH_3NH_3PbI_3$ (right side) structures: (a) pristine, (b) CuBr-, (c) CuI-, (d) NaI- and (e) AgI-based perovskite samples deposited on a mesoporous TiO_2-coated FTO. (f) Macroscopic pictures of PbI_2 (top) and $CH_3NH_3PbI_3$ (bottom) films for pristine (left) and NaI-based samples (right).

We further characterized the perovskite films obtained from pristine and additives based lead halide precursors by atomic force microscopy (AFM) (Figure 5.2). The root mean-squared roughness of the pristine, CuBr, CuI, NaI, and AgI based perovskite films was found to be 51,

28, 21, 63 and 18nm, respectively. Expectedly, perovskite film including NaI additive exhibits a branched morphology with the highest roughness whereas the roughness of CuI and AgI based films are greatly reduced compared with the pristine sample, as is evident from both, AFM line segments (Figure 5.2f) and height distribution analysis (Figure 5.2g). It is worth emphasizing that the perovskite films including CuI and AgI additives are nearly pinhole free as compared to pristine and other samples (see circles in Figure 5.2a, b and d). It is encouraging that by adding small amount of additives inside the lead halide precursor solution, the smoothness of the perovskite films prepared by two-step deposition method enhanced strongly.

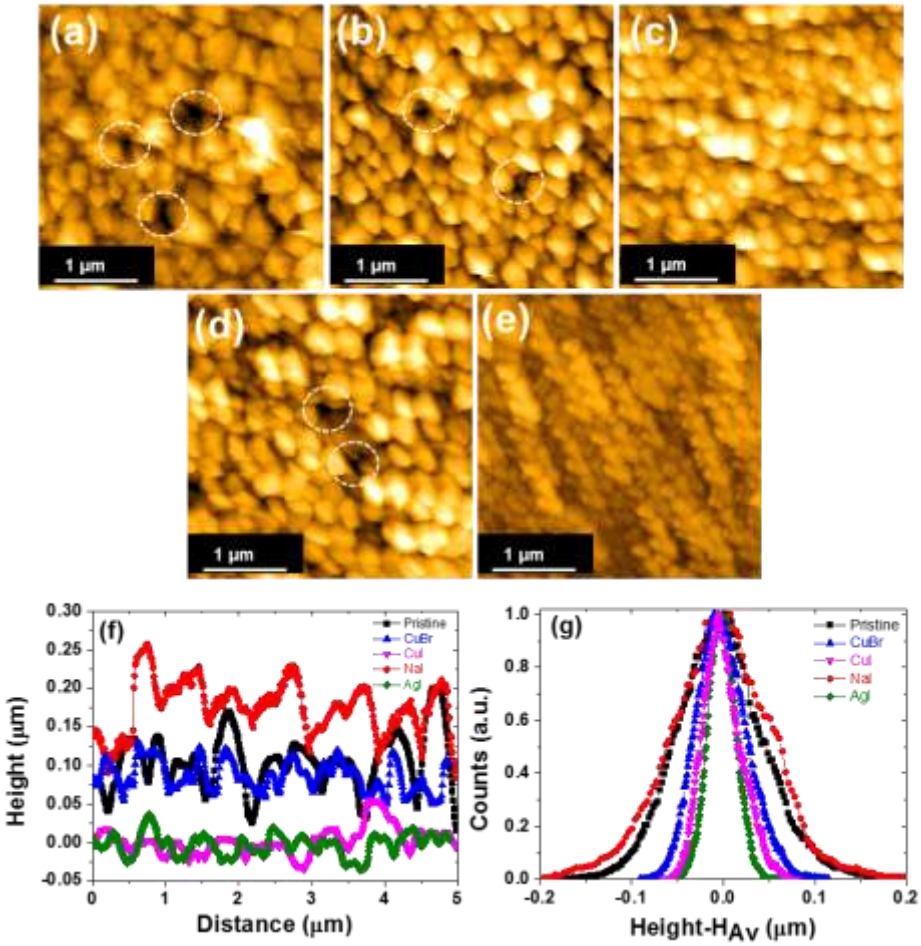

Figure 5.2. AFM images of perovskite structures: (a) pristine, (b) CuBr-, (c) CuI-, (d) NaI- and (e) AgI-based $CH_3NH_3PbI_3$ deposited on a mesoporous TiO_2-coated FTO. Examples of pinholes in pristine, CuBr and NaI derived films are circled, which are notably absent in the CuI and AgI based films. Line segments from each scan (f) and the height distribution (g) around the average height, H_{Av}, show the exceptional smoothness of the AgI and CuI-derived films.

5.2.2 Structral characterization

To investigate the effect of monovalent cation halide additives on the crystal structure of PbI_2 and $CH_3NH_3PbI_3$ perovskite, X-ray diffraction spectroscopy was carried out. In Figure 5.3, we show the X-ray diffraction patterns of pristine- and additive based-PbI_2 and -$CH_3NH_3PbI_3$ films, respectively. These diffraction patterns are indexed based on the standard JCPD file number 01-072-1147 and 21-1272 for FTO and TiO_2, respectively, as well as using literature data for PbI_2 and $CH_3NH_3PbI_3$ perovskite[214].

According to the literature data, it is evident that the PbI_2 deposited by spin-coating from DMF solution crystallizes in the form of the hexagonal 2H polytype[215]. The presence of the most intense diffraction peak (2θ=12.60) indexable to the (001) lattice planes (Figure 5.3a, black curve), is indicative of preferential growth of PbI_2 crystallites along the c-axis.

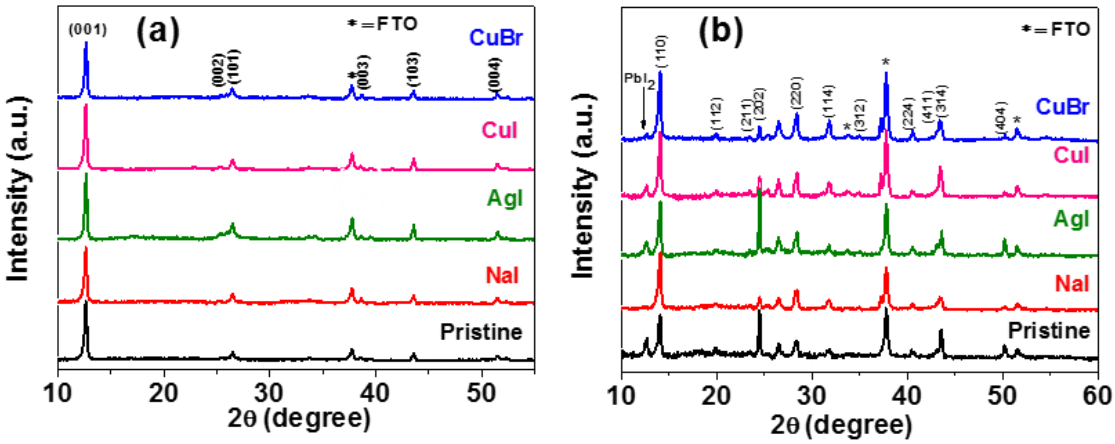

Figure 5.3. X-ray diffraction spectra of pristine and additives based (a) PbI_2 and (b) $CH_3NH_3PbI_3$ perovskite. All the films were grown on mesoporous TiO_2 layer which is deposited on the FTO coated glass.

It should be noted that CuBr, CuI and AgI-based perovskite films show similar intensity in various diffraction peaks to the pristine one, however the NaI-based sample depicts sharper diffraction peaks for the (001) lattice plane. Moreover, sharpness of the diffraction peak (001) for NaI based sample compare to broad one for the pristine can

be attributed to the larger crystallite size of PbI_2 structures which demonstrates that NaI additive influences the growth of PbI_2 structures (Figure 5.1d).

The conversion of PbI_2 into CH_3NH_3I was ascertained by X-ray diffraction (XRD). All the diffraction peaks present in the XRD patterns could be indexed to the tetragonal phase of the $CH_3NH_3PbI_3$ perovskite[216]. In addition, presence of diffraction peak (2θ=12.6) attributable to PbI_2 indicates the presence of unconverted PbI_2 within the $CH_3NH_3PbI_3$ film. XRD patterns obtained from the additives based samples perfectly match with that of pristine $CH_3NH_3PbI_3$ sample which confirms that the presence of additives do not alter the crystal structure of the final $CH_3NH_3PbI_3$ material (Figure 5.3b). However, based on an analysis using the Scherrer equation,[217] the average crystallite sizes of pristine, CuBr, CuI, NaI and AgI based perovskite vary and were estimated to be 62±10, 73±12, 56±9, 95±14 and 45±11 nm, respectively. It is important to note that these values are based on the assumption of spherical perovskite crystals.

In addition, it was also observed that the diffraction peak of PbI_2 in NaI-based sample vanished and its intensity dropped significantly in CuBr-based one. This observation can be attributed to the following two reasons; first, presence of additive is enhancing the extent of conversion reaction of PbI_2 into $CH_3NH_3PbI_3$ which eventually leaves less amount of unreacted PbI_2. Secondly, morphological modifications of PbI_2 overlayer, i.e., from a relatively compact layer to a more porous one, facilitates the conversion further. As the NaI-based sample reveals a full conversion of PbI_2 into the $CH_3NH_3PbI_3$, which has been already established from the XRD pattern, the second hypothesis seems more feasible. It is to be noted that significant variations in the morphology of PbI_2 overlayer were observed in SEM analysis (Figure 5.1). On the other hand, a relatively high intense PbI_2 diffraction peak is observed in the XRD patterns of CuI and AgI based samples. This further confirms that the morphology of PbI_2 overlayer strongly influences the extent of PbI_2 conversion into $CH_3NH_3PbI_3$.

5.2.3 Steady state optical characterizations

5.2.3.1 UV-visible Absorption

Steady state optical absorption and PL spectra of pristine and additives based methylammonium lead iodide perovskite films, are presented in Figure 5.4a. The optical absorption spectrum of pristine $CH_3NH_3PbI_3$ perovskite film (solid black line) shows

broad absorption band covering the entire visible spectral range with a band edge at around 780 nm. Large extinction coefficient and typical spectral behaviour of methyl ammonium lead iodide perovskite film is consistent with the previous reports[98]. The comparative analysis of absorption spectra of pristine and additives based $CH_3NH_3PbI_3$ films do not show any noticeable position alterations i.e. the absorption onsets at 780 nm are very similar nevertheless, we observed a slight deviation in the absorption slopes which are below the band edge. Such deviations (without base line correction) could appear from strong light scattering, which originates from rough perovskite surface, rather than from the effect of additives. However, in order to verify whether presence of additive have any influence on the band gap position, we evaluated approximate band gap positions from the measured spectra. By performing scattering subtraction which is proportional to λ^{-4} and by applying extrapolation to the linear part of absorption edge, we obtained that optical band gap of all synthesized films to be around 1.58eV, which is in agreement with literature[218]. Notably, due to a very high perovskite layer thickness, which is ≈300 nm, absorption spectrum below 600 nm becomes saturated and therefore precise interpretation of the results in this region becomes difficult.

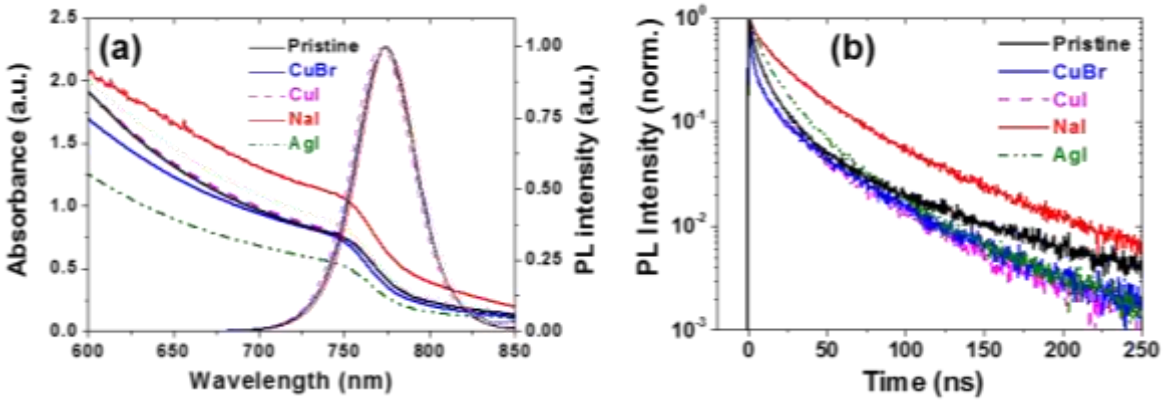

Figure 5.4. (a) Steady state absorption and PL spectra for pristine and additives based perovskite films. (b) Photoluminescence decay kinetics measured at 780 nm upon excitation at 406 nm with fluence of 11 $pJ.cm^{-2}$ for pristine and additives based perovskite films.

5.2.3.2 Photoluminescence study

Steady state PL spectra of perovskite films are presented in Figure 5.4a. Strong and narrow fluorescence bands with full-width half maximum of about 40 nm appear at around 775 nm upon sample excitation at 460 nm. It is observed that the PL spectra are similar for all $CH_3NH_3PbI_3$ films, i.e. pristine and additives based, confirming that the additives did not affect band edge of perovskite semiconductors. This could be due to the tendency of additives to be at the crystalline surfaces rather than having impact on the band gap of perovskite films. Most likely, the effect of additives on the perovskite crystallization is more pronounced and influences film morphology which, can affect the photovoltaic performances[196].

Table 5.1. The summarized emission lifetime "τ" and corresponding intensities "A" for various perovskite samples obtained using three exponential fit.

	Pristine	**CuI**	**CuBr**	**NaI**	**AgI**
A_1, %	32.6	18.2	17.8	57.4	43.8
τ_1, ns	17.6	20.8	21.25	22.3	20.7
A_2, %	5.6	5.2	5.6	18	6.7
τ_2, ns	87.7	64.5	69.2	72.7	63.6

In Figure 5.4b, we performed PL decay measurements of perovskite films deposited on mesoporous TiO_2 in the absence of hole transport materials (HTM) using time-correlated single photon counting technique. The estimated PL lifetimes and their relative contributions are summarized in Table 5.1. It is evident that PL decay kinetics experience several important differences depending on the type of additive. In comparison to pristine sample a fast PL decay component becomes slightly slower whereas long lived decay becomes accelerated in additive based samples. Moreover, the contribution of τ_1 relaxation components became slightly higher (>50 %) upon addition of silver and sodium iodides, whereas its contribution decreases significantly for copper halide based samples. Although the addition of additives does not modify the bandgap

of $CH_3NH_3PbI_3$ perovskite, the presence of low amount of additives can influence free or bound carrier dynamics. These observations can have implications in the recombination processes and disorder dynamics. However, a detailed analysis of these is beyond the scope of this chapter.

5.2.4 Photothermal deflection spectroscopy (PDS)

We used photothermal deflection spectroscopy (PDS), which is an ultrasensitive absorption measurement technique, to explore the optical absorption of the $CH_3NH_3PbI_3$ films near the band edge (Figure 5.5a). PDS has a dynamic sensitivity range of 4-5 orders of magnitude and is less affected by optical light scattering. From Figure 5.5a, it is evident that the pristine perovskite has the highest sub-bandgap absorption. In addition, both copper-based perovskite (e.g. CuI and CuBr) samples shows relatively higher absorption compared to the AgI and NaI based perovskite films in the sub-bandgap region. It is notable that Cu based additives create a tail in the absorption spectra of perovskite which confirm the presence of these monovalent cations inside the film. In contrast to AgI and NaI, copper-based additives absorb intrinsically (Figure 5.5b), which generate aforementioned tail. Comparing the PDS absorption spectra for CuBr based PbI_2 and perovskite shows that these additives are not fully incorporated in the perovskite film.

As reported by Sadhanala et al. for $CH_3NH_3PbI_3$, we observe sharp band edges for all the samples with an exponential decay of the density of states after the band edge, known as the Urbach tail[98,219]. The extent of the absorption tail below the band gap is correlated with the degree of electronic disorder within the material, which could originate from structural disorder, thermal fluctuation of the ions comprising the material and defects in the crystalline structure. Indeed, there have been several recent reports which suggest that the presence of defects within $CH_3NH_3PbI_3$ perovskite crystals would induce localized states in the range of a few hundred meV from the extended states of the bands, which could result in the broadening of the Urbach tail[220]. Assuming the same level of thermal disorder, the slope of the exponential part of the Urbach tail gives an estimation of the defect density, in terms of Urbach energy 'Eu'[98,219]. The estimated Urbach energies for the pristine and additive-based perovskite films are shown in the inset of Figure 5.5a, along with the respective fitting error, which are 15.6, 11.8, 12.8, 13.5 and 15.2 meV for pristine, NaI, CuBr, CuI and AgI based perovskite, respectively. These

values suggest that within the measurement error, additive-based perovskite, particularly NaI, CuBr and CuI, have a lower level of electronic disorder compared to the pristine perovskites.

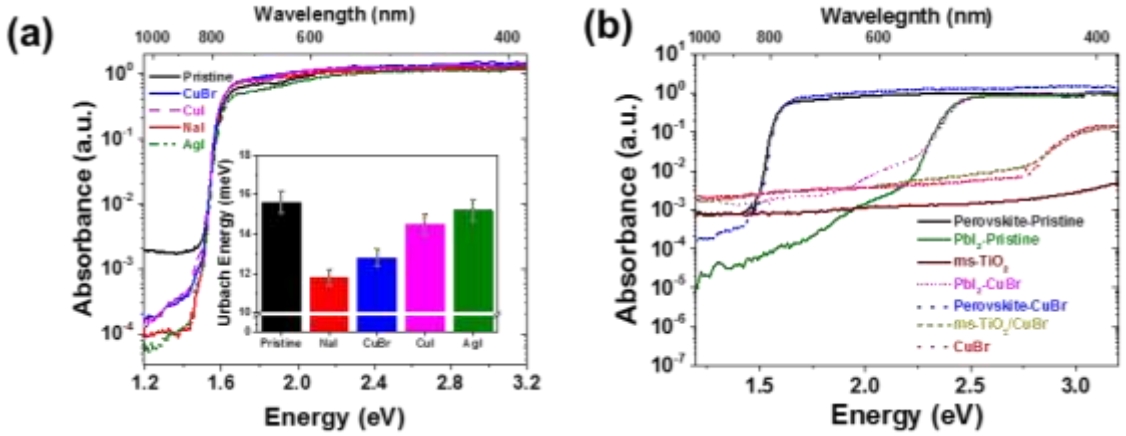

Figure 5.5. Optical properties of perovskite films. (a) The absorption spectra of perovskite films derived from pristine and additive-based lead sources measured using the PDS technique. The inset shows the corresponding Urbach energies for all samples. The error bar is defined by the SD in fitting the Urbach tail. (b) Comparison of the PDS absorption spectra of pristine and CuBr-based lead iodide and perovskite films, as well as CuBr deposited on mp-TiO_2 and CuBr-only films.

5.2.5 Kelvin probe force microscopy (KPFM)

We then used Kelvin probe force microscopy (KPFM), an electrical operation mode of scanning force microscopy (SFM), to investigate the effect of adding monovalent cation halide on $CH_3NH_3PbI_3$ perovskite Fermi level. KPFM is a powerful technique based on measuring and compensating the electrostatic forces between a sample and an AFM tip to determine the local contact potential difference (CPD)[221,222], which is a measure of the Fermi level energy if the electron affinity is known. Previously, it has been used to study the electrical potential distribution across the internal interfaces of inorganic solar cells[223,224]. KPFM was recently used to characterize the perovskite top layer[225,226], where the presence of a small potential barrier at the grain boundaries was found. Bergmann et al. have recently measured cross-sections of a complete perovskite based solar cell

under illumination with KPFM and showed that the potential is similar to a p-i-n type junction[227]. Figure 5.6 shows CPD of line profiles recorded at pristine and additive-based perovskite films which is sensitive to the surface work functions Φ of the materials. The line scan is carried out at the interface of perovskite and gold layer as shown in topography AFM image (Figure 5.6). Assuming that the tip work function remains constant during a line scan, the CPD reflects the built-in potential of the device. It is notable that adsorbed water on the surface may have altered the absolute value of the CPD, but not the relative difference between the studied materials.

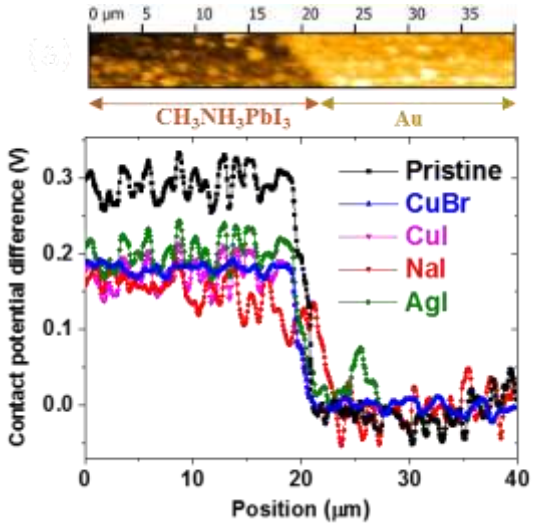

Figure 5.6. Contact potential difference line profiles recorded from pristine and additive based perovskite films using KPFM. The AFM topography image is shown on the top.

We found a decreasing CPD from the pristine perovskite (0.3 V) towards the Au electrode (≈0V, black line profile in Figure 5.6). The difference between these two values corresponds to the differences of the work function of perovskite ($\Phi_{perovskite}$ / e≈ 4.8 V) and Au (Φ_{Au}/e≈5.1 V) which are comparable to the previous reports[227,228]. Surprisingly, the work function of additive based perovskite shifted significantly (about 0.1V) toward the Au work function. This shift in the work function can be attributed to the following two reasons; first, substitutional doping of perovskite in which Pb^{2+} is replaced by Cu^{+}, Na^{+} and Ag^{+} cations resulting in generation of valance band holes. Thus, the Fermi level of the bulk perovskite thin film comes closer to the valence band. Secondly, these

additives can potentially passivate the surface of perovskite film (where there is a missing iodide) and as a result reduce the contact potential difference, which is measured by KPFM. It is notable that the chance of substitutional doping at the room temperature is very low since the excess energy associate with putting these monovalent cation (e.g. Ag^{+}) in place of Pb^{2+} is very high[229]. Thus, the second scenario is more probable in which the crystalline surfaces of $CH_3NH_3PbI_3$ are passivated in the presence of these monovalent cations.

5.2.6 Charge transport measurement

To further understand the role of the monovalent cations on the properties of the perovskite material, extensive charge transport measurements were performed. Both electron and hole only devices were fabricated with all the different perovskite materials to estimate the bulk carrier mobility (μ_{SCL}). A clear transition from the linear to space charge limited trap free behavior is observed in all the materials (Figure 5.7a). The onset voltage of the trap-free space charge limited (TFSCL) transport regime is directly related to the density of trap states at the transport level[230]. In general, all the perovskite devices with typical thickness in the range of 0.5 - 1 μm demonstrated TFSCL in a voltage range of < 5V, indicating low trap density. Child's law given by: $J = \frac{9}{8}\,\varepsilon_0\epsilon_r\mu_{SCL}\frac{V^2}{d^3}$ where, J is the current density, ε_o is the vacuum permittivity, ε_r is the dielectric constant of the active material which is measured to be in the range of 15 - 25 (at 1 kHz) for different materials and d is the thickness of the active layer was utilized to estimate the bulk mobility of electrons and holes in the TFSCL regime[191].

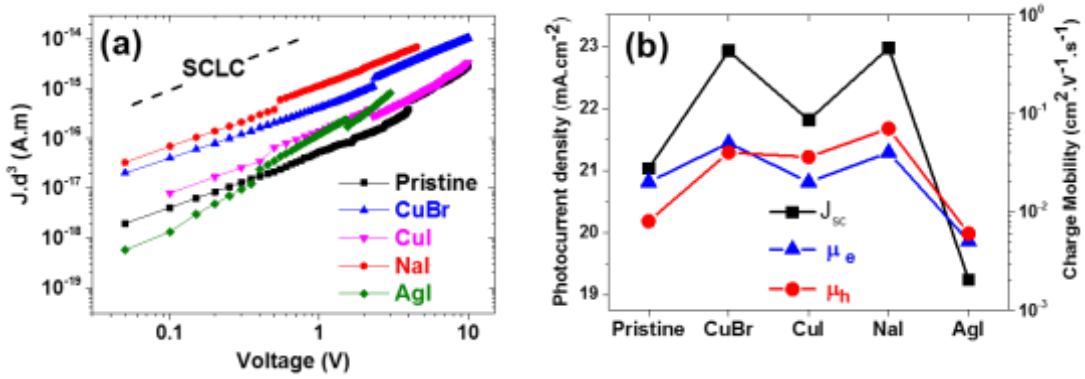

Figure 5.7. (a) J-V characteristics of hole only devices (ITO/PEDOT:PSS/Perovskite/Au), utilized for estimating the SCLC hole mobility. Note that the current density (J) is scaled with

thickness of perovskite layers. (b) The trends in the J_{sc}, μ_h and μ_e for pristine and additive-based perovskite.

Typical electron mobility (μ^e_{SCL}) of 0.02 $cm^2.V^{-1}.s^{-1}$ and hole mobility (μ^h_{SCL}) of 0.008 $cm^2.V^{-1}.s^{-1}$ was obtained for pristine perovskite films. This magnitude of bulk mobility is lower than that reported for a single crystal of perovskite[230]. It should be noted that hysteresis was observed in the J-V measurements and hence for a conservative estimate of the μ_{SCL}, forward sweep is considered. Moreover, factors like injection-limited behavior have to be considered carefully to obtain the actual magnitude of μ_{SCL} in thin films. For TFSCL behavior, $J(E) \propto d^{-3}$, hence devices were also fabricated with different thickness to confirm the TFSCL behavior compared to injection limited behavior.

Nevertheless, under similar conditions upon addition of the monovalent cation additive, the μ_{SCL} increased significantly (up to an order of magnitude) for holes compared to that for electrons. Hole mobility as high as 0.07 $cm^2.V^{-1}.s^{-1}$ was obtained for NaI based perovskite thin films (Figure 5.7b). However, electron mobility increased to around 0.04 cm^2/Vs resulting in a more balanced charge transport. It should be noted that these values of bulk mobility are one of the highest in the community for perovskite thin films. Correspondingly, the conductivity magnitude estimated from the linear regime were obtained to be as high as 5×10^{-8} $S.cm^{-1}$ for NaI based perovskite compared to 10^{-9} $S.cm^{-1}$ for pristine films. It is evident from the charge transport measurements that the addition of monovalent cations strongly affect the balanced charge transport properties and the overall conductivity which can enhance the J_{sc} of the solar cells (Figure 5.7b). Thus it can be concluded that one of the strategies to increase the J_{sc} in perovskite solar cells could be to increase the balance between the bulk electron and hole transport.

To further understand the reason for the increased μ^h_{SCL} in additive based perovskite films, temperature dependent bulk transport measurements were performed. Arrhenius fits were utilized to estimate the activation energy (E_A) for the charge transport (Table 5.2). Adding of monovalent cations in the perovskite films results in a decrease of E_A for hole transport from 198 meV to 137 meV and electron transport from 135 meV to 77 meV. In the framework of a mobility edge model, it is expected that the increase in carrier concentration due to doping can result in filling up of the traps at the transport

level and decrease the barrier for transport, which can diminish the activation energy. This is consistent with the observed change in the Fermi level of perovskite upon the addition of monovalent cation halide additives. Hence, it is plausible that the presence of stable +1 oxidation states of the cations results in passivation of traps in the system. Thus, it can be concluded from the charge transport measurements that the addition of monovalent cation halide additive results in enhancing the overall mobility of the charge carriers which is expected to enhance the J_{sc} of the perovskite solar cell devices.

Table 5.2. Summary of the photovoltaic parameters derived from J-V measurements and charge mobilities along with activation energy for the pristine and additive based perovskite solar cells (showing the best performance) fabricated using two-step deposition method.

Type of Sample	J_{SC} (mA cm^{-2})	V_{OC} (V)	FF	PCE (%)	μ_e (cm^2/Vs)	μ_h (cm^2/Vs)	E_A^e (meV)	E_A^h (meV)
Pristine	21.٠3	0.9٥	0.7٠	14.01	0.02	0.008	135	198
CuBr	22.92	0.95	0.72	15.61	0.05	0.040	88	132
CuI	21.81	0.99	0.71	15.25	0.02	0.036	94	157
NaI	22.97	0.90	0.73	15.14	0.04	0.070	77	137
AgI	19.24	1.02	0.72	14.18	0.005	0.006	105	177

5.2.7 Photovoltaic performance

Current density-voltage (J–V) characteristics of the pristine and additive-based perovskite solar cells were measured under simulated air mass 1.5 global (AM1.5G) solar irradiation. The devices were fabricated based on the optimized procedure, which is explained in the experimental section. A typical device has the structure of FTO/compact TiO_2/mesoporous TiO_2/$CH_3NH_3PbI_3$/Spiro-OMeTAD/Au, as shown in the previous chapter (Figure 4.1).

The influence of additive concentration on the photovoltaic performance of PSC was demonstrated by examining three different concentrations of CuBr (0. 01, 0.02 and 0.04 mol.L^{-1}) additive based perovskite devices (Figure 5.8a). As summarized in Figure 5.8b, the lowest concentration slightly increased photocurrent density (J_{sc}) by 0.5 mA.cm^{-2}. By increasing the concentration of CuBr to 0.02 mol.L^{-1} photovoltaic performance of the device revealed an average PCE of 15.4% while further increase in the amount of additive decreases J_{sc} and open circuit voltage (V_{oc}) which eventually brought down the overall power conversion efficiency (PCE) of the device. Therefore, a concentration of 0.02 mol.L^{-1} can be stated as the optimum level of the additive to realize the high performance of PSC.

(a)

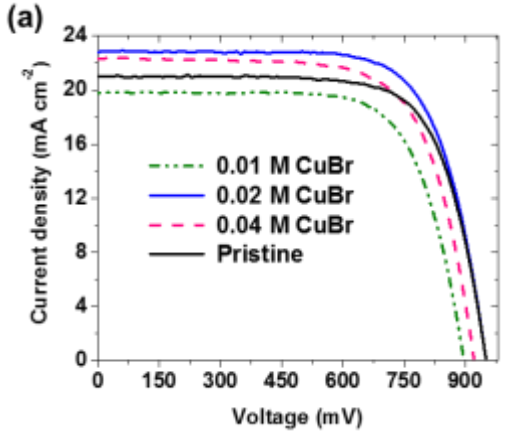

(b)

Type of Sample	Dopant Concentration (moll^{-1})	J_{sc} (mA cm^{-2})	V_{oc} (mV)	FF	PCE (%)
Pristine	-	20.7±0.4	945±13	0.69±0.02	13.7±0.3
CuBr	0.01	22.1±0.6	921±10	0.69±0.03	14.3±0.3
CuBr	0.02	22.5±0.1	948±7	0.70±0.02	15.2±0.4
CuBr	0.04	19.8±0.5	896±16	0.71±0.01	12.6±0.7

Figure 5.8. (a) Current-voltage characteristics of devices under illumination of 100 mW cm^{-2} obtained with varying concentration of CuBr additive. (b) Summary of the photovoltaic parameters derived from J-V measurements for the pristine and CuBr based perovskite solar cells (batch of 30 devices) with various concentration fabricated using two-step deposition method.

Figure 5.9a and Table 5.2 show the influence of different additives on the photovoltaic parameters of the PSC. For the additive-free reference cell, J_{sc} of 21.03 mA.cm^{-2}, V_{oc} of 0.95 V, fill factor (FF) of 0.70 and PCE of 14.01% are achieved. The J_{sc} of AgI based device dropped nearly by 2 mA.cm^{-2} compare to the pristine cell which could be attributed to the lower loading of $CH_3NH_3PbI_3$ in AgI based sample (as it shows the lowest absorption in Figure 5.4a). On the other hand, because of the ideal surface

coverage of AgI based perovskite, high V_{OC} of 1.02 V is achieved (Figure 5.1). In addition, since the fill factor of AgI based device improved due to the relatively balanced charge transport (Figure 5.7 and Table 5.2), the overall efficiency of the device slightly improved to 14.18%.

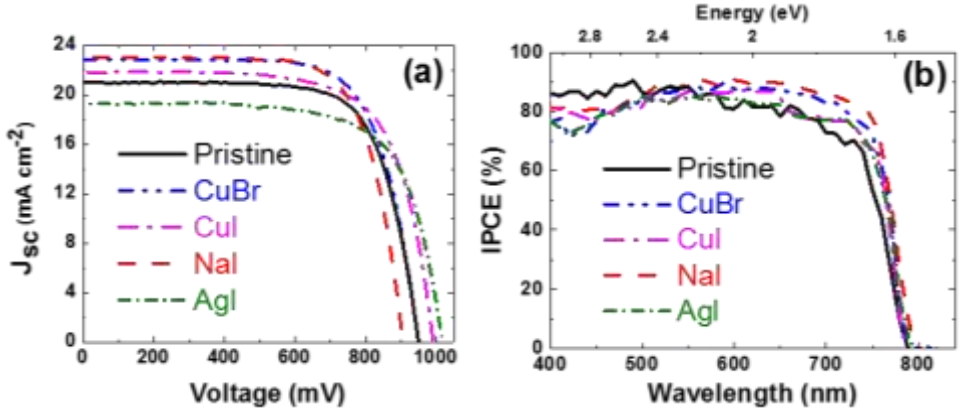

Figure 5.9. (a) Current-voltage characteristics of devices under illumination of 100 mW cm-^{2} obtained using different type of monovalent cation halide added to the lead source solution. (b) Incident photon-to-current efficiency (IPCE) spectra as a function of the wavelength of monochromatic light for the pristine, CuBr-, CuI-, NaI- and AgI-based perovskite solar cells.

Surprisingly, all other additives including NaI, CuBr and CuI enhanced the PCE of PSC notably to 15.14%, 15.61% and 15.25%, respectively. The open-circuit voltage of CuBr based device (0.95 V) was similar to that of pristine one while a considerable drop of around 50mV is noticed for NaI based cells (0.90 V). The lower voltage in NaI based derived samples can be explained due to the presence of increased shunting pathways because of detrimental contact between Spiro-OMeTAD and mesoporous TiO_2 layer which is quite expected from a rougher perovskite films, (SEM images in Figure 5.1d). In contrast, a uniform and pinhole free surface of CuI based $CH_3NH_3PbI_3$ sample lead to the improvement in V_{oc} (0.99 V vs 0.95 V for additive-free reference) (Figure 5.1c).

Moreover, a substantial enhancement in the J_{sc} of 21.81 mA.cm^{-2} for CuI, 22.92 mA.cm^{-2} for CuBr and 22.97 mA.cm^{-2} for NaI based devices compared to 21.03 mA.cm^{-2} for pristine solar cells was observed. The highest J_{sc} exhibited by NaI based device can be

attributed to the better conversion of PbI_2 into $CH_3NH_3PbI_3$ as revealed by XRD pattern (Figure 5.3) and therefore higher loading of perovskite inside the mesoporous-TiO_2 scaffold, which is consistent with the PDS data (Figure 5.5). However, diminished photocurrent density observed in other samples (i.e. AgI) could be attributed to the relatively low conversion of lead halide into $CH_3NH_3PbI_3$ under given conditions. The enhancement in current densities of PSC based on NaI-, CuBr- and CuI-based $CH_3NH_3PbI_3$ are supported by the improvement in the incident photon to current conversion efficiency (IPCE) spectra shown in Figure 5.9b. In addition, IPCE of all the devices as a function of wavelength shows that the generation of photocurrent starts at around 780 nm, which is in agreement with the band edge of pristine $CH_3NH_3PbI_3$. This confirms further that the presence of additives does not change the band gap of the perovskite material, which is consistent with PDS results. We also noticed that the fill factors (FFs) of devices based on the NaI and CuBr based perovskite improved noticeably, in comparison with the pristine reference cell. Arguably, improvement of FFs could be due to the enhancement in conductivity and presence of lower level of electronic disorder in the additive based $CH_3NH_3PbI_3$ films (Figure 5.5a, and Table 5.2).

5.2.8 Conclusions

In summary, we have systematically studied the role of the monovalent cation halide based additives on the morphological, optical and electrical properties of $CH_3NH_3PbI_3$ perovskite films. We found that a better conversion of lead iodide into $CH_3NH_3PbI_3$ structure is achieved for NaI and CuBr based films which was confirmed by XRD and, for CuI and AgI based perovskite a uniform film with a continuous coverage is formed. Detailed experiments based on PDS, KPFM and bulk transport measurements on the pristine and additive based perovskites indicate that the additives can possibility cause a passivation of states at the crystallite surfaces. This minimizes the extrinsic doping at the crystallite boundaries and improves the overall charge transport properties as well as the solar cell performance. These observations indicate that the additives seem to passivate the hole traps in the surface (or grain boundaries) of perovskite films that results in an enhancement of J_{sc} and hence, the overall efficiency of the solar cell. The confluence of aforementioned favourable properties led to the enhancement of PCE to 15.14%, 15.25% and 15.61% for NaI, CuI and CuBr, respectively, in comparison with 14.01% for the additive-free reference cell. The photovoltaic results, particularly for AgI

based cell, confirm that the ideal surface coverage of perovskite is not the only sufficient factor to achieve a high efficiency but also a full conversion of lead iodide into the perovskite is required. In summary, this work demonstrates the possibility of enhancing the structural and optoelectronic properties that play a very crucial role in improving the performance of perovskite based solar cells by simple addition of a rational amount of low cost monovalent cation based inorganic salts.

5.3 Dedoping of lead halide perovskites incorporating monovalent cations (Na, Cu and Ag)

In this section, we explore the chemical distribution, chemical bonding, electronic and structural effects of Na, Cu and Ag monovalent cation iodide dopants in hybrid organic-inorganic perovskite films. These monovalent cations have similar ionic radii (116 pm Na, 91 nm Cu and 129 pm Ag) to that of Pb (133 pm), and can potentially replace lead within the perovskite lattice[164] or occupy the interstitial sites as observed for potassium ion[231]. We investigate the effect of incorporating these dopants on the crystal growth of PbI_2 and $CH_3NH_3PbI_3$ perovskite with Grazing-Incidence Wide-Angle X-ray Scattering (GI-WAXS). We use soft X-ray Photoelectron Spectroscopy (XPS) and synchrotron Hard X-ray Photoelectron Spectroscopy (HAXPES) using synchrotron radiation to detect the cations and analyse the chemical composition and electronic structure of the perovskite from surface to bulk. We also performed Scanning Transmission Electron Microscopy-Energy Dispersive X-ray Spectroscopy (STEM-EDX) to probe the local chemistry of doped-perovskite thin films. We then perform a comprehensive Density Functional Theory (DFT) calculation to explore how the incorporation of these dopants in the perovskite lattice affects chemical bonding, atomic rearrangement in a unit cell, charge densities, and band structure. Our findings reveal a clear picture of the distribution of monovalent cation dopants and their effects on the structure and growth of perovskite films.

We processed $CH_3NH_3PbI_3$ perovskite films doped with Na, Cu and Ag monovalent cation dopants using solution-based sequential deposition technique[187]. We also used single step deposition technique to confirm that the incorporation of the monovalent cation dopants are independent of the processing methods (see Experimental Methods Chapter, page 36). Absorption spectra from Photo-thermal Deflection Spectroscopy (PDS) (Figure 5.10) indicate that the band gap remains unperturbed upon doping. In Cu-doped perovskites we observe an

absorption tail originating from the intrinsic absorption of copper[194], while in Ag- and Na-doped perovskites we measure the lowest sub-bandgap absorption and the lowest electronic disorder.

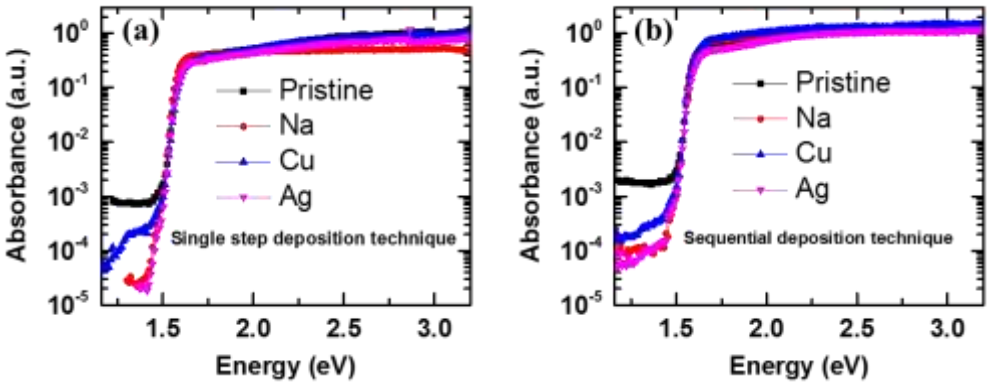

Figure 5.10. The PDS absorption spectra of pristine and doped-perovskite films fabricated using (a) single step, (b) sequential deposition techniques measured.

5.3.1 Crystal growth and structural characterization

Next, we investigate the influence of these dopants on the growth of PbI_2 with synchrotron Grazing Incidence Wide Angle X-ray Scattering[232] (GI-WAXS) measurements (Figure 5.11) performed at the XMaS beamline (ESRF, France). With the Ag dopant (Figure 5.11d), the hexagonal PbI_2 crystals are preferentially oriented with the *c* lattice vector perpendicular to the substrate (out-of-plane orientation), as is clear from azimuthal distribution of the (001) PbI_2 ring at $q \approx 0.9$ Å^{-1} in the GI-WAXS pattern. When Na and Cu are added (Figure 5.11b-c), the PbI_2 crystals display patterns similar to that of the pristine PbI_2 (Figure 5.11a), i.e. a broader azimuthal distribution of the (001) PbI_2 ring, indicating that a certain amount of crystals are randomly oriented with respect to the substrate. Plots of integrated radial line profiles (intensity vs azimuthal angle χ) are used to compare the relative orientation of the PbI_2 crystals of the four samples (Figure 5.11e). Interestingly, the incorporation of Na, Cu, and Ag dopants results in an expansion of the PbI_2 unit-cell along the *c*-axis, as evident from the shift of the (001) peak in the in-plane (Figure 5.11f) and out-of-plane (Figure 5.11g) azimuthally integrated line profiles.

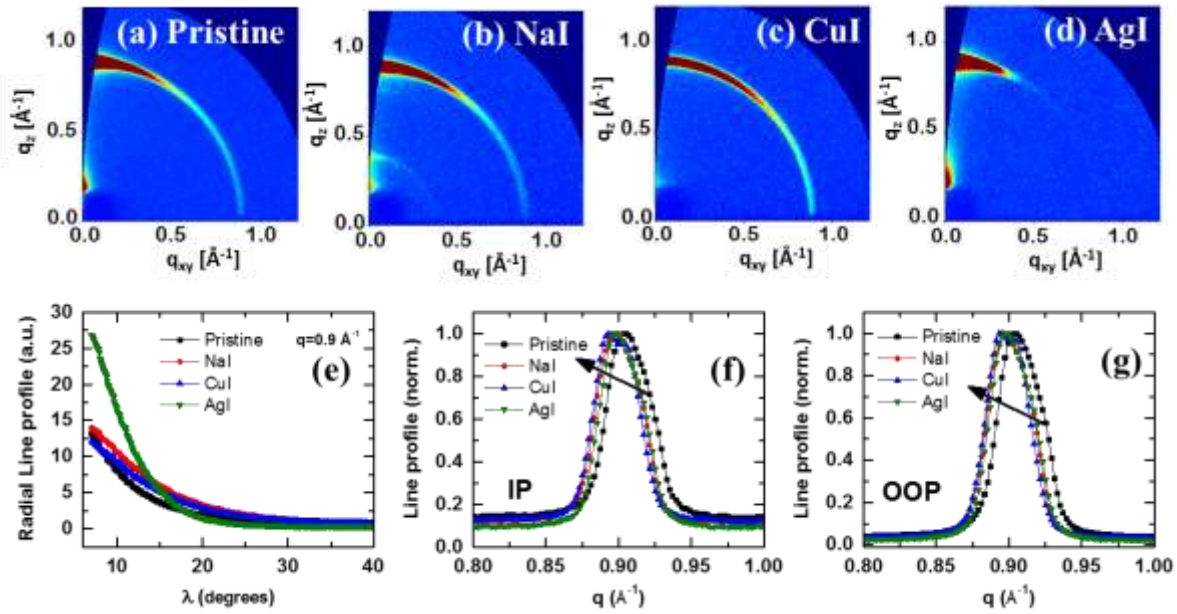

Figure 5.11. GI-WAXS (collected at the XMaS beamline) diffraction patterns of (a) pristine, (b) NaI, (c) CuI and (d) AgI based PbI_2. (e) Radial line profiles of the main lead iodide peak at q = 0.9 Å-1. Line profiles azimuthally integrated (f) In-Plane (IP) ($\chi = 78°$, $\Delta\chi = 10°$) and (g) Out-Of-Plane (OOP) ($\chi = 12°$, $\Delta\chi = 10°$) for pristine and additive based PbI_2. The OOP line profiles suffer from refraction effects[233]. However, the IP line profiles are unaffected by this issue.

In Figure 5.12a-d, we compare GI-WAXS diffraction patterns of pristine and doped-$CH_3NH_3PbI_3$ (from conversion of PbI_2 into perovskite using sequential deposition technique) measured with a laboratory beamline (XEUSS, XENOCS). We note a shift in the main perovskite peak (110) at $q \approx 1$ Å^{-1} in the in-plane azimuthally integrated line profiles for the doped-perovskites (Figure 5.13), indicating that the aforementioned expansion of the PbI_2 unit-cell along the *c*-axis seems to take place in the doped perovskite unit-cell as well, indicating the possibility of substitutional or interstitial doping with these monovalent cations.

In the Ag-doped perovskite system, we observe a strong preferential orientation at $\chi \approx 54°$ and a weaker preferential orientation at $\chi < 10°$ in the main perovskite ring (Figure 5.12d and Figure 5.13d). The other films (Na-doped, Cu-doped, and pristine perovskites) display a more uniform azimuthal distribution in the main perovskite ring, with some preferential orientation at intermediate angles ($40° < \chi < 60°$) and at $\chi < 10°$ (Figure 5.12a-c and Figure 5.13). This

suggests that the incorporation of Ag as a dopant in the precursor solution has a strong influence on the growth and final orientation of both PbI_2 and perovskite crystallites.

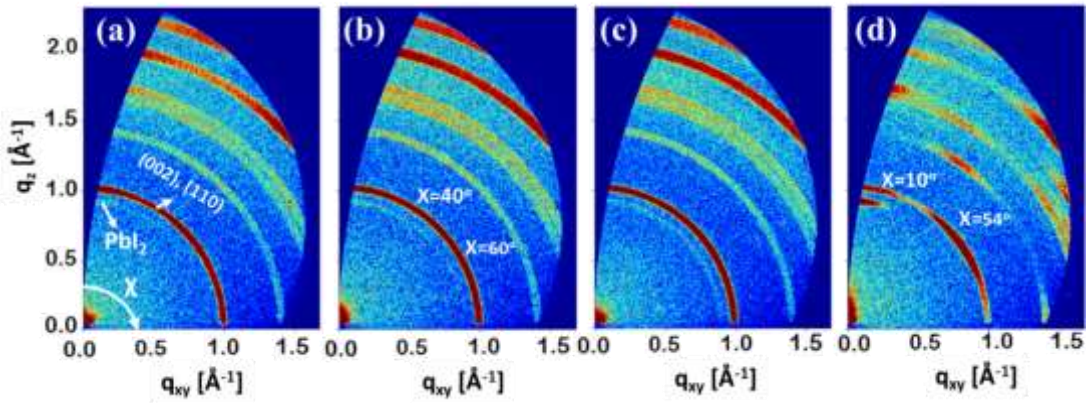

Figure 5.12. GI-WAXS diffraction patterns of (a) pristine, (b) Na-, (c) Cu- and (d) Ag-doped perovskite films. a, PbI_2 indicates the (001) reflection of lead iodide and (002), (110) indicates the main perovskite diffraction ring, χ indicates the azimuthal angle. The initial concentration of the dopants is 10 mol% with respect to Pb.

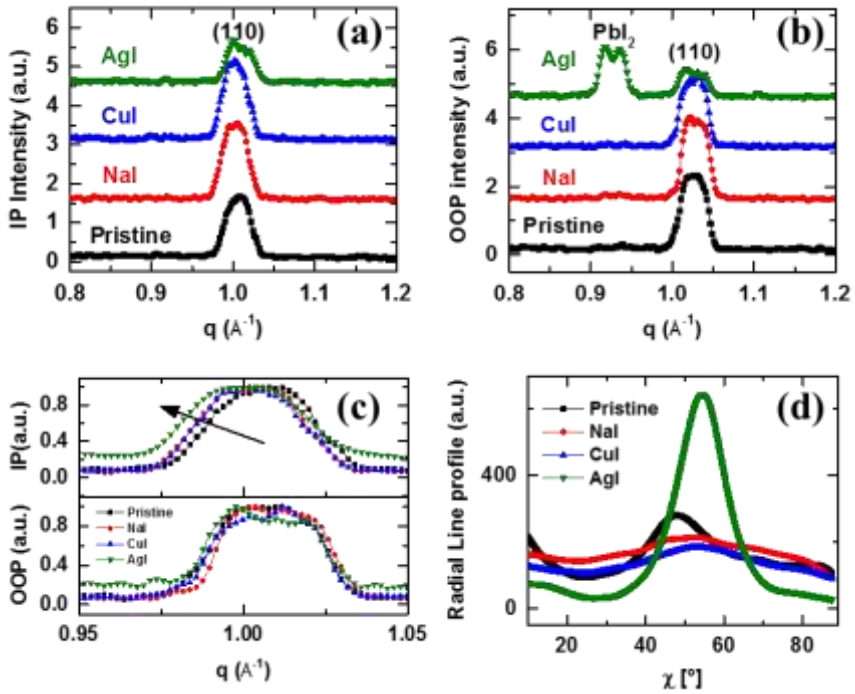

Figure 5.13. Azimuthally and radially integrated line profiles of pristine, Na-, Cu- and Ag-doped perovkite films extracted from the GI-WAXS (XEUSS system) diffraction patterns

shown in Figure 5.12. (a) In-Plane (IP) line profiles (χ = 78°, $\Delta\chi$ = 10°). (b) Out-Of-Plane (OOP) line profiles (χ = 12°, $\Delta\chi$ = 10°). (c) Zoom of the normalised IP and OOP line profiles around the main perovskite peak. (d) Radial line profile of the main lead iodide peak at q ≈ 1 $Å^{-1}$.

5.3.2 Chemical distribution and electronic structure

5.3.2. 1 Hard and Soft X-ray Photoelectron Spectroscopy

To get a deeper insight into the chemical composition, distribution, and electronic structure of the perovskite films at the surface and bulk we use soft X-ray Photoelectron Spectroscopy (XPS, 1486.6 eV photon energy) and synchrotron Hard X-ray Photoelectron Spectroscopy (HAXPES, 4000 eV photon energy) at the KMC-1 beamline (BESSY II, Germany), respectively. We show the overview spectra of the perovskite films recorded with two different energies in Figure 5.14 and the Pb 5d and I 4d spectra in Figure 5.16a-d.

We observe a significant shift towards lower photon energies in the Pb5d and I4d spectra for the Ag- and Cu-doped perovskite films that overlap in binding energy. This shift is present in both the XPS and HAXPES spectra but it is larger in the latter. We also find a similar trend for the C 1s and N 1s core level (Figure 5.17) as well as for the valence band (VB) edge (Figure 5.15 and Figure 5.16e-f). The observed shift in all the core level peaks as well as the valence band region is attributed to a modification of the Fermi level position within the bandgap of the doped-perovskites (e.g. Cu and Ag) as illustrated in Figure 5.16g. It is notable that we calibrated the spectra vs. the Fermi level and we detect a shift in all the core level peaks.

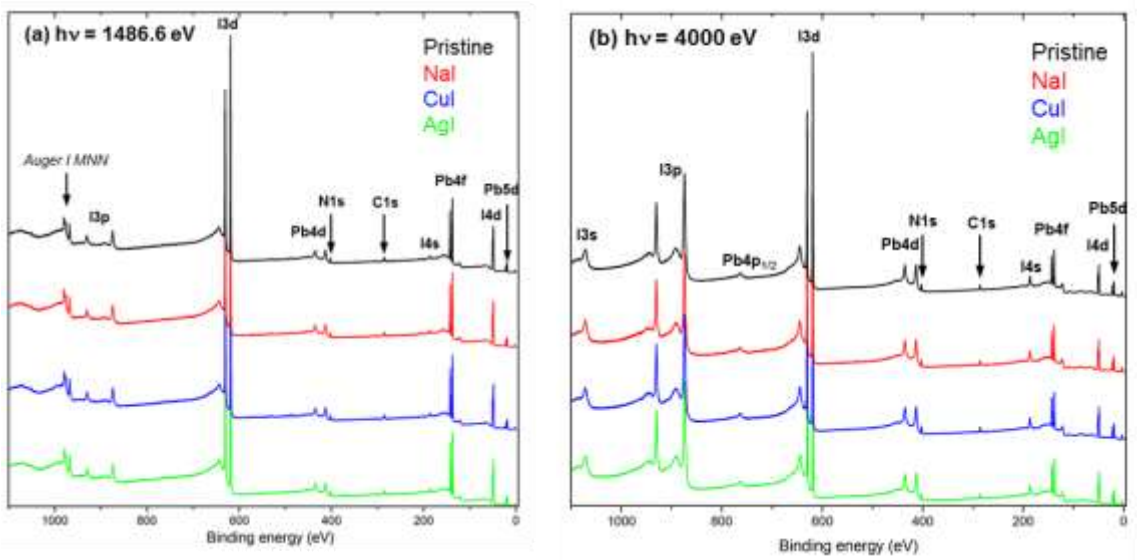

Figure 5.14. Overview spectra of the pristine and additive-based perovskite thin films collected with photon energy of (a) 1486.6 eV and (b) F4000 eV. The spectra were normalized versus the Pb 4f7/2 core level.

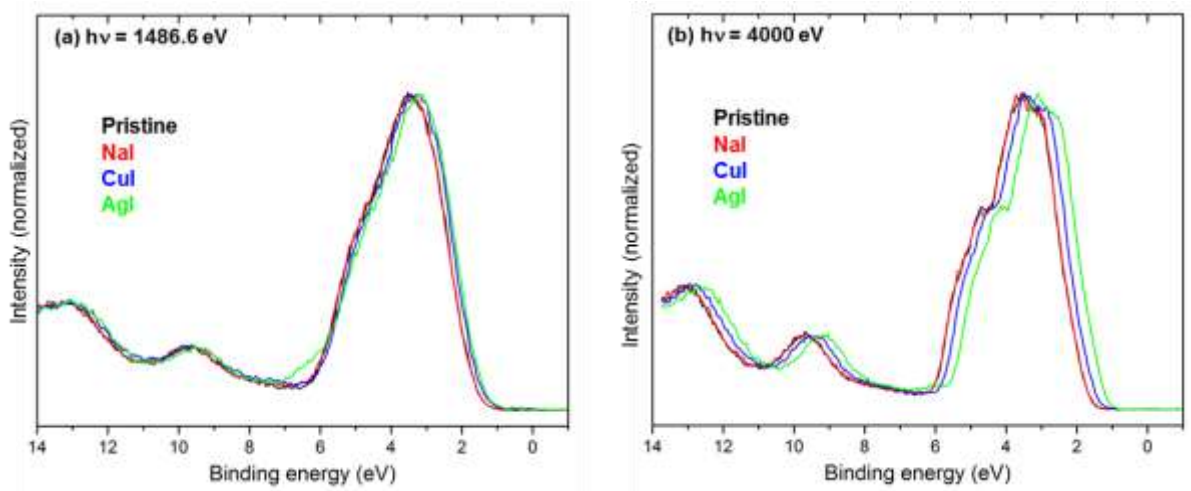

Figure 5.15. The valence band spectra (14 to -1 binding energy range area) for the pristine and additive-based perovskite thin films measured with photon energy of (a) 1486.6 eV and (b) 4000 eV. The spectra were normalized to the maximum for a better comparison.

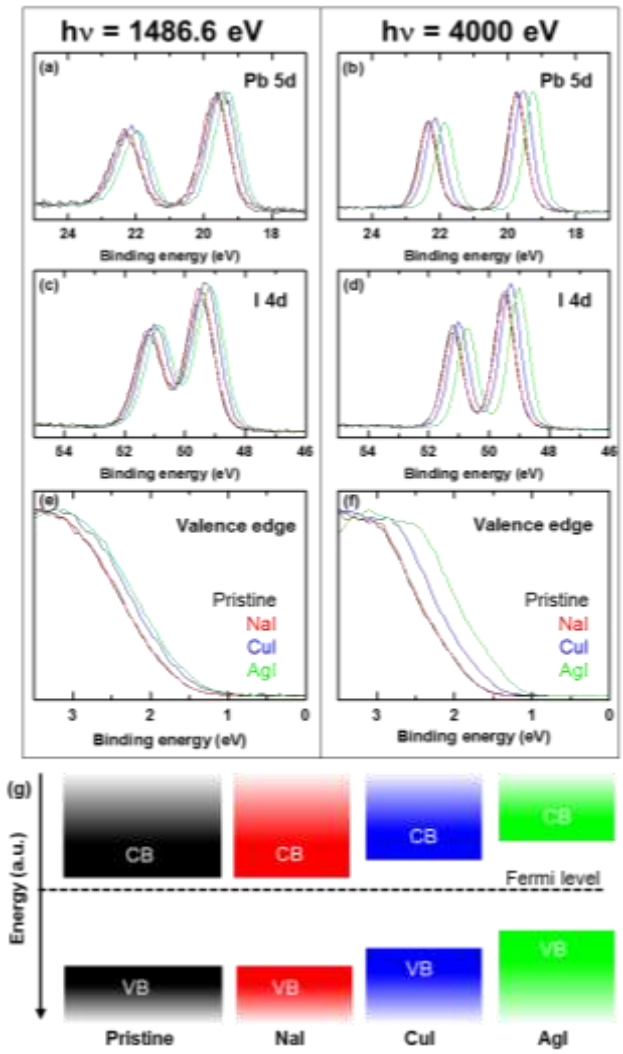

Figure 5.16. (a)(b) Pb 5d, (c)(d) I 4d core level spectra and (e)(f) valence band edge of pristine and doped-perovskite thin films measured with a photon energy of 1486.6 eV (left panels) and 4000 eV (right panels). The I4d and Pb5d spectra were normalized versus their maximum. See full valence spectra between -1 and 14 eV binding energy in Figure 5.15. (g) Schematic representation of the valence and conduction band edges position vs. the Fermi level (black dot line) induced by the incorporation of dopants.

In Figure 5.18, we measure the core level spectra of the dopants (i.e. Na 2s, Cu 2p and Ag 3d) in both photon energies (1486.6 and 4000 eV). Despite introducing small dopant quantity, the overlap of the lines with more intense core levels (e.g. Cu 2p with I 3p, Na 1s with I 3s) and the low photoionization cross section of the core levels (e.g. Na 2s, Na 2p) particularly at 4000 eV, we detect all the monovalent cations introduced in the precursor solution by comparing the doped-perovskite spectra with the pristine one.

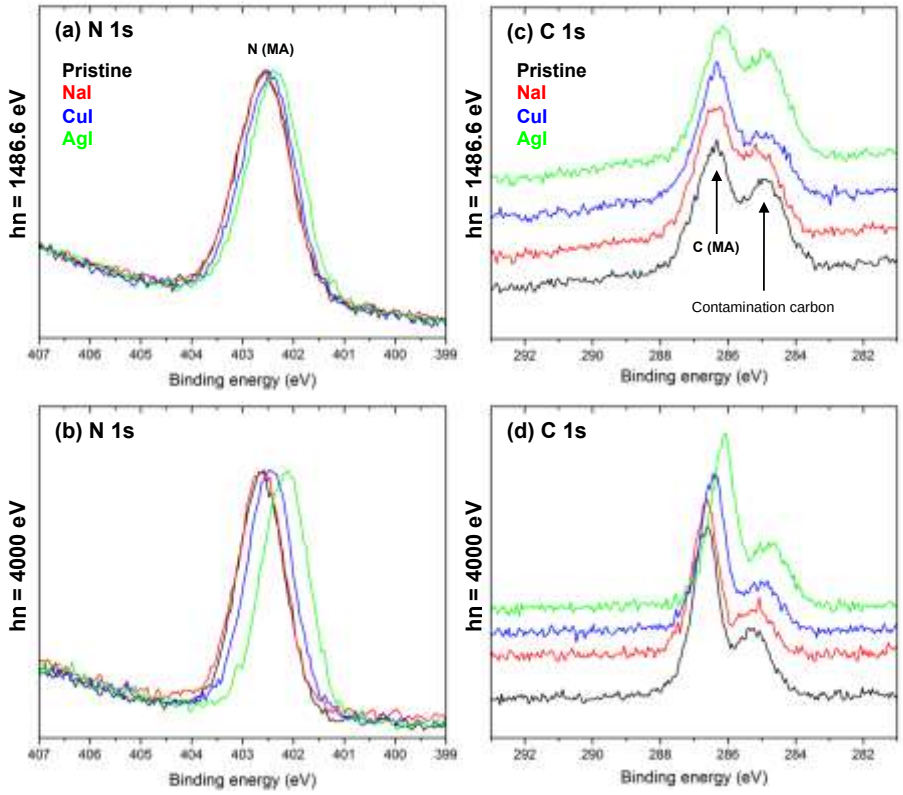

Figure 5.17. High-resolution core level spectra of the additive-based perovskite thin films. (a)(b) N1s and (c) (d) C1s core level peaks measured with photon energy of 1486.6 eV (top panels) and 4000 eV (bottom panels). The spectra were normalized to the maximum for better comparison.

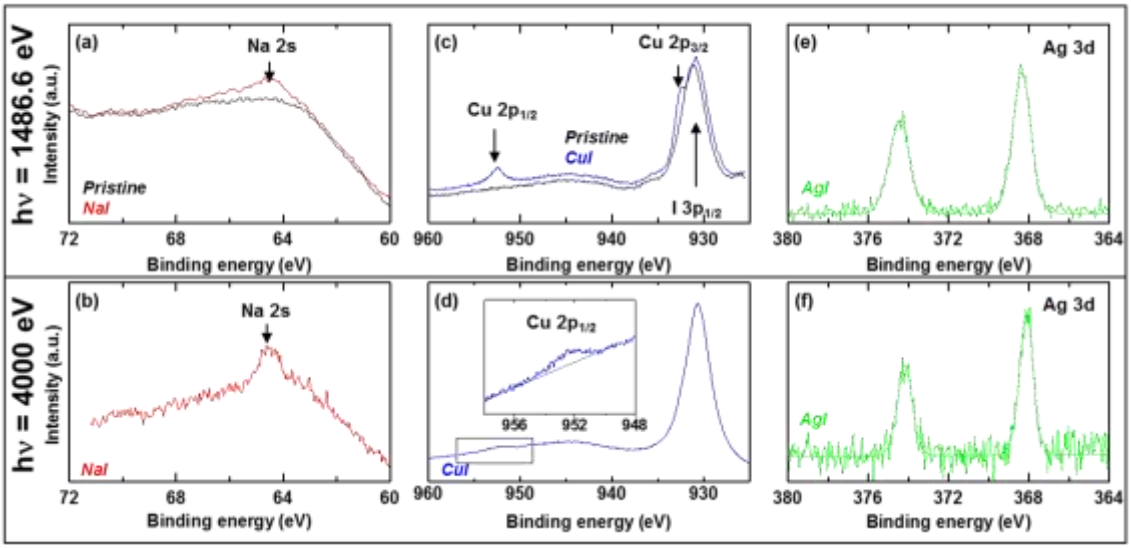

Figure 5.18. (a)(b) Na2s, (c)(d) Cu2p and (e)(f) Ag3d core level spectra of the different perovskite films recorded with a photon energy of 1486.6 eV (top panels) and 4000 eV (bottom panels).

In Table 5.3, we summarize the ratio between the main elements in the perovskite films and the degree of dopants' inclusion based on the intensity ratios between different atomic core levels acquired at 1486.6 eV and 4000 eV photon energies. We calculated the initial composition (IC) ratios based on the concentration of the precursors. We also show the experimental I/Pb ratio in Table 5.3a, which is comparable to the IC value of 3 for the pristine and 3.1 for the doped-perovskite films. The content of iodide detected in the bulk (4000 eV) is very close to the IC value, however, at the surface (1486.6 eV) an excess of iodide can be detected.[234] We also notice that the content of iodide is slightly higher for the doped-films due to the addition of iodide from the initial salts (NaI, CuI and AgI). The excess of halide can fill halide vacancies and passivates traps[235].

Table 5.3. Intensity ratios between different core levels calculated from HAXPES measurements; (a) I/Pb ratio, (b) Na/Pb, Cu/Pb and Ag/Pb ratio for the different doped-perovskites as a function of the excitation energy (1486.6 and 4000 eV). The values for the initial composition correspond to the calculated ratios within the precursor solution. The error bar for these ratios is about ±0.01.

(a) I/Pb intensity ratio *(initial composition)*	Pristine *(3.0)*	Na *(3.1)*	Cu *(3.1)*	Ag *(3.1)*
1486.6 eV	3.18	3.29	3.21	3.30
4000 eV	3.00	3.07	3.08	3.05

(b) Intensity ratio *(initial composition)*	Na/Pb *(0.1)*	Cu/Pb *(0.1)*	Ag/Pb *(0.1)*
1486.6 eV	0.126	0.009	0.029
4000 eV	0.097	0.051	0.012

In Table 5.3b, we also list the proportion of Na, Cu and Ag with respect to Pb based on the ratios between their core level peaks. These values suggest that Na has the highest inclusion into the perovskite film compare to the other dopants and has higher concentration at the top surface compare to the deeper in the bulk. On the other hand, Cu penetrates more towards the bulk while traces of Ag can be detected more at the surface. The presence of Na does not affect

the electronic structure of perovskites due to the complete overlap of its valence band with the pristine film. As for Cu and Ag, we find a lower inclusion of the monovalent cation compared to the IC value of 0.1 (i.e. ratio of monovalent cation to Pb) but, surprisingly, this smaller quantity of Cu and Ag leads to a stronger impact on the valence and conduction band energy positions (Figure 5.16g).

5.3.2. 2 Electron Microscopy

To investigate the local chemical and morphological composition of the doped-$CH_3NH_3PbI_3$ thin films, we performed Scanning Transmission Electron Microscopy-Energy Dispersive X-ray spectroscopy (STEM-EDX)[236]. In Figure 5.19, we show a stack of STEM High Angle Annular Dark Field (HAADF) cross sectional views of a lamellae from the Na, Ag and Cu doped perovskite films. To secure the perovskite layer during specimen preparation, we deposited capping layers of 2,2′,7,7′-tetrakis(N,N-di-p-methoxyphenylamine)-9,9′-spirobifluorene (i.e. Spiro-OMeTAD, spin-casted) and platinum (ion-beam deposited), respectively (Figure 5.19a).

From the STEM-EDX elemental analysis, we observe silver-rich inclusions well distributed within some of the perovskite grains (Figure 5.19b) while we find sodium-rich phases mostly at the grain boundaries of the perovskite as well as the interface with the substrate (Figure 5.19c). To study the Cu-doped thin film, stray Cu signal has been limited by the use of a molybdenum TEM grid and a low-background TEM holder, but the overall signal level makes isolating signal from the incorporated Cu in the perovskite layer very challenging (Figure 5.19d). In Figure 5.19e, f, we observe a relatively homogeneous distribution of lead and iodine within the perovskite layer across the entire specimen area. We also analysed the STEM-EDX dataset using multivariate analysis methods, specifically a Non-negative Matrix Factorisation (NMF) algorithm[237], which indicates the presence of a similar perovskite phase for all of the doped perovskite films (Figure 5.20).

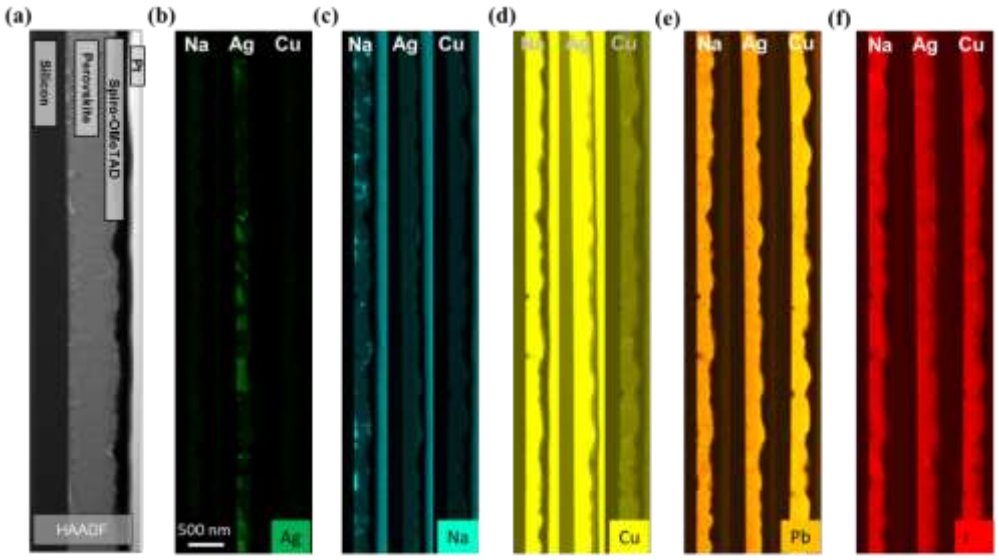

Figure 5.19. (a) Stack of HAADF STEM cross sectional images of perovskite thin films with different doping. Elemental maps for (b) Ag, (c) Na, (d) Cu, (e) Pb and (f) I. For each element, we show Na, Ag and Cu- doped perovskite films from left to right. See the intensity spectra acquired from NMF decomposition dataset for each dopants in Figure 5.20.

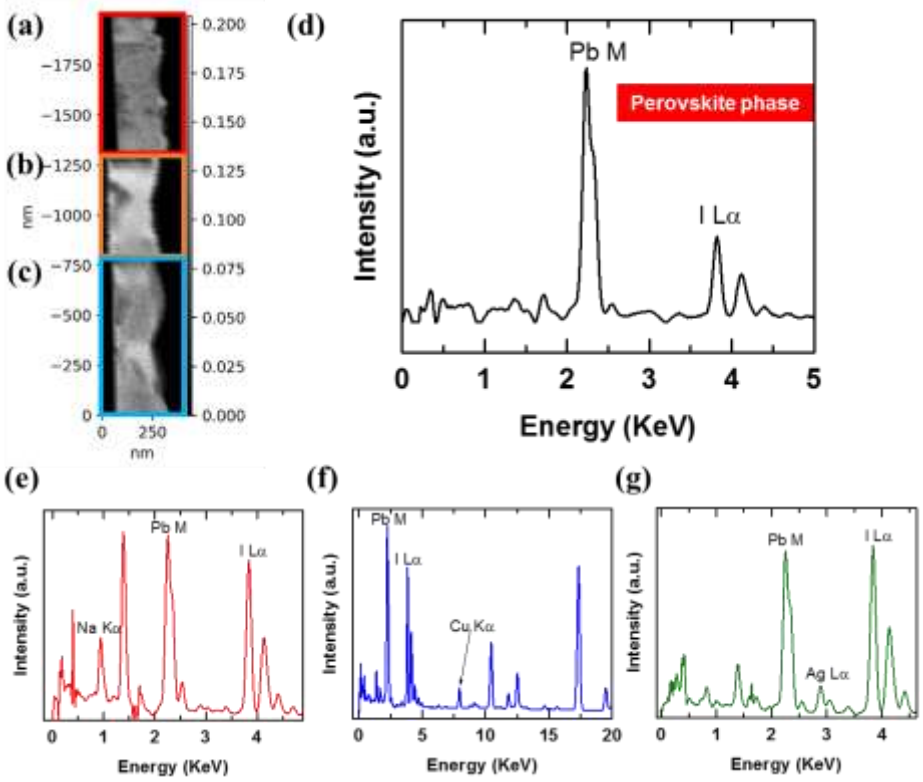

Figure 5.20. HAADF STEM cross sectional image of a (a) Na-, (b) Ag- and (c) Cu- doped perovskite thin films. (d) NMA decomposition results in similar perovskite phase for all the

doped perovskite films and the corresponding EDX spectra for (e) Na-, (f) Cu- and (g) Ag-doped perovskite films.

Furthermore, we performed Scanning Electron Microscopy- Energy Dispersive X-ray spectroscopy (SEM-EDX) to probe the chemical distribution at the surface of the doped perovskite thin films on larger areas compared to the TEM specimens. We observe Na-rich regions that are mostly located at the grain boundaries across the entire sample area (Figure 5.21a and Figure 5.22a). For Cu- and Ag-doped perovskites, we find a distribution of Cu and Ag across the entire area of perovskite films (Figure 5.21b, c and Figure 5.22b, c). We also detect regions rich in metallic Ag and Cu (Figure 5.22b, c and Figure 5.23) that can be attributed to the higher concentration of dopants (e.g. 15 mol%) that were used in order to maximise the EDX signal being analysed.

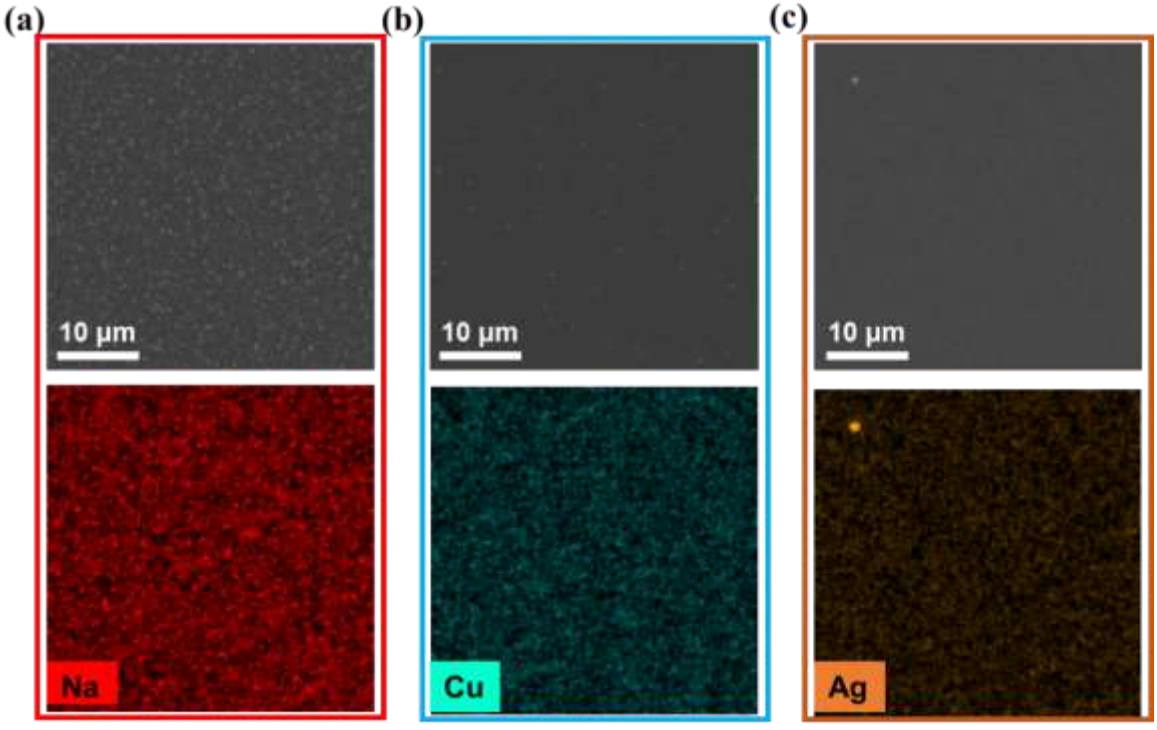

Figure 5.21. SEM-EDX maps for (a) Na-, (b) Cu- and (c) Ag-doped perovskite thin films. The top panels shows the top-view SEM images of the same EDX mapping area.

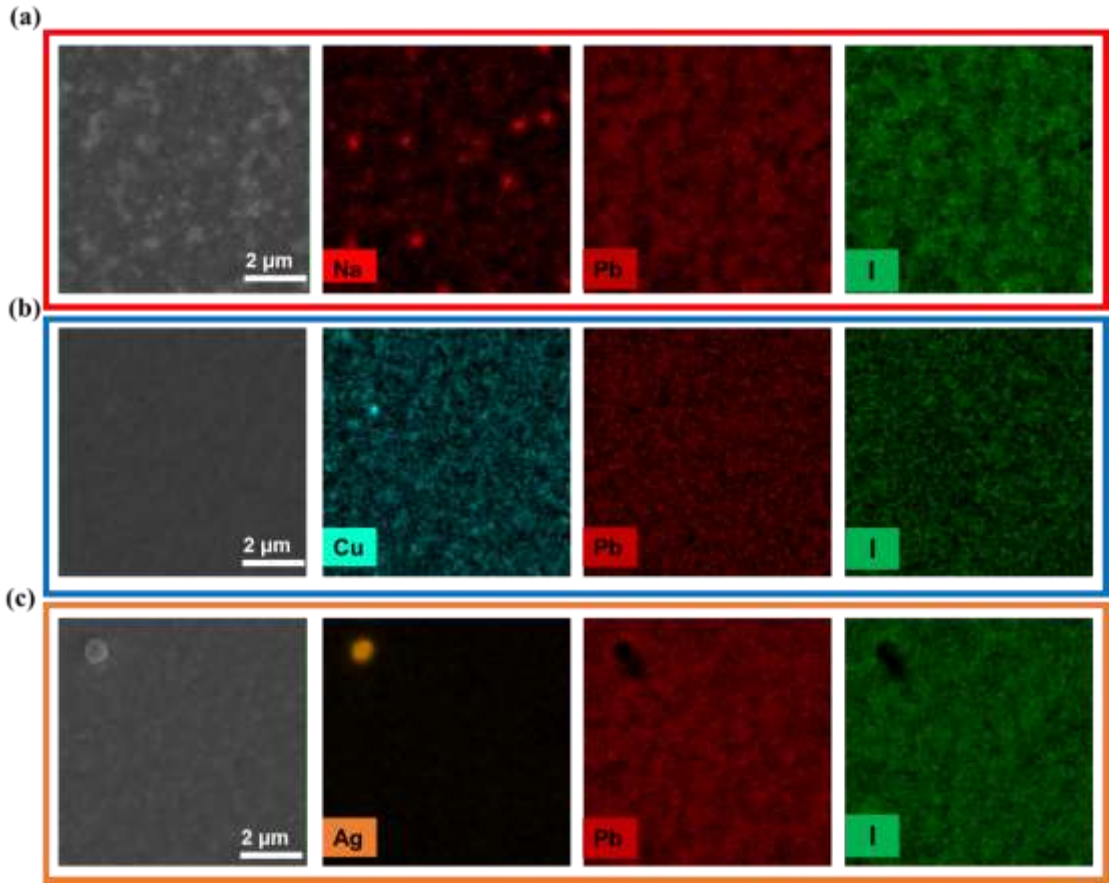

Figure 5.22. SEM-EDX images with the corresponding elemental maps for (a) Na-, (b) Cu- and (c) Ag-doped perovskite thin films.

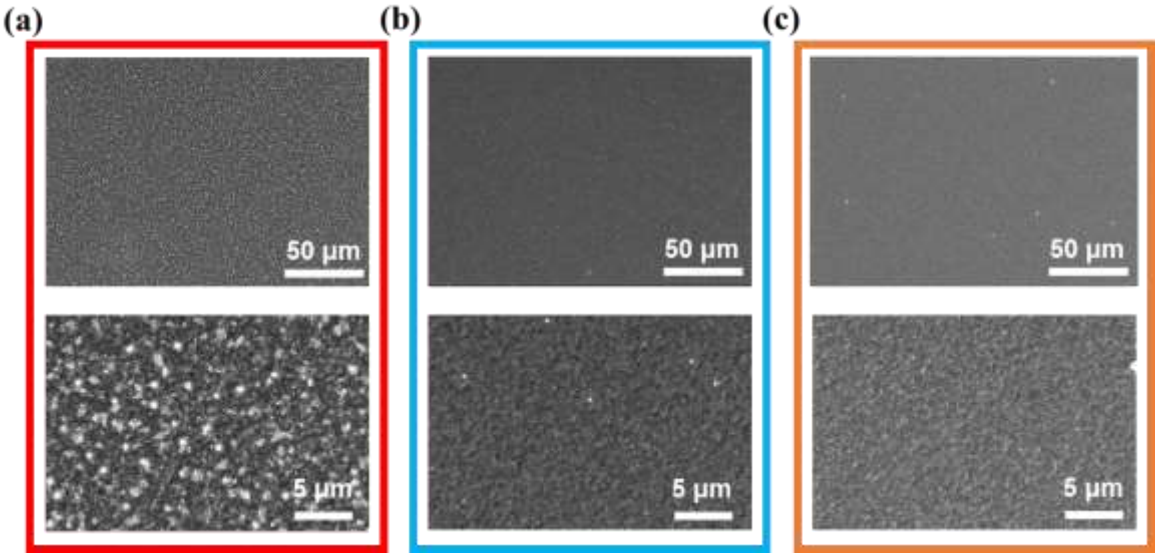

Figure 5.23. SEM images of (a) Na-, (b) Cu- and (c) Ag-doped perovskite thin films prepared for SEM-EDX analysis in two different magnifications.

5.3.3 Modelling doped-perovskite structures

We performed periodic DFT calculations[164] in atomistic-scale to examine how chemical bonding and band structure of the perovskite are affected by partial substitutions of a Pb with Na, Cu and Ag atoms (see Experimental Method Chapter for calculation details, page 53). The estimated formation energies for pristine and 3% Na-, Cu-, and Ag-perovskite single crystals (-30.95, -32.73, -41.25 and -66.86 kcal/mol, respectively) indicate preference for doping rather than phase separation. In the doped perovskites, we observe perturbations within the surrounding I_6 octahedron due to the imbalance in chemical bonds i.e. different cation size and oxidation states of Na, Ag and Cu compared to Pb (Figure 5.24). Since Na is not able to bond to all the neighbouring atoms (due to its ionic nature and smaller ionic radii), it forms a single bond with one iodide atom, which tilts the I_6 octahedron (Figure 5.25b, f). However, Cu and Ag can form 3 and 4 chemical bonds with iodide, respectively, due to their flexibility in rearranging themselves to the local environment with dissipation of their d shell (Figure 5.25). Based on the distribution of the charge density in between the atoms, we can predict the nature of the chemical bonds. In the case of Na-I, bond charge densities are distinct and dense at the nuclei of Na and I, while for Cu-I and Ag-I, we observe a uniform distribution of charge densities between these atoms showing a covalent nature for these bonds (Figure 5.25e-h).

In Table 5.4, we summarize the details of chemical bonds (bond length, tilting angle and average distortion factor) for pristine and doped perovskite structures. Since the chemical bonds between the dopants and iodide atoms are all in the *ab*-plane of the perovskite lattice, we calculate a small elongation of the lattice along the *c*-axis as well as an increase in the unit cell volume for Ag and Cu doped perovskite (Table 5.4). We also find tilting of PbI_6 octahedral in the doped structures. This can slightly affect the electronic structure of the perovskite and the orientation of the MA dipoles[201]. In Table 5.4, we also calculated the distortion factor (DF) defined as the averaged and squared difference of Pb−I bond lengths within the octahedron minus the average Pb−I bond length[238]. It is clear that DF increases upon incorporation of the dopants particularly for the Cu doped film. These increases originated from the broken symmetry in chemical bonding, which are reflected in the charge density plots near the dopants in Figure 5.25e-h (e.g. the change in the bond length and number of attached iodide to each atom).

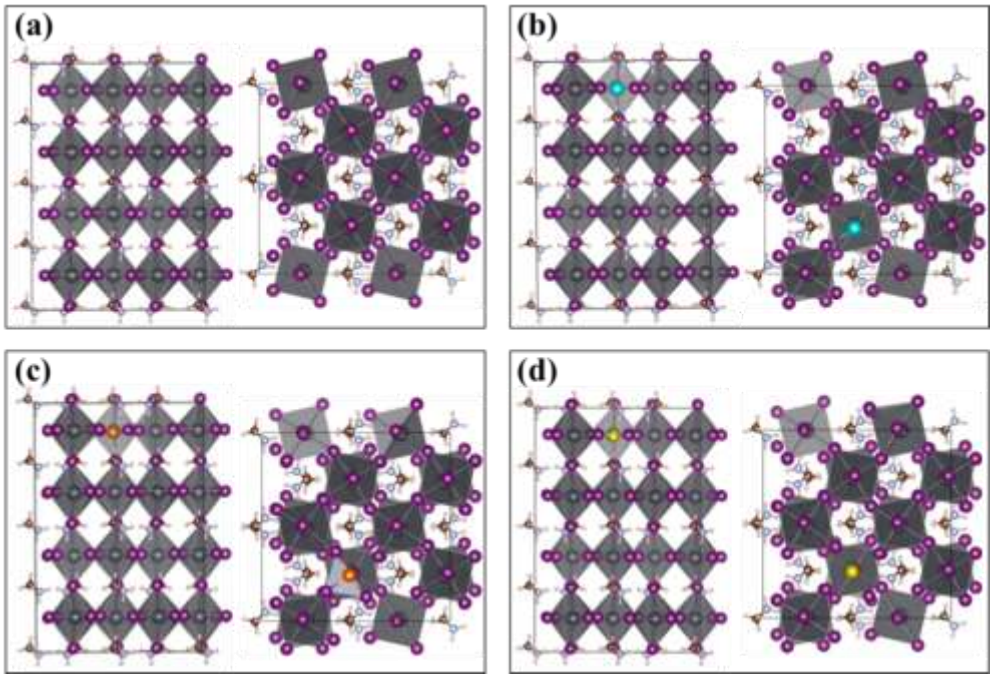

Figure 5.24. DFT calculated perovskite structures for (a) pristine, (b) Na doped, (c) Cu doped and (d) Ag doped lattices. Note that purple, black, blue, grey and cyan, big cyan, orange and yellow sphere are representative of I, C, N, Pb, H, Na, Cu and Ag, respectively.

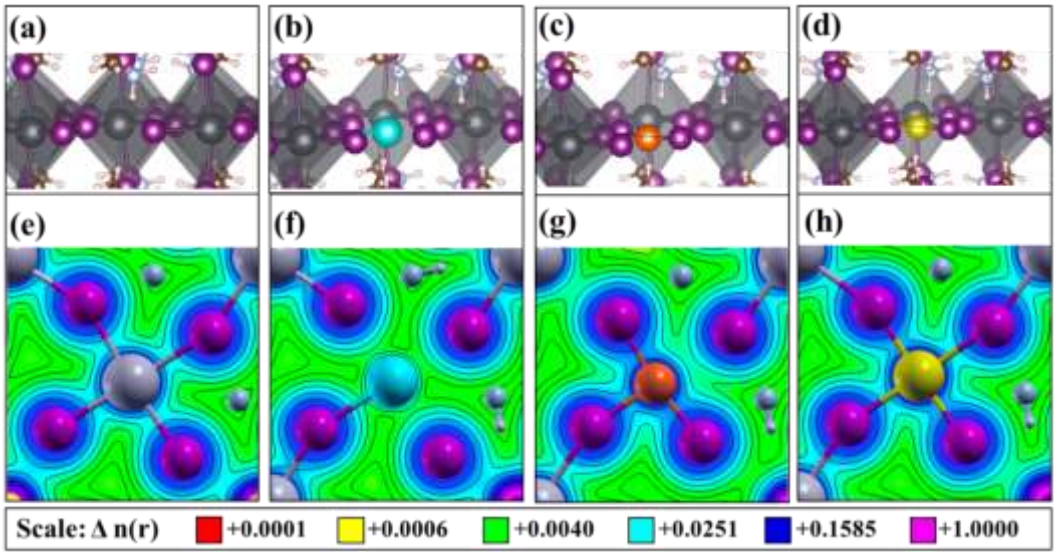

Figure 5.25. Schematic of the local lattice structure for the metal iodide octahedral (top panels) and the corresponding charge density plots (bottom panels) for the (a),(e) pristine, (b),(f) Na, (c),(g) Cu, and (d),(h) Ag-doped $CH_3NH_3PbI_3$ perovskites. Gray, purple, brown, light blue,

cyan, orange and yellow spheres represent lead, iodide, carbon, nitrogen, sodium, copper and silver atoms, respectively.

Table 5.4. DFT calculated average values of tilting angle, average distortion factor and bond length as well as the unit cell volume for pristine, Na, Cu and Ag –doped perovskite.

Sample	Tilting Angle (Degrees)	Distortion Factor (a.u.)	Unit cell volume ($Å^3$)	Bond length (Å)	Horizontal bond length (Å)	Vertical bond length (Å)
Pristine	28.5	1.74	991.80	3.206	3.217	3.185
Na	24.5	2.21	991.80	3.202	3.210	3.187
Cu	26.0	3.50	1029.48	3.213	3.246	3.149
Ag	24.2	2.37	1028.68	3.238	3.221	3.272

Furthermore, the simulated XRD spectra of the geometrically optimized pristine and doped perovskite single crystals (Figure 5.26), show a 0.5^o shift of the main perovskite peak for the Ag and Cu-doped perovskite crystals, which is consistent with the GI-WAXS measurements. We also calculate the Partial Density of States (PDOS) of the doped and pristine perovskites and the corresponding band structures. We do not observe any contribution from the dopant orbitals near the band-edge features of the electronic structure, and conclude that doping does not introduce new energy states within the gap in agreement with the experimental data (Figure 5.27). The main contribution of dopant orbitals in the DOS is far away from the CB or VB edges. Therefore, the estimated band gap was the same for doped and pristine structures (1.58 eV). However, the dopants affect the curvature of the CB minimum and VB maximum (Figure 5.28) and thus the corresponding charge carrier effective masses, which are calculated using the standard effective mass equations and shown in Table 5.5 (See Experimental Methods in Chapter 3, page53).

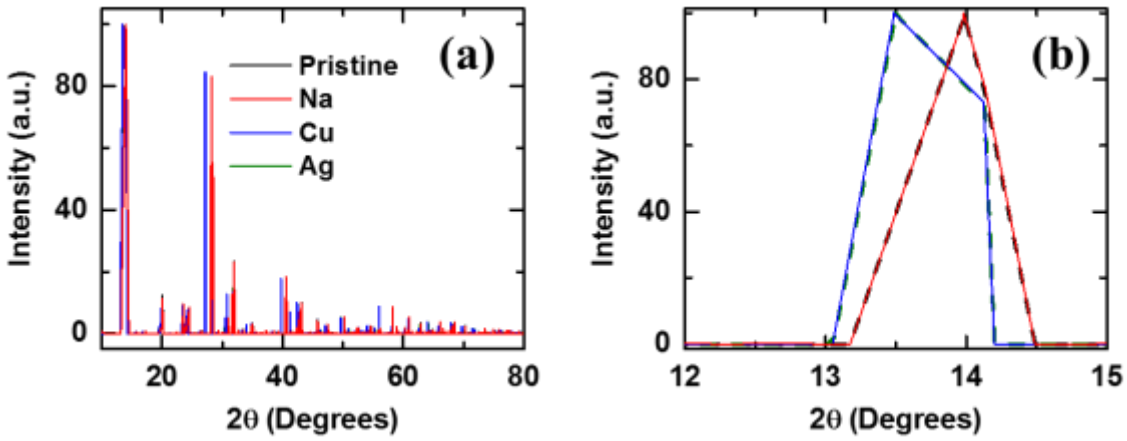

Figure 5.26. (a) Simulated XRD spectra of the pristine and doped perovskite. (b) The perovskite main peak of the additive-based perovskites. A peak shift is observed for the Cu and Ag doped perovskites.

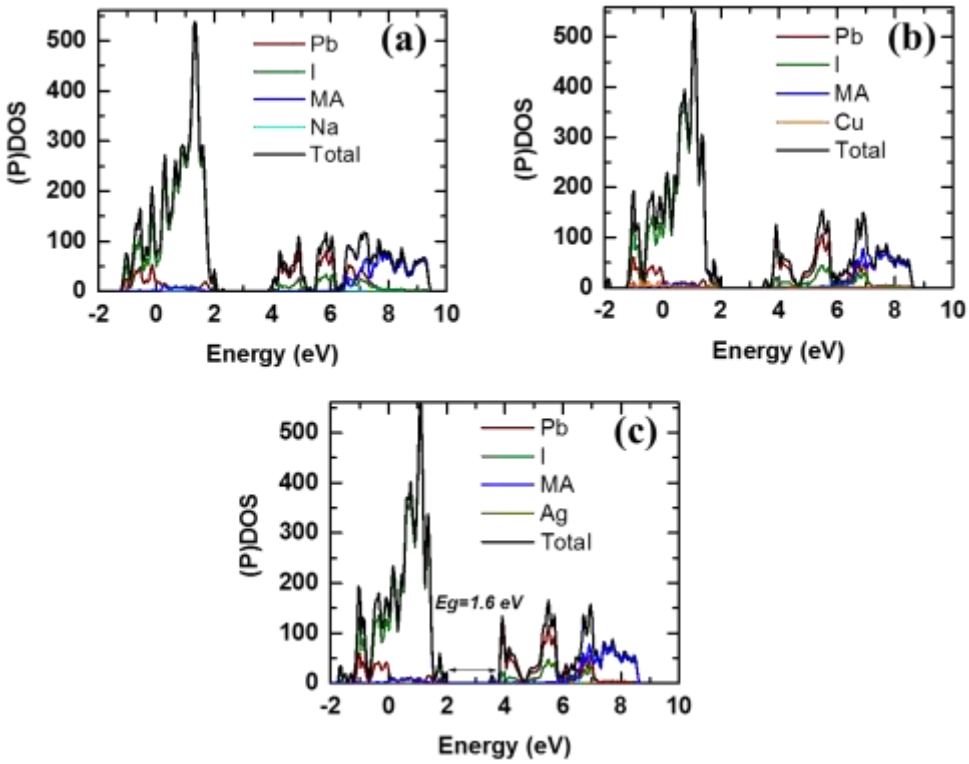

Figure 5.27. DFT calculated PDOS of the (a) Na, (b) Cu and (c) Ag -doped perovskite structures. No intra band gap states observed upon substitutional doping.

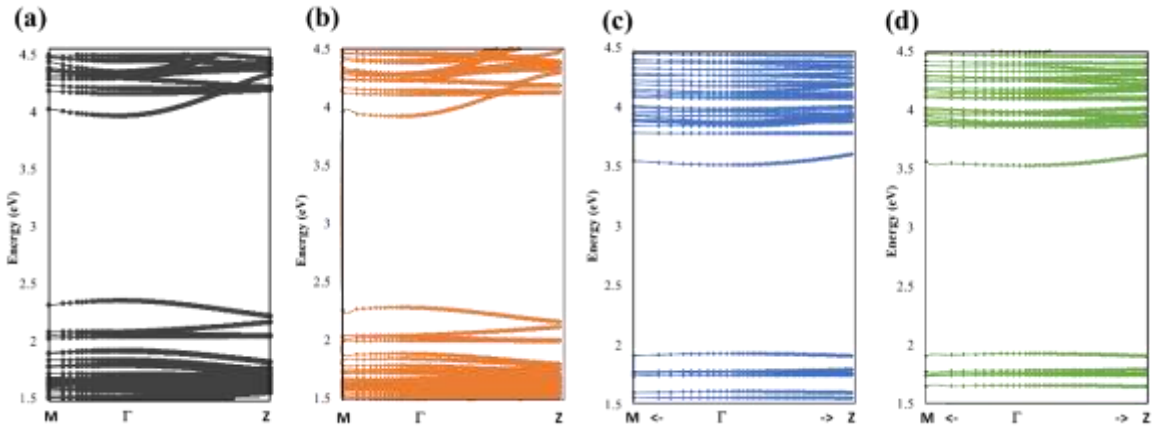

Figure 5.28. Band structure of the (a) pristine, (b) Na-, (c) Cu- and (d) Ag-doped perovskite structure near the Gamma point. Note that the reference energy levels are arbitrary and not corrected against the vacuum level. In a, c and d, part of the band structure near the Gamma point, which is the most relevant for the effective mass evaluation, is plotted**.**

Table 5.5. Calculated values of the effective mass (m*) for pristine and doped perovskite structures.

Gamma to M	**Pristine**	**Ag doped**	**Cu doped**	**Na doped**
m*e/m*0	0.18	0.24	0.24	0.20
m*h/m*0	0.21	0.21	0.26	0.17
Gamma to Z				
m*e/m*0	0.17	0.14	0.14	0.11
m*h/m*0	0.23	0.37	0.42	0.19

Furthermore, due to the high dipolar nature of the material with negatively charged octahedrons and positively charged MA cations together with different dipolar orientations of the MA cations inside the lattice, it is difficult to find a stable absolute reference for the vacuum level in the DFT calculations[164]. Therefore, we estimate the amount of plausible VB and CB shifts based on the change in the VB edge with respect to the carbon core level. We then observe that the VB/CB edge of the Na-, Cu- and Ag-doped perovskites shifted negatively with respect to

the vacuum level (away from the vacuum level by 5 meV, 240 meV and 490 meV respectively) which is consistent with our XPS results (Figure 5.16e, f).

The energy level of intra-band gap trap states, effective mass of charge carriers, position of Fermi level, nature of VB and CB edges and the structural parameters of the perovskite crystals greatly influence the photovoltaic performance of the subsequent devices[112]. The driving potential for charge transfer from the perovskite layer to the charge selective contacts is directly proportional to the energy difference between the VB/CB edges of the perovskite and that of the electron/hole selective contacts. Therefore, optimization and further band alignment at the contacts is vital for obtaining high efficiencies for devices based on monovalent metal-doped-perovskite materials. Furthermore, our predicted Fermi level shifts show that Cu- and Ag-doped films have better charge balance in between the electron and hole densities and thus a superior charge collection efficiency compared to the pristine films. This could pave the way to realise efficient charge separation at the interfaces between perovskite and charge selective contacts. The movement of the fermi level towards the middle of the bandgap for the Cu- and Ag-doped films confirms dedoping of the highly n-doped pristine perovskite films, suggesting clearer bandgap consistent with the lower energetic disorder and sharper absorption edge for the doped perovskite films (Figure 5.10).

We also investigate the possibility of the interstitial doping via allocation of the abovementioned monovalent cations in a preferential location and relaxing the position of all the atoms inside the unit cell accordingly (Figure 5.29). In Figure 5.30, we show formation of chemical bonds between monovalent cations and iodine atoms, where Cu and Ag atoms are located within the same plane of Pb and equilateral iodine atoms while Na shows a displacement out of this plane. The formation energies for interstitial doping (e.g. 3%) of Na, Cu and Ag are -38.25, -70.43 and -75.82 kcal/mol, respectively, which are more favourable compared to substitutional doping. In Figure 5.30, we also show the charge density plots for the interstitial doping, indicating imbalance charge distribution near to the covalent bonding of monovalent cation dopants and iodide. We find no intra band gap states for interstitial doping and a slight change in effective mass of charge carriers with no impact on the optical band gap similar to the substitutional doping (Figure 5.31).

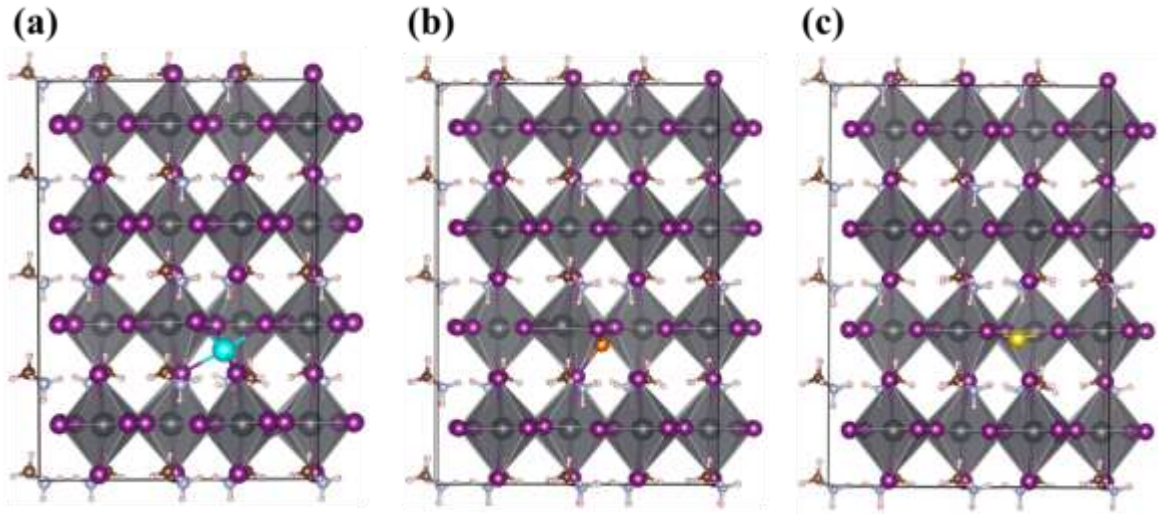

Figure 5.29. Side view of the DFT calculated perovskite structures for (a) Na-, (b) Cu- and (c) Ag-doped lattices via interstitial doping. Note that purple, black, blue, grey and cyan, big cyan, orange and yellow sphere are representative of I, C, N, Pb, H, Na, Cu and Ag, respectively.

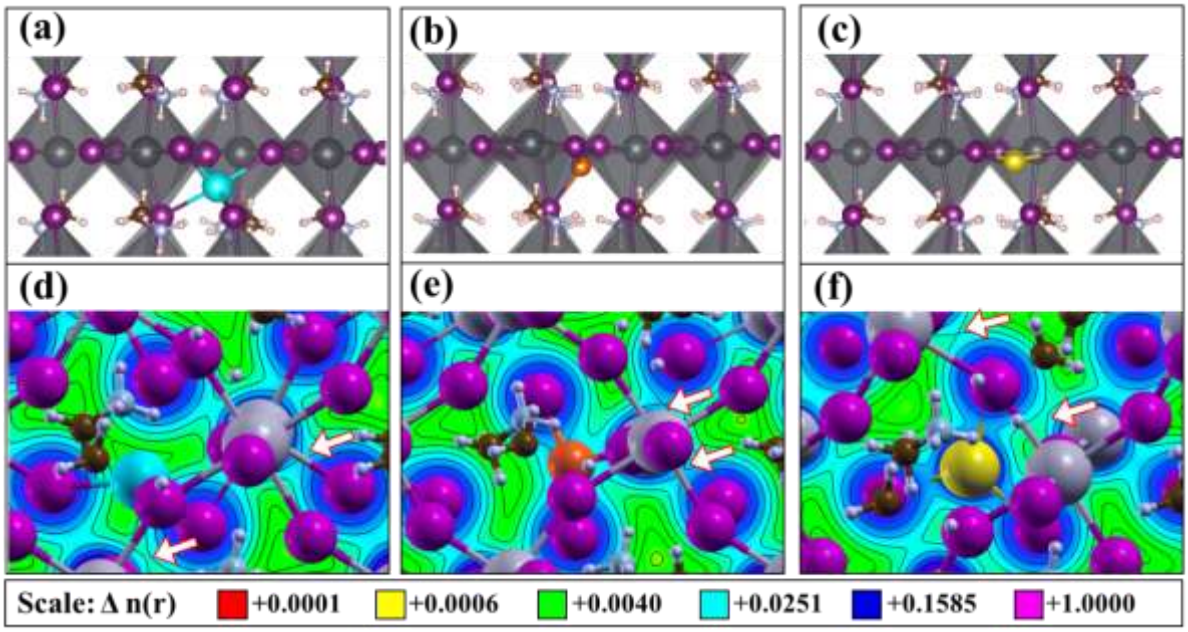

Figure 5.30. Schematic of the local lattice structure for the metal iodide octahedral (top panels) and the corresponding charge density plots (bottom panels) for the interstitial doping of $CH_3NH_3PbI_3$ perovskite with (a),(d) Na, (b),(e) Cu, and (c),(f) Ag. Gray, purple, brown, light blue, cyan, orange and yellow spheres represent lead, iodide, carbon, nitrogen, sodium, copper and silver atoms, respectively. The white arrows indicate the charge imbalance close to Pb-I bonds.

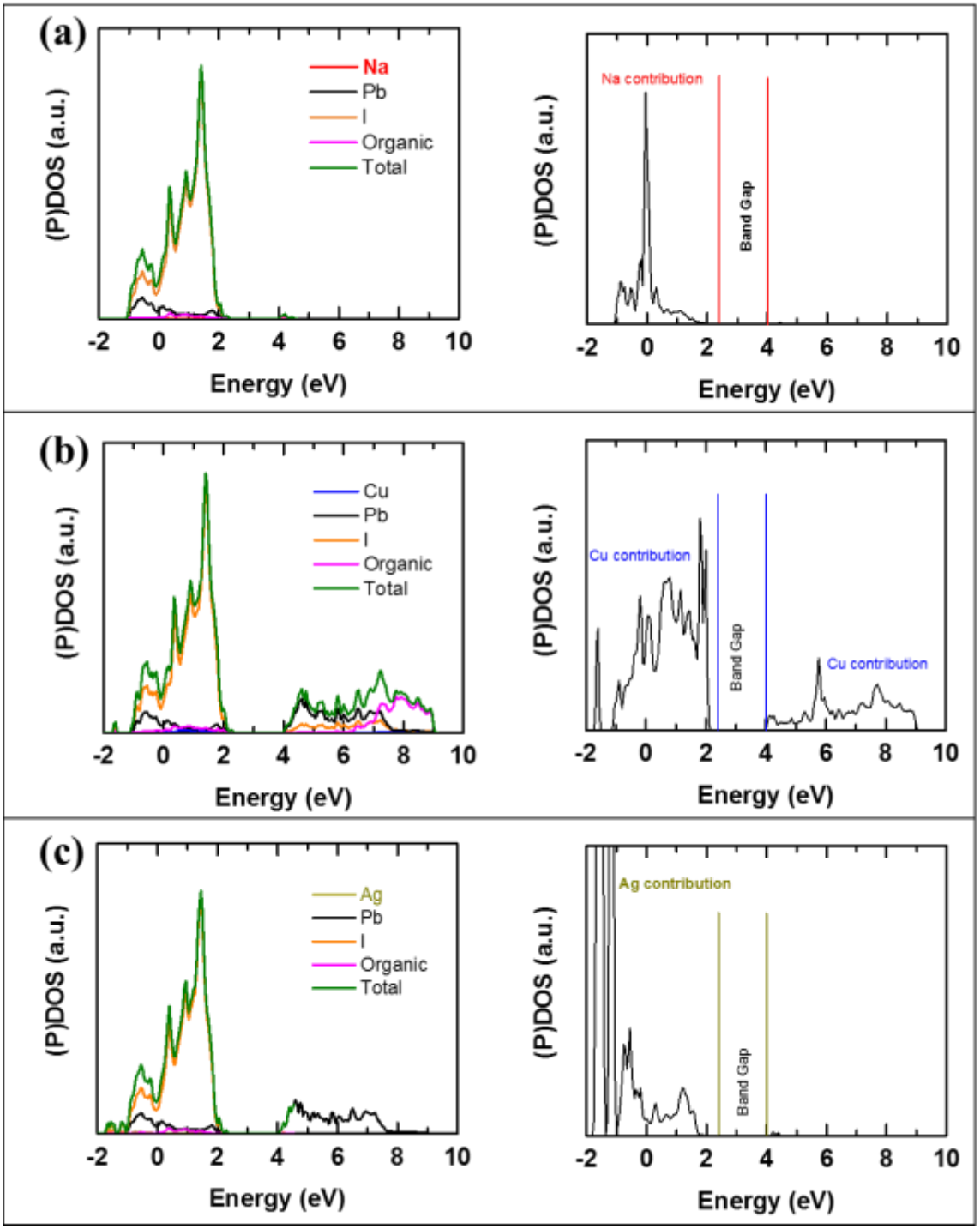

Figure 5.31. DFT calculated (P)DOS of the (a) Na-, (b) Cu- and (c) Ag-doped perovskite structures. Right panels show the contribution of each monovalent cation where no intra bandgap states observed upon interstitial doping.

5.3.4 Conclusions

In summary, we have investigated the influence of monovalent cation halide dopants (e.g. Na, Cu and Ag) on the growth, and crystal structure of lead halide perovskite with a comprehensive insight on the chemical distribution of these dopants within the lattice and their effect on the band structure. We observe a distinct shift in the main diffraction peak of both PbI_2 and $CH_3NH_3PbI_3$ upon addition of the above-mentioned monovalent cations, which is a sign of partial incorporation in the perovskite structure. We then detected all the dopants via soft XPS and HAXPES and we recognize that the concentration of Cu is significantly higher in the bulk compared to the surface in contrast to the other dopants. We detect the highest inclusion for Na with the least active interaction into the perovskite band structure as per the overlap between their valence band edges with the pristine perovskite films. However, we show that introducing Cu and Ag into the perovskite film dedope the highly n-doped pristine perovskite by moving the fermi level towards the middle of the gap leading to cleaner bandgaps as reflected in the lower energetic disorder for the doped perovskite films. From the STEM-EDX results, we find formation of Na-rich phases at the grain boundaries and top/bottom interfaces while Ag-doped perovskite showed Ag-rich inclusions within the perovskite films. Our DFT calculations show how the chemical bonds, lattice arrangement and band structure of perovskite will respond to the substitutional and interstitial doping of perovskite with a monovalent cation (e.g. Na, Cu and Ag). We also find intestinal doping is more favourable than substitutional doping based on the calculated formation energies. Our findings show a fundamental insight for the local chemistry and changes due to the monovalent metal doping and the corresponding impacts on the electronic structure that pave the way for further in-depth investigations.

Chapter 6

Potassium Passivation of Alloyed Perovskites; Maximizing and stabilizing luminescence

Ion segregation and parasitic non-radiative losses are still key barriers preventing the full exploitation of the continuous bandgap tunability and potential for high-performance of metal halide perovskites in device applications. Here, we passivate alloyed perovskite films by decorating the surfaces and grain boundaries with potassium halides. This leads to luminescence quantum yields approaching unity while maintaining high mobilities exceeding 40 $cm^2V^{-1}s^{-1}$, along with the inhibition of transient photo-induced ion migration processes even in mixed halide perovskites that otherwise show bandgap instabilities. We propose that potassium iodide additives minimize halide vacancies, which are responsible for charge carrier trapping, while also immobilizing the surplus halides into benign products. We demonstrate a wide range of bandgaps stabilized against photo-induced ion migration, leading to solar cell power conversion efficiencies of 21.6% for a 1.56 eV absorber and 18.3% for a 1.78 eV absorber ideally suited for tandem solar cells. Our work represents a critical breakthrough in the fabrication of tunable metal halide perovskite thin films that can approach the efficiency limits. A detailed explanation of all these results is presented below and can also be found in the published article - ref. [62].

Contributions. This work was the result of collaborative research with the following contributions: I and Dr Samuel D. Stranks conceived and planned the experiments with additional input from prof. Richard Friend. I fabricated all samples and devices, performed, and analysed the SEM, XRD, UV-Vis, PDS, PL, PLQE, TRPL, JV and EQE measurements. Dr Eline M. Hutter performed and analysed the TRMC measurements (Figure 6.3c, Figure 6.6). Dr Johannes M. Richter calculated the internal PLQE (Figure 6.3a). Zahra Andaji-Garmaroudi and I obtained and analysed the confocal PL maps (Figure 6.4). Mejd Alsari and Dr Samuele Lilliu performed the GIWAXS experiments and analysed the data (Figure 6.11). Dr Stefania Cacovich and Dr Giorgio Divitini performed and analysed the STEM–EDX measurements (Figure 6.9, Figure 6.10). Dr Bertrand Philippe performed and analysed HAXPES measurements (Figure 6.12). I and Dr Andrew Pearson carried out the device stability tests (Figure 6.16e, f).

6.1 Introduction

Metal halide perovskites are attracting tremendous interest for a variety of high-performance optoelectronic applications[239]. The ability to continuously tune the perovskite bandgap by tweaking the chemical compositions opens up new applications for perovskites as coloured emitters, in building-integrated photovoltaics, and as components of tandem photovoltaics to further increase the power conversion efficiency[240–242]. Nevertheless, parasitic non-radiative losses are still limiting performance, with luminescence yields in state-of-the-art perovskite solar cells still far from 100% under standard solar illumination conditions[58,79,156]. Furthermore, in mixed halide perovskite systems designed for continuous bandgap tunability (bandgaps ~1.7-1.9 eV)[240], photo-induced ion segregation leads to bandgap instabilities[235,243]. Here, we substantially mitigate both non-radiative losses and photo-induced ion migration in perovskite films and interfaces by decorating the surfaces and grain boundaries with passivating potassium-halide layers. We demonstrate external photo-luminescence quantum yields of 66%, translating to internal yields exceeding 95%. The high luminescence yields are achieved while maintaining high mobilities over 40 $cm^2V^{-1}s^{-1}$, giving the elusive combination of both high luminescence and excellent charge transport[244]. We find that the external luminescence yield when interfaced with electrodes in a solar cell device stack, a quantity that must be maximised to approach the efficiency limits, remains as high as 15%, indicating very clean interfaces. We also demonstrate the inhibition of transient photo-induced ion migration processes across a wide range of mixed halide perovskite bandgaps that otherwise show bandgap instabilities. We validate these results in full operating solar cells, highlighting the importance of maximising and stabilising luminescence in device structures. Our work represents a critical breakthrough in the construction of tunable metal halide perovskite films and interfaces that can approach the efficiency limits in both tandem solar cells, coloured LEDs and other optoelectronic applications.

6.2 Optoelectronic properties of potassium passivated perovskite

We fabricated a series of passivated triple-cation perovskite thin films on glass[245] $(Cs_{0.06}FA_{0.79}MA_{0.15})Pb(I_{0.85}Br_{0.15})_3$, where MA = methylammonium, CH_3NH_3; FA =

formamidinium, $CH_3(NH_2)_2$, by diluting the precursor solution with potassium iodide (KI) solution. We herein denote the perovskite as (Cs,FA,MA)Pb($I_{0.85}Br_{0.15}$)$_3$ and the passivated samples with x = [K]/([A]+[K]) and A = (Cs,FA,MA), where x represents the fraction of K out of the A-site cations in the precursor solution. We note that the standard triple-cation precursor solution recipe (x = 0) has a slight halide deficiency but introducing KI leads to samples with a small excess of halide, along with very slight changes to the I/Br ratio (Figure 6.1). The films have uniformly packed grains each of size ~200-400 nm (Figure 6.1). Absorption and photoluminescence measurements reveal a reduction in the optical bandgap of the perovskite film with increasing KI addition, consistent with the additives selectively interacting with the bromide (Figure 6.2). The absorption and photoluminescence (PL) (Figure 6.2a and b) spectra reveal a reduction in the optical bandgap of the perovskite film with increasing KI. The PL peaks at 770 nm for x = 0 and red-shifts to 807 nm for x = 0.4. From Hard X-ray Photoelectron Spectroscopy (HAXPES) measurements, we find that increasing amounts of KI have no effect in the valence band (VB) edge, suggesting that the conduction band (CB) must decrease (Figure 6.2b, inset). We note that this is in contrast to the case of the bandgap tunability achieved through directly changing mixed halide fractions, where the VB was shown to change but the CB remained almost fixed[246]. Measurements on similar perovskite systems without Br did not show such a strong red-shift upon adding K (Figure 6.2f, g, h) suggesting that the additives are selectively interacting with the bromide. These results highlight the combination of K-additives and mixed halides as levers for selectively tuning the bandgap and conduction band. We also note that the samples show a small fraction (<1% of material) with a low bandgap component (Figure 6.2c) but the emission is predominantly from the slightly higher energy component. It is currently unclear why the luminescence is not dominated by the low gap component but it is possible that these low-concentrations, low-bandgap components are electronically isolated from the remaining material, for example being surrounded by potassium-rich passivating material. We also note that the decrease in PLQE for x = 0.6 could be due to the much smaller grain size at these high passivation levels (Figure 6.1). Finally, we note that the absorptance changes due to thickness changes with KI addition over the ranges for our devices (x = 0 - 0.2) are negligible and thus are not a significant cause of the observed enhancements in device performance.

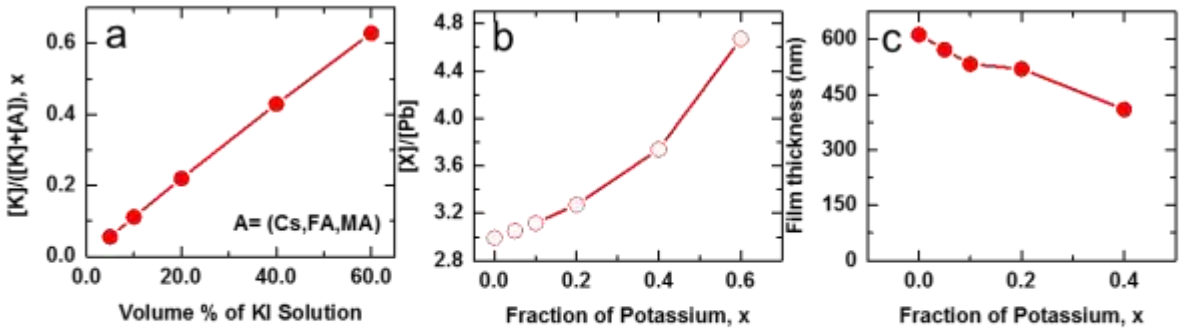

d Calculated	x=0.0	x=0.05	x=0.10	x=0.20	x=0.40
[I]/[Pb]	2.545	2.604	2.669	2.825	3.292
[Br]/[X]	0.149	0.146	0.143	0.137	0.120
[I]/[X]	0.851	0.854	0.857	0.863	0.880
[X]/[Pb]	2.992	3.051	3.117	3.272	3.739
[K]/([A]+[K])	0	0.056	0.111	0.220	0.429

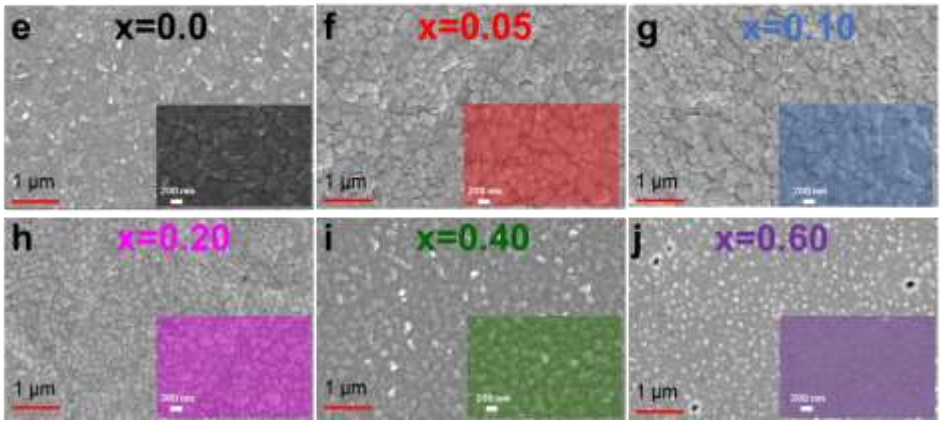

Figure 6.1. Stoichiometries of the precursor solutions, and thickness measurements and scanning electron microscope images of the (Cs,FA,MA)Pb($I_{0.85}Br_{0.15}$)$_3$ films. The calculated values for (a) [K]/([K]+[A]) as a function of KI volume ratio added to the (Cs,FA,MA)Pb($I_{0.85}Br_{0.15}$)$_3$ perovskite precursor solution, (b) halide (X) to lead ratio ([X]/[Pb]) for different fraction of potassium in perovskite films based on stoichiometric calculations, (c) Thickness of the films deposited on c-TiO_2/m-TiO_2. (d) The calculated ratios between different elements. Note that X represents halides (i.e. sum of iodide and bromide). (e-j) Scanning electron micrograph of (Cs,FA,MA)Pb($I_{0.85}Br_{0.15}$)$_3$ perovskite thin films with potassium fraction ranging from x = 0.0 to x = 0.6. The coloured insets show higher magnification images.

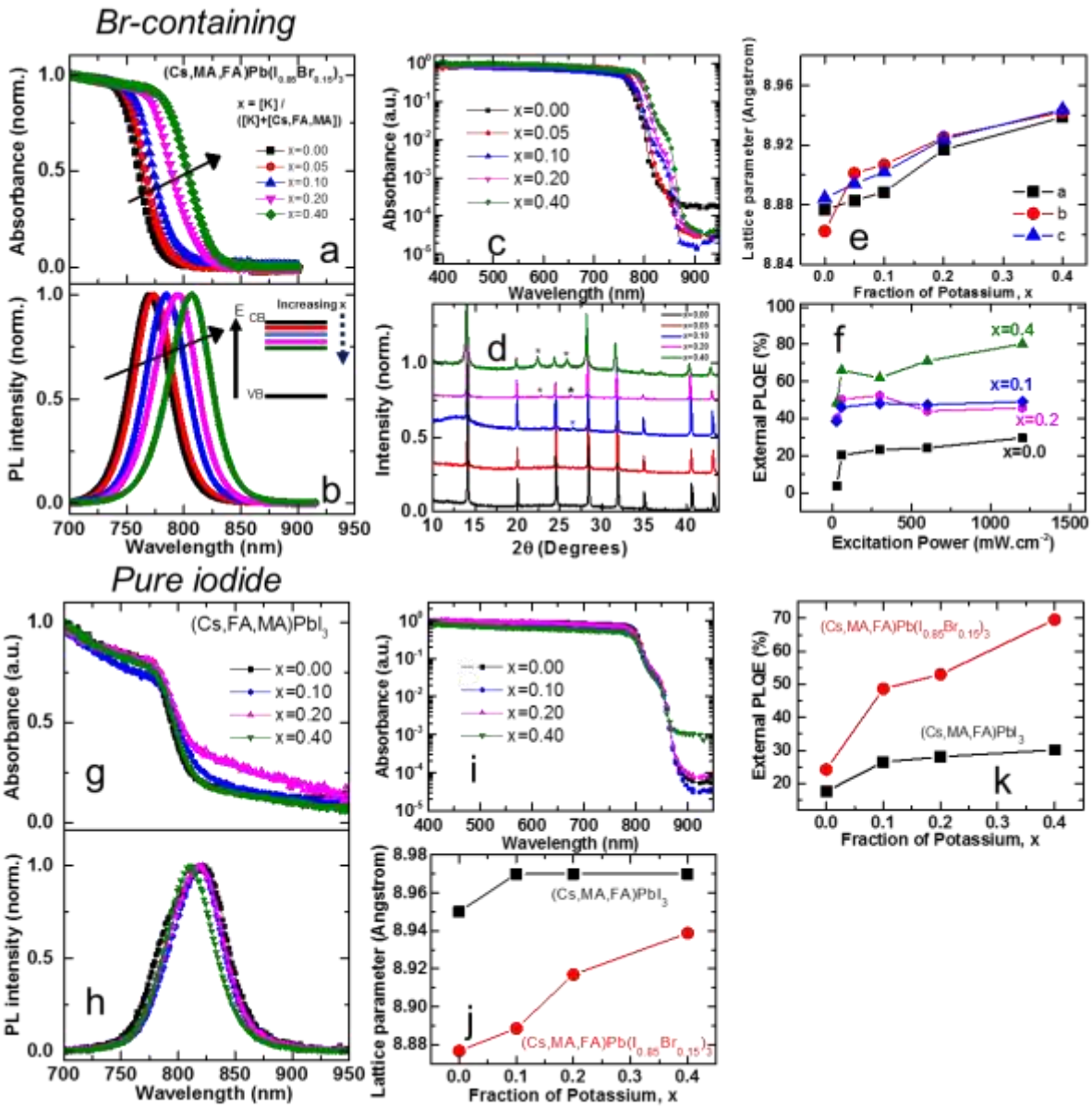

Figure 6.2. Absorption, photoluminescence and X-Ray diffraction characteristics of the (Cs,FA,MA)Pb($I_{0.85}Br_{0.15}$)$_3$ (Br-containing) and (Cs,FA,MA)PbI_3 (pure-iodide) films. Results for (a-e) Br-containing (Cs,FA,MA)($I_{0.85}Br_{0.15}$)$_3$, and (f-j) (Cs,FA,MA)PbI_3 perovskite films. (a) Normalised UV-vis absorption and (b) photoluminescence (PL, 532-nm CW excitation) of the (Cs,FA,MA)($I_{0.85}Br_{0.15}$)$_3$ perovskite films with different K content (x). Inset: schematic of the change in conduction band with increasing x. (c) The absorption spectra of (Cs,FA,MA)Pb($I_{0.85}Br_{0.15}$)$_3$ perovskite thin films with different potassium fractions measured by photo-thermal deflection spectroscopy (PDS), showing a decreased sub-gap density of states with potassium passivation. (d) X-Ray Diffraction (XRD) data of the (Cs,FA,MA)Pb($I_{0.85}Br_{0.15}$)$_3$ thin films, with new peaks arising from increasing K labelled with a *. (e) Calculated lattice parameters using a Le Bail analysis as a function of K fraction on the

XRD data. (f) PLQE as a function of excitation power measured by a 532-nm CW laser for (Cs,FA,MA)Pb($I_{0.85}Br_{0.15}$)$_3$ perovskite thin films in ambient atmosphere. (g) Normalized UV-vis absorption, (h) photoluminescence (PL, 532-nm CW excitation) and (i) Photo-thermal deflection spectroscopy (PDS) absorption spectra of the (Cs,FA,MA)PbI_3 perovskite films with different K content. (j) Calculated lattice parameters as a function of K, determined using a Le Bail analysis on X-Ray Diffraction data, for the (Cs,FA,MA)PbI_3 perovskite thin films (black square) compared to (Cs,FA,MA)($I_{0.85}Br_{0.15}$)$_3$ (red circles). (k) PLQE of different passivated perovskite thin films with and without bromide measured under illumination with a 532-nm laser at an excitation intensity equivalent to ~1 sun (~60 mW.cm^{-2}) in ambient air.

For a solar cell or light-emitting diode to approach its efficiency limit, all recombination should be radiative and luminescence maximised[247]. In state-of-the-art perovskite films, there are still substantial non-radiative losses originating from charge-carrier trap states present in the perovskite layer[150]. The origin of the trap states is still unclear, but they may be associated with ionic defects such as halide vacancies[220,248]. In Figure 6.3a, we show the external photoluminescence quantum efficiency (PLQE) of the (Cs,FA,MA)Pb($I_{0.85}Br_{0.15}$)$_3$ perovskite films with increasing K content measured at excitation densities equivalent to solar illumination. The PLQE shows a significant jump from the 8% (x = 0) to 41% (x = 0.05) reaching a remarkably high PLQE of 66% for x = 0.40. By accounting for photon recycling and light-out-coupling effects[249], these values translate to an internal PLQE exceeding 95% for the passivated compositions (Figure 6.3a). Furthermore, the PLQE does not change significantly with excitation power for the passivated samples, unlike the x = 0 sample in which the PLQE increases with intensity due to a filling of the high density of trap states[250] (Figure 6.2f). These results are also reflected in micro-PL measurements (Figure 6.4).

The confocal PL intensity maps are shown in Figure 6.4a-d from perovskite films with x = 0 – 0.4, with the intensity distributions shown in Figure 6.4i. For example, we observe a broad distribution of emission intensity peaking at 2×10^4 counts for x = 0.20 compared to a narrower distribution but with a maximum at only 5×10^3 counts for the reference film (x = 0). Although the intensity distribution is broader for the x = 0.2 sample, the lowest counts for this sample are as high in number as the highest counts for the reference. We find that the absolute emission intensity increases continuously with increasing content of potassium (Figure 6.4i), peaking at an order of magnitude enhancement at x = 0.40, consistent with the PLQE data in Figure 6.3a.

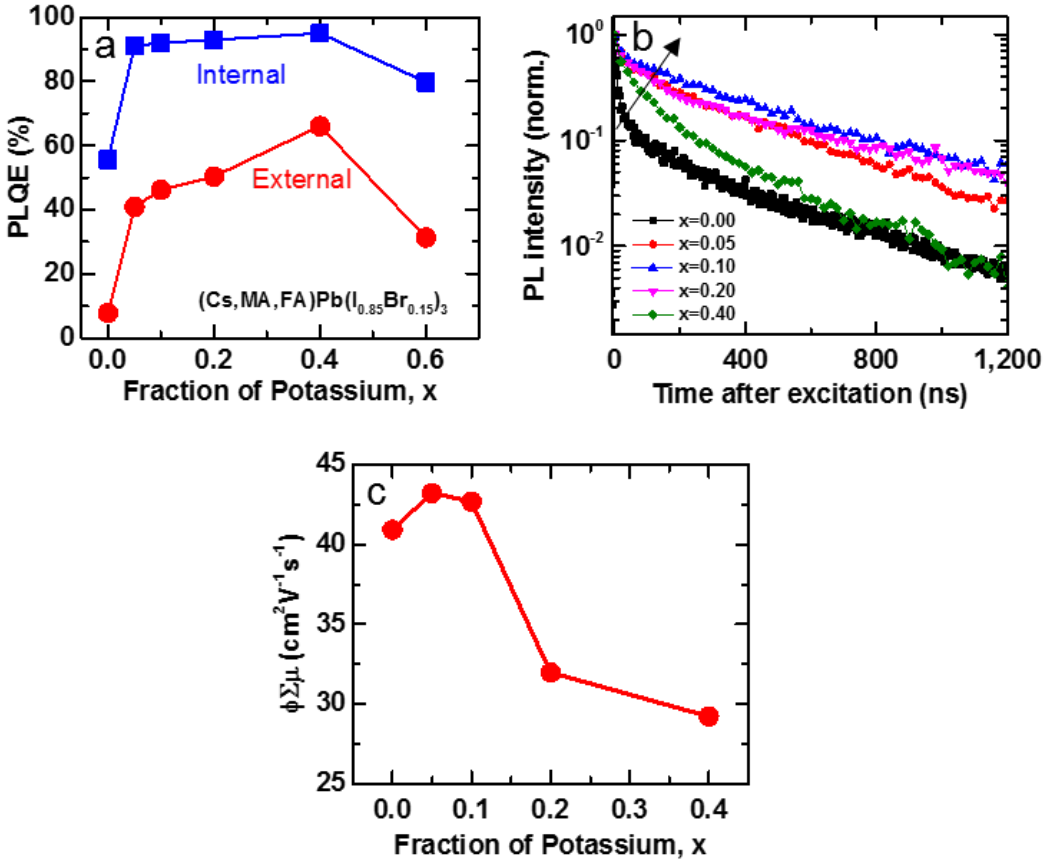

Figure 6.3. Increased radiative efficiency and charge carrier mobility through passivation. (a) PLQE of passivated perovskite thin films with increasing fraction of potassium measured under illumination with a 532-nm laser at an excitation intensity equivalent to ~1 sun (~60 mW.cm^{-2}) after 300 seconds of illumination. (b) Time-resolved PL decays of the films with excitation at 407 nm and pulse fluence of 0.5 μJ.cm^{-2} (excitation density ~10^{16} cm^{-3}). (c) Maximum photo-conductance for each of the K contents extracted from TRMC measurements with an excitation density of ~10^{14} cm^{-3} (Figure 6.6).

We also show the centre-of-mass PL wavelength maps for the same perovskite films in Figure 6.4e-h, along with the corresponding histograms in Figure 6.4j. This further confirms the red-shifting of the microscale PL upon addition of K, consistent with the absorption and bulk PL data. Interestingly, we find a statistically-significant correlation between the PL wavelength and the intensity for each local site (i.e. the most emissive sites are the most red-shifted, see Figure 6.4k). This is consistent with the bulk absorption and PL data, where the PL intensity increases and red-shifts with increasing K content.

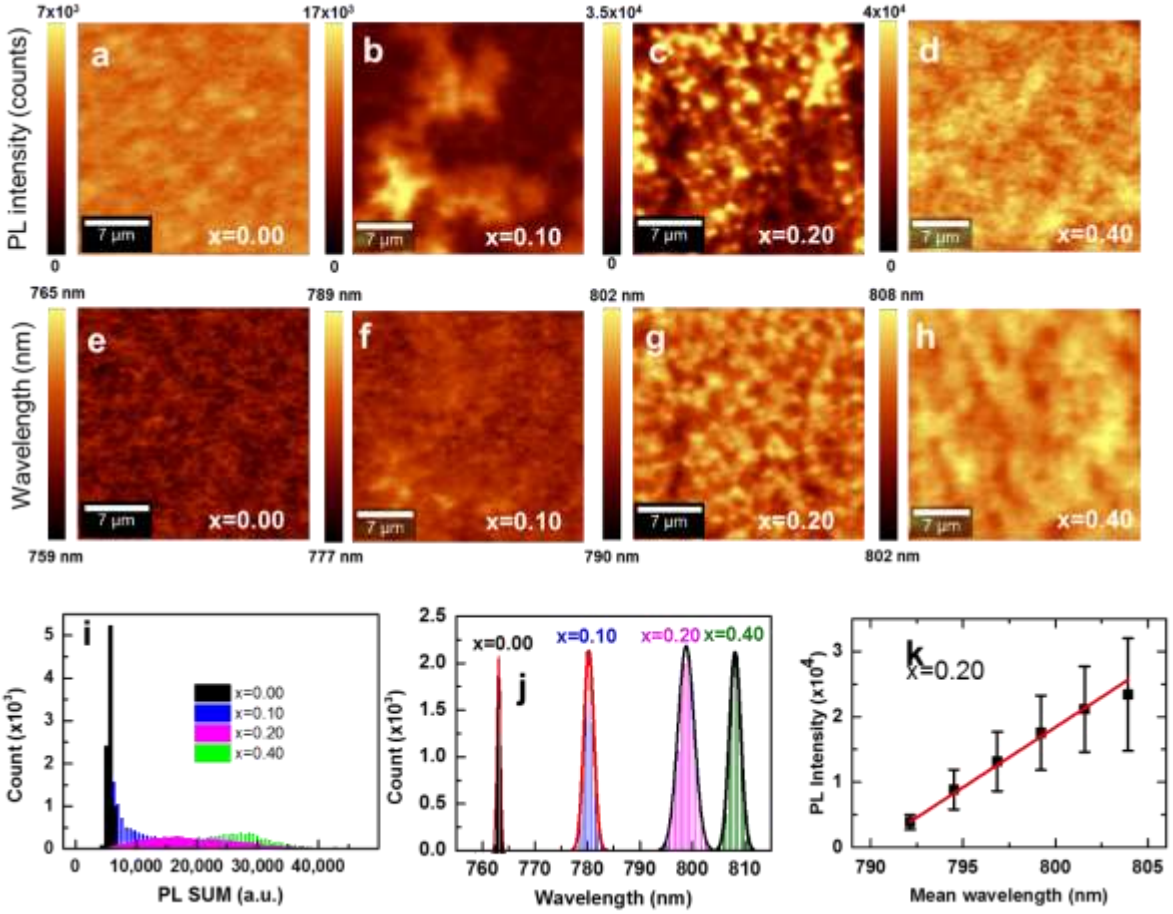

Figure 6.4. Confocal photoluminescence maps of passivated (Cs,FA,MA)Pb($I_{0.85}Br_{0.15}$)$_3$ films. Confocal PL intensity map with 405-nm excitation measured in ambient atmosphere for (Cs,FA,MA)Pb($I_{0.85}Br_{0.15}$)$_3$ perovskite thin films with (a) x = 0.0, (b) x = 0.10, (c) x = 0.20 and (d) x = 0.40. Centre-of-mass PL wavelength of the films for (e) x = 0.0, (f) x = 0.10, (g) x = 0.20 and (h) x = 0.40. Histograms of the (i) absolute PL intensities and (j) PL wavelength extracted from the respective maps for x = 0 – 0.40. (k) Correlation between the local PL intensity and mean wavelength for x = 0.20.

Time-resolved PL (TRPL) measurements (Figure 6.3b) show the removal of the fast non-radiative decay component with passivation, leading to radiative bimolecular recombination (Figure 6.5). For the unpassivated control film (x = 0), there is a significant initial non-radiative component (Figure 6.3b). With increasing passivation, this component is gradually removed with a peak 'lifetime' occurring at x = 0.1. In this regime, the recombination is still somewhat trap-limited for this excitation density (i.e. the carrier density does not exceed the trap density

to fill all traps). As the passivation increases further, the trap density is further reduced and now the density of excited carriers is above the trap density and recombination is radiative and bimolecular. In this regime, the recombination follows a power law and the lifetime is 'faster' with decreasing trap density (increasing passivation, i.e. x = 0.2 to 0.4). We note that the total area under the non-normalized curves in each case matches the increasing PLQE trend.

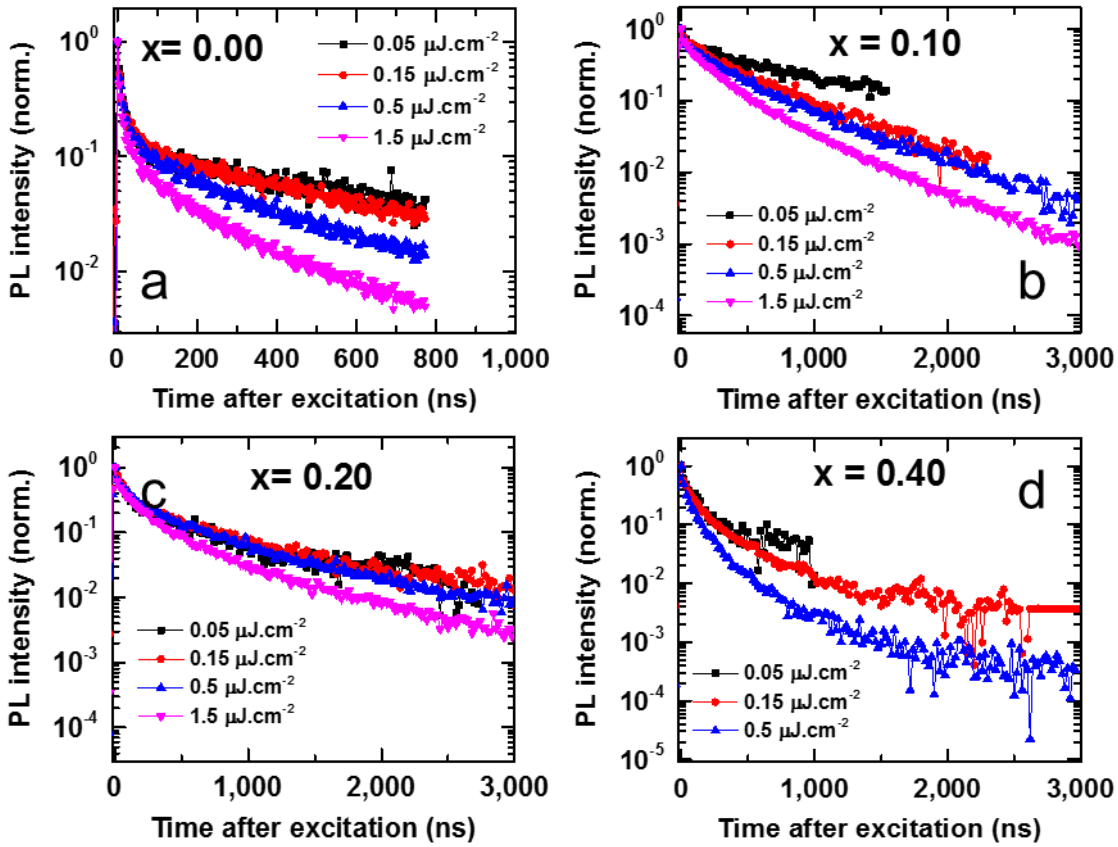

Figure 6.5. Time-resolved PL measurements of passivated $(Cs_{0.05}FA_{0.78}MA_{0.17})Pb(I_{1-y}Br_y)_3$ films. (a-d) Intensity dependent time-resolved PL decays of the $(Cs,MA,FA)Pb(I_{0.85}Br_{0.15})_3$ perovskite films with different fraction of potassium. The pulse fluences of the 407-nm excitation are quoted on the panels.

We use time-resolved microwave conductivity (TRMC) to assess the impact of the passivation on charge transport in the $(Cs,FA,MA)Pb(I_{0.85}Br_{0.15})_3$ perovskite thin films (Figure 6.6)[244,251]. In Figure 6.3c, we show the maximum photo-conductance (charge mobility) for each of the K contents. We find that the carrier mobility remains mostly constant at a large value of ~42

$cm^2V^{-1}s^{-1}$ for perovskite with $x = 0$ and $x = 0.1$, before dropping for higher K content to ~30 $cm^2V^{-1}s^{-1}$ ($x = 0.4$), which could be an effect of decreasing grain sizes for $x > 0.2$[252]. These results are consistent with lower trap densities[150] for the passivated samples, with the elimination of almost all non-radiative channels and retention of excellent charge transport up to $x = 0.1$.

In Figure 6.6, we show the ΔG as a function of time after pulsed excitation at 600 nm for different fractions of K acquired at different fluences. The TRMC signal depicts a fast rise, originating from the formation of mobile charges, followed by decays attributed to charge recombination or immobilization of charge carriers through the traps. In Figure 6.3c, we show that at least up to $x = 0.1$, the charge transport remains unperturbed with addition of K. That is, in view of the low electric field strength of the microwaves (100 V/cm), the charges are not effectively displaced by this field but instead the charges are perturbed in their diffusional motion. As a result, the distance R crossed by the charges is limited by the charge carrier diffusion coefficient and half the oscillation period ν (8.5 GHz), which amounts to:

$$R = \sqrt{\mu(k_B T/e)\frac{1}{2}\upsilon^{-1}} = \sqrt{42 \times 0.0259 \times 0.5 \times (8.5 \times 10^9)^{-1}} = 8.0 \times 10^{-6}\ \text{cm} = 80\ \text{nm} \qquad (6\text{-}1)$$

As shown in Figure 6.1, the grain sizes are ~ 200-400 nm and independent of the K concentration up to $x = 0.1$. Thus, for $x < 0.1$, the grains are larger than the probing length (80 nm) of the measurement and the TRMC mobility as probed will not be affected by their size. However, smaller grain sizes are observed for $x > 0.2$, which is most likely the reason for the lower mobilities at higher x values[252].

Furthermore, we show the resulting half lifetimes $\tau_{1/2}$ (time taken to decay half of the initial value) for the different samples in Figure 6.6f across a range of excitation fluences. At low fluence, one of the carriers is trapped, leading to a long-lived signal from the untrapped carrier, which recombines following monomolecular kinetics[105,150]. At higher fluence in which the traps are filled, the recombination is bimolecular. We find that charge-carrier recombination is substantially slower for the $x = 0.1$ composition compared to the $x = 0$ reference, with the low-fluence monomolecular lifetime increasing from 1 μs ($x = 0$) to 1.5 μs ($x = 0.1$).

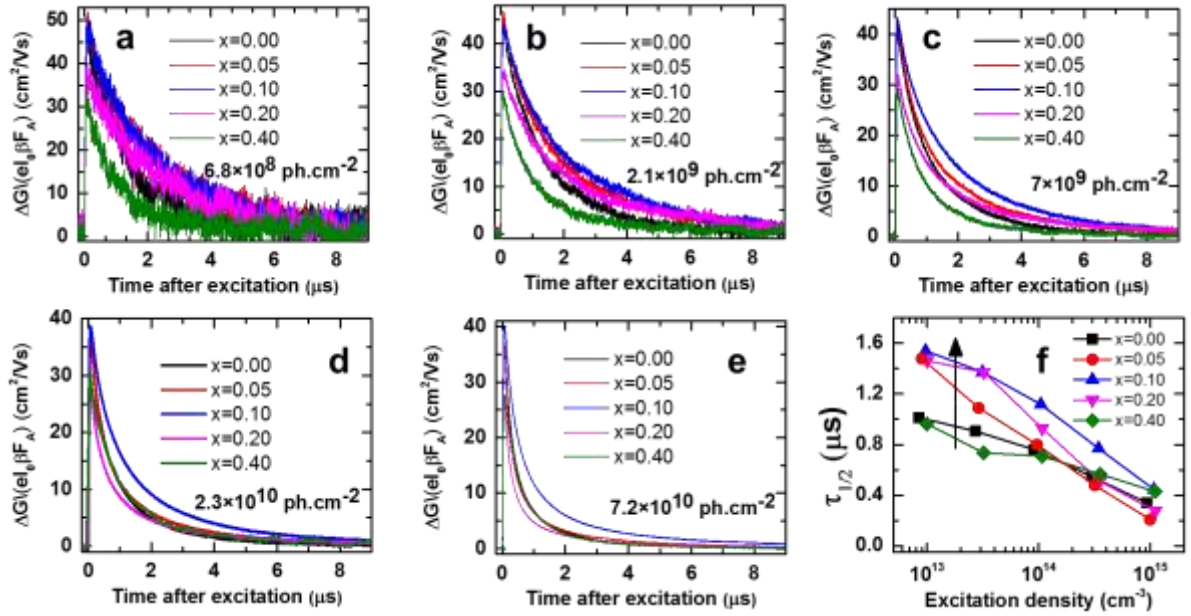

Figure 6.6. Time-resolved microwave conductivity measurements on passivated (Cs,FA,MA)Pb($I_{0.85}Br_{0.15}$)$_3$ films. (a-e) Time-resolved microwave conductivity measurements for (Cs,FA,MA)Pb($I_{0.85}Br_{0.15}$)$_3$ perovskite films with different fractions of K (x = 0 – 0.4) showing the change in photoconductance after pulsed excitation at 600 nm, with excitation densities (photons.cm^{-2}) as quoted on the panels. (f) Half lifetime extracted from the decays, with the excitation density quoted after accounting for the absorbed fraction and film thickness of each sample.

6.3 Photo-stability of potassium passivated perovskite

In Figure 6.7a, we show the PLQE from (Cs,FA,MA)Pb($I_{0.85}Br_{0.15}$)$_3$ thin films as a function of time under continuous illumination with intensity equivalent to 1-sun. We find a substantial but slow transient rise for the reference film (x = 0) associated with photo-induced halide migration[253]. In contrast, the high values of PLQE for the passivated films are stable under continuous illumination, suggesting that the photo-induced migration processes are substantially inhibited. To further investigate the latter claim, we add KI to precursor solutions with higher fractions of Br, which typically show substantial PL shifts due to photo-induced halide segregation and subsequent emission from low-bandgap iodide-rich components[243]. We show that the PL spectral output of passivated films (Cs,FA,MA)Pb($I_{0.4}Br_{0.6}$)$_3$ is remarkably stable at the optimal bandgap for perovskite/silicon tandems (1.75 eV)[240] under 1-sun

illumination (Figure 6.7c). In contrast, the sample without passivation shows substantial red shifts and bandgap changes over time (Figure 6.7b). In Figure 6.7d, we show that this photo-stability is also seen across bromide fractions covering the range of idealised wide bandgaps for perovskite-perovskite tandems (1.7-1.9 eV)[240], albeit with slightly reduced stability at the highest bromide fractions (Figure 6.8). We also find that the critical bandgaps for tandems can even be stabilised at low passivation levels (x = 0.1, Figure 6.7d). This is the first report showing such exceptional stability in mixed halide compositions across a wide range of bandgaps under solar illumination in ambient conditions[241].

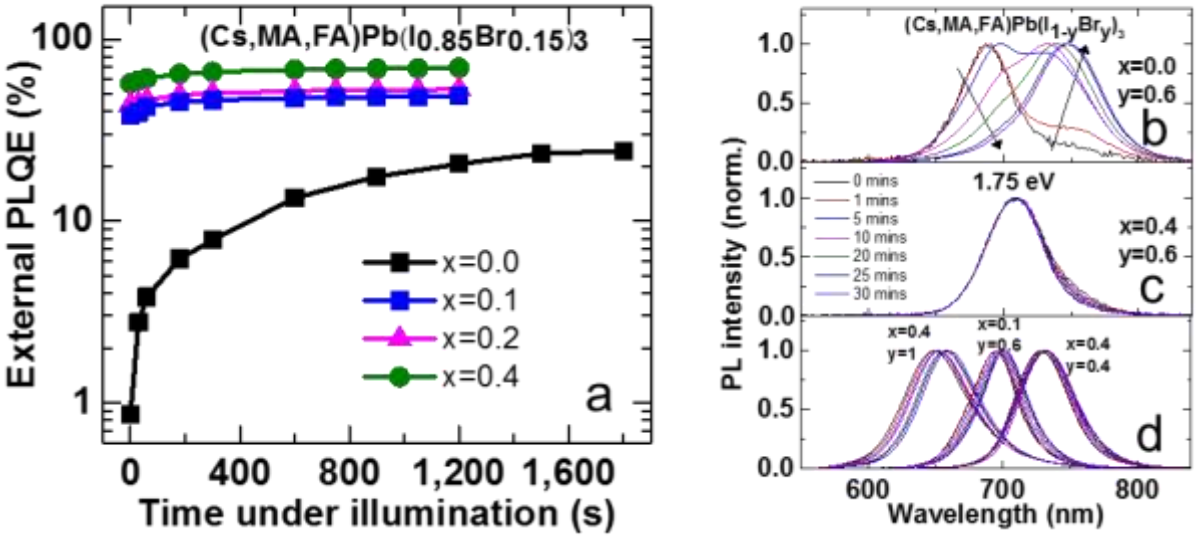

Figure 6.7. Stabilised PLQE and inhibition of photo-induced ion migration. (a) PLQE for (Cs,FA,MA)Pb($I_{0.85}Br_{0.15}$)$_3$ films illuminated over time with a 532-nm laser at an excitation intensity equivalent to ~1 sun (~60 mW.cm^{-2}) in ambient atmosphere. PL from (Cs,FA,MA)Pb($I_{1-y}Br_y$)$_3$ with y = 0.6 (b) without passivation (x = 0) compared to the (c) passivated sample (x = 0.4), illuminated continuously in ambient conditions with the same conditions as (a). (d) The PL from the passivated (x = 0.4) compositions with y = 0.4, x = 0.4 (peak at 1.70 eV), y = 0.6, x = 0.1 (1.78 eV) and y = 1, x = 0.4 (1.89 eV), measured over time under the same conditions.

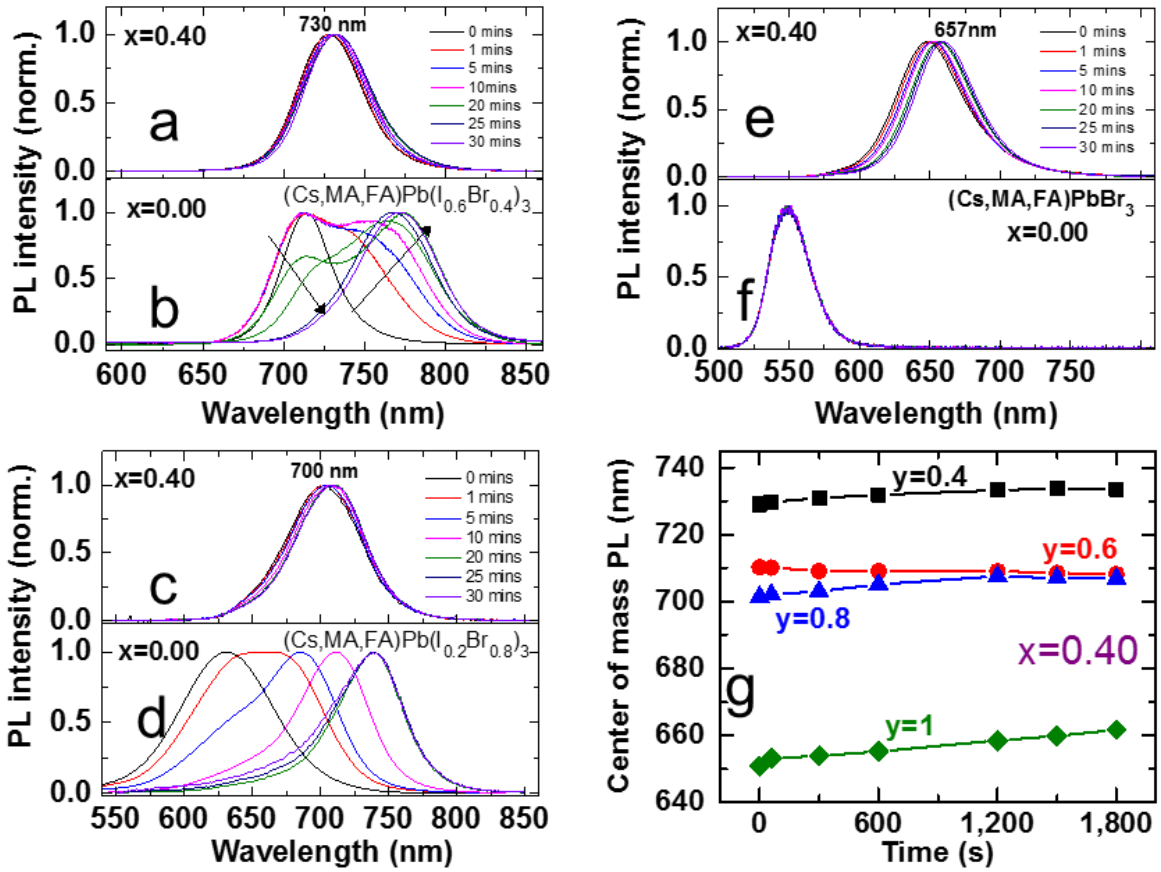

Figure 6.8. Photo-stabzility of passivated $(Cs_{0.05}FA_{0.78}MA_{0.17})Pb(I_{1-y}Br_y)_3$ films. PL from $(Cs_{0.05}FA_{0.78}MA_{0.17})Pb(I_{1-y}Br_y)_3$ films with (a,b) y = 0.4 passivated (x = 0.4, e) and unpassivated (x = 0, f), (c,d) y = 0.8 passivated (x = 0.4, g) and unpassivated (x = 0, h), (e,f) y = 1 passivated (x = 0.4, i) and unpassivated (x = 0, j). The samples were illuminated and the PL acquired continuously with a 532-nm laser at an excitation intensity equivalent to ~1 sun (~60 $mW.cm^{-2}$) in ambient atmosphere. (g) Center of mass for the PL wavelength of the passivated perovskite films (x = 0.4).

6.4 Chemical and structural characterisation of potassium passivated perovskite

We now investigate the chemical composition of the $(Cs,FA,MA)Pb(I_{0.4}Br_{0.6})_3$ perovskite thin films, performing scanning transmission electron microscopy-energy dispersive X-ray spectroscopy (STEM-EDX). In Figure 6.9a, we show a cross sectional view of a lamella of the

x = 0.2 composition. From the STEM-EDX elemental analysis, we observe a potassium-rich phase at the grain boundaries of the perovskite as well as the interface with the substrate (Figure 6.10).

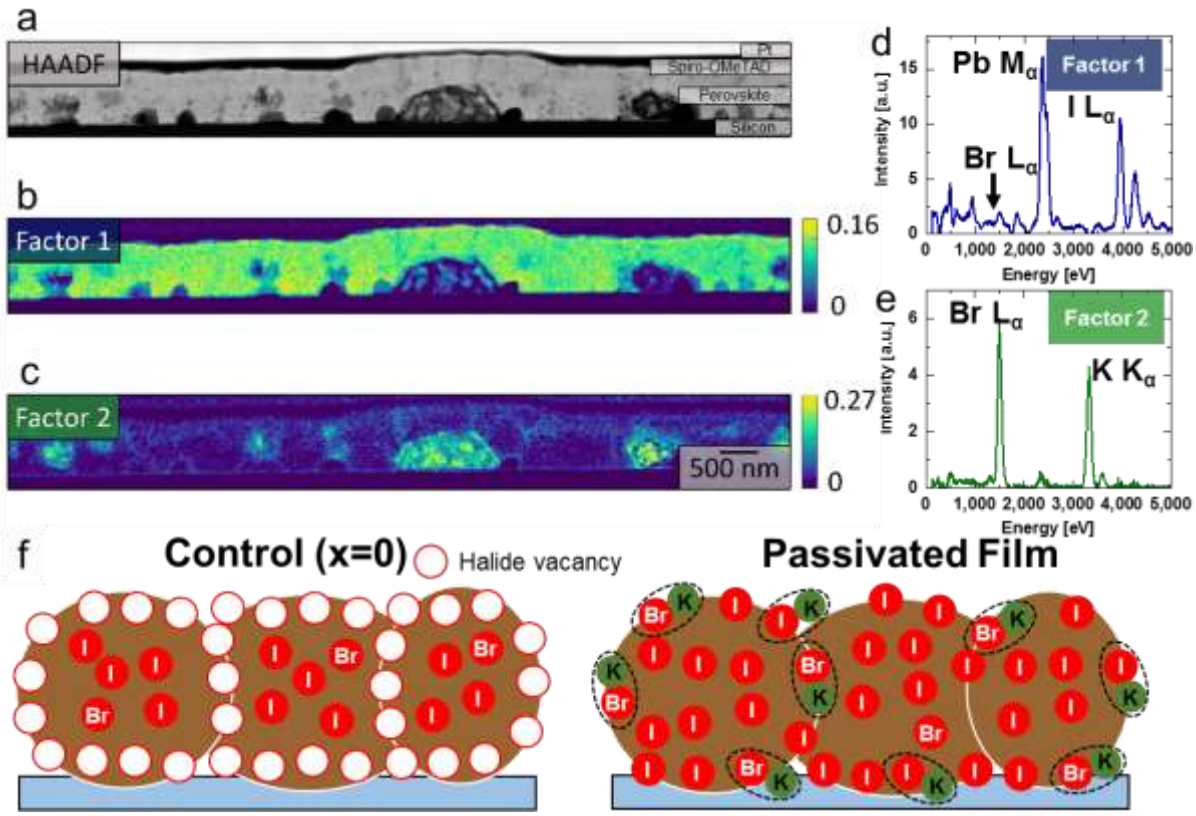

Figure 6.9. Cross-section chemical characterisation. (a) HAADF STEM cross sectional image of a (Cs,FA,MA)Pb($I_{0.85}Br_{0.15}$)$_3$ passivated perovskite thin film (x = 0.20). NMF decomposition results in (b) factor 1 associated to the perovskite layer and in (c) factor 2 indicating the presence of a K and Br rich phase. The profiles for (d) factor 1 and (e) factor 2. (f) Schematic of a film cross-section showing halide vacancy management with excess halide, where the surplus halide is immobilised through complexing with potassium into benign compounds at the grain boundaries and surfaces.

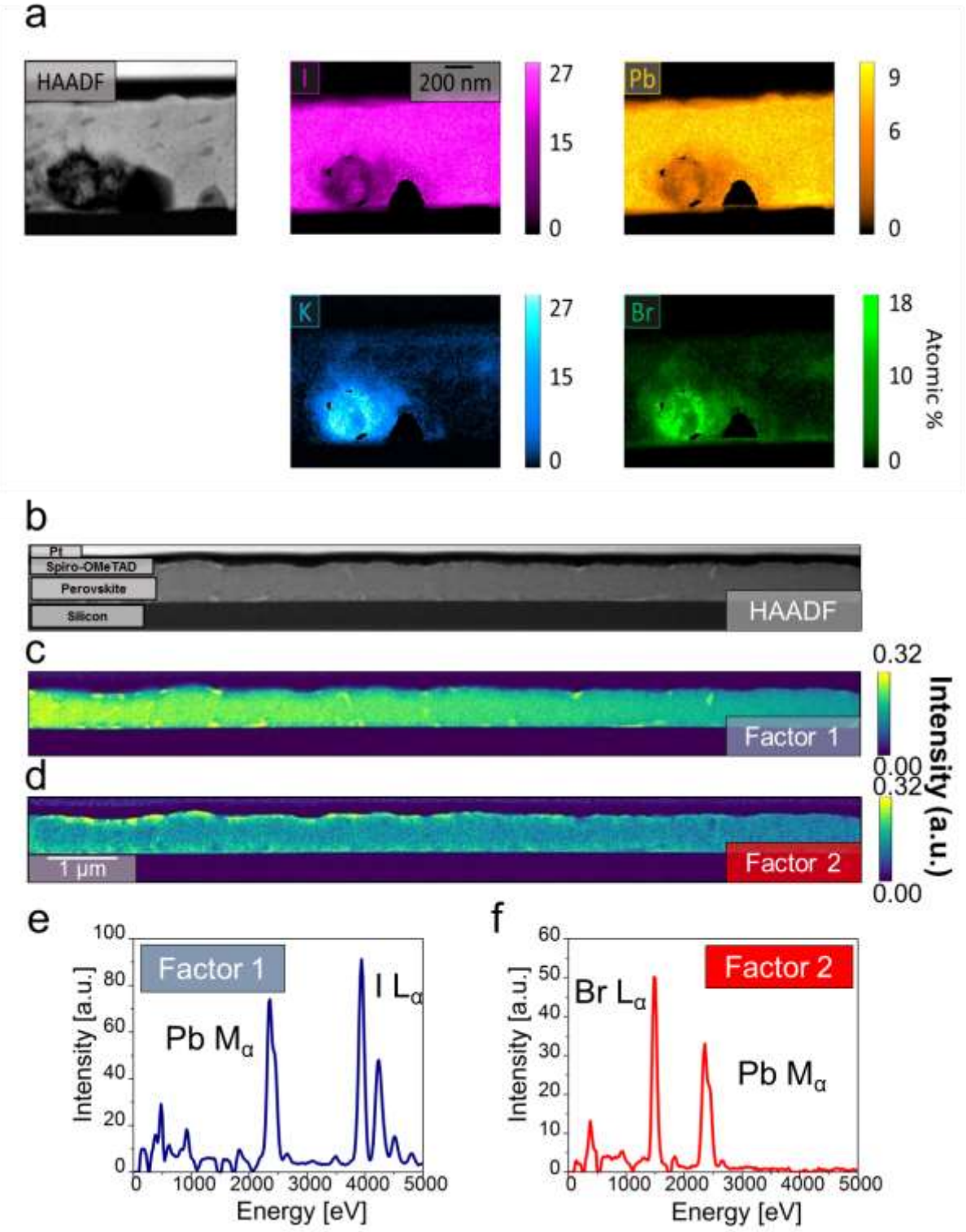

Figure 6.10. STEM-EDX chemical maps of the passivated and unpassivated (Cs,FA,MA)Pb($I_{0.85}Br_{0.15}$)$_3$ samples. The HAADF image and corresponding STEM/EDX quantitative maps for iodine, lead, potassium and bromine in a (Cs,FA,MA)Pb($I_{0.85}Br_{0.15}$)$_3$

perovskite specimen with x = 0.20 fraction of potassium. (b) HAADF STEM cross sectional image of an unpassivated (Cs,FA,MA)Pb($I_{0.85}Br_{0.15}$)$_3$ perovskite thin film (x = 0). NMF decomposition results in (c) factor 1 associated to the perovskite layer and in (d) factor 2 indicating the presence of a Pb and Br rich phase. The profiles for (e) factor 1 and (f) factor 2.

Analysis of the dataset using a Non-negative Matrix Factorisation (NMF) algorithm[237] highlights the presence of two compositional phases present in the specimen, reported as Factor 1 and Factor 2 in Figure 6.9b-c. Factor 1 shows characteristic EDX features, including Br L_α, Pb M_α, I L_α lines (Figure 6.9d), which can be associated with the perovskite phase, while Factor 2 is rich in bromine and potassium (Figure 6.9e) and interestingly, particularly prominent at the grain boundaries and top and bottom surfaces of the perovskite film. This is likely related to a new crystalline phase observed in Grazing-Incidence Wide-Angle X-Ray Scattering (GIWAXS) experiments (Figure 6.11).

As shown in Figure 6.11a (x = 0) and d (x = 0.2), the GIWAXS diffraction patterns collected at an incident angle of 0.3° show the main perovskite diffraction ring at q=1 Å^{-1}. A PbI_2 peak can be detected at q=0.9 Å^{-1} for the reference film, which originates from a small fraction of excess lead iodide in the reference precursor solution. In Figure 6.11f and g, we plot the line profiles azimuthally-integrated over the entire image for perovskite films with x = 0 – 0.4. The PbI_2 peak diminishes with higher potassium content and disappears at x = 0.2. Furthermore, we observe a new diffraction peak at q = 0.7 Å^{-1} that appears for $x \geq 0.10$ and can be assigned to a non-perovskite K-rich crystalline phase which grows with increasing K. We also observe the growth of new peaks with increasing K content in laboratory XRD results (highlighted by * in Figure 6.2d). We cannot currently unambiguously assign these peaks, for example to KBr or KI, which points to this phase (or phases) having more complicated chemical compositions (such as KBr_xI_{1-x}, K_2PbI_4 or K_2PbBr_4 [254]) and crystallinities. However, given the observations in the STEM-EDX experiments (Figure 6.9), we expect that at least one of the phases present is rich in K and Br and is likely to be the halide-sequestering species proposed in our model. Identifying the precise composition of these sequestering species should be the subject of exciting future work in the community.

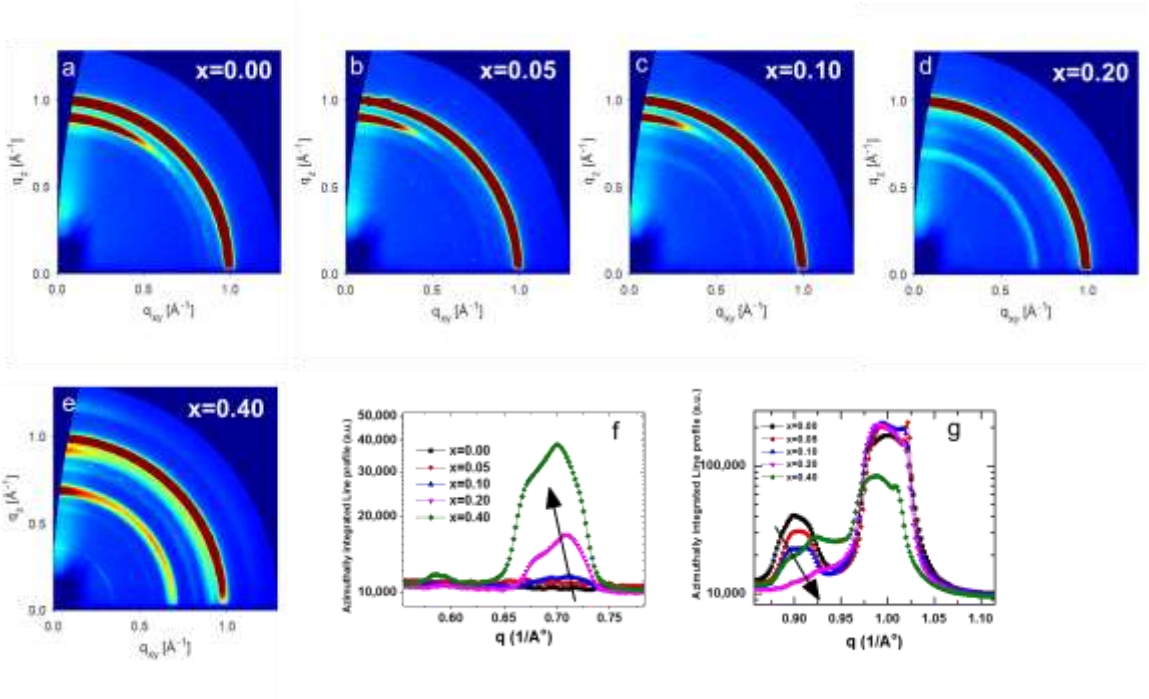

Figure 6.11. GIWAXS measurements of passivated (Cs,FA,MA)Pb($I_{0.85}Br_{0.15}$)$_3$ films. The diffraction patterns of thin (Cs,FA,MA)Pb($I_{0.85}Br_{0.15}$)$_3$ films collected at low angle using GIWAXS for (a) x = 0.00, (b) x = 0.05, (c) x = 0.10, (d) x = 0.20 and (e) x = 0.40. The high-resolution line profiles azimuthally integrated over the entire GIWAX profile for different fraction of potassium at (f) $0.5 \leq q \leq 0.8$ and (g) $0.8 \leq q \leq 1.1$.

These results are also consistent with Hard X-ray Photoelectron Spectroscopy (HAXPES) measurements, which reveal a decrease in K moving from the film surface into the bulk (Figure 6.12). These results collectively indicate the formation of potassium halide (particularly Br-rich) passivation layers decorating the surfaces, with the potassium not incorporating into the perovskite lattice. We note that this is in contrast to other works reporting the addition of small monovalent cation to the perovskite including Na, Rb or K, which propose incorporation of these components into the lattice[58,194,254–256], though a recent report shows that Rb does not incorporate and suggests the same for K[257].

The overview spectra of the perovskite thin films shows all the core levels peaks corresponding to the elements forming the perovskite material, including Cs (Figure 6.12a, b and c). The high-resolution spectra of the core level peaks further confirms the quality of the perovskite films as there is only a single Pb 4f component at 138.6 eV without any metallic lead feature[234] (Figure 6.12). In Figure 6.12d, we summarise a quantitative analysis of the potassium content in

perovskite films with $x = 0 – 0.2$ at different photon energies of 758, 2200 and 6600 eV, which corresponds to moving from probing the surface (~2-4 nm) to probing further into the bulk (~20 nm). We observe that the concentration of K decreases when moving from the surface into the bulk for each of the K compositions. Interestingly, we note that the Cs content rises moving into the bulk concomitant with the decrease in K, suggesting that the K pushes the Cs further into the bulk (Figure 6.12d). Furthermore, the I/Pb ratio increases at higher K content (Figure 6.12e), particularly at the surface, consistent with the addition of excess I from the KI source and in agreement with a previous report showing a higher concentration of iodide at the surface[234]. Finally, the Br/I ratio decreases at higher K content particularly deeper in the film (probed with the higher photon energies), consistent with the K more selectively drawing out the Br from the lattice (Figure 6.12f). These results suggest that K is predominantly at the surfaces and the addition of KI also leads to excess halides on the surfaces with a more selective interaction with bromides.

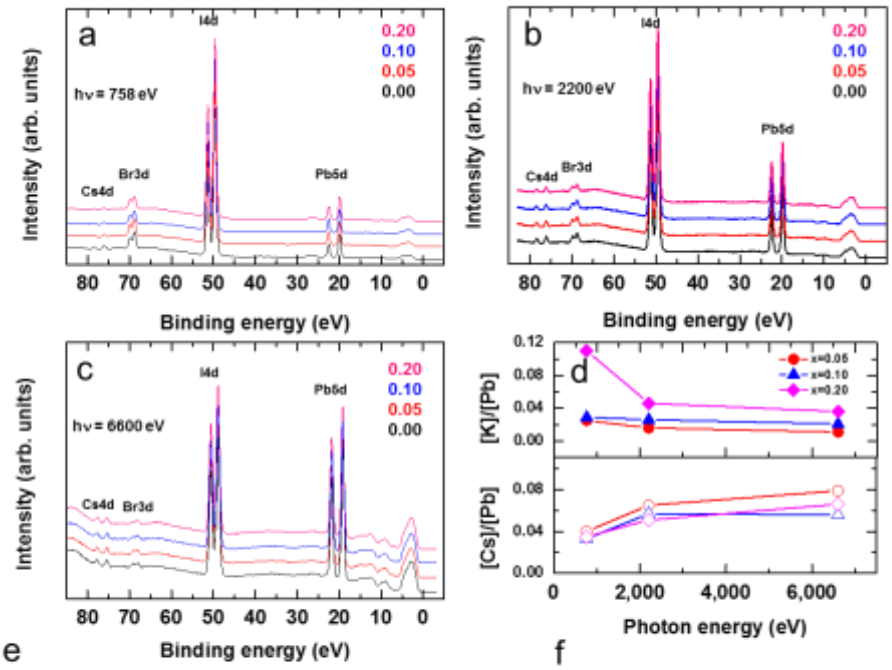

I/Pb	x=0.00	x=0.05	x=0.10	x=0.20
Calculated	2.545	2.604	2.670	2.825
758 eV	3.05	3.41	3.64	3.87
2200 eV	2.71	2.78	2.85	3.14
6600 eV	2.35	2.41	2.47	2.55

Br/I	x=0.00	x=0.05	x=0.10	x=0.20
Calculated	0.176	0.172	0.167	0.158
758 eV	0.095	0.098	0.067	0.067
2200 eV	0.114	0.111	0.102	0.073
6600 eV	0.132	0.129	0.101	0.086

Figure 6.12. HAXPES spectra for passivated (Cs,FA,MA)Pb($I_{0.85}Br_{0.15}$)$_3$ perovskite thin films. HAXPES spectra for (Cs,FA,MA)Pb($I_{0.85}Br_{0.15}$)$_3$ perovskite thin films ($0 \leq x \leq 20$)

between 85-0 eV binding energy range recorded with a photon energy of (a) 758 eV, (b) 2200 eV and (c) 6600 eV. (d) Intensity ratio between core levels ([Cs]/[Pb] and [K]/[Pb]) calculated from the experimental results as a function of photon energy (measurements at 758, 2200 and 6600 eV). Intensity ratios between different core levels calculated from experimental results: (e) I/Pb and (f) Br/I of the perovskite thin films with different fraction of potassium ($0.0 \leq x \leq 0.20$). It is notable that we used Pb 5d, K 2p, Cs 4d, I 4d and Br 3d core levels for all different energies with the exception of K 1s, which is used for 6600 eV.

In Figure 6.9f, we summarise our interpretation of the results. Here, we are introducing excess iodide through the KI source into the perovskite precursor solutions, which compensates for any halide vacancies. The excess halides fill these vacancies, thereby passivating the non-radiative recombination pathways, leading to exceptionally high luminescence efficiencies. The excess halides are immobilised in the form of benign potassium-rich halide-sequestering species at the grain boundaries and surfaces, thereby inhibiting halide migration and suppressing any additional non-radiative decay arising from interstitial halides. At K content beyond $x = 0.1$, these non-perovskite species are too large and perturb charge transport. This suggests there is an optimal K content at $x \sim 0.1$, which is a compromise between high radiative efficiency and retention of high charge carrier mobility. Finally, we propose that potassium selectively depletes Br from the perovskite crystal structure, which is consistent with an increased lattice parameter, red-shifting band-edge, and decreasing Br/I ratio in the bulk with K addition (Figure 6.2 and Figure 6.12). We note that these observations and enhanced properties are not achieved in the absence of Br (Figure 6.2). The addition of small fractions of bromide to the perovskite precursor solutions has been shown to improve perovskite film formation[188]. However, bromide-rich perovskites typically have increased trap states and inferior charge carrier mobility compared to their iodide-based counterparts[151]. Here we exploit the beneficial properties of bromide in the grain formation process while suppressing the formation of Br-induced defect states in the bulk of the crystal.

6.5 Impact of potassium passivation on the luminescence properties of the perovskite when interfaced with solar cell device contacts

At open-circuit in a solar cell, external luminescence should be maximised[247], and we must minimise any additional non-radiative losses upon introduction of device electrodes. In Figure 6.13a and d, we show the time-resolved PL decays and PLQE, respectively, for the (Cs,FA,MA)Pb($I_{0.85}Br_{0.15}$)$_3$ perovskite with and without potassium passivation when deposited on a standard n-type mesoporous TiO_2 electron-accepting contact (see Figure 6.14 for other excitation intensities).

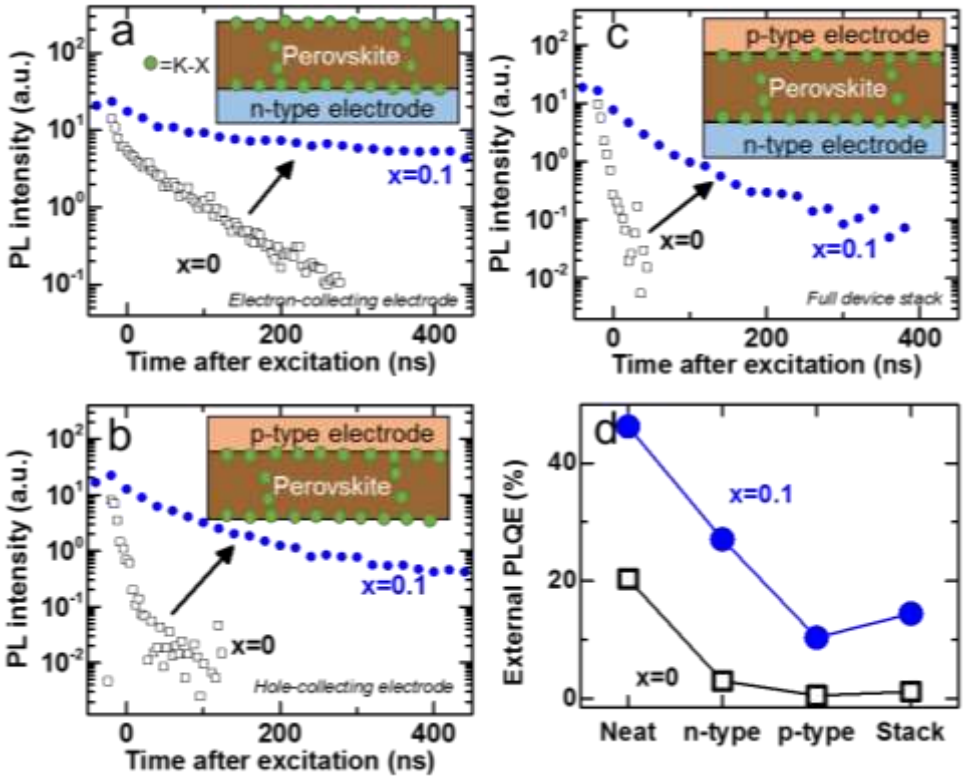

Figure 6.13. Luminescence properties of the perovskite when interfaced with solar cell device contacts. Time-resolved PL decays of encapsulated (Cs,FA,MA)Pb($I_{0.85}Br_{0.15}$)$_3$ films (x = 0 and x = 0.1) with excitation at 407 nm and pulse fluence of 0.05 µJ.cm^{-2} (1.5×10^{15} cm^{-3} , equivalent to ~5 sun) when the perovskite is interfaced with (a) an n-type electron-collecting electrode (compact-TiO_2/thin-mesoporous TiO_2), (b) a p-type hole-collecting electrode (Spiro-OMeTAD), and (c) both electrodes in a full device stack. (d) External PLQE measurements of the perovskite in each configuration measured under illumination with a 532-nm laser at an excitation intensity equivalent to ~1 sun (~60 mW.cm^{-2}).

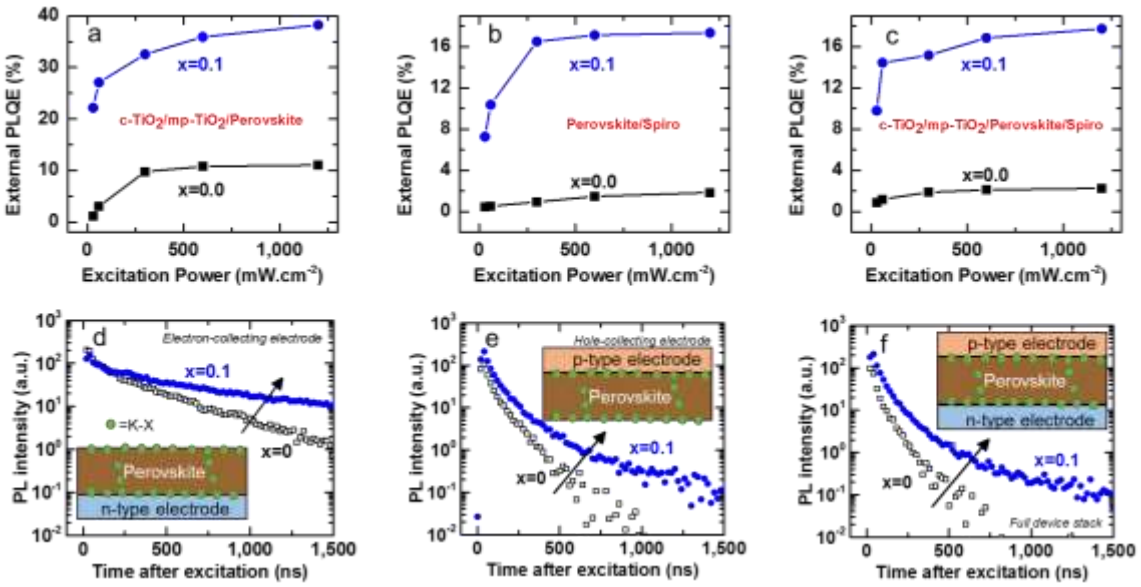

Figure 6.14. Excitation-dependent PL quantum efficiency and time-resolved PL measurements of (Cs,FA,MA)Pb($I_{0.85}Br_{0.15}$)$_3$ device stacks. PLQE of reference (x=0) and passivated (x=0.1) (Cs,FA,MA)Pb($I_{0.85}Br_{0.15}$)$_3$ perovskite thin films with (a) n-type contact, (b) p-type contract and (c) both contacts, each measured under illumination with a 532-nm laser at different excitation intensity. Time-resolved PL decays of encapsulated (Cs,FA,MA)Pb($I_{0.85}Br_{0.15}$)$_3$ films (x = 0 and x = 0.1) with excitation at 407 nm and pulse fluence of 0.17 µJ.cm^{-2} (5×10^{15} cm^{-3}, equivalent to ~15 sun) when the perovskite is interfaced with (d) an n-type electron-collecting electrode (compact-TiO_2/thin-mesoporous TiO_2), (e) a p-type hole-collecting electrode (Spiro-OMeTAD), and (f) both electrodes in a full device stack.

We find that charge-carrier recombination in the presence of the electrode is slower and more radiative (higher integrated TRPL intensity) in the presence of potassium, with the PLQE dropping by a factor of only 1.7 (to 27.1%) compared to a drop of factor 6.7 (to 3.0%) without passivation. In Figure 6.13b, we show the time-resolved PL decays for the perovskite containing a top layer of a standard p-type Spiro-OMeTAD hole-accepting contact. We again find that the passivation leads to slower charge carrier recombination and a less significant drop in PLQE upon introduction of the electrode (Figure 6.13d), with a drop of factor 4.5 to 10.4% compared to a drop by factor 38 to 0.5% without passivation. Finally, we show the time-resolved PL decays for the full device stack (i.e. both electrodes) in Figure 6.13c, clearly showing the slower recombination and vastly reduced PLQE drop with the potassium sample. The external PLQE of the full stack is retained at 14.5% with the passivating interlayers (a

reduction of factor 3.2 upon addition of the electrodes), an order of magnitude higher than the 1.2% of the control stack (reduction of factor 17). These results show that the potassium interlayers not only improve the optoelectronic properties of the neat material, but also lead to vastly improved interfaces with device electrodes.

6.6 Photovoltaic characterisation of perovskite solar cells with potassium passivation

To validate our findings, we construct full solar cells using the device architecture fluorinated-tin oxide (FTO) / compact-TiO_2 (~30 nm) / thin-mesoporous TiO_2 (~200 nm) / perovskite (~500 nm) / Spiro-OMeTAD (~150 nm) / Au (80 nm). In Figure 6.15a, we show the forward and reverse current-voltage (J-V) curves of champion devices containing the (Cs,FA,MA)Pb($I_{0.85}Br_{0.15}$)$_3$ absorbers with x = 0 and x = 0.1 under full simulated sunlight, with the extracted parameters given in Table 6.1 (see Figure 6.16 and Figure 6.17 and Table 6.2 for other K compositions, dark J-V curves, and device statistics).

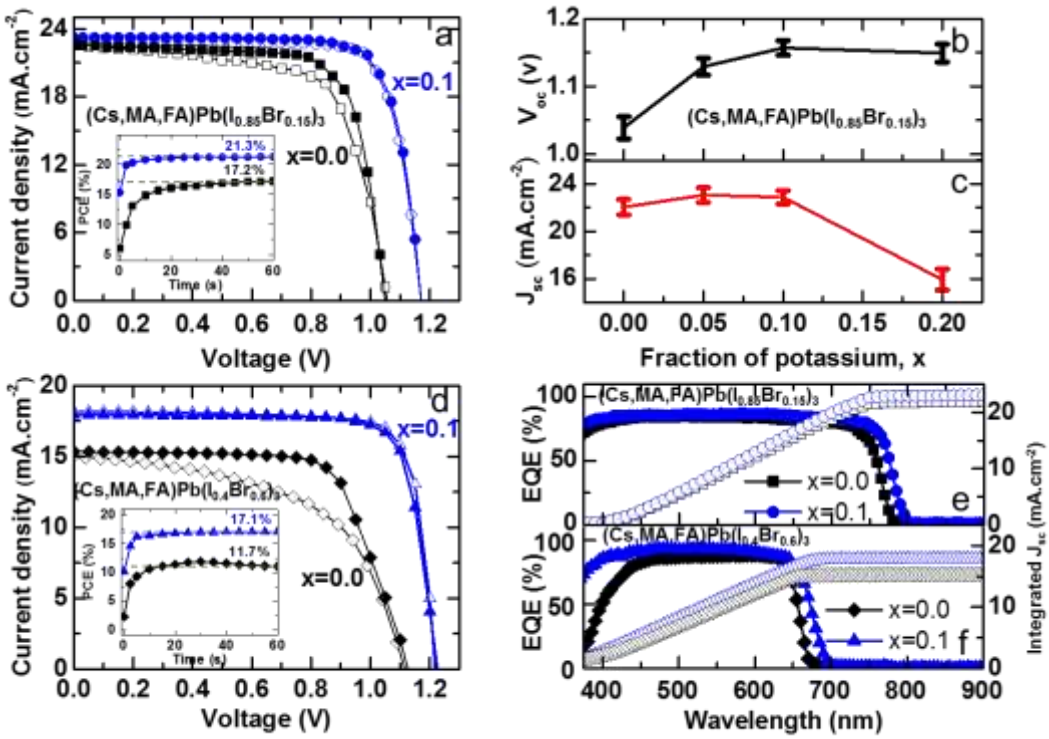

Figure 6.15. Enhanced solar cell power conversion efficiency. (a) Forward (open symbols) and reverse (closed symbols) J-V curves of champion solar cells with

$(Cs,MA,FA)Pb(I_{0.85}Br_{0.15})_3$ absorbers without (x = 0) and with (x = 0.1) passivation, measured under full simulated solar illumination conditions (AM1.5, 100 $mW.cm^{-2}$). Inset: Stabilised power output under the same conditions. (b) Open-circuit voltage (V_{oc}) and (c) short-circuit current (J_{SC}) as functions of potassium fraction x, with error bars representing the standard deviation across 10 devices for each composition. (d) J-V curves of champion solar cells with $(Cs,MA,FA)Pb(I_{0.4}Br_{0.6})_3$ absorbers without (x = 0) and with (x = 0.1) potassium passivation. External quantum efficiencies (EQE) and integrated short-circuit current for the (e) $(Cs,MA,FA)Pb(I_{0.85}Br_{0.15})_3$ and (f) $(Cs,MA,FA)Pb(I_{0.4}Br_{0.6})_3$ devices.

Table 6.1. Champion photovoltaic device parameters. The bandgaps are extracted from the EQE onsets, and the V_{oc} loss is the difference between the bandgap radiative limit V_{oc} and measured V_{oc}.

Potassium fraction, *x*	Bandgap [eV]	J_{sc} [mA.cm^{-2}]	V_{oc} [V]	Fill factor	PCE [%]	V_{oc} loss [V]
$(Cs,MA,FA)Pb(I_{0.85}Br_{0.15})_3$						
0.0	1.59	22.6	1.05	0.73	17.3	0.26
0.1	1.56	23.2	1.17	0.79	**21.5**	**0.11**
$(Cs,MA,FA)Pb(I_{0.4}Br_{0.6})_3$						
0.0	1.83	15.3	1.12	0.72	12.3	0.42
0.1	1.78	17.9	1.23	0.79	**17.5**	**0.27**

We find that the device efficiency increases from 17.3% (*x* = 0) to 21.5% (*x* = 0.1) with passivation, with the elimination of hysteresis in the latter case consistent with an inhibition of ion migration[239,253]. This is also consistent with a rapid rise to a stabilised power efficiency of 21.3%, compared to a slower rise to just 17.2% for the control (Figure 6.15a inset). We see an increase in open-circuit voltage (V_{oc}) with passivation from 1.05 V (*x* = 0) to 1.17 V (*x* = 0.1) (Figure 6.15c), with the calculated V_{oc} difference from the increase in PLQE of the device stacks from 1.2 to 14.5% (Figure 6.13d) matching within error the difference in the V_{oc} distributions from the device statistics. The V_{oc} loss from the radiative limit is only 0.11 V and is one of the lowest losses reported in a perovskite solar cell to date[58]. We also see an increase in the short-circuit current (J_{SC}) with K addition up to x = 0.1 (Figure 6.15c), consistent with the increased carrier mobility and lifetime[198]. The optimal device performance at x = 0.1 therefore validates the compromise between radiative efficiency and carrier mobility. We

conducted preliminary stability tests and found a negligible drop in shelf-life performance over a month, and that the devices retain over 80% of their initial performance after 300 hours of continued operation at maximum power (Figure 6.16e, f). We show device results for larger bandgap (Cs,FA,MA)Pb($I_{0.4}Br_{0.6}$)$_3$ absorbers (Figure 6.16d, f), attaining a PCE of 17.9% with minimal hysteresis for the x = 0.1 composition and stabilised power output of 17.1% (see Table 6.1 and Figure 6.17 for device statistics). This is one of the highest efficiencies to date for a large bandgap (1.78 eV) perovskite ideally suited for tandem applications[241].

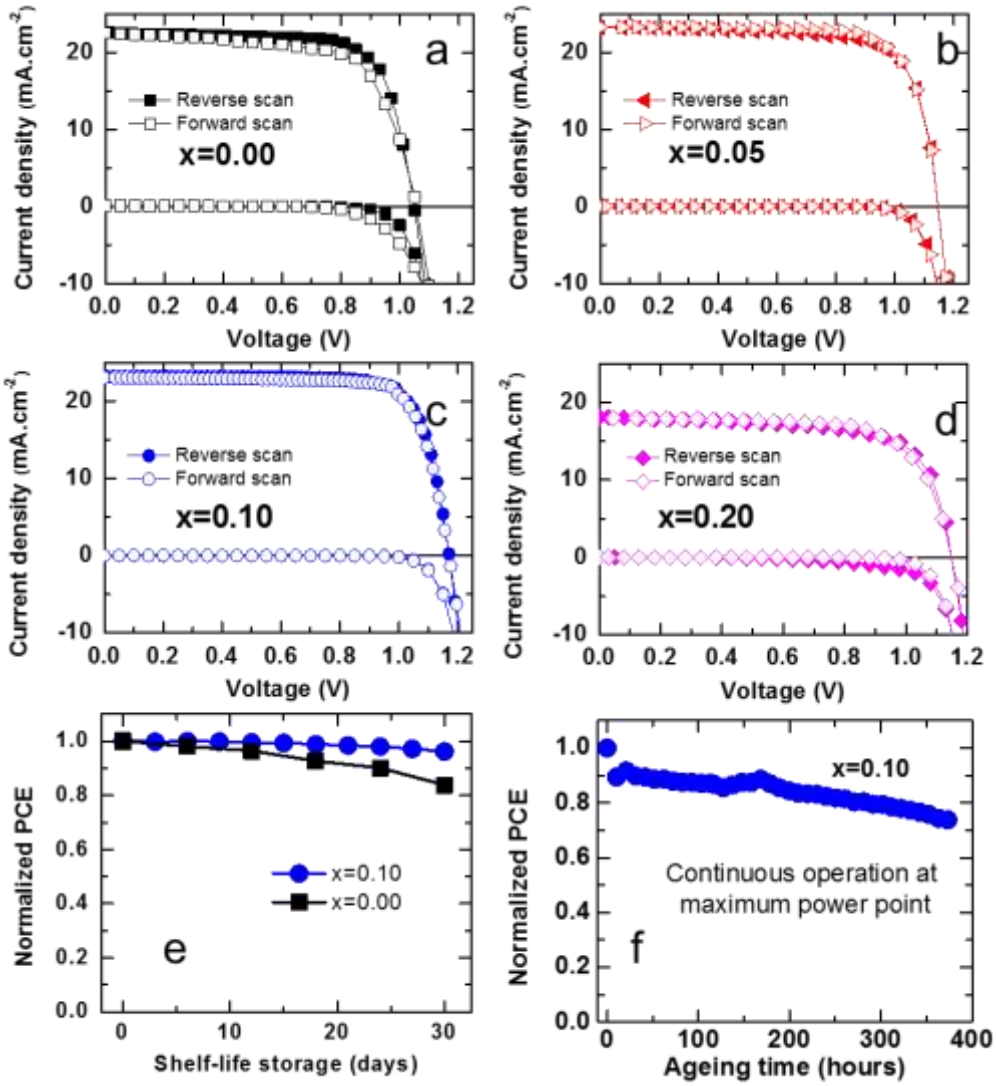

Figure 6.16. Current-voltage curves of passivated (Cs,FA,MA)Pb($I_{0.85}Br_{0.15}$)$_3$ devices and tabulated results for the (Cs,FA,MA)Pb($I_{0.85}Br_{0.15}$)$_3$ and (Cs,FA,MA)Pb($I_{0.4}Br_{0.6}$)$_3$ champion devices. Forward (open symbols) and reverse (closed symbols) J-V curves of champion solar cells with (Cs,FA,MA)Pb($I_{0.85}Br_{0.15}$)$_3$ absorbers with (a) x = 0.00, (b) x = 0.05,

(c) x = 0.10 and (d) x = 0.20 measured under full simulated solar illumination conditions (AM1.5, 100 $mW.cm^{-2}$) with a scan rate of 15 mVs^{-1}. The corresponding dark J-V curves are also shown. Preliminary stability tests of (Cs,FA,MA)$Pb(I_{0.85}Br_{0.15})_3$ perovskite devices: (e) Shelf-life of devices for x = 0.00 and x = 0.10 stored in a nitrogen glovebox over a month and tested regularly under full AM1.5 simulated sunlight. (f) Stability of a device with x = 0.10 aged at 0.8 V under continuous UV-filtered simulated sunlight in nitrogen atmosphere >350 hours.

Table 6.2. Device parameters for the passivated (Cs,FA,MA)$Pb(I_{0.85}Br_{0.15})_3$ (upper) and (Cs,FA,MA)$Pb(I_{0.4}Br_{0.6})_3$ (lower) perovskite solar cells measured under full simulated solar illumination conditions (AM1.5, 100 $mW.cm^{-2}$).

x		J_{sc} [$mA.cm^{-2}$]	V_{oc} [V]	FF	PCE [%]
(Cs,FA,MA)$Pb(I_{0.85}Br_{0.15})_3$					
0.00	Reverse	22.6	1.05	0.73	17.3
	Forward	22.5	1.05	0.69	16.3
0.05	Reverse	23.3	1.14	0.75	20.1
	Forward	23.2	1.14	0.74	19.7
0.10	Reverse	23.2	1.17	0.79	21.5
	Forward	23.1	1.17	0.79	21.3
0.20	Reverse	18.1	1.15	0.70	14.6
	Forward	17.9	1.15	0.70	14.4
(Cs,FA,MA)$Pb(I_{0.4}Br_{0.6})_3$					
0.00	Reverse	15.3	1.12	0.72	12.3
	Forward	15.1	1.13	0.55	9.4
0.10	Reverse	17.9	1.23	0.79	17.5
	Forward	18.1	1.22	0.79	17.8

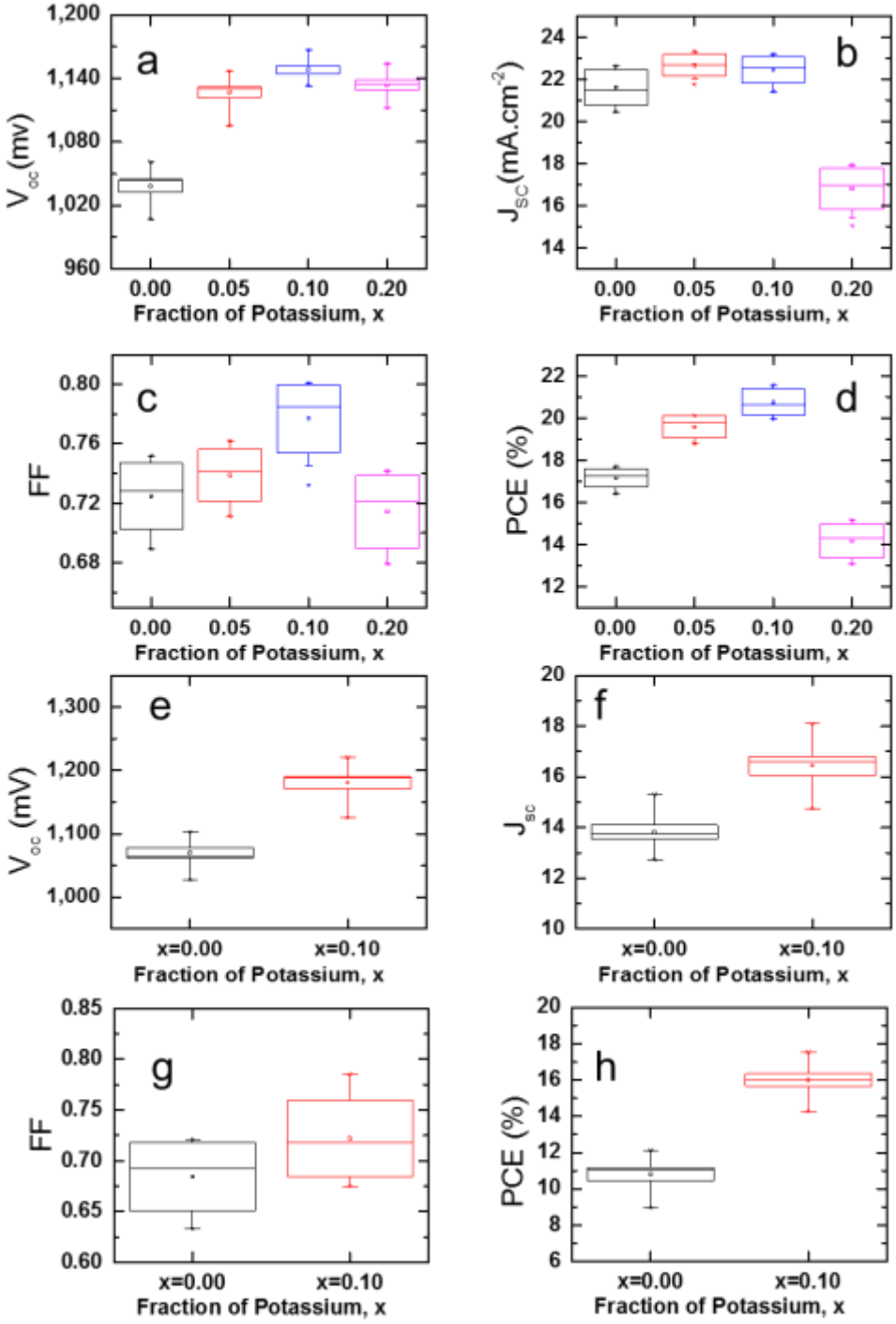

Figure 6.17. Device statistics. Box and whisker plots to summarise the statistics of photovoltaic parameters of (a-d) 10 devices with passivated (Cs,FA,MA)Pb($I_{0.85}Br_{0.15}$)$_3$ solar cells and (e-h) 8 devices of passivated (Cs,FA,MA)Pb($I_{0.4}Br_{0.6}$)$_3$ solar cells, each measured under full simulated solar illumination conditions (AM1.5, 100 mW.cm^{-2}) and scanned at a rate of 15 mV/s. The boxes represent the interquartile range, with the median represented by the line dividing the boxes, and the whiskers are determined by the 5th and 95th percentiles. The

mean is given by the open square symbols, and the starred symbols represent the maximum and minimum values.

6.7 Conclusions

These results are particularly remarkable for two key reasons. First, the perovskite films and interfaces are surprisingly tolerant to passivating additives. Here, we have introduced additives at high enough loading to passivate surfaces and stabilise luminescence across a range of bandgaps without compromising charge transport or extraction. This tolerance is in contrast to conventional semiconductors such as GaAs, which require more complicated passivation approaches such as controlled growth on lattice-matched substrates[258]. Second, these results directly show the importance of obtaining high, stable external luminescence yields in full device stacks containing luminescent absorbers capable of recycling photons[247,259]. The internal luminescence yields approaching 100%, along with small loss in external luminescence yield in the full device stack, shows that perovskites can sustain the necessary photon gas to achieve voltage losses low enough to rival GaAs. We note that the perovskite compositions and passivating interlayers shown in this work lead to far greater luminescence and broader stability enhancements than reported previously for Rb or K[58,254–256,260]. Further work will be required to explore the limits of the K-based passivation including its efficacy on different perovskite compositions, deposition methods and contacts, and how it could be ultimately exploited (or even mimicked with other halide-sequestering species) to eliminate interfacial non-radiative losses and ionic migration. The combination of high radiative efficiency, excellent charge transport and truly photo-stable bandgaps makes these passivation approaches an extremely promising route to take perovskite devices to their efficiency limits across a range of bandgaps.

Chapter 7

Passivation Tolerance in Alloyed Perovskites; Optoelectronic properties and moisture stability

We study the optoelectronic properties of multiple cation perovskite films with a particular focus on the passivated triple-cation lead mixed halide perovskite with potassium and rubidium species. The optoelectronic and chemical studies reveal that the alloyed perovskites are tolerant towards higher loadings of potassium than rubidium. Whereas potassium complexes with bromide from the perovskite precursor solution to form thin passivation layers that decorate perovskite grain boundaries and interfaces, rubidium additives, at similar concentrations, favour the formation of phase-segregated micron-sized rubidium-halide crystals. This tolerance by the mixed-cation lead mixed-halide perovskite to higher loadings of potassium allows us to achieve superior luminescent properties with potassium passivation. We also find that exposure to humid atmosphere drives phase segregation and grain coalescence for all compositions, with the rubidium-passivated sample showing the highest sensitivity to non-perovskite phase formation, which we consider is due to the greater water solubility of rubidium-halide species. Our work highlights new strategies toward maximising the optoelectronic performance and stability of complex metal halide perovskite compositions via cation passivation and humidity treatments.

Contributions. This work was the result of collaborative research with the following contributions: I and Dr Samuel D. Stranks conceived and planned the experiments with additional input from prof. Richard Friend. I fabricated all samples and devices, performed, and analysed the SEM, UV-Vis, PDS, PL, PLQE, TRPL, JV and EQE measurements. Dr Satyaprasad P. Senanayak performed and analysed the EIS and SCLC charge transport measurements (Figure 7.5, Figure 7.6). Dr Stefania Cacovich and Dr Giorgio Divitini performed and analysed the STEM–EDX measurements (Figure 7.9, Figure 7.10, Figure 7.11, Figure 7.13). Dr Andrew Pearson carried out humidity treatment on the samples and helped with ex-situ XRD measurements (Figure 7.18, Figure 7.19).

7.1 Introduction

There has been intensive research on the addition of monovalent cations and halides into the perovskite precursor solutions to enhance the crystallinity[206], phase stability[261] and optoelectronic properties of the perovskite materials[194]. In particular, an alloyed perovskite (i.e. the 'triple cation' (TC), $(Cs_{0.05}MA_{0.15}FA_{0.80})Pb(I_{0.85}Br_{0.15})_3$) shows superior PV performance and moisture stability compared to single-cation compositions (cf. $MAPbI_3$) and as a result has become the state of the art perovskite composition[59,241,262,263]. Recently, the addition of rubidium (Rb) halide into the TC perovskite has led to further enhanced performance and stability of perovskite solar cells, with an optimal loading for performance at 5% Rb with respect to the other A-site cations[264,265]. Furthermore, we and others have recently shown that passivation of TC films with potassium (K) halides can also significantly enhance the optoelectronic properties of perovskite device structures, with photoluminescence quantum efficiencies of ~15% in complete solar cell stacks and the inhibition of photo-induced ion-migration processes across a wide range of perovskite bandgaps[62,255,256]. The optimal loading of potassium for achieving both high luminescence yield and excellent charge carrier transport is 10% K relative to the A-site cation[62]. Recent evidence in the literature suggests that neither K or Rb are incorporating into the perovskite lattice[62,266]. Despite the apparent similarities between the passivation routes of the TC films with Rb or K, a direct comparison between the two in terms of tolerance to loading fractions, overall effectiveness and the viability of these approaches for stable perovskite optoelectronic devices has not yet been performed.

Here, we directly compare the optoelectronic properties, and chemical and structural stability of TC films passivated with rubidium (Rb) or Potassium (K) additives. We find that the TC films can incorporate higher loadings of K than of Rb before undergoing large-scale phase segregation at larger loading fractions, an observation that correlates with K-passivated films with optimal loading levels exhibiting superior optoelectronic properties (such as luminescence efficiency) over Rb-passivated films. We find that both passivation routes lead to the formation of non-perovskite phases; for K, these phases are selectively decorating the grain boundaries and interfaces even up to high loadings (~10%), while for Rb above ~5% loading they readily form large micron-sized crystallites. We track the structural, chemical and morphological changes of these perovskites over time under humid conditions. We find superior moisture stability in ambient conditions for K-passivated TC films compared to Rb-passivated films, though in both cases over extended ageing times non-perovskite phases form. Interestingly, we

also observe a substantial grain coalescence concomitant with a further enhancement in the luminescence quantum yield for the TC and K-passivated samples under humid conditions. Our work reveals critical insight into the behaviour and stability of passivations perovskite compositions, revealing key benefits and shortfalls of each approach.

7.2 Optoelectronic properties of multiple cation lead halide perovskite

Here, we compare the optoelectronic properties of a series of mixed lead halide perovskite (i.e. $APb(I_{0.85}Br_{0.15})_3$) with single (MA= $CH_3NH_3^+$), double (MA and FA= $CH_3(NH_2)_2^+$),) and triple (MA, FA and Cs) A-site cations as well as rubidium and potassium passivated triple cations perovskite denoted as SC, DC, TC, Rb-TC and K-TC, respectively, throughout the chapter. It is notable that in all of these perovskites, we used similar ratio of Bromide to Iodide in order to directly compare the effect of compositional change in A site cation and the passivation agents. In Figure 7.1, we show the SEM images of the fabricated perovskite films with uniformly packed grains, each with a size of around 200-400 nm.

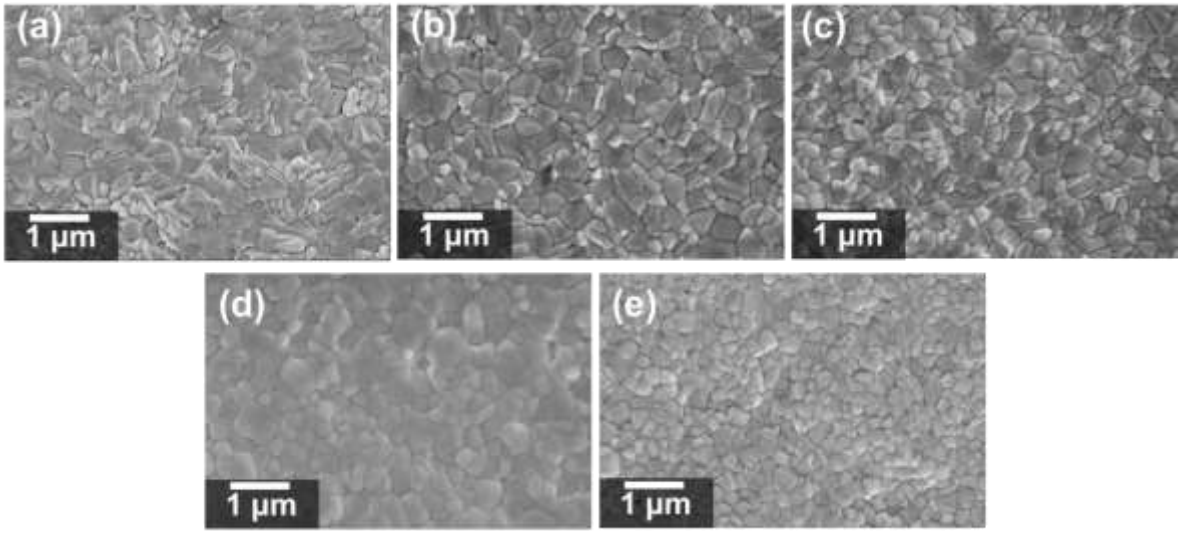

Figure 7.1. Morphologies of alloyed perovskites. Scanning electron micrograph of (a) single cation, (b) double cation, (c) triple cation, (d) Rb-passivated TC and (e) K-passivated TC perovskite thin films.

In Figure 7.2a, we show the photo-thermal deflection optical absorption spectra of the perovskite thin films with a slightly red-shifted bandgap for the mixed cations samples due to the higher concentration of FA. Importantly, the sub-bandgap absorption slightly reduces from SC to DC and then significantly drop for TC and passivated TC perovskites. We also calculated the Urbach energy (E_u), that is representative for degree of energetic disorder in the semiconductor, for the abovementioned perovskite thin films where the TC and passivated TC have the lowest electronic disorder (~12 meV) as shown in Figure 7.2b.

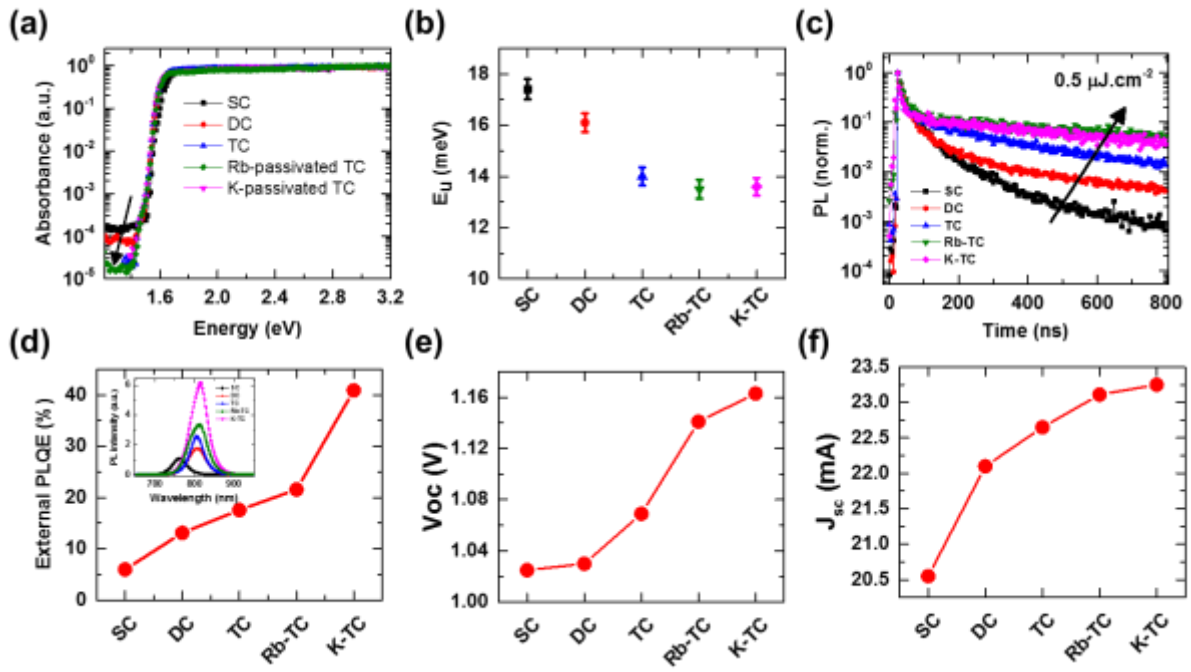

Figure 7.2. Optoelectronic characterisation of multiple cation and passivated perovskite thin films. (a) The absorption spectra, (b) Urbach energy (E_u) for perovskite thin films measured by photo-thermal deflection spectroscopy. (c) Time-resolved photoluminescence decays of the perovskites with excitation at 400 nm and a pulse fluence of 0.5 μ J cm^{-2} (excitation density of approximately 10^{16} cm^{-3}). (d) PLQE of perovskite thin films measured under illumination with a 532-nm laser at an excitation intensity equivalent to approximately 1 sun (60 mW cm^{-2}) after 600 s of illumination. (e) Open circuit voltage (V_{oc}) and (f) short circuit current (J_{sc}) as a function of perovskite composition.

Next, we performed time-resolved photoluminescence (TRPL) experiments where we show a significant enhancement in the charge carriers lifetime for the double cation perovskite compared to the single cation one. The carriers lifetime further improve for the triple cation sample and reach the longest lifetime for the passivated TC perovskites. In Figure 7.3, we also show the TRPL of these perovskite measured at different fluences. We then plotted the setup-limited (time resolution about 1.5ns), initial PL signal, PL_0, for pulsed optical excitation (Figure 7.3f). We find that the initial PL signal scales quadratically with pump power and thus carrier density for all the different compositions resulting in bimolecular process for all the investigated charge carrier densities[249].

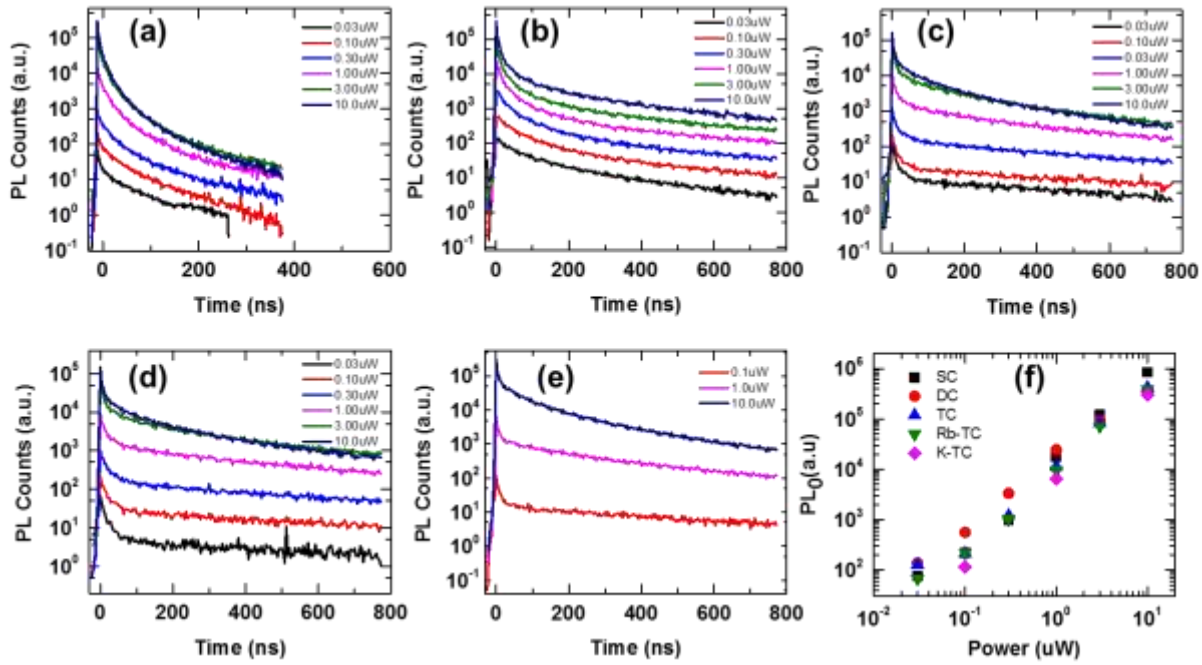

Figure 7.3. Recombination kinetics in alloyed perovskites. Intensity dependent time-resolved photoluminescence decays of the (a) SC, (b) DC, (c) TC, (d) Rb-TC and (e) K-TC perovskite films. The laser power of the 407- nm excitation are quoted on the graphs. (f) Initial transient PL signal (time integrated for 2 ns after excitation with a 100 fs laser pulse) plotted over the initial laser power.

In Figure 7.2d, we show the external PL quantum efficiency (PLQE) of the perovskite thin films with different cations and passivation agents measured at excitation densities equivalent

to solar illumination conditions. We observe a significant increase in PLQE from 6% for SC to 13% for DC followed by further enhancement to 18% for TC and 22% for Rb-TC and reach a remarkable value of 41% for K-TC. The corresponding PL spectrum for each of the perovskite compositions is shown in the inset of Figure 7.2d.

To validate how these optical characterisation results translate to device performance, we also fabricated perovskite solar cells using the device architecture fluorinated-tin oxide (FTO) / compact-TiO_2 (~30 nm) / thin-mesoporous TiO_2 (~200 nm) / perovskite (~500 nm) / Spiro-OMeTAD (~150 nm) / Au (80 nm). We summarise the changes in the open-circuit voltage (V_{oc}) and the short circuit current (J_{sc}) under full simulated sunlight for the abovementioned perovskite compositions in Figure 7.2e and Figure 7.2f, respectively. The corresponding JV curves and the photovoltaic parameters are shown in Figure 7.4 and Table 7.1 respectively. As expected from the relationship between luminescence and open-circuit voltage, the changes in V_{oc} of the devices closely follow the PLQE trends. From the J–V characteristic of the devices under dark conditions, the dark current onset of perovskite solar cells also validate the V_{oc} trend.

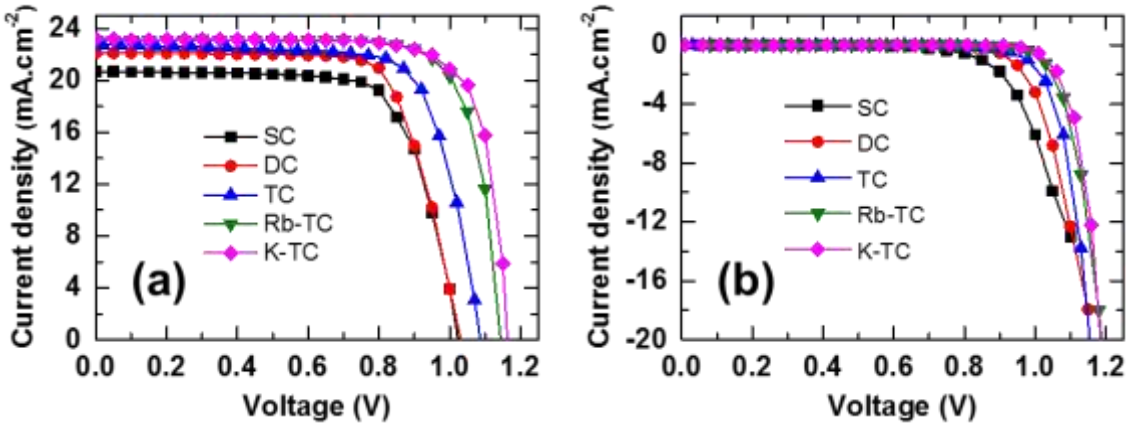

Figure 7.4. Photovoltaic performance of alloyed perovskite based solar cells. (a) Reverse J–V curves of the best-performing solar cells with perovskite absorbers with different compositions and passivation agents measured under full simulated solar illumination conditions (AM1.5, 100 mW cm^{-2}) with a scan rate of 15 mV s^{-1}. (b) The corresponding dark J-V curves for the abovementioned perovskites.

Furthermore, we see a similar trend for J_{sc} peaking for the passivated TC perovskites with Rb and K as expected from their substantial longer charge carriers lifetime from TRPL

measurements. We also reach higher values for fill factor of the solar cells with K- and Rb-passivated TC suggesting suppression of Shockley Reed Hall type trap assisted recombination due to the passivation effect particularly from K and Rb monovalent cations at the grain boundaries and interfaces. Finally, the enhanced photovoltaic parameters for the passivated perovskite films reflected in the power conversion efficiency (PCE) of the devices reaching more than 20% for K- and Rb-Passivated TC compare to 15% for SC, 17% for DC and 18% for TC based perovskite solar cells.

Table 7.1. Photovoltaic parameters for the best-performing solar cells with perovskite absorbers with different compositions and passivation agents. All the device measurements performed under full simulated solar illumination conditions (AM1.5, 100 mW cm^{-2}).

Sample		J_{sc} [$mA.cm^{-2}$]	V_{oc} [V]	FF	PCE [%]
SC	Reverse	20.55	1.025	0.74	15.5
	Forward	20.46	1.024	0.66	13.9
DC	Reverse	22.10	1.030	0.74	16.8
	Forward	21.98	1.027	0.70	15.8
TC	Reverse	22.65	1.069	0.75	18.2
	Forward	22.54	1.061	0.71	17.0
Rb-TC	Reverse	23.11	1.141	0.78	20.6
	Forward	23.01	1.138	0.78	20.4
K-TC	Reverse	23.25	1.163	0.77	20.8
	Forward	23.18	1.161	0.76	20.5

In order to investigate the effect of modification of A-site cation and addition of passivation agents on the charge transport behaviour in perovskite absorber, we fabricated electron only (Glass/ FTO/ c-TiO_2/ mp-TiO_2/ Perovskite/Al) and hole only (Glass /FTO /Perovskite / SpiroOMeTAD/ Au) devices for space charge limited current (SCLC) measurements and the corresponding I-V characteristics of them are shown in Figure 7.5a and Figure 7.5b. It is notable that both electron and hole mobilities significantly enhanced for DC and TC compare to the SC and further increased to the highest values for the K- and Rb-passivated TC samples (Figure 7.5c). Interestingly, the trends in the charge mobilities closely followed the J_{sc} changes in the subsequent solar cells. Furthermore, the extracted activation energies (E_A) for the charge

transport form temperature-dependent bulk SCLC measurements show the lowest charge transport barriers for Rb- and K-passivated TC perovskites (Figure 7.5c).

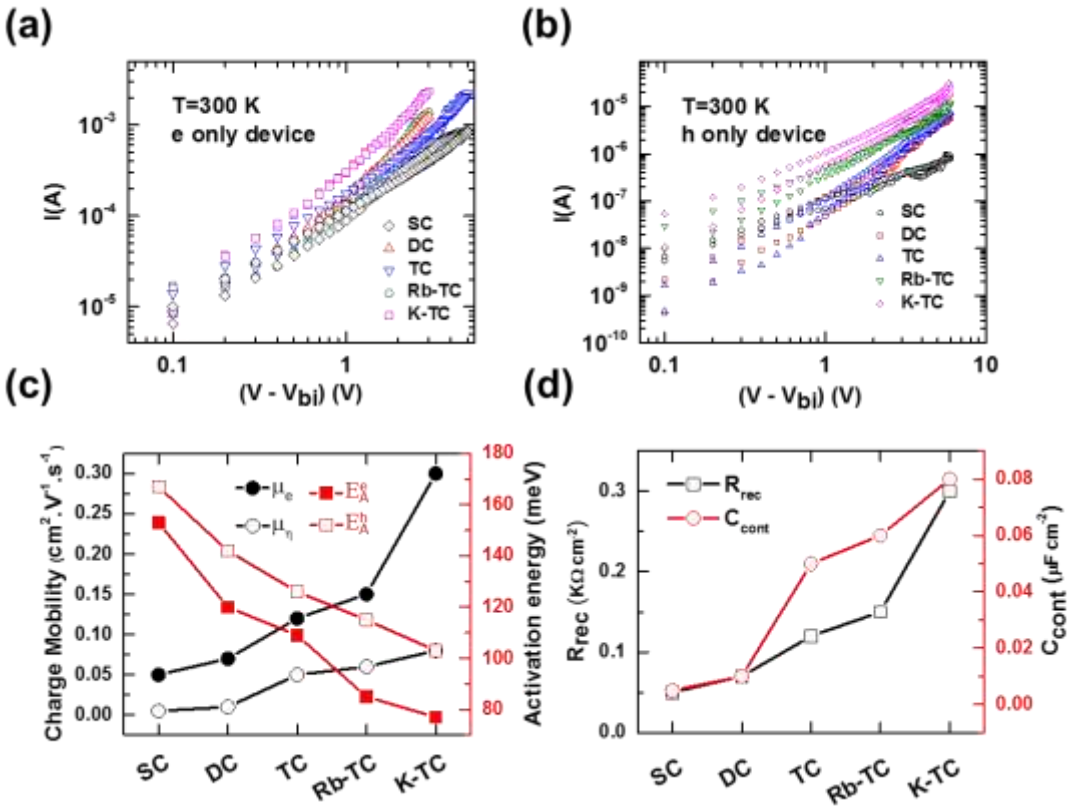

Figure 7.5. Charge transport behaviour in alloyed perovskite devices. I-V characteristics of (a) electron only devices (Glass/ FTO/ c-TiO_2 (~50nm)/mp-TiO_2 (~200 nm)/ Perovskite (~450nm)/ Al (~80nm)), (b) hole only (Glass/ FTO/ Perovskite (~550 nm)/ Spiro OMeTAD (~200nm)/ Au (~80nm)) devices utilized for estimating the SCLC mobilities. (c) The trends in the extracted SCLC electron and hole mobilities and activation energies for perovskite solar cells with different perovskite compositions and passivation agents. (d) The trends in the extracted recombination resistance (R_{rec}) and capacitance at the contacts (C_{cont}) from electrochemical impedance spectroscopy measurements for the above-mentioned perovskites.

To further understand the transport mechanism, we utilize electrochemical impedance spectroscopy (EIS) on the perovskite solar cells with different compositions and passivation agents. As explained in chapter 4, after fitting of the equivalent circuit to the EIS data, we extracted the recombination resistance (R_{rec}) and the capacitance at the contacts (C_{cont}) which

can directly correlate with J_{sc} and V_{oc} of the solar cells. As expected, the passivated TC particularly the K-TC shows the highest recombination resistance and C_{cont} and outperform the other compositions. These results collectively shows that K- and Rb-passivated TC possess superior optoelectronic and transport properties and further investigations are needed on their loading capacity as well as their stability.

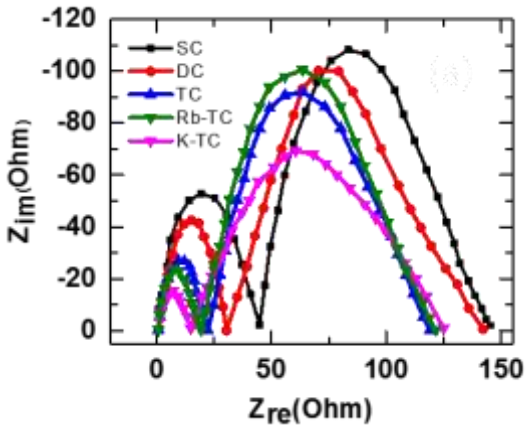

Figure 7.6. Transport mechanism in alloyed perovskite solar cells. Typical EIS Nyquist profile of perovskite solar cells with different perovskite compositions and passivation agents.

7.3 Potassium- and Rubidium-Passivated Perovskite Films: Optoelectronic properties and moisture stability

7.3.1 Optoelectronic properties

We spin-coated a series of perovskite thin films on glass by diluting the concentration of the A-site cations in the TC precursor solutions with KI- and RbI-based solutions in different volume ratios. We denote the resulting passivated samples as *x* = [K or Rb]/([K or Rb]+[A]) where A = (Cs, FA, MA) and *x* represents the fraction of K or Rb out of the A-site cations in the precursor solution. In Figure 7.7a, we show the photoluminescence quantum efficiency (PLQE) of the $(Cs_{0.06}MA_{0.15}FA_{0.79})Pb(I_{0.85}Br_{0.15})_3$ perovskite films with increasing K and Rb content measured at excitation densities equivalent to 1-sun solar illumination conditions. We observe a large increase from the initial value of 18% for TC to 41% for K-passivated TC (*x* =

0.05), which increases further to 52% for x = 0.20[62]. However, we do not find an appreciable increase in PLQE in the Rb-passivated samples beyond x = 0.05.

To validate how these luminescence results translate to device performance, we also fabricated perovskite solar cells using the device architecture fluorinated-tin oxide (FTO) / compact-TiO_2 (~30 nm) / thin-mesoporous TiO_2 (~200 nm) / perovskite (~500 nm) / Spiro-OMeTAD (~150 nm) / Au (80 nm). We summarise the changes in the open-circuit voltage (V_{oc}) and the short circuit current (J_{sc}) under full simulated sunlight for different loading of K or Rb in Figure 7.7b and Figure 7.7c, respectively (see Figure 7.8 and Table 7.2 for current-voltage (J-V) curves and device parameters, respectively). As expected from the relationship between luminescence and open-circuit voltage, the changes in V_{oc} of the devices closely follow the PLQE trends. Furthermore, we see an increase in J_{sc} with K/Rb loading up to x = 0.05 for Rb-passivated TC films and x = 0.10 for K-passivated TC analogues,[62,264,267] followed by a decrease in J_{sc} for higher concentration of passivating additives. In the previous chapter, we showed that this decrease is consistent with a decrease in carrier mobility, which was related to an increasing concentration of non-perovskite precipitates[263]. These results collectively show that we can achieve superior optoelectronic properties through passivation with K than with Rb; the potassium route offers greater versatility because wider ranges of loadings are possible before detrimental effects on performance parameters are observed.

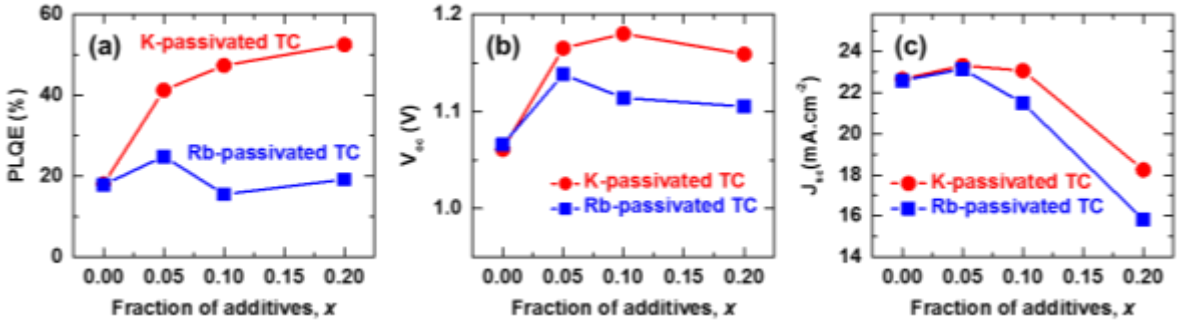

Figure 7.7. (a) PLQE of passivated perovskite thin films measured under illumination with a 532-nm laser at an excitation intensity equivalent to ~1 sun (~60 mW.cm^{-2}). (b) Open-circuit voltage (V_{oc}) and (c) short-circuit current (J_{SC}) extracted from current-voltage characteristics of pristine and passivated TC perovskite devices measured under full simulated solar illumination conditions (AM1.5, 100 mW.cm^{-2}) and scanned at a rate of 15 mV/s.

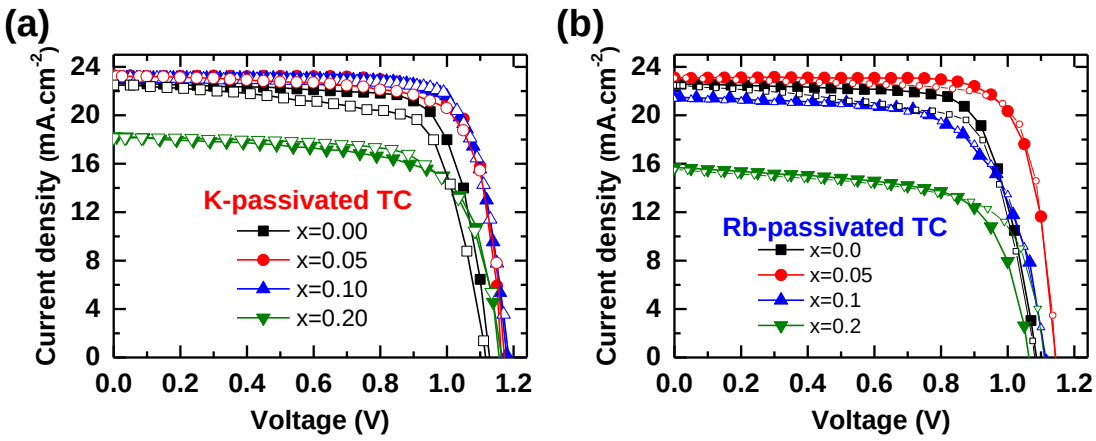

Figure 7.8. Reverse (closed symbols) and forward (open symbols) current density-voltage characteristics of perovskite solar cells for different loading (*x*) of passivation agents (a) K and (b) Rb into the TC perovskite layers. The scans were measured under full-simulated solar illumination conditions (AM1.5, 100 mW.cm^{-2}) and scanned at a rate of 15 mV/s.

Table 7.2. Device photovoltaic parameters for different loading (*x*) of passivation agents K (upper) and Rb (lower) into the TC perovskites measured under full-simulated solar illumination conditions (AM1.5, 100 mW.cm^{-2}) and scanned at a rate of 15 mV/s.

Sample	*x*		J_{sc} [mA.cm^{-2}]	V_{oc} [V]	FF	PCE [%]
K-passivated TC	0.00	Reverse	22.65	1.07	0.75	18.2
		Forward	22.48	1.06	0.71	16.9
	0.05	Reverse	23.25	1.17	0.77	20.9
		Forward	23.22	1.17	0.76	20.6
	0.10	Reverse	23.06	1.18	0.79	21.6
		Forward	23.09	1.19	0.79	21.7
	0.20	Reverse	18.24	1.16	0.70	14.8
		Forward	18.14	1.16	0.71	14.9
Rb-passivated TC	0.00	Reverse	22.58	1.09	0.74	18.1
		Forward	22.47	1.08	0.71	17.2
	0.05	Reverse	23.11	1.14	0.78	20.6
		Forward	23.07	1.14	0.79	20.7
	0.10	Reverse	21.48	1.12	0.67	16.1
		Forward	21.36	1.11	0.67	16.0
	0.20	Reverse	15.83	1.11	0.64	11.3
		Forward	15.53	1.10	0.67	11.5

7.3.2 Chemical and morphological composition

To investigate the local chemical and morphological composition of the passivated TC perovskite thin films, we performed scanning transmission electron microscopy-energy dispersive X-ray spectroscopy (STEM-EDX) measurements. We prepared a lamella of the x = 0.10 sample for both K- and Rb-passivated-TC perovskite films with Spiro-OMeTAD and platinum capping layers to preserve the active layer during the specimen preparation (see Figure 7.9 and Figure 7.10a for STEM high angle annular dark field (HAADF) cross sectional images).

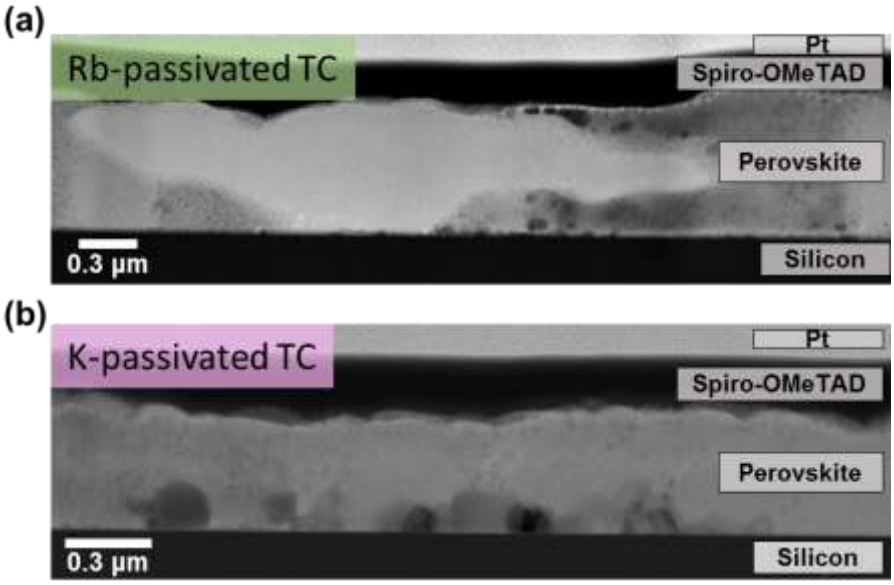

Figure 7.9. HAADF STEM cross sectional image of (A) Rb-passivated TC and (B) K-passivated TC deposited on silicon substrate with Spiro-OMeTAD and platinum capping layers to preserve the perovskite layer during lamella preparation.

We use a Non-negative Matrix Factorisation (NMF) algorithm[237] to decompose different phases in the cross-sectional STEM-EDX of the thin films. This analysis reveals the presence of two different compositional phases in both K- and Rb-passivated TC samples, namely a perovskite phase (identified from Br L_α, Pb M_α and I L_α lines) and an additive-rich phase (Figure 7.10b-j, and Figure 7.11). In the K-passivated TC, we find most of the potassium-(additive)-rich phase is composed of K and Br and situated at the grain boundaries (GBs) and

interfaces of the perovskite film (Figure 7.10c), as we observed previously at higher loadings[62]. However, in the Rb-passivated TC at the same loading as the potassium sample, we observe that the majority of the Rb is contained in large, micron-sized crystals rich in rubidium and iodide (Figure 7.10f-j) with no evidence for the presence of Rb throughout the bulk or surfaces of the film within our experimental resolution (estimated to be ~1 atomic percent). These results highlight an important finding: in the K-passivated samples, the K (even when added as KI) complexes selectively with the Br present in the TC precursor solution with an almost 1:1 atomic percent ratio, while the rubidium interacts primarily with iodide with an atomic percent ratio of 1:2, with only smaller fractions of Br (I:Br ~8, see Table 7.3 for atomic percent analyses). These differences are consistent with the lower formation energies of bonds comprising KBr and RbI relative to KI and RbBr, respectively[268,269].

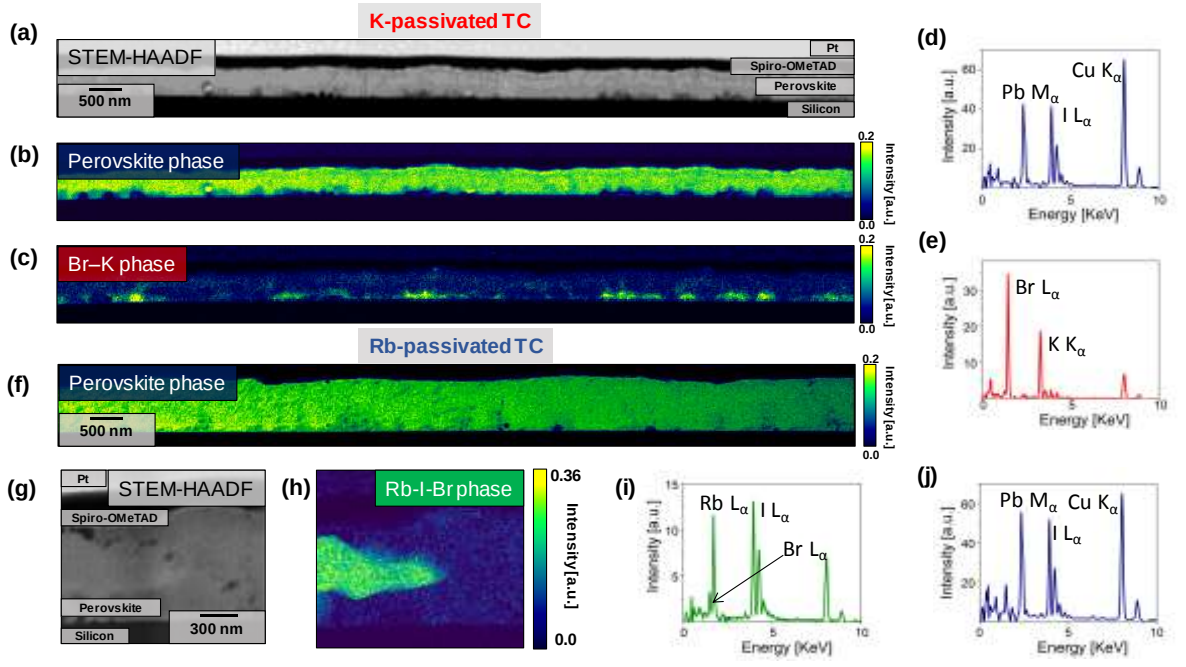

Figure 7.10. (a) HAADF STEM cross sectional image of a TC perovskite thin film passivated with x = 0.10 of potassium (K) and rubidium (Rb). NMF decomposition of K-passivated TC results in (b) perovskite phase and (c) K-Br phase. The corresponding EDX spectra of (d) perovskite phase and (e) K-Br phase. NMF decomposition of Rb-passivated TC, indicating (f) perovskite phase, (g) HAADF, (h) Rb-I-Br phase. The corresponding EDX spectra for the (i) Rb-rich phase and (j) perovskite phase.

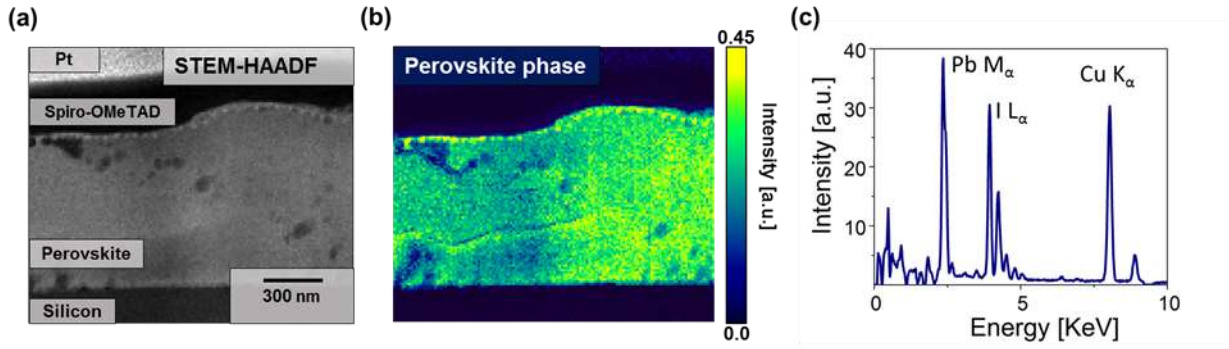

Figure 7.11. (a) HAADF STEM cross sectional image, (b) intensity plot and (c) elemental profile for Rb-passivated TC perovskite phase from NMF decomposition analyses.

Table 7.3. Summary of quantitative analysis on the NMF components that are rich in additives (i.e. K and Rb) extracted from the STEM-EDX results. Note that due to the convolution of the signal from this phase from the surrounding signal (due to several phenomena, including absorption and fluorescence) the measurement provides an estimate with a confidence of a few atomic percent points.

Atoms	Rb-passivated TC (atomic%)	K-passivated TC (atomic%)
Rb_Ka	١٨	-
K_Ka	-	٢٨
Pb_La	١,٤	٠,٥
I_La	٣٨	٣
Br_Ka	٥	٢٨
C_Ka	١٠	١١

In the previous chapter, we proposed that the K selectively draws out the Br from the lattice in the precursor solution. This allows the exploitation of the beneficial effects of Br in the seeding

of high-quality grain growth but then the removal of a fraction of the Br from the lattice of the final film, which would otherwise negatively impact optoelectronic properties[270]. By contrast, the Rb binds the iodide more strongly and we do not see the same effects. Furthermore, the inferior solubility of RbI compared to KBr in the dimethylformamide (DMF) / dimethyl sulfoxide (DMSO) precursor solution[268,269] means that Rb precipitates into large Rb-halide crystals at a lower loading than KBr, with the K-passivated samples primarily showing GB and surface decoration with the KBr species. These results provide an explanation for the superior optoelectronic properties of the K-passivation route over Rb-passivation: the greater solubility of the key non-perovskite phase in the former (KBr) than the latter (Rb-I-Br-based phase) means the system is tolerant to a higher loading of beneficial passivating species of K than Rb, and the specificity of K for Br also contributes to the particularly large enhancements.

7.3.3 Moisture stability of the passivated perovskite films

We then compared the atmospheric stability of the passivated films in each case, with the passivated samples fixed herein at $x = 0.05$ to ensure reasonable optoelectronic properties for both Rb and K. In Figure 7.12, we show top-view scanning electron microscopy (SEM) images of perovskite thin films exposed to ambient air (30% relative humidity, RH) for a week in dark conditions. We observe that the TC and K-passivated TC films remain unchanged while needle-like crystals, distributed homogenously across the sample area, form in the Rb-passivated TC films. Recent work suggests that these crystals are Rb-rich and that humidity accelerates their formation[263]; these crystals are likely to be similar species to those we observe distributed more sparsely in the films with higher Rb loadings without humidity exposure (x = 0.10, Figure 7.10h). The formation of crystallites in the Rb samples but not in the K (or TC) samples can be attributed to the higher solubility of RbI at room temperature in water (1.69 g/ml) compared to KBr (0.681 g/ml)[268,269].

In order to further investigate the moisture stability and the local chemistry of the passivated-TC perovskite thin films, we stored the films under elevated humidity conditions (50% RH, N_2) for a period of 24 hours. In Figure 7.13, we show the morphology of the TC and Rb- and K-passivated TC perovskite films before (Figure 7.13a-c) and after (Figure 7.13d-f) this humidity treatment. We observe uniformly packed grains each of size ~200-400 nm for all the unexposed perovskite films (Figure 7.13a-c). However, following humidity exposure for 24

hours we observe the formation of material on the surfaces of all films. We propose that the surface material for the TC specimen corresponds primarily to PbI_2 (cf. X-Ray Diffraction studies below), which is particularly abundant at the grain boundaries (Figure 7.13, g). This is similar to degradation in other polycrystalline materials where GBs are centres for degradation, often called an intergranular degradation[271]. We also find sparsely-spaced long needle-like crystals (≥ 30 μm) that, based on SEM-EDX analyses (Figure 7.14 and Figure 7.15), are rich in Cs. Furthermore, we again observe the formation of rubidium-rich crystals in Rb-passivated TC, which appear to be primarily rich in I but also smaller fractions of Br (Figure 7.13e, h). Finally, we also observe the formation of KBr-rich surface crystallites in the K-passivated TC films after the humidity treatment, which have similar composition to those in our cross-sectional STEM-EDX decomposition profile but are of larger size and distributed across the surface. These results suggest that moderate humidity exposure promotes the formation of non-perovskite material in each of the film compositions, with the composition of the non-perovskite material being consistent with that observed at elevated loadings of additives.

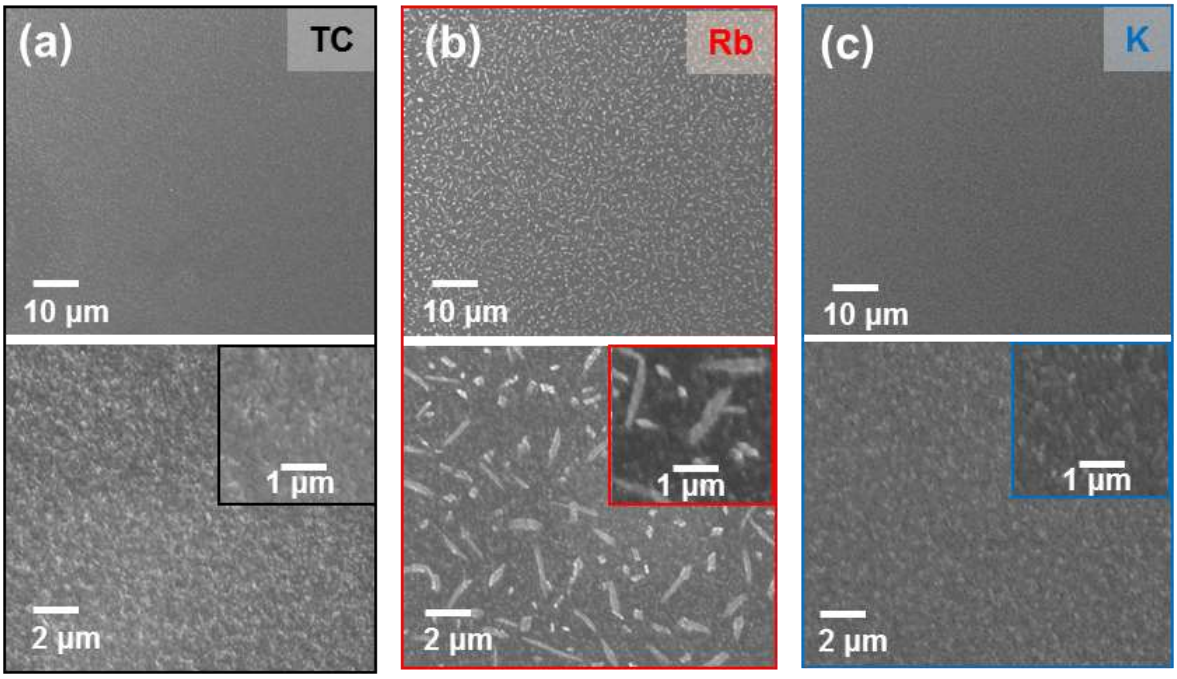

Figure 7.12. SEM top-view images at different magnifications of (a) TC, (b) Rb-passivated TC and (c) K-passivated TC films prepared on glass/FTO/TiO_2, with the images acquired after storage of the films in ambient laboratory air (30% RH) for one week in the dark.

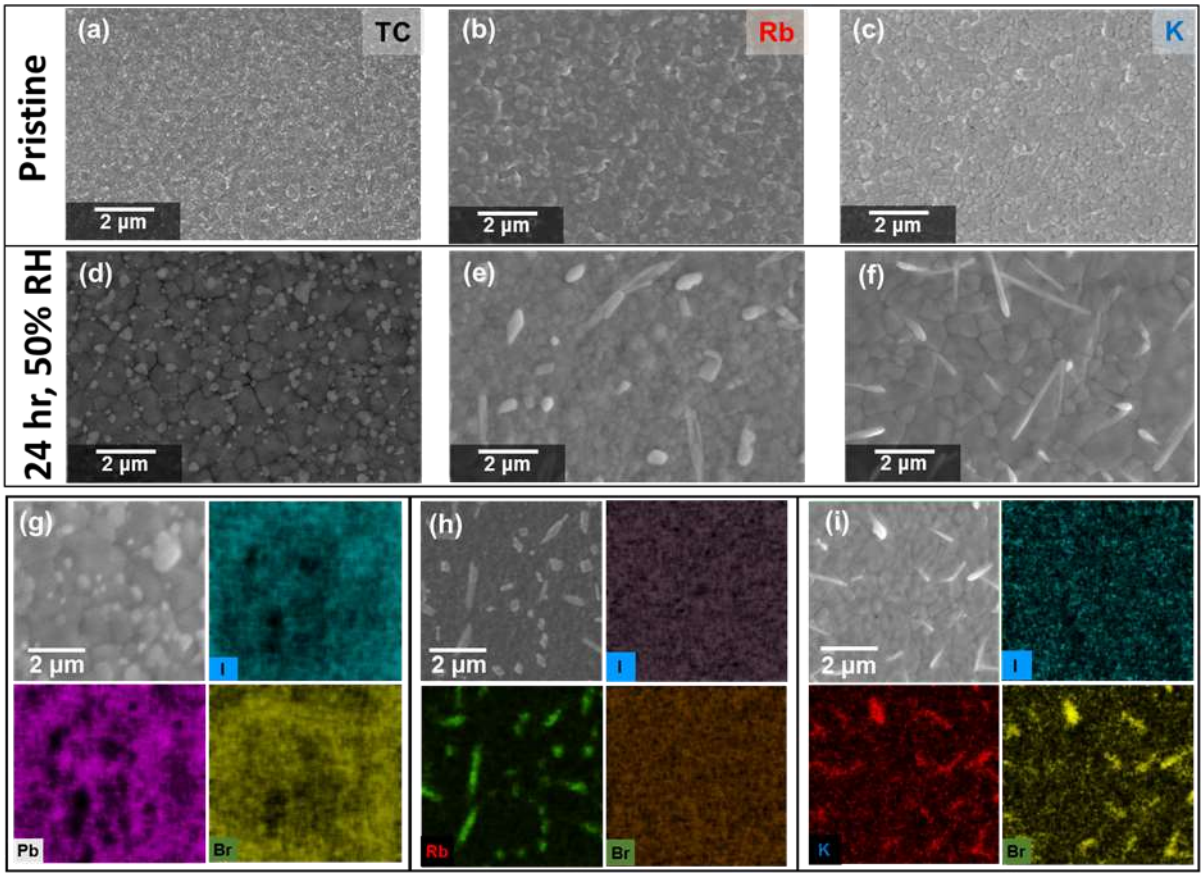

Figure 7.13. Top view SEM images of pristine (Top panel) and humidity treated (50% RH) over a course of 24 hours (middle panel) (a, d) TC, (b, e) Rb-passivated TC and (c, f) K-passivated TC perovskite thin films. SEM-EDX Elemental maps of (g) TC, (h) Rb-passivated TC and (i) K-passivated TC perovskite films exposed to humid nitrogen at 50% RH for a day.

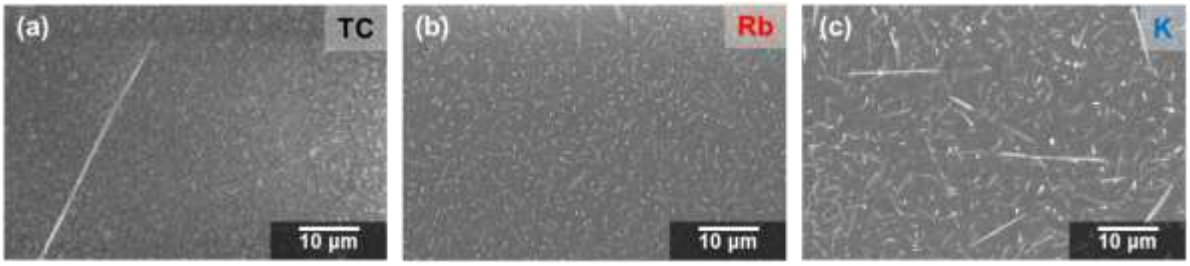

Figure 7.14. Top view SEM images of (A) TC, (B) Rb-doped TC and (C) K-doped TC perovskite thin films exposed to 50% RH for 24 hours.

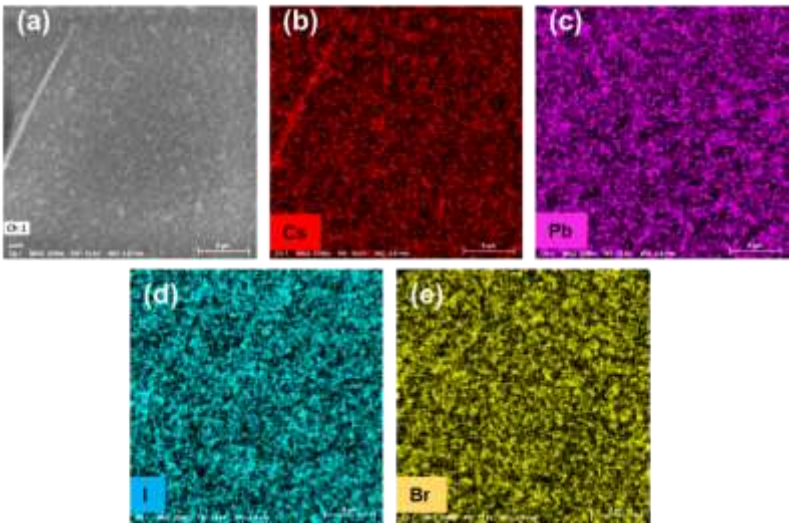

Figure 7.15. Top view SEM image of TC perovskite and the corresponding SEM-EDX elemental maps measured after humidity exposure of 50% RH.

Interestingly, we observe a significant coalescence of small perovskite grains into larger 'fused' domains in the perovskite thin films upon the 50% RH treatment in the TC and K-passivated TC (Figure 7.13a,d and e,f). We find that the average grain size increases remarkably from ~200 nm to ~2 μm in both samples (see Figure 7.16, for grain size distributions). Curiously, the perovskite grains in Rb-passivated TC preserve their original average grain size distribution (Figure 7.16), though we note that under more extreme humidity conditions (i.e. 75% RH), we also see the coalescence in the Rb-passivated TC (Figure 7.17). This suggests that the Rb-passivated TC perovskite films are more resistant to grain reconstruction.

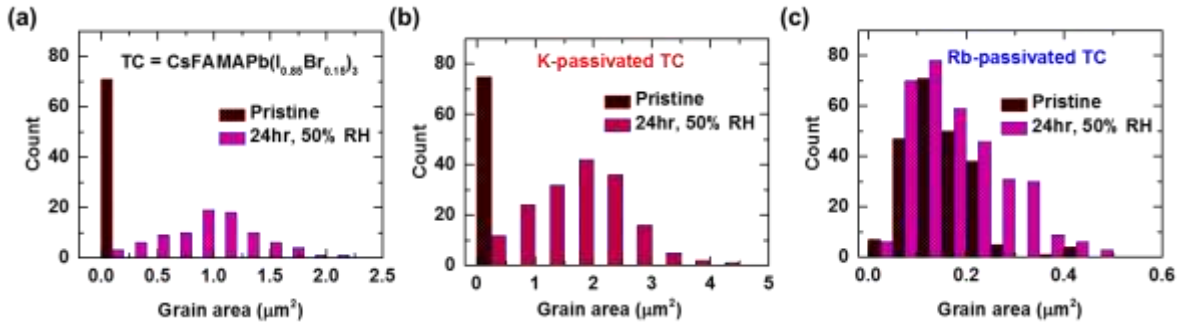

Figure 7.16. Grain area distributions. Histogram of the grain areas for (a) TC, (b) K-passivated TC and (c) Rb-passivated TC before (pristine) and after 24hr humidity exposure of 50% RH.

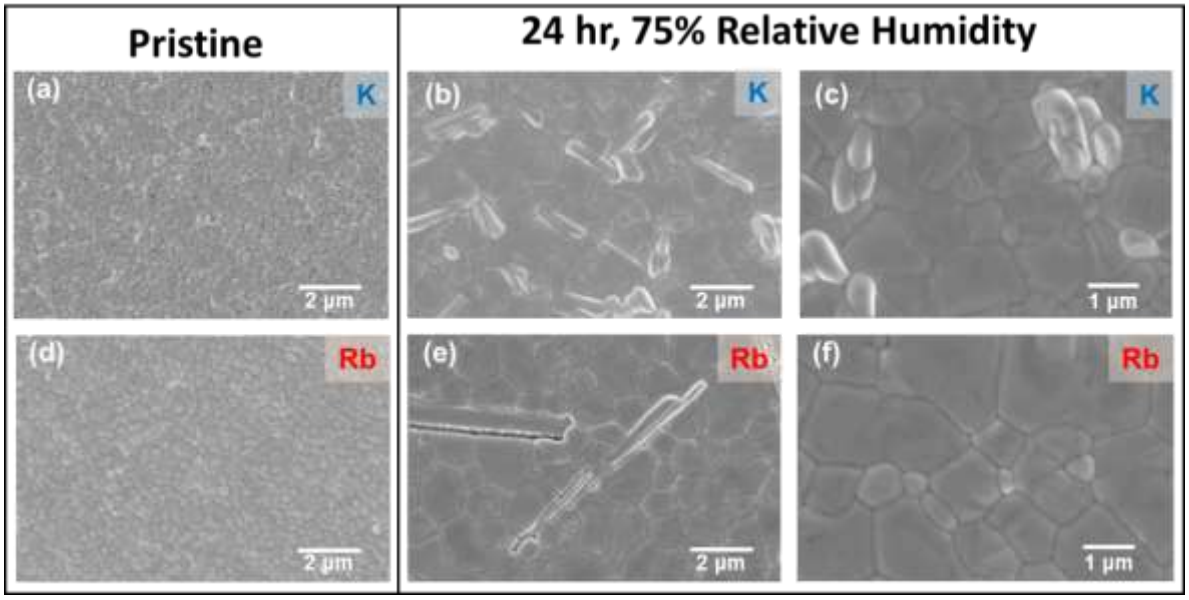

Figure 7.17. Top view SEM image of pristine and the exposed K- and Rb-doped perovskite thin films to 75% RH at different magnification.

In Table 7.4, we show the PLQE of the perovskite thin films before and after storage in the moderate humid environment (50% RH, N_2). We observe a significant enhancement in the radiative efficiency of the perovskite films for TC and K-passivated TC, with PLQE increasing from 18.6% and 39.5%, respectively, to 27.9% and 49.2%, respectively. In contrast, the PLQE of Rb-passivated TC drops from 22.8% to 12.9% after the exposure. We therefore find that the PLQE trend mirrors the grain fusing phenomena as the radiative efficiency of the humidity-treated TC and K-passivated sample with substantial grain coalescence increases substantially. This observation is consistent with previous reports showing that crystal (grain) coalescence is observed concomitant with enhanced optoelectronic properties of $MAPbI_3$ perovskite thin films and the photovoltaic performance of the subsequent devices[272,273], but to the best of our knowledge this is the first time this has been observed in the alloyed perovskite structures. We and others have also previously reported enhancements in $MAPbI_3$ device performance with controlled exposure to humidity but did not observe grain coalescence in these cases[274,275]. We speculate that the drop in PLQE of the Rb-passivated TC films can be attributed to the degradation of perovskite to the non-perovskite Rb-rich phases but without any beneficial grain coalescence. This is consistent with the reported drop in performance of the similarly treated Rb-passivated TC based perovskite solar cells[263].

Table 7.4. PLQE of the perovskite thin films before and after storage in humid nitrogen (50% RH) for 24 hours measured under illumination with a 532-nm laser at an excitation intensity equivalent to 1 sun (~ 60 mW cm^{-2}).

Sample	PLQE (%)	
	Before	After
TC	18.6	27.9
Rb-passivated TC	22.8	12.9
K-passivated TC	39.5	49.6

To further explore the structural stability of the perovskite thin films and to track the growth of perovskite and non-perovskite crystals upon humidity exposure, we performed XRD measurements on pristine films that were aged in humid nitrogen (50% RH) over the course of one day (Figure 7.18 and Figure 7.19). For the TC film, we observe a PbI_2 peak ($2\theta = 12.7^o$) that becomes narrower and more intense with extended ageing (Figure 7.18a), consistent with the formation of larger PbI_2 crystallites at the perovskite surfaces and grain boundaries (cf. Figure 7.13d). The humidity exposure also leads to the emergence of new reflections with peaks at $2\theta = 10.0^o$ and $2\theta = 11.2^o$ that we assign to the yellow δ-phase of Cs-rich $(Cs,FA,MA)(I_{0.85}Br_{0.15})_3$[276] and $CsPb_2I_4Br$[263], respectively, in agreement with the segregation of highly crystalline Cs-rich phases observed in the SEM-EDX analyses (Figure 7.14 and Figure 7.15). For the pristine Rb-passivated perovskite (Figure 7.18b), we find a diffraction peak at $2\theta = 9.9^o$ that we tentatively ascribe either to the rubidium-based perovskite $RbPb(I_{0.85}Br_{0.15})_3$[263] or to the yellow δ-phase of Cs-rich $(Cs,FA,MA)(I_{0.85}Br_{0.15})_3$[276] (as for the TC sample). During humidity exposure, this feature remains stable but after 24 hours we also see the emergence of two new peaks at $2\theta = 11.4^o$ and $2\theta = 12.3^o$ that we attribute to a segregated $RbPb_2I_4Br$ phase[263]. In Figure 7.18c, it is evident that similar PbI_2 and $CsPb_2I_4Br$ reflections are present in the XRD data for the K-passivated TC albeit at much weaker intensities compare to the TC. The XRD pattern corresponding to the K-passivated samples exposed for 24 hours also contains a weak reflection at $2\theta = 8.9^o$ that may correspond to a hydrated lead-passivated potassium bromide compound (e.g., $KPbBr_3.H_20$)[277], with the SEM-EDX showing the presence of K- and Br-rich needle-like crystals on the sample surface (Figure 7.18c); a precise chemical identification is not possible at this stage[278].

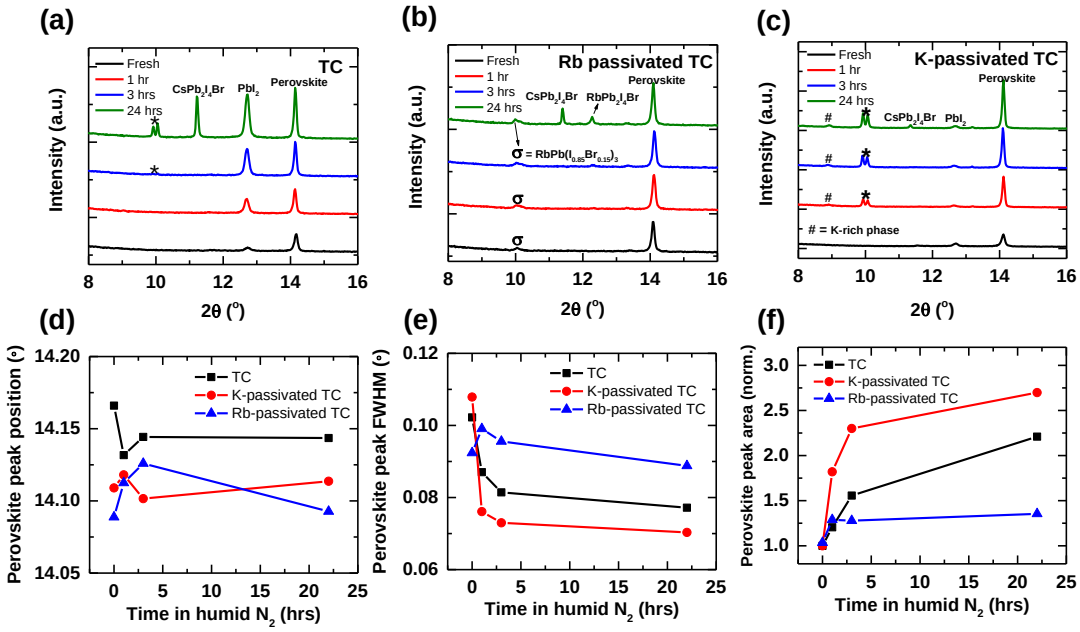

Figure 7.18. XRD patterns of (a) TC, (b) Rb-passivated TC and (c) K-passivated TC perovskite thin films on glass exposed to humid nitrogen (50% RH) for the stated times. The features are assigned as stated; we assign the feature marked * to be the yellow δ-phase of Cs-rich $(Cs,FA,MA)(I_{0.85}Br_{0.15})_3$. (d) Peak position, (e) FWHM and (f) peak area for the perovskite thin films over time.

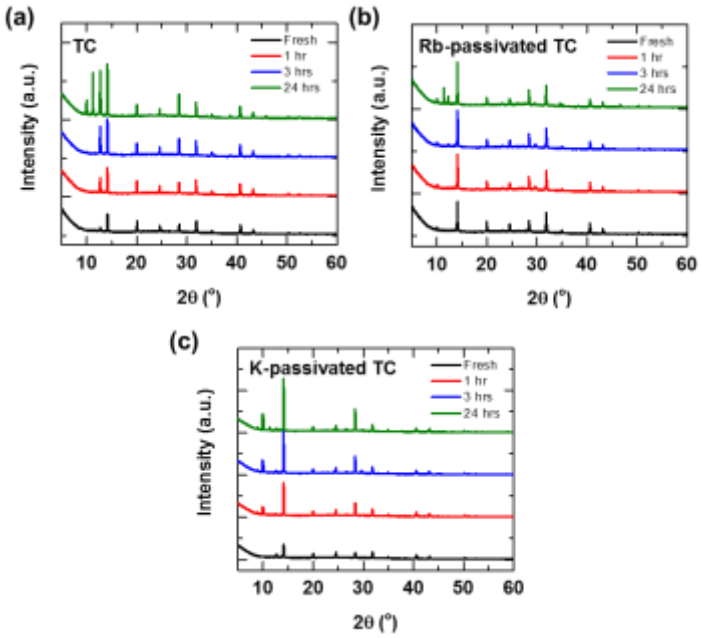

Figure 7.19. Complete XRD patterns of (A) TC, (B) Rb-doped TC and (C) K-doped TC measured fresh and after different exposure time to air with 50% RH.

In Figure 7.18d-f, we analyse the changes in the primary perovskite peak at $2\theta \sim 14.1^{o}$ (Figure 7.18d), full-width at half-maximum (FWHM) (Figure 7.18e) and peak area (Figure 7.18f) for the films at different exposure times. We observe that for both Rb- and K-passivated TC films, the perovskite peak is shifted towards lower angles relative to the peak from the TC sample, which indicates an expansion of the perovskite lattice and is in agreement with previous reports[62,263]. This could be due to the partial extraction of bromide from the perovskite lattice by the passivating additives or due to the passivating species occupying interstitial sites. We note that we have not seen any significant trend on the perovskite peak position upon humidity treatment suggesting these effects are not further affected by humidity exposure. We find that the FWHM drops significantly and the peak intensity (area) increases upon the humidity treatment for the TC and K-passivated TC perovskite films, which is in agreement with the grain coalescence that we reported earlier (Figure 7.13). By contrast, these parameters remain similar for the Rb-passivated TC after the humidity exposure in which the grain sizes remain similar.

7.4 Conclusions

We investigated the optoelectronic properties and chemical stability of state-of-the art triple cation (TC) perovskite films passivated with potassium and rubidium halides. We find that the luminescence efficiency increases to higher levels with potassium than with rubidium owing to the tolerance of the TC perovskites for higher loadings of potassium than rubidium. We find that potassium selectively binds to bromide and rubidium to iodide, and the increased tolerance of the perovskites to K over Rb is dictated by the enhanced solubility of KBr over Rb-halides in the precursor solvents (i.e. DMF/DMSO)[268,269]. At loadings above 5% Rb, large Rb-halide-rich crystals form which negatively impact the performance, while K-based films retain their optimal performance even at 10% loading. We also observe that this unwanted crystal formation is exaggerated when exposed to humidity. At low humidity levels (~30%) the rubidium-rich phases form while the pristine and potassium-passivated TC perovskite films remain unaffected; this is attributed to the greater solubility of Rb-halides in water over KBr and PbI_2. Under higher humidity conditions (~50%) we detect the appearance of PbI_2 at the grain boundaries and Cs-rich crystals for the TC films, segregation of Rb-rich phases in Rb-passivated TC films, and formation of a potassium-bromide phase in the K-passivated TC films. Interestingly, we find a significant grain coalescence in the TC and K-passivated TC

upon the humidity treatment that further enhances the radiative efficiency of the perovskite thin films.

These results represent an important advance in understanding the local chemistry and the structural stability of the state-of-the-art perovskite thin films to push optoelectronic devices to their efficiency limits. Our work highlights the benefits but also the deficiencies of these passivation approaches. We speculate that the primary role of these additives is to manage halides and vacancies, but the resulting potassium- or rubidium-rich species that immobilize the unwanted excess halide yet are redundant after processing (albeit electrically-benign) may even compromise humidity stability. Future efforts should consider facile post-treatment processes to remove the additives after their role in film formation and passivation is complete, as well as novel approaches to exploit the grain coalescence to maximise optoelectronic properties such as luminescence.

Chapter 8

Charge Kinetic at Perovskite/Tetracene Interface; From possibility of singlet fission to highly efficient hole extraction

We first explore the possibility of singlet exciton fission from tetracene as the triplet sensitizer and synthesised low-bandgap perovskite films based on mixture of lead (Pb) and tin (Sn) as the divalent cation ($CH_3NH_3Sn_xPb_{1-x}I_3$). We found no significant energy transfer from tetracene to perovskite based on the collected negative feature from tetracene in the excitation scan of perovskite as well as no magnetic field photoluminescence response for perovskite peak when it is interfaced with tetracene. In the second part of this chapter, we use tetracene as a dopant free and efficient hole-extraction layer in the rubidium passivated perovskite solar cells. We found that tetracene provide clean interfaces with perovskite layer leading to high photoluminescence yield (e.g. ~18%) while it shows poor ohmic contact with the metal electrode. We then demonstrate a capping layer of another hole-extraction layer (e.g. doped Spiro-OMeTAD) to provide a graded hole-injection interface with superior ohmic contacts. For complete solar cell devices containing tetracene and a capping layer of doped Spiro-OMeTAD as the graded hole transport layers, we demonstrate PCEs of up to 21.5% and extended power output over 550 hours continuous illumination, validating our approach.

Contributions. This work was the result of collaborative research with the following contributions: I conceived and planned the experiments with additional input from prof. Richard Friend. I fabricated all samples and devices, performed, and analysed the SEM, UV-Vis, PDS, PL, PLQE, TRPL, JV and EQE measurements. Dr Maxim Tabachnyk performed and analysed the magnetic PL measurements (Figure 8.13). Dr Andrew Pearson carried out device stability tests (Figure 8.21d). Dr Bertrand Philippe performed and analysed UPS data (Figure 8.20). Dr Satyaprasad P. Senanayak performed and analysed the EIS and SCLC charge transport measurements (Figure 8.26, Figure 8.27 and Figure 8.28).

8.1 Coupling of tetracene and low bandgap perovskite based on Pb-Sn mixture; possibility of singlet exciton fission

8.1.2 Introduction

As stated in chapter 2, the efficiency of a conventional single-junction solar cells as calculated by Schockley and Queisser is about 33%[21], mainly because of non-absorbed below-bandgap photons and loss of energy via thermalization of high energy carriers. Singlet fission is a down-conversion process that could raise this theoretical limit[28] to about 45%[279] by doubling the current obtained from high-energy photons. In order to benefit from the mechanism of singlet fission, the organic singlet fission sensitizer must be coupled to a lower-bandgap semiconductor. In previous studies, a combination of pentacene as the singlet fission sensitizer with lead chalcogenide quantum dots or amorphous silicon as the low-band gap semiconductor was achieved[280,281]. Recently, an efficient triplet energy transfer from pentacene to PbSe nanocrystals was reported by Tabachnyk et al[26,282]. In addition, tetracene has been proposed as the best candidate to couple with low band-gap semiconductor due to its higher triplet energy (≈1.3 eV) in comparison with pentacene (≈0.8-0.9 eV)[283].

In order to achieve energy transfer from tetracene into a semiconductor, the bandgap of the semiconductor must be equal or lower than the triplet level of tetracene for this process to be efficient and thermodynamically favourable. The triplet level of tetracene is estimated around 1.2-1.3 eV. Thus, in order to fulfil the mentioned condition, the semiconductor must have a bandgap below 1.3 eV. Hybrid metal halide perovskite can be a suitable option to be used in this structure due to its ease of processing, low cost and tunable properties. However, the conventional perovskite materials are based on either Pb or Sn with bandgap of 1.55 and 1.3 eV, respectively, which are slightly high to be used for singlet fission purpose.

Recently, several groups have reported different solution processing methods to prepare mixed Sn and Pb perovskites $CH_3NH_3Sn_xPb_{1-x}I_3$ [$0 \leq x \leq 1$] in order to achieve tunable band gap and high carrier mobilities. Particularly, Ogomi et al.[284] reported a linear reduction of band gap with increasing the Sn content, while Hao et al.[203] observed a nonlinear relationship between the band gap and the content of Sn. This is particularly interesting as they reported that the mixture of Sn and Pb can lead to a band gap lower than both Sn and Pb based perovskite individually, reaching values as low as 1.17 eV.

In this study, we propose to synthesize low band-gap hybrid metal halide perovskite based on a mixture of Sn and Pb and investigate the possibility of energy transfer between the $CH_3NH_3Sn_xPb_{1-x}I_3$ and thermally evaporated polycrystalline tetracene as an organic singlet fission sensitizer. This could potentially enhance the maximum potential efficiency for such perovskite systems due to efficient utilization of high-energy photons, using singlet fission as a down converting mechanism. For this purpose, a series of Pb and Sn mixtures based perovskites were synthesized and their optical properties were explored using steady state PL and PDS. In addition, morphology and structure of them were characterize using FE-SEM and XRD respectively. Finally, the possibility of energy transfer between $CH_3NH_3Sn_xPb_{1-x}I_3$ and tetracene was explored using fluorescence techniques.

As per the protocol mentioned in the experimental methods chapter, a series of Pb and Sn mixture perovskite ($CH_3NH_3Sn_xPb_{1-x}I_3$) including $CH_3NH_3Sn_{0.2}Pb_{0.8}I_3$ (20Sn), $CH_3NH_3Sn_{0.4}Pb_{0.6}I_3$ (40Sn), $CH_3NH_3Sn_{0.6}Pb_{0.4}I_3$ (60Sn), $CH_3NH_3Sn_{0.8}Pb_{0.2}I_3$ (80Sn) were synthesize by mixing different ratio of $MAPbI_3$ and $MASnI_3$. It is notable that the $CH_3NH_3SnI_3$ and $CH_3NH_3PbI_3$ are denoted as 100Sn and 100Pb, respectively.

8.1.3 Morphological Characterization

To compare the surface morphology of different mixtures of $CH_3NH_3Sn_xPb_{1-x}I_3$ deposited on mesoporous TiO_2 photoanode, field emission scanning electron microscopy (FESEM) is employed (Figure 8.1). The $CH_3NH_3PbI_3$ film is composed of interconnected nanoscale domains with sizes ranging from 200 to 500 nm with decent film coverage and needle like structures, which are the same as those reported in the previous work[203]. However, the 20Sn film displays better film quality and coverage in which wider needles form. This significantly increased film coverage ensures connectivity between grains, which is crucial to mitigate short-circuiting, charge leaking, and charge trapping at the crystalline boundaries. Further increase in Sn content lead to appearance of hexagonal shape crystals in between the needles as can be seen in the SEM image of 40Sn and 60Sn (Figure 8.1 c, d). Surprisingly, in the 80Sn and 100Sn films, the needle like crystals completely disappear and large, 3-5 µm, randomly oriented flowerlike crystals appear. It is notable that the surface coverage in these films decrease significantly.

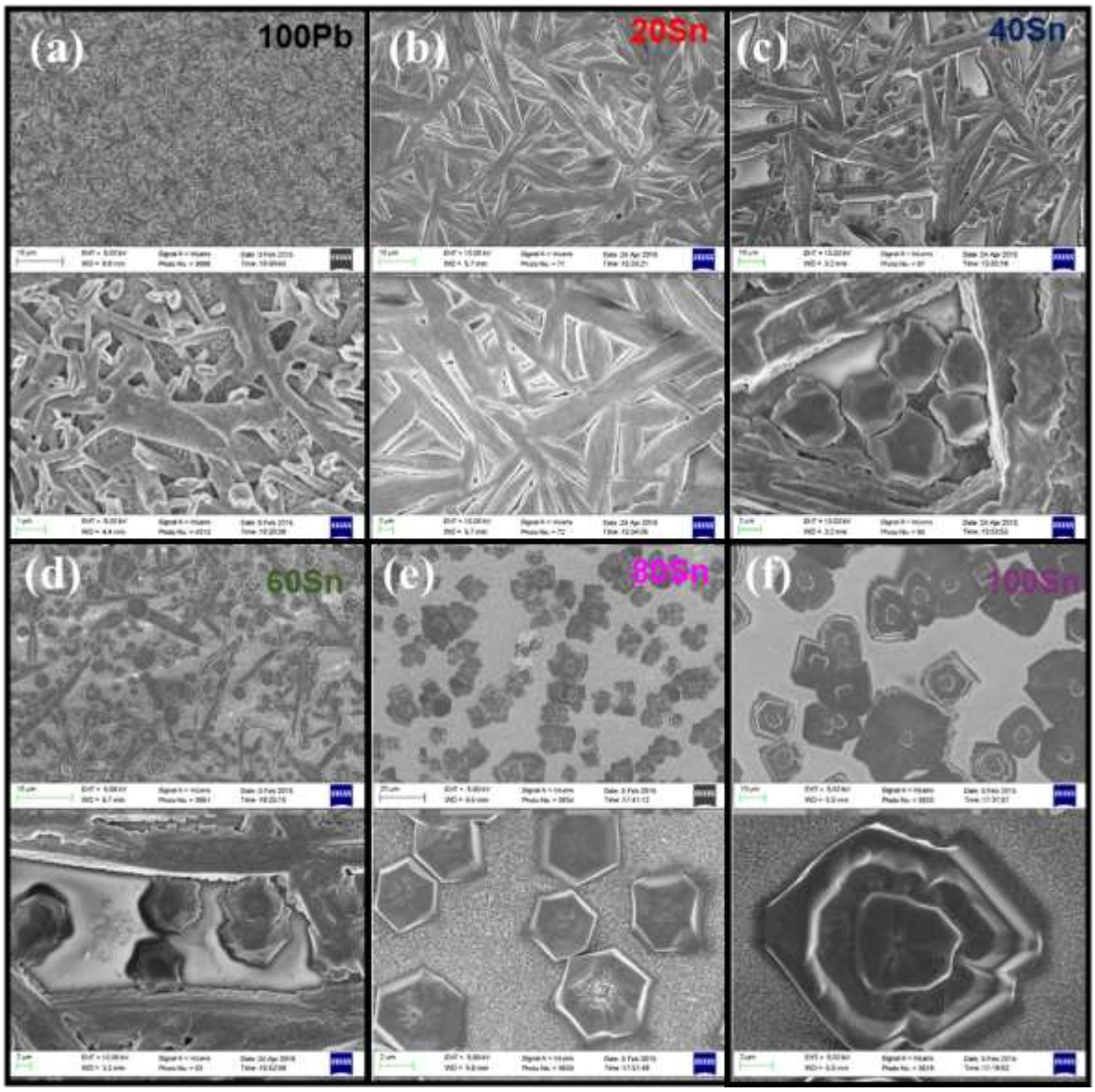

Figure 8.1. Top-view SEM images of (a) 100Pb, (b) 20Sn, (c) 40Sn, (d) 60Sn, (e) 80Sn and (f) 100Sn perovskite films deposited on a mesoporous TiO_2-coated FTO in two different magnifications**.**

8.1.4 Structural Characterization

To investigate the crystal structure of $CH_3NH_3Sn_xPb_{1-x}I_3$ perovskite, X-ray diffraction spectroscopy was carried out. The $CH_3NH_3Sn_xPb_{1-x}I_3$ adopts the perovskite structure type (ABX_3) consisting of corner-sharing $[Sn_{1-x}Pb_xI_6]^{-4}$ octahedra in which the metal site is randomly occupied by either Sn or Pb atoms and the A cation is selected to balance the total

charge. It is notable that $CH_3NH_3SnI_3$ and $CH_3NH_3PbI_3$ crystallize in the pseudocubic P4mm (α-phase) and tetragonal I4cm (β-phase) space groups, respectively, at ambient conditions. It is reported that $CH_3NH_3PbI_3$ undergoes a reversible structural phase transition to the P4mm space group becoming isostructural to its Sn analogue at higher temperatures (~330K)[285].

Identical structural transition can be also realized in the $CH_3NH_3Sn_xPb_{1-x}I_3$ for an $x \geq 0.5$ value at room temperature. It is obvious from the X-ray diffraction patterns in Figure 8.2 that the two peaks within the range between 22°−25° 2θ ($x < 0.5$), which could be indexed to (211) and (202) planes in the tetragonal I4cm space group, can gradually merge to a single peak corresponding to the (113) plane in the P4mm space group when x becomes >0.5 due to the higher symmetry of P4mm[285].

According to the Scherrer equation, the mean size of the crystallite is inversely proportional to the full width half the maximum (FWHM) of the XRD peak intensity of the material. Thus, the crystallite size for $CH_3NH_3Sn_xPb_{1-x}I_3$ is increased for the perovskite containing higher amount of Sn with the exception of 80Sn, which has the lowest FWHM (Figure 8.3).

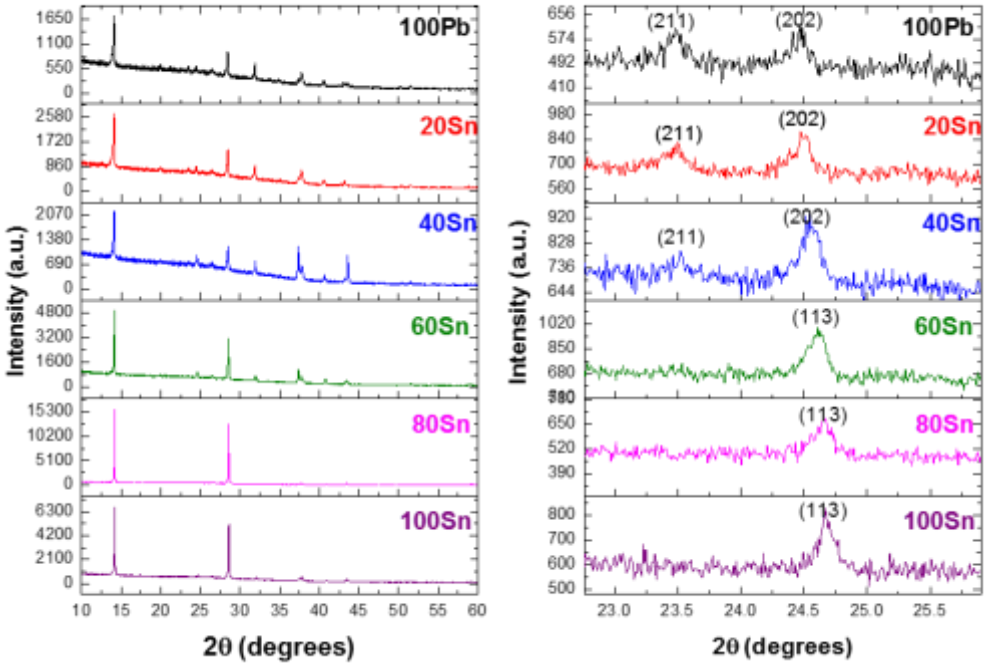

Figure 8.2. X-ray diffraction spectra of $CH_3NH_3Sn_xPb_{1-x}I_3$ where x=0, 0.2, 0.4, 0.6, 0.8 or 1. The right side XRD shows the structural transition from tetragonal I4cm (β-phase) to pseudocubic P4mm (α-phase) space groups happening for x>0.5.

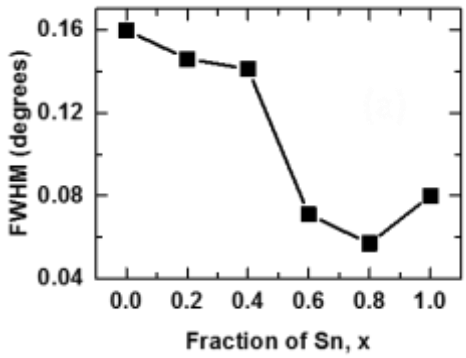

Figure 8.3. Full width half maxim (FWHM) of the main perovskite peak at 2Θ=14.1 for $CH_3NH_3Sn_xPb_{1-x}I_3$.

8.1.5 Photothermal deflection spectroscopy (PDS)

We used PDS to explore the optical absorption of the synthesized $CH_3NH_3Sn_xPb_{1-x}I_3$ perovskite near the band edge (Figure 8.4). A clear red shift in the band edge of perovskite based on Pb and Sn mixture is observed for x>0. Notably, by stoichiometrically mixing the divalent metal iodides of Sn and Pb with methylammonium iodide, we can easily synthesize the $CH_3NH_3Sn_xPb_{1-x}I_3$ solid solutions with a tunable bandgap tunable between 1.17 and 1.55 eV. The intermediate compounds with x = 0.8 and 0.6 show the smallest bandgaps of 1.17 eV. It is important to note that the optimal bandgap for a single-junction solar cell is between 1.1 and 1.4 eV, currently beyond the range of most investigated methylammonium lead trihalide systems. The $CH_3NH_3Sn_xPb_{1-x}I_3$ series is therefore promising for more efficient photovoltaic devices for both the single junction and also tandem architecture device where the optimum bandgap for a bottom cell lies in around 1 eV[286].

It is also apparent that the above bandgap absorption of 100Pb, 20Sn and 40Sn are higher compare to the other compounds. This is mostly due to the better surface coverage of these film as we observed in SEM images (Figure 8.1a). In addition, the absorption tail shifts up by increasing the content of tin, which can be attributed to the oxidation of $CH_3NH_3Sn_xPb_{1-x}I_3$ compounds (Figure 8.1b). Oxidation of Sn based compounds happened during the PDS measurement since there is a certain amount of oxygen inside the FC72 liquid, which is used as a heat transfer medium for the sample. Figure 8.5 compare the absorption spectra of 20Sn sample, which is loaded in air and inside the control atmosphere of glovebox. It is evident that

the absorption tail of the sample shifts up considerably which further confirms the effect of oxidation on the absorption spectra of Sn based perovskite.

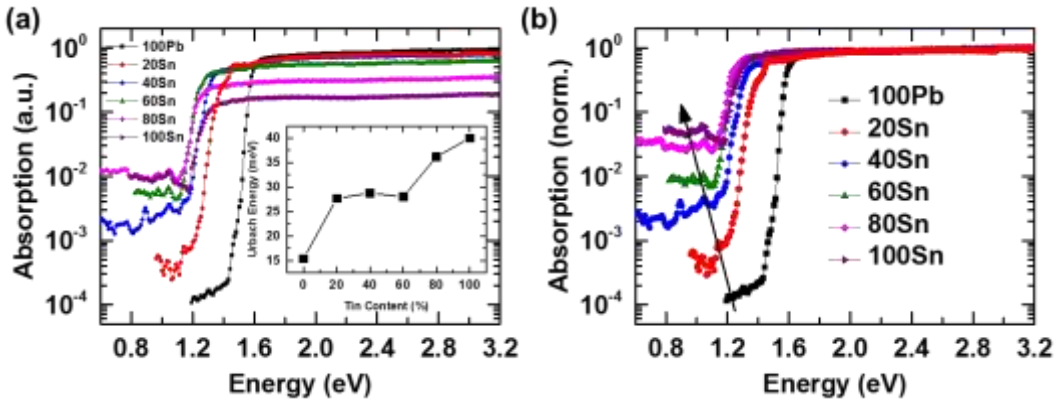

Figure 8.4. The (a) un-normalised and (b) normalised absorption spectra of the synthesized $CH_3NH_3Sn_xPb_{1-x}I_3$ serial compounds measured using the PDS technique. The inset shows the corresponding Urbach energies for all samples. The error bar is defined by the s.d.

As explained in the previous chapters, Urbach energy 'E_u' as the slope of the exponential part of the Urbach tail gives an estimation about the concentration of defects and level of electronic disorder. The estimated Urbach energies for $CH_3NH_3Sn_xPb_{1-x}I_3$ serial compounds and their corresponding data fittings are shown in the inset of Figure 8.4 and Figure 8.6. These values suggest that the $CH_3NH_3Sn_xPb_{1-x}I_3$ compounds with higher amount of tin have a higher level of electronic disorder.

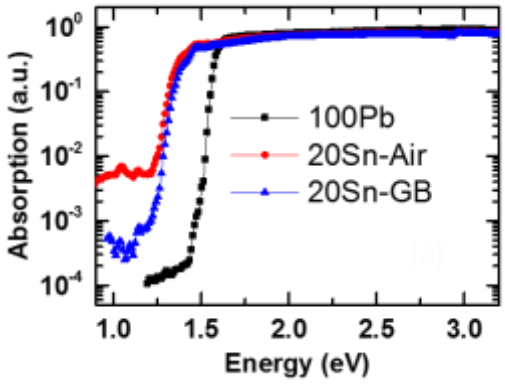

Figure 8.5. The absorption spectra of the $CH_3NH_3Sn_{0.2}Pb_{0.8}I_3$ which is loaded in air (20Sn-Air) and inside the control atmosphere of glovebox (20Sn-GB).

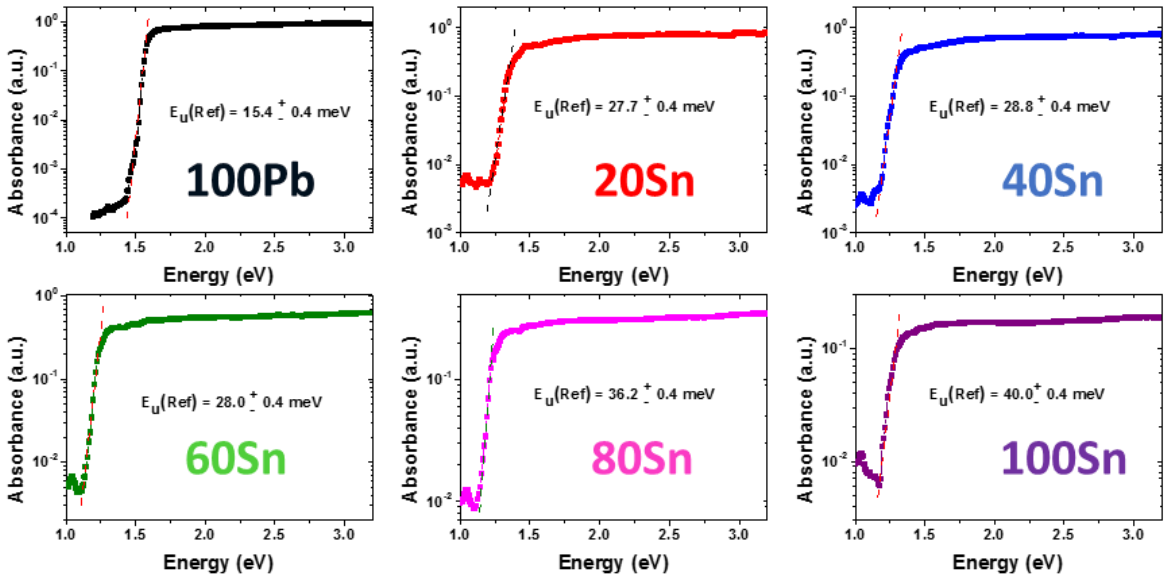

Figure 8.6. Data fittings of Urbach energy for PDS measurements of $CH_3NH_3Sn_xPb_{1-x}I_3$ serial compounds. The dotted lines in each plot are the linear fits used to calculate the Urbach energy and the obtained Urbach energy 'Eu' is indicated in each plot.

8.1.6 Photoluminescence characterisation

Steady state PL spectra of $CH_3NH_3Sn_xPb_{1-x}I_3$ serial compounds are presented in Figure 8.7. A clear red shift of PL is observed for all Sn contained perovskite compound compared to the $CH_3NH_3PbI_3$ which shows a narrow peak at 795nm. The intermediate compounds with x = 0.8 and 0.6 show the highest red shift and PL peak at 1015nm and 1035nm, respectively. It is notable that the position of PL peak for 100Sn and 40Sn is identical while the 40Sn shows a broader peak to the red. In addition, the PL peak for 20Sn sample represent a slight blue shift in comparison with the 100Sn. The PL data are consistent with the PDS data in which the intermediate compounds with lower band-gap have the most red-shifted absorption edge.

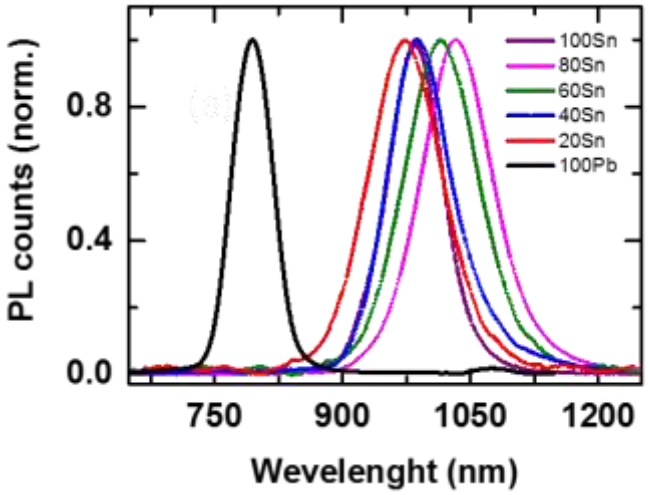

Figure 8.7. Photoluminescence spectra of $CH_3NH_3Sn_xPb_{1-x}I_3$ serial compounds measured using 532 nm continuous laser excitation.

8.1.7 Coupling of tetracene and low band gap $CH_3NH_3Sn_xPb_{1-x}I_3$

Next, we investigate the possibility of coupling tetracene with synthetized low bandgap $CH_3NH_3Sn_xPb_{1-x}I_3$ perovskite. Thus, a film of 25nm of tetracene was thermally evaporated on top of perovskite layer. All the samples were then sealed in nitrogen using glass coverslips and epoxy. In Figure 8.8, we show the surface morphology of these bilayer of tetracene and perovskites. We see that islands of tetracene formed homogeneously on the surface of perovskite and does not change the perovskite morphology.

In addition, UV-Vis absorption spectra of these bilayer films were measured and is shown in Figure 8.9. It is evident that absorption features of tetracene consisting of three peaks between 400 nm to 550 nm can be seen in all bilayer samples. It is notable that the perovskite absorption spectra can only be detected for 100Pb sample since the bigger size of crystals lead to high scattering effect for other films. Therefore, PDS were used to explore the absorption spectra of bilayer samples (Figure 8.10). It is apparent that the similar trend is achieved for absorption spectra of the bilayer films compare to the single layer of perovskite.

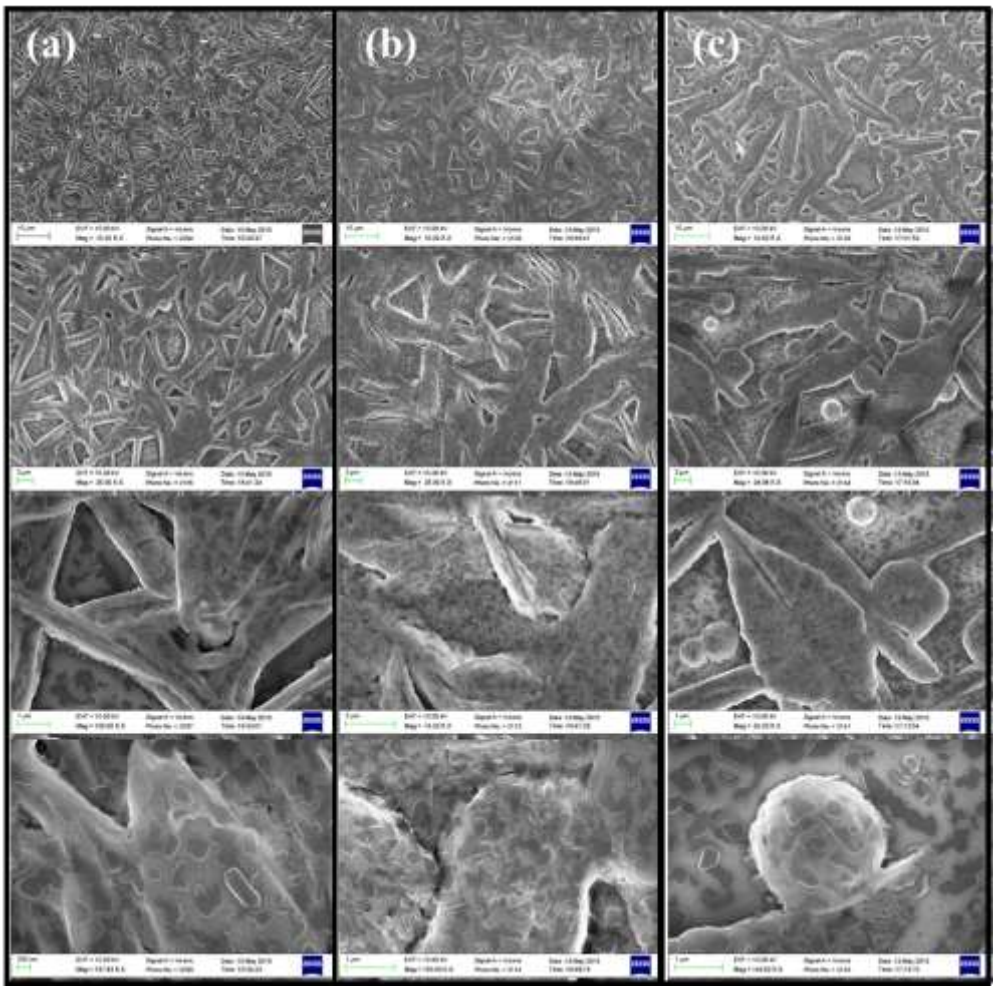

Figure 8.8. Top-view SEM images of bilayer of (a) 100Pb, (b) 20Sn and (c) 40Sn and thermally evaporated tetracene in different magnifications.

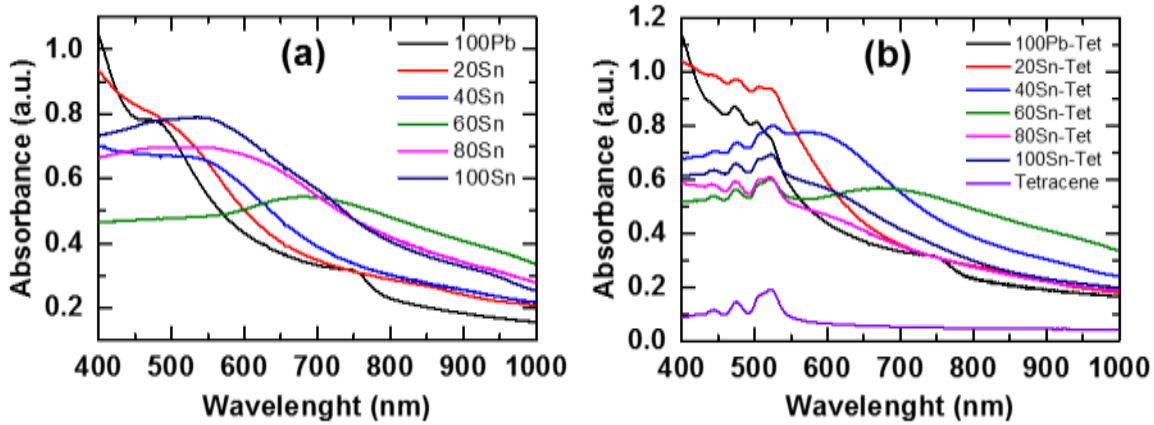

Figure 8.9. UV-Vis absorption spectra of a) single layer of $CH_3NH_3Sn_xPb_{1-x}I_3$ serial compounds, b) double layer of perovskite and tetracene.

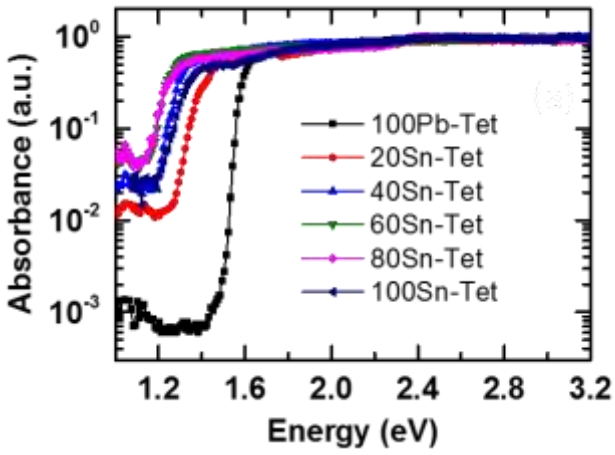

Figure 8.10. The absorption spectra of the bilayer of tetracene and synthesized low bandgap perovskite ($CH_3NH_3Sn_xPb_{1-x}I_3$) serial compounds measured using the PDS technique.

Emission scans for the bilayer of tetracene and synthesized $CH_3NH_3Sn_xPb_{1-x}I_3$ perovskite, which were excited at 532nm, are shown in Figure 8.11. These scans were detected by a photodiode and a monochromator choosing the detection colour. It is evident that the intensity of emission for the bilayer dropped significantly, particularly for the compound with higher percentage of Sn, since some part of light is absorbed by tetracene. In addition, hole transfer from perovskite to tetracene is potentially a reason for the drop in steady-state PL from the bilayer of perovskite and tetracene. Surprisingly, a blue shift of emission peak is observed for the bilayer of $CH_3NH_3Sn_xPb_{1-x}I_3$ with $x \geq 0.4$ and tetracene compare to the single layer of perovskite.

In order to investigate the possibility of energy transfer between tetracene and low bandgap perovskite based on mixture of Pb and Sn, fluorimeter excitation scans were employed. In Figure 8.12, a negative contribution from tetracene can be seen in the excitation scan of bilayer sample as the drops in the black curve (excitation scan counts of bilayer sample) matches the absorption peaks of tetracene. Therefore, there is no significant energy transfer from tetracene to the perovskite since the light does not reach perovskite and absorbed only by tetracene. This might be because of the poor quality of the interface between tetracene and perovskite leading to high density of trap states. Another reason could be due to presence of charge transfer between these layers.

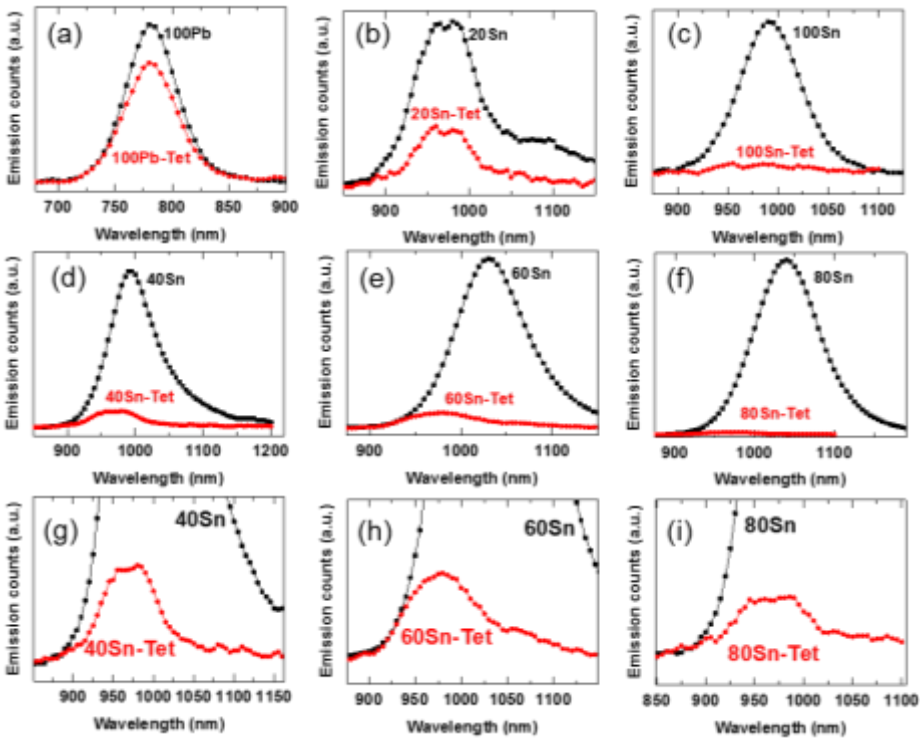

Figure 8.11. Emission scan for single (black curves) and bilayer (red curves) of (a) 100Pb, (b) 20Sn, (c) 100Sn, (d, g) 40Sn, (e, h) 60Sn, (f, i) 80Sn and tetracene measured using 532 nm continuous laser excitation.

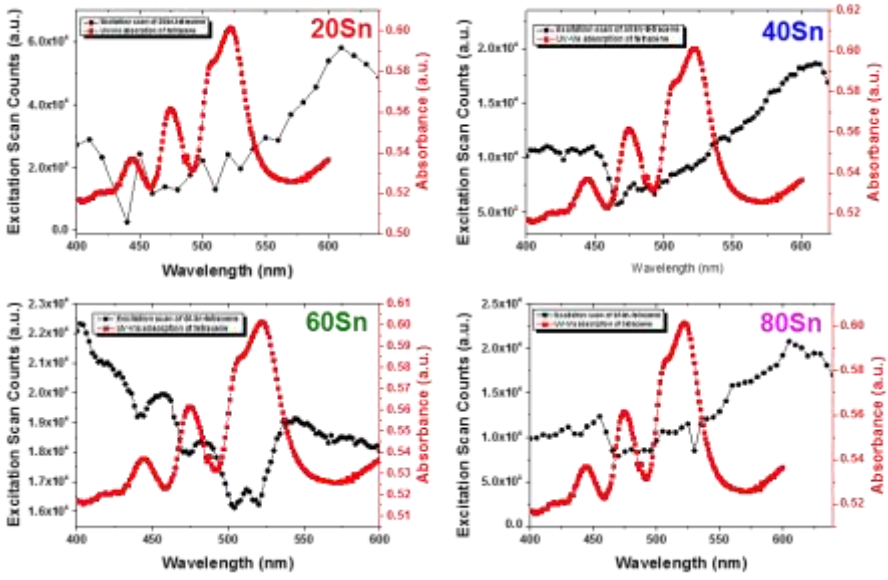

Figure 8.12. Excitation scans for mixture of Sn and Pb perovskite compounds (black curve). The red axis and curve shows the UV-Vis absorption spectra of tetracene.

To further explore the possibility of energy transfer between low bandgap perovskite (80Sn, 1.17 eV) and tetracene, we performed magnetic PL measurements where we measure the changes in the PL upon applying a magnetic field and 405 nm continuous laser excitation. It is well known that the transfer of either singlets or triplets from the triplet sensitizer (e.g. Tetracene) to the low bandgap semiconductor (e.g. 80Sn perovskite) induces magnetic field modulation on the PL from the later material[26,287]. In Figure 8.13, we show the magnetic field responses for Tetracene PL peak at 530 nm and 80Sn perovskite PL peak at 1030 nm in single layer of each and bilayer of 80Sn perovskite and thermally evaporated tetracene. As expected, the magnetic field response of singlets in tetracene is about 30% for single layer and interestingly the PL changes reduces to just above 20% for bilayer of 80Sn-tetracene. In Figure 8.13b, we observed no significant magnetic response for the perovskite peak at 1030 nm of the single layer and bilayer of 80Sn-tetracene. This further confirms that there is no obvious energy transfer from tetracene to the low bandgap perovskite.

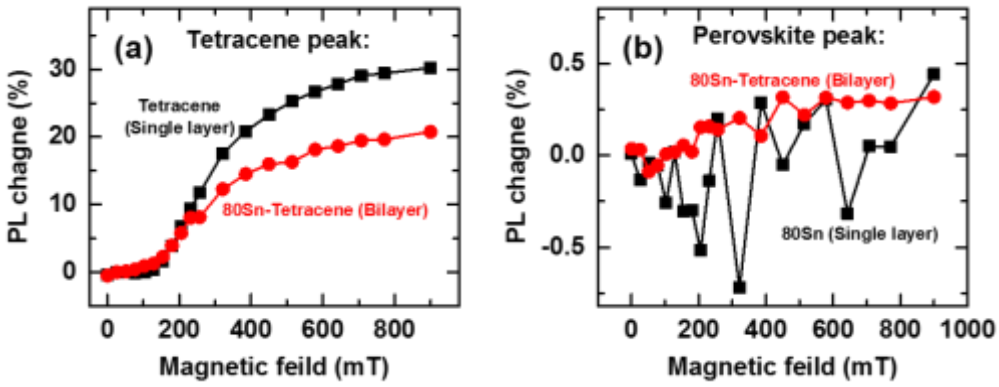

Figure 8.13. Magnetic field effect on fluorescence of (a) tetracene PL peak at 530 nm and (b) 80Sn perovskite peak at 1030 nm for single layer of each and bilayer of 80Sn-tetracene. Note that in the bilayer films, the 405nm continuous laser excitation is from tetracene side.

8.1.8 Conclusions

We have synthesized low bandgap perovskite (e.g. 1.17eV) using the alloyed perovskite solid solutions of methylammonium lead iodide ($CH_3NH_3PbI_3$) and its tin analogue ($CH_3NH_3SnI_3$). The morphology of $CH_3NH_3Sn_xPb_{1-x}I_3$ alter significantly with x consisting needle like or

flowerlike crystals or a mixture of them. A structural transition from tetragonal I4cm (β-phase) to pseudocubic P4mm (α-phase) space groups is realized in the $CH_3NH_3Sn_xPb_{1-x}I_3$ for $x \geq 0.5$ using XRD. In addition, the crystallite size is increased significantly by raising the content of Sn in the perovskite structure. The significant red shift of bandgap is measured for the intermediate compounds with x = 0.8 and 0.6 which shows the smallest bandgap of about 1.17 eV using PDS. Moreover, the values for Urbach energy suggest that the $CH_3NH_3Sn_xPb_{1-x}I_3$ compounds with higher content of tin have a higher level of electronic disorder. Photoluminescence spectroscopy further confirm the red-shift in the bandgap of intermediate compounds of $CH_3NH_3Sn_xPb_{1-x}I_3$ in which a PL peak at 1035 is observed for x=0.8. Finally, the possibility of triplet energy transfer between synthesized low bandgap perovskite and tetracene were investigated. However, a negative feature from tetracene in the excitation scan as well as no magnetic field PL response of bilayer films shows there is no significant energy transfer between the layers, which leads to the future investigation of the possible charge transfer between perovskite and tetracene.

8.2 Hole Extraction via Tetracene Layers Gives Highly Luminescent and Stable Metal Halide Perovskite Devices

8.2.1 Introduction

As we stated earlier, non-radiative losses remain significant in perovskite devices, mainly originating from interfacial defects, that prohibit them from reaching their full potential[79]. An effective way to remove these defects is to introduce passivation treatments and interlayers between the perovskite and the electron/hole transport layers (ETL/HTL)[288–290]. It has been intensively shown that treating mesoporous-TiO_2, arguably the most common ETL in perovskite solar cells (PSC), reduces electron trap state density and enables faster electron transport[177,291–293]. The interface between perovskite and the HTL (e.g., doped 2,2′,7,7′-tetrakis(N,N-di-p-methoxyphenyl-amine)9,9′-spirobifluorene denoted as Spiro-OMeTAD) is equally crucial and to obtain maximal PCE this needs to be enhanced simultaneously (e.g., to achieve faster hole transport). We and others have recently shown that p-type contact is the main origin for the quenching of photoluminescence (PL) in perovskite devices and passivation interlayers can significantly enhance the PL quantum efficiency in the complete device architecture[58,62,294]. However, many of these passivation approaches can potentially introduce some side-products that disrupt the long-term stability of perovskite solar cells[263].

An efficient strategy to accelerate charge transport through the layers of a photovoltaic device is to utilize a graded bandgap concept[295]. For PSCs, this has been shown through stacking two different perovskite layer to obtain a graded bandgap that improves the output photocurrent significantly[296]. Since operational stability is also a prerequisite for PSC commercialisation it is important that any interlayers and treatments introduced to the PSC do not reduce its lifetime [297]. Sources of instability in PSCs not only originate from its individual layers (e.g. perovskite layer[298] and charge transporting layers[299,300]) but also from their interfacial regions[301,302]. The stability of PSCs has improved significantly through changes to the perovskite composition[303,304] (e.g. doping with monovalent cations[58,194,206]) and substitution of organic HTLs for inorganic counterparts[305–307]. However, the overall device stability is still far from the industrial standard where the most prominent source of instabilities arises from HTL electrode (e.g. Spiro-OMeTAD), for example, the migration of dopants[308] (e.g. Li) and metal from the PSC electrode, particularly at elevated temperatures[309]. Therefore, development of HTLs with clean interfaces and long-term device stability is still one of the major challenges.

Herein, we demonstrate a dopant free p-type electrode with ultra-clean interfaces via thermal evaporation of tetracene on top of perovskite. Tetracene is a molecular organic semiconductor and the four-ringed member of the acene series; common applications of this material include organic field-effect transistors and organic light emitting diodes. As an efficient singlet exciton fission material, tetracene also shows potential for energy down-conversion applications. Given its location behind the perovskite layer in our PSCs however, and the mismatch in energy levels that enable energy transfer, we expect that its ability to absorb light and contribute to the PSC photocurrent will be limited. On the other hand, tetracene as a wide bandgap semiconductor with a favourable highest occupied molecular orbital (HOMO) level[282], can be a suitable HTL for perovskite solar cells. To date, this is the first report that employs tetracene as a HTL in perovskite solar cells. In order to obtain highly efficient and barrier free hole-extraction to the top electrode (e.g. gold), we show that it is advantageous to deposit a capping layer of Spiro-OMeTAD, where gradated HTLs accelerate the injection of holes from perovskite to the external circuit in PSCs. We further demonstrate external photo-luminescence quantum yields of 15% for perovskite/tetracene/Spiro samples and, for complete devices, PCEs of up to 21.5%, both indicating very clean interfaces. These devices also demonstrate longer lifetimes under 550 hours continuous illumination, preserving more than 90% of their initial efficiency compared to only 70% for control PSCs, suggesting that tetracene acts as an effective

barrier towards extrinsic ion migration from the PSC electrode. Our work represents an important step towards realising PSCs that exhibit high efficiency and long-term stability.

8.2.2 Morphological characterisation

In this study, we use the state of the art rubidium doped multiple cation based perovskite, $Cs_{0.06}FA_{0.79}MA_{0.15}Pb(I_{0.85}Br_{0.15})_3$, where MA = methylammonium, CH_3NH_3; FA = formamidinium, $CH_3(NH_2)_2$, by mixing the precursor solution with rubidium iodide (RbI) stock solution. It is notable that this composition shows one of the lowest non-radiative losses in perovskite solar cells with reasonable device stability[58]. Furthermore, we use fluorinated-tin oxide/compact-TiO_2/mesoporous-TiO_2/Perovskite/Spiro-OMeTAD/Au as the standard device architecture, hereafter denoted as Spiro, and an equivalent architecture with tetracene evaporated onto the perovskite layer with a capping layer of Spiro, hereafter denoted Spiro-Tc. In Figure 8.14, we show the surface morphologies of different layers using top-view scanning electron microscope (SEM) at different magnifications. Whereas both tetracene and perovskite form compact polycrystalline films containing micron-sized grains (Figure 8.14 parts a-c), Spiro adopts a conformal coating (Figure 8.14 d), ensuring total surface coverage of the combined HTLs.

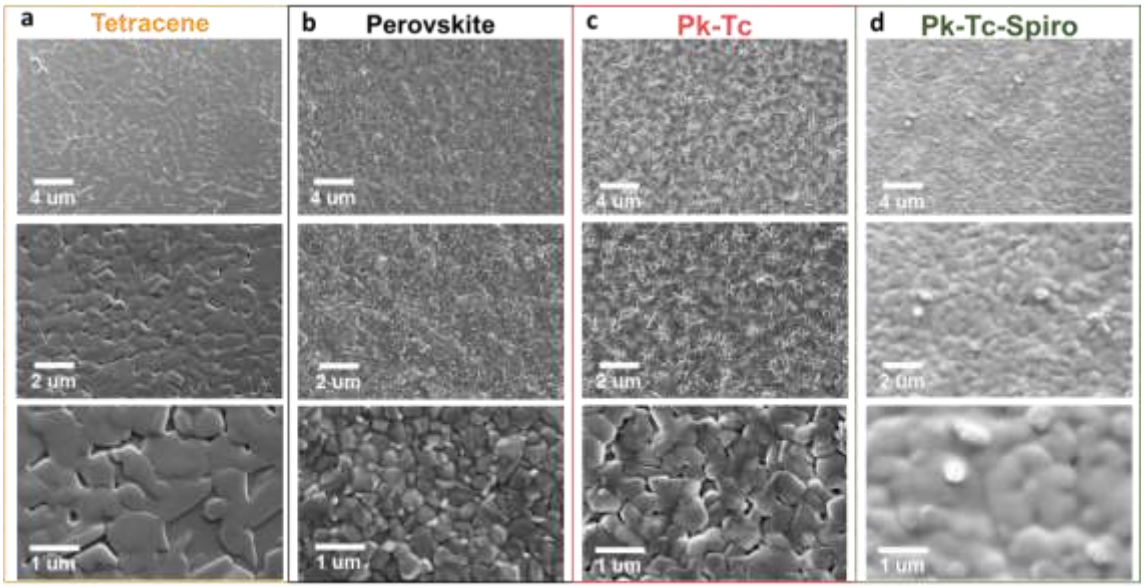

Figure 8.14. Scanning electron microscopy images. Top view SEM of (a) tetracene single layer, (b) perovskite, (c) perovskite/tetracene and (d) perovskite/tetracene/Spiro films at three different magnifications. Note that Pk and Tc refer to perovskite and tetracene, respectively.

8.2.3 Optoelectronic characterisation

In Figure 8.15a, we show the normalized UV-vis absorption spectra of tetracene and perovskite in different configurations. The three absorption peaks of tetracene that originate from its vibronic structure remain present in the Pk-Tc and Pk-Tc-Spiro films. In Figure 8.15b, we present photothermal deflection optical absorption spectroscopy (PDS) data that provides insight into sub-bandgap states and energetic disorder in each sample. We observe that the sub-gap state in the double layer of Pk-Tc matches with the pure Tc sub-gap. Furthermore, there is no change in the bandgap of perovskite upon the introduction of other layers. We observe a broad peak at low energies for the samples containing a Spiro layer that is attributed to oxidized Spiro[310].

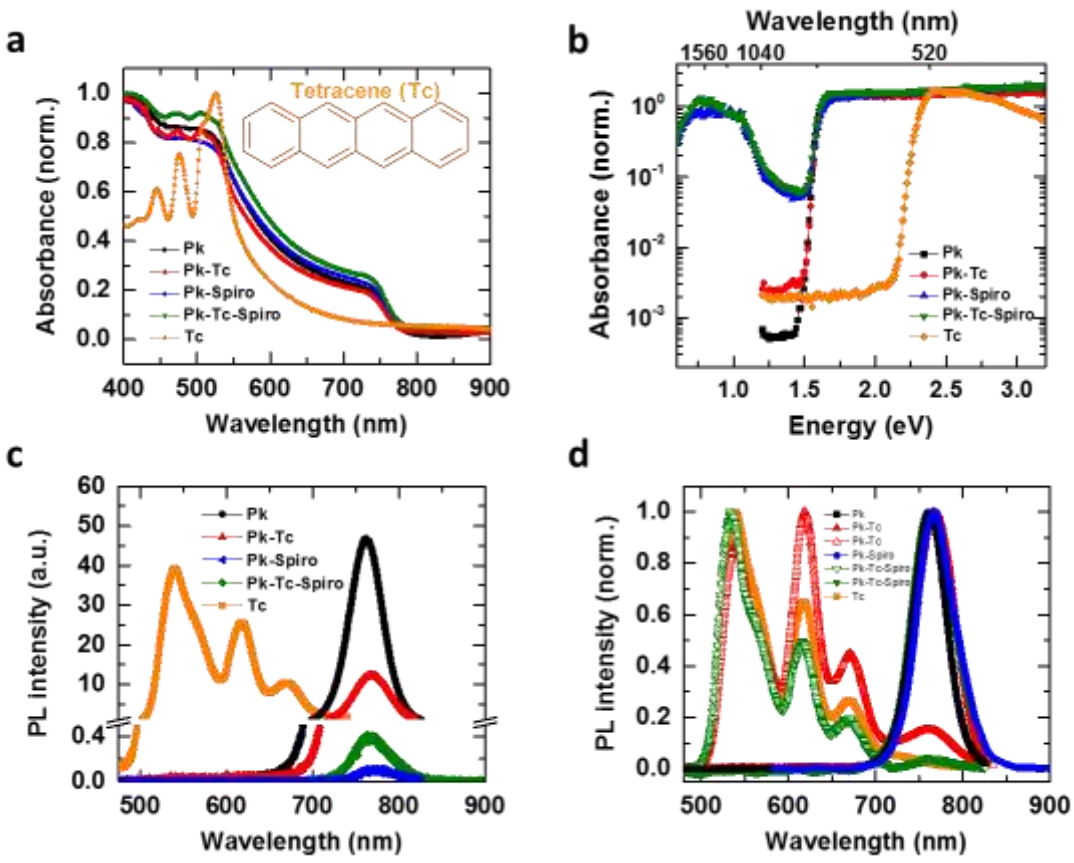

Figure 8.15. Optical absorption and emission properties. (a) UV-vis absorption spectra, (b) Photothermal deflection optical absorption spectroscopy, (c) photoluminescence, (d) Normalized PL spectra, excitation at 407 nm, of the single, double and triple layer of perovskite, Spiro and tetracene. The front (HTL side) and back (perovskite side)

photoluminescence excitation showed as open and closed symbols, respectively. The breaks in panel c is from 0.5 to one.

In Figure 8.15c, we show the corresponding steady-state photoluminescence (PL) spectra of the above-mentioned films. Photoluminescence from tetracene in the perovskite/tetracene sample is not detected when exciting the perovskite layer first, an observation that can be explained by the large optical density of the perovskite at the excitation wavelength. However, if we illuminate the samples from the tetracene side its luminescence can be measured (Figure 8.15d). As expected, the PL of perovskite at 770 nm is quenched significantly when the material is in contact with the charge extracting layers, both Spiro and tetracene. This confirms that tetracene can act as an efficient hole extraction layer when it is interfaced with perovskite. In Figure 8.16, we show the PL spectra for the tetracene and tetracene-Spiro films where the huge quench in the PL represents the efficient hole transfer between tetracene and Spiro.

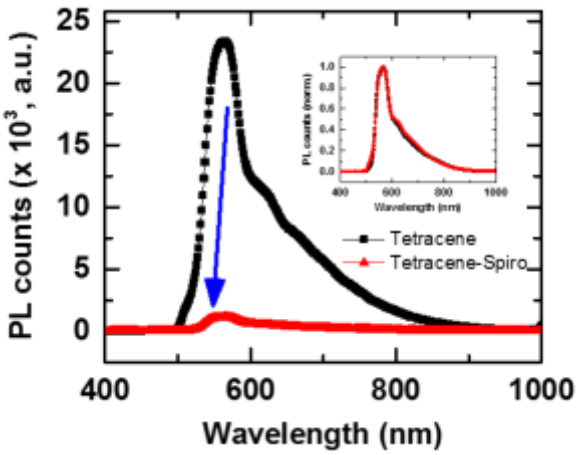

Figure 8.16. Photoluminescence spectra, excitation at 405 nm, of the Tetracene and Tetracene-Spiro layers. Inset: Normalized PL spectra for these films.

A solar cell's external luminescence efficiency is one important factor that must be maximised to ensure device operation close to its theoretical limit. The p-type electrode is the main source of luminescence quenching in the perovskite device architectures[62] and therefore providing a

clean interface between perovskite and HTL is essential to maximise the external luminescence in PSCs. In Figure 8.17, we show time-resolved photoluminescence decays and PLQE for the perovskite when interfaced with different HTL configurations. We found that charge-carrier recombination of perovskite in contact with tetracene is slower and more radiative compare to Spiro. The PLQE drop form 21% to 4% for Perovskite-Spiro (by a factor of 5.2) compare to significantly lower decrease to a factor of 1.4 (to 14.8%) for perovskite-tetracene-Spiro configuration indicating reduced interfacial non-radiative recombination and cleaner interface in Perovskite/tetracene (Figure 8.17b). At lower injection condition (lower fluences) where the PL decay is dominant through the non-radiative process rather than extraction process, we observe a rapid decay followed by a long tail, indicating fast charge collection and longer lifetime for the charge carriers in Perovskite-tetracene-Spiro compare to the quenched PL after the slower injection for the Perovskite-Spiro (Figure 8.18). These results further confirm lower non-radiative recombination and cleaner interface in perovskite-tetracene.

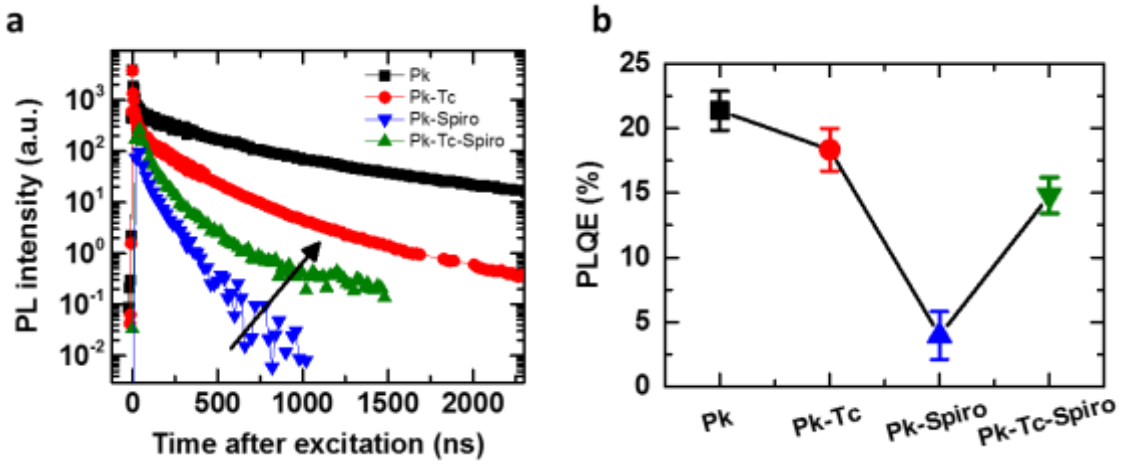

Figure 8.17. Luminescence properties of the perovskite when interfaced with different p-type contacts. (a) Time-resolved PL decays of the films with excitation at 400 nm and a pulse fluence of 0.05 μJ.cm^{-2} (~1.5 × 10^{15} cm^{3}, equivalent to about 1 sun). (b) External PLQE of the perovskite interfacing with hole-transport layers in different configuration measured under illumination with 532-nm laser at an excitation intensity equivalent to approximately one sun (60 mW.cm^{-2}). Note that Pk and Tc refer to perovskite and tetracene, respectively.

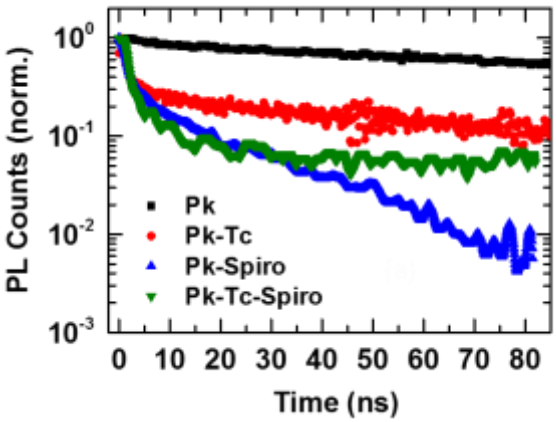

Figure 8.18. Time-resolved PL decays of the films with excitation at 407 nm and pulse fluence of 0.01 μJ.cm^{-2}. Note that Pk and Tc refer to perovskite and tetracene.

Furthermore, we extracted the setup limited (time resolution about 1.5 ns), initial photoluminescence signal, $PL_{t=0}$, that has a direct correlation with the charge extraction in the thin film[249]. We observe that the fastest hole extraction occurs in the triple layer of perovskite-tetracene-Spiro (Figure 8.19). This confirms that tetracene can act as an efficient interlayer for hole transfer, leading to efficient extraction from the perovskite layer into the external circuit. This can be attributed to the mobility mismatch between perovskite and tetracene that can enhance the charge dissociation.

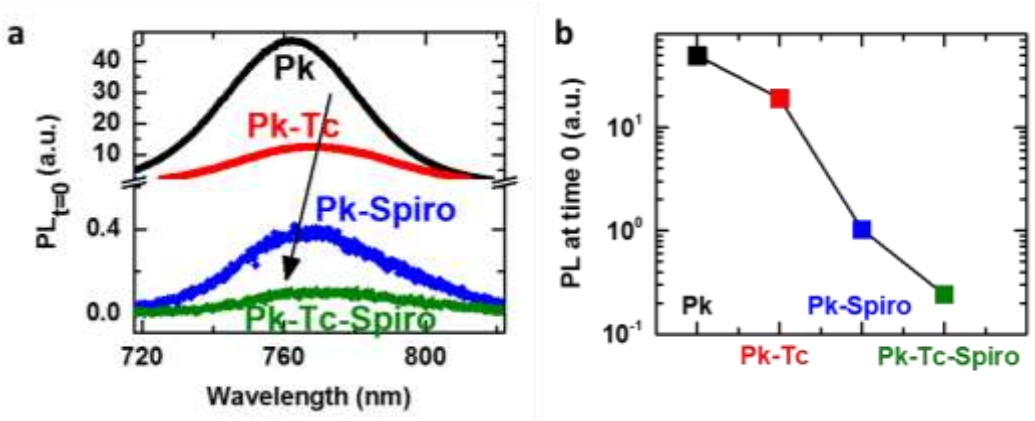

Figure 8.19. (a) Photoluminescence spectra and (b) the initial PL values at 1.5 ns after excitation at 400 nm with a 100 fs laser pulse. Note that Pk and Tc refer to perovskite and tetracene, respectively.

8.2.4 Photovoltaic characterisation

To validate our findings, we fabricated complete solar cells using the device architecture fluorinated-tin oxide (FTO) / compact-TiO_2 (~30 nm) / thin-mesoporous TiO_2 (~200 nm) / perovskite (~500 nm) / tetracene (~120 nm) /Spiro-OMeTAD (~150 nm) / Au (80 nm), a SEM cross sectional image of which is shown in Figure 8.20a. In Figure 8.20b, we show the respective energy levels of each layer as determined by ultraviolet photoelectron spectroscopy (UPS) and the calculated bandgaps from the absorption spectra. As expected, the tetracene highest occupied molecular orbital (HOMO) level lies between the valence band of perovskite and the HOMO level of Spiro. This graded bandgap can facilitate effective hole injection from perovskite into the top electrode as we observe the fastest hole charge extraction from the triple layer of Perovskite-tetracene-Spiro (Figure 8.19). Furthermore, tetracene acts as an efficient electron blocking layer due to the significant difference between its lowest unoccupied molecular orbital (LUMO) and the conduction band of perovskite, a characteristic could therefore diminish carrier recombination[311].

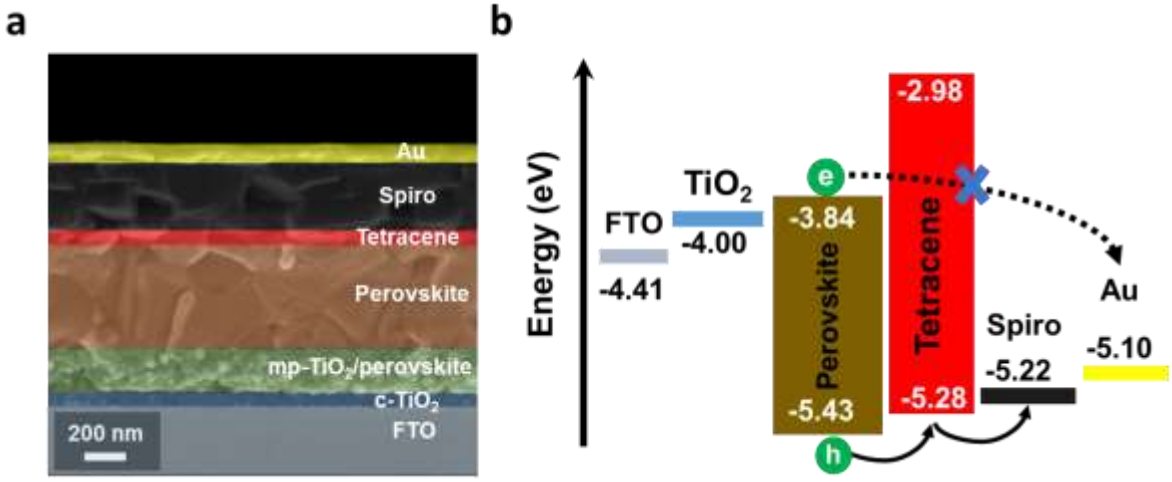

Figure 8.20. Solar cell architecture and energy diagram. (a) A coloured high-resolution cross-sectional SEM image and (b) energy level diagram obtained from UPS measurements of a complete solar cell including tetracene with Spiro capping layer. The perovskite composition is Rb-passivated $Cs_{0.06}FA_{0.79}MA_{0.15}Pb(I_{0.85}Br_{0.15})_3$.

In Table 8.1 and Figure 8.21a, we show device data for PSCs containing only tetracene as a HTL with average PCE of 14.3%. To date, this is the highest PCE reported for a dopant free linear acene derivative in perovskite solar cells that is relatively cost effective compare to Spiro-OMeTAD. However, the average performance of these devices is lower than the Spiro based solar cells (18.5% on average). This difference is primarily attributed to the poor ohmic contact between tetracene and Au leading to higher series resistance as it is evident from the lowest average fill factor for the tetracene-based PSCs (Figure 8.23). To address this issue, we employ a capping layer of Spiro to cover the tetracene layer and make a superior contact with the top electrode. We then explored three different thicknesses of tetracene via thermal evaporation: 60 nm, 120 nm and 240 nm. Based on the photovoltaic results shown in Table 8.2 and Figure 8.22, we find that 120 nm of tetracene is the optimum thickness for achieving the maximum photocurrent and the highest enhancement in overall PCE.

Table 8.1. Photovoltaic parameters derived from J-V measurements of champion solar cells. The V_{oc} loss is the difference between the bandgap (1.59 eV, extracted from the EQE onset) radiative limit V_{oc} and measured V_{oc}.

Device		J_{sc} [mA.cm^{-2}]	V_{oc} [V]	Fill factor	PCE [%]	V_{oc} loss[V]
Tetracene	Reverse	20.49	0.97	0.72	14.26	0.35
	Forward	20.23	0.95	0.71	13.70	
Spiro	Reverse	22.68	1.125	0.76	19.30	0.19
	Forward	22.64	1.116	0.75	18.94	
Tetracene-Spiro	Reverse	23.37	1.180	0.78	21.50	0.13
	Forward	23.26	1.178	0.77	21.09	

In Figure 8.21b, we show forward and reverse current-voltage *(J-V)* curves of champion devices for Spiro and Tc-Spiro under dark and full simulated sunlight (1 sun), with the extracted parameters given in Table 8.1 (see Figure 8.23 for device statistics). We find that device PCE, as calculated from current density-voltage (*J-V*) scans, increases from 19.3% to 21.5% when employing Spiro capping layer between tetracene and gold, with a maximum stabilized PCE of 21.4%. IV hysteresis, commonly observed in PSCs[144], is negligible in our devices, confirming the high quality of the perovskite layer and its limited susceptibility for ion migration[239]. The remarkable increase in PSC open-circuit voltage (V_{oc}) from Spiro to

tetracene-Spiro devices, 1.12 to 1.18 V, is consistent with the enhanced PLQE and reduced non-radiative recombination of perovskite when contacted with tetracene-Spiro (data in Figure 8.17 and related discussion). The increase in short-circuit current (J_{sc}) for the tetracene/Spiro PSCs, from 22.7 mA.cm^{-1} to 23.4 mA.cm^{-1}, is also consistent with the increased hole extraction efficiency. Furthermore, the higher average fill factor in Tetracene-Spiro devices can attributed to the more efficient hole transfer in these devices that leads to lower series resistance due to the presence of gradated HOMO level of Tetracene and the HOMO level of Spiro (Figure 8.20).

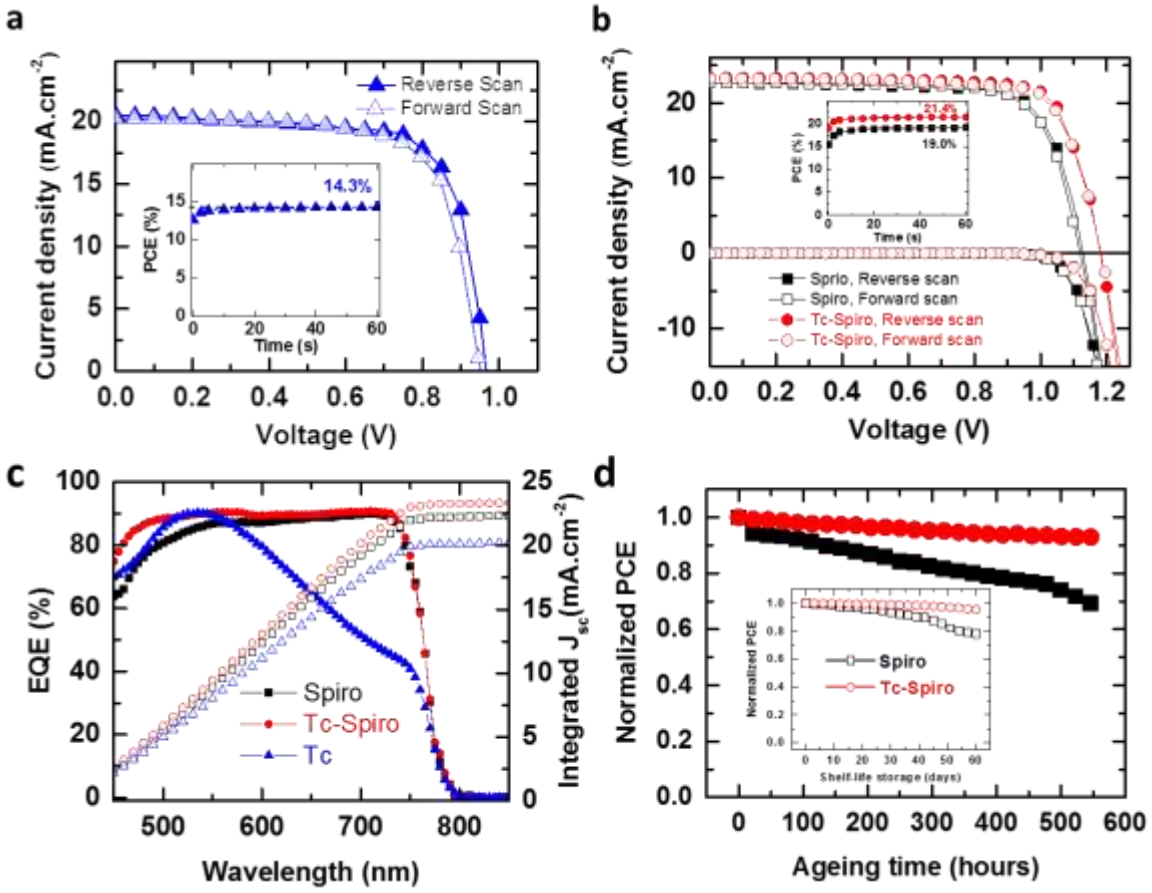

Figure 8.21. Enhanced photovoltaic performance and stability of solar cells. Forward (open symbols) and reverse (closed symbols) J-V curves of champion solar cells with (a) tetracene, (b) Spiro and tetracene-Spiro as HTL, measured under simulated solar illumination (AM1.5, 100 mW.cm^{-2}) and dark conditions. Inset: Stabilised power output under the same conditions. (c) Stability curve of the solar cells at maximum power point under continuous AM 1.5 G illumination, N_2 atmosphere and stabilised temperature of 55 ºC. Inset: Shelf life of devices stored in a nitrogen glovebox over two months and tested regularly under full AM1.5 simulated

sunlight. (d) External quantum efficiencies (EQE) and integrated short-circuit current for Spiro, Tc-Spiro and Tc based solar cells. Note that Tc refer to tetracene.

Table 8.2. Device parameters for different thickness of thermally evaporated Tetracene interlayer measured under full-simulated solar illumination conditions (AM1.5, 100 mW.cm^{-2}). Note that Tc refer to tetracene.

Device	J_{sc} [mA.cm^{-2}]	V_{oc} [V]	Fill factor	PCE [%]
Spiro	21.8	1.080	0.65	15.36
60 nm Tc-Spiro	22.4	1.122	0.66	16.68
120 nm Tc-Spiro	23.0	1.165	0.70	18.76
240 nm Tc-Spiro	22.5	1.176	0.61	16.12

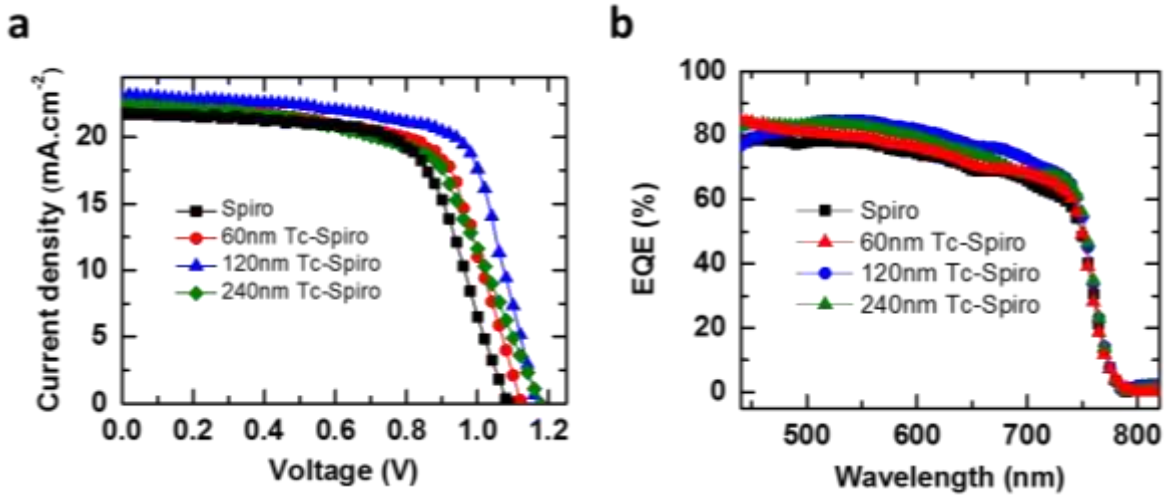

Figure 8.22. (a) J-V characteristics and (b) external quantum efficiencies (EQE) of solar cells with different thickness of thermally evaporated Tetracene interlayer, measured under simulated solar illumination (AM1.5, 100 mW.cm^{-2}). Note that Tc refer to tetracene.

In Figure 8.21c, we show J_{sc} values obtained from the *J-V* characteristics is well matched (within 4%) with the external quantum efficiency (EQE) obtained by the integration of the spectral response. In Figure 8.21d, we conducted stability tests at maximum power conditions

under simulated solar illumination (1000 Wm^{-2}). The ambient temperature during these tests was 55 ^{o}C and the atmosphere was dry N_2. We observe a remarkable enhancement in the stability when using gradated HTLs of tetracene and Spiro, with such devices retaining over 90% of their initial performance after 550 hours of continued operation. In contrast, only 68% of the initial PCE value was maintained for the Spiro devices. Furthermore, we found a negligible shelf-life performance of the Tc-Spiro device over two months, >95% of the initial PCE was retained. These stability figures are amongst the highest reported for PSCs. The significant enhancement in the stability of Tc-Spiro based PSCs likely originates from clean interface between tetracene and perovskite as well as presence of tetracene acting as a barrier layer towards the migration of dopants from Spiro-OMeTAD and metal diffusion from the Au electrode into the perovskite.

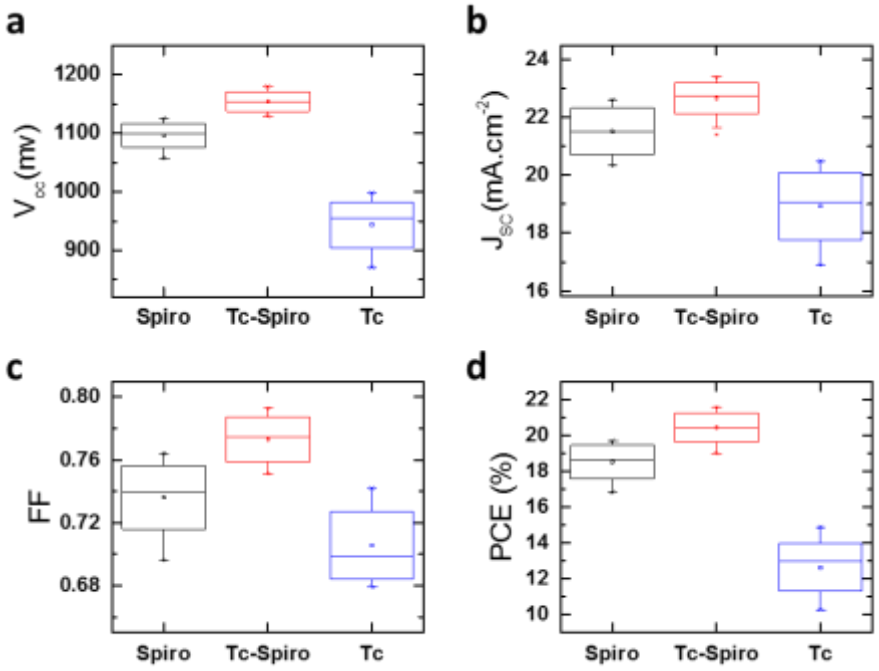

Figure 8.23. (a-d) Box and whisker plots to summarise the statistics of photovoltaic parameters of Spiro, Tc-Spiro and Tc based perovskite solar cells, 15 of each that measured under full simulated solar illumination conditions (AM1.5, 100 mW.cm^{-2}) and scanned at a rate of 15 mV/s. The boxes represent the interquartile range, with the median represented by the line dividing the boxes, and the whiskers are determined by the 5th and 95th percentiles. The mean is given by the open square symbols, and the starred symbols represent the maximum and minimum values. Note that Tc refer to tetracene.

To probe the impact of gradated HTLs on charge recombination in the PSC, we performed light intensity dependent PV characterization on the Spiro and tetracene-Spiro devices (Figure 8.24). In Figure 8.25a, we demonstrate the power law dependence of the J_{sc} on incident light intensity, where tetracene-Spiro solar cells exhibit α=0.99 compare to α=89 for Spiro devices, suggesting enhanced charge extraction in the former[312]. In Figure 8.25b, we show the V_{oc} as a function of incident light intensity on a linear–log scale where the ideality factor (n) calculated from the slope is representative of the charge carrier recombination process[313]. It is noted that for bimolecular charge carrier recombination the ideality factor n approaches unity, whilst for Shockley Reed Hall (SRH) trap assisted recombination n approaches two[314]. We found the ideality factor for Tc-Spiro devices approaches n=1.01, pointing towards the bimolecular type of carrier recombination. This shows that the carriers in the Tc-Spiro devices recombine primarily via a band-to-band radiative process where traps can be passivated within thermal equilibrium condition, enabling the Tc-Spiro devices to reach higher PCE and minimal V_{oc} losses (Table 8.1). However, for Spiro devices the ideality factor is 1.37, resulting in an SRH type trap-assisted charge carrier recombination process primarily at the charge collection interfaces. This can further confirm the cleaner interfaces between perovskite and the HTL (i.e. tetracene) in Tc-Spiro devices. In addition, suppression of SRH type recombination in Tc-Spiro devices reflected in the significant enhancement of the corresponding average fill factor[25] (Figure 8.23).

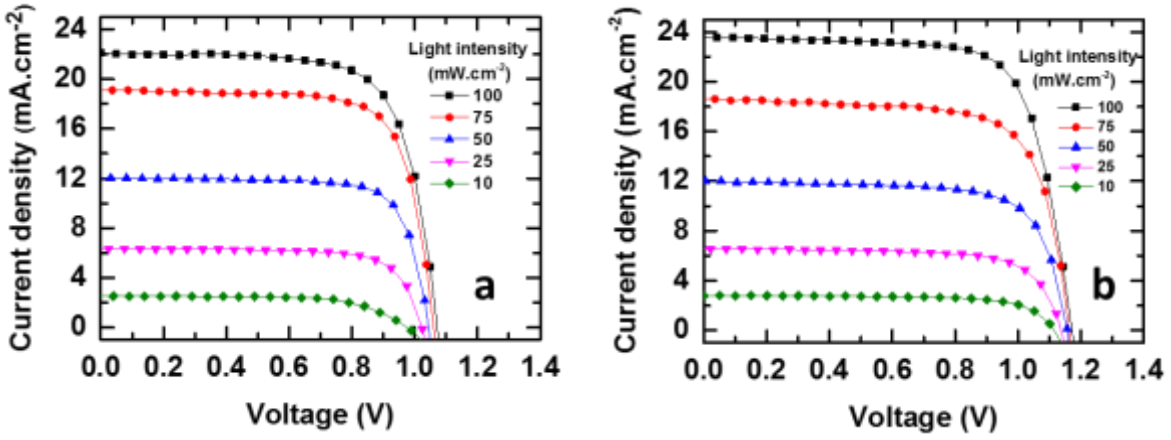

Figure 8.24. J-V characteristic of (a) Spiro and (b) Tc-Spiro under different light intensities.

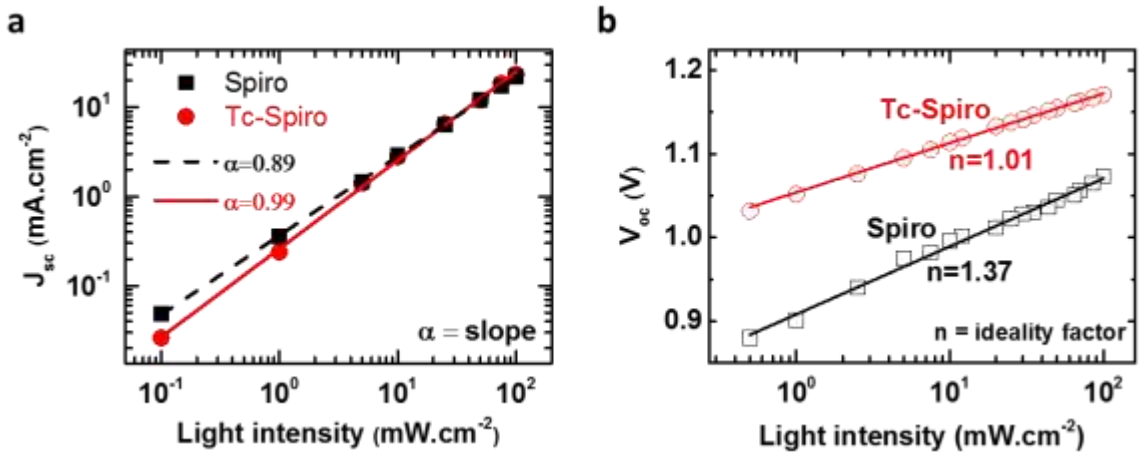

Figure 8.25. (a) Short-circuit current (J_{SC}) and (b) open-circuit voltage (V_{OC}) Spiro and Tc-Spiro devices plotted versus incident light intensity. Note that Tc refer to tetracene.

8.2.5 Charge transport characterisation

In order to investigate the hole transport behaviour in different configuration of HTLs, we fabricated hole-only (FTO/Perovskite/HTL/Au) devices for SCLC measurement. In Figure 8.26a, we show the plot of the current density (J) at 0.3 V where the transport is expected to be hole-injection limited. We observed a remarkable enhancement in the *J* for tetracene-Spiro devices compared to Spiro only devices. Furthermore, we estimated the activation energy for hole transport (E^h_A) from temperature-dependent *J-V* measurements (Figure 8.27). The activation energy is then estimated from a typical Arrhenius fits to current density in the $J \propto V^2$ regime. In this device geometry, the magnitude of current density has a contribution from the bulk conductivity of the perovskite layer and the effective injection barriers at the electrodes. Considering the fact that only the HTL on top of the perovskite film is varied in these devices, this variation in the current density and activation energy of these hole-only devices could be attributed to the decreased injection barrier for hole transport due to the gradated energy levels of tetracene and Spiro as the HTL. The observed enhancement in the current density and the decrease in E^h_A are consistent with the enhancement in the J_{sc} and decrease in the recombination, which could boost the V_{oc}, resulting in an overall improvement in the PCE.

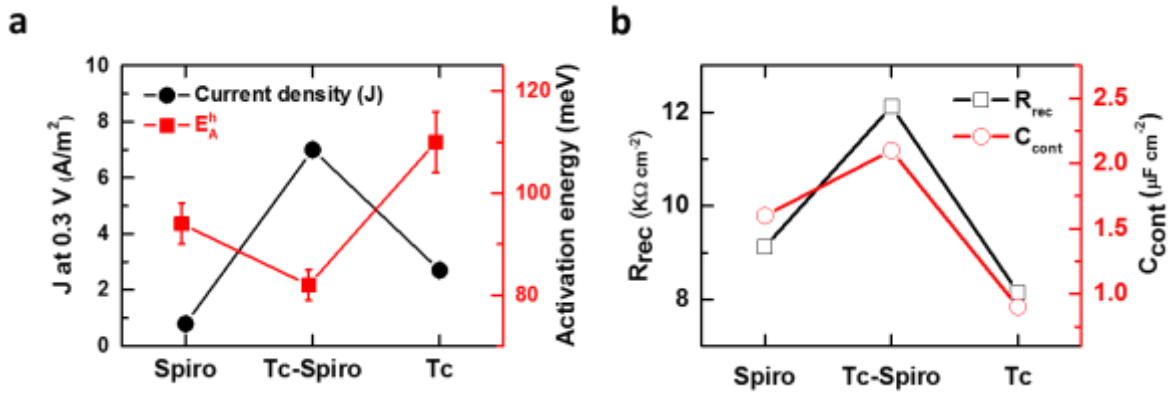

Figure 8.26. Enhanced hole transport in PV devices. (a) The trends in current density (J) and activation energy (E^{h}_{SCL}) for Spiro, Tc-Spiro and Tc based devices extracted from J-V characteristics of hole only devices (FTO/Perovskite/HTL/Au). (b) The evolution for recombination resistance (R_{rec}) and contact capacitance (C_{cont}) extracted from the EIS measurements on the complete solar cells consisting of different HTLs (see Figure 8.28).

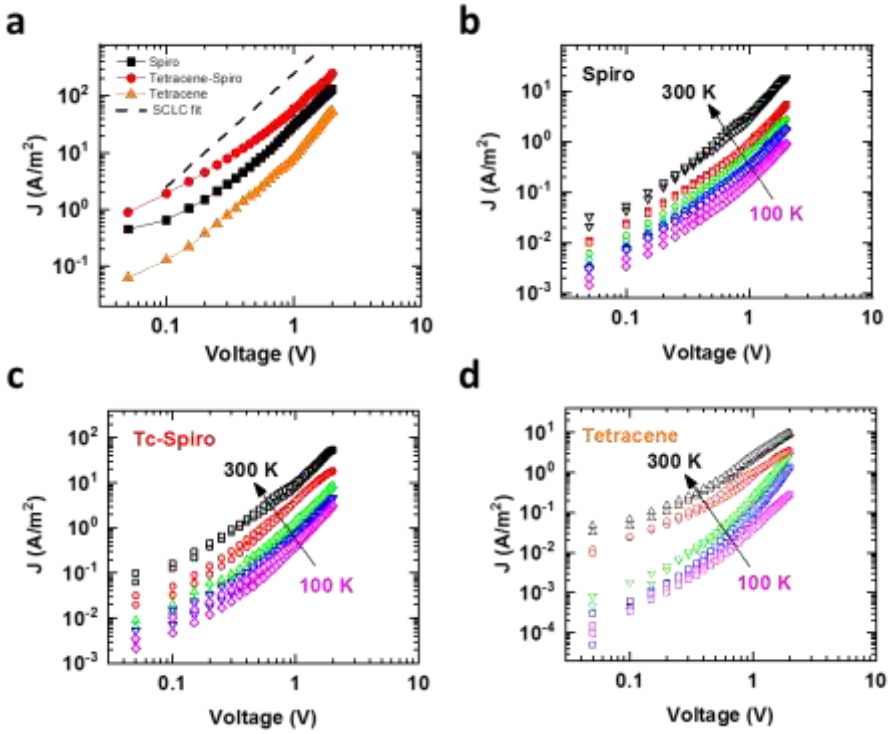

Figure 8.27. (a) I-V characteristic of hole only perovskite devices with different HTL measured at room temperature. I-V characteristic of (b) Spiro, (c) Tc-Spiro and (d) Tetracene hole only

devices (FTO/perovskite/HTL/Au) at different temperatures, utilized for estimating the SCLC activation energy for hole transport. The temperature gradient between each curve is 50 K.

To understand further the transport mechanism, we performed electrochemical impedance spectroscopy (EIS) on PSC fabricated with different HTLs. We performed the EIS measurement on the complete solar cells operating under one sun illumination and bias conditions close to the open-circuit conditions (Figure 8.28a-c). The EIS spectra were fitted with an appropriate equivalent circuit to estimate parameters related to the charge recombination and polarization relaxation of the perovskite layers (Figure 8.27b and Figure 8.28d). After fitting the equivalent circuit to the EIS data, we found the recombination resistance (R_{rec}) to be maximum for tetracene-Spiro that is consistent with the trend of higher J_{sc} magnitude (Table 1). Furthermore, we observe an enhancement in the contact capacitance (C_{cont}) of the complete tetracene-Spiro devices over Spiro devices that is consistent with the V_{oc} trend (Table 8.2).

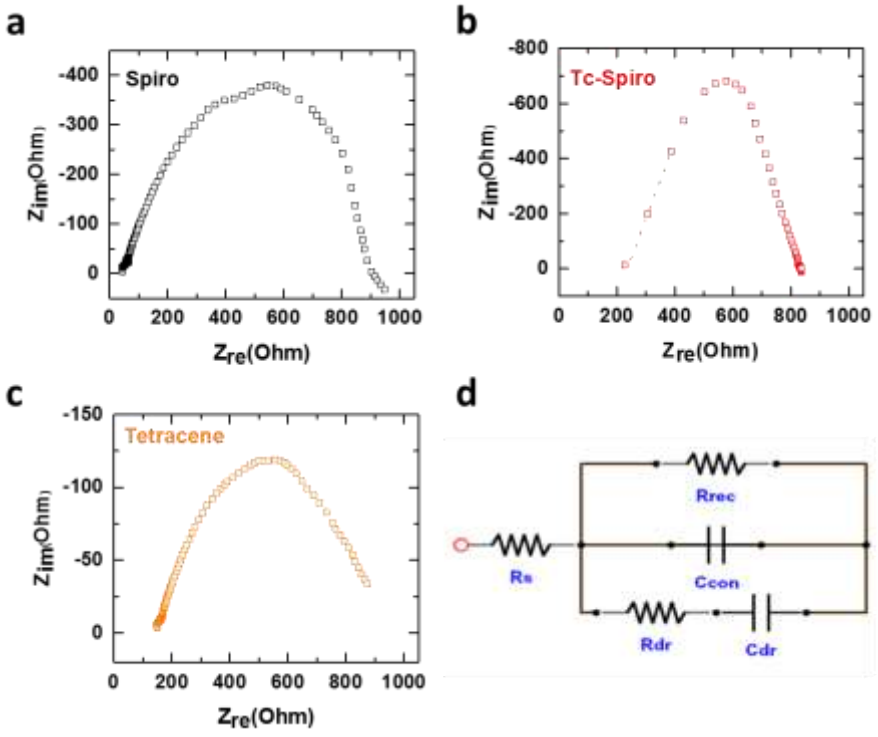

Figure 8.28. Typical EIS spectra measured on the perovskite solar cells with (a) Spiro, (b) Tc-Spiro and (c) Tetracene as HTL. (d) Equivalent circuit for electrochemical impedance spectroscopy (EIS) measurement.

8.2.6 Conclusions

In summary, we have demonstrated that thermally evaporated, dopant free tetracene can act as an efficient hole transport layer in perovskite solar cells while maintaining high luminesce yield of perovskite in the device architecture. However, due to the poor ohmic contact between tetracene and metal electrode, we found that depositing a capping layer of Spiro-OMeTAD is not only beneficial to make a superior interface with top contact, but also facilitate the hole injection from perovskite into the external circuit via gradated energy levels. We performed a series of measurements including pulsed PL, time resolved PL and external PLQE to confirm faster hole injection perovskite to HTL, slower and more radiative charge carrier recombination of the perovskite when interfaced with tetracene-Spiro (e.g. external photoluminescence yield of 15% for perovskite-tetracene-Spiro compare to 5% for perovskite-Spiro). These results collectively show the beneficial effects of an energy level cascade at a charge collection electrode as well as a clean interface between perovskite and tetracene minimising the interfacial non-radiative recombination losses. We further validate the applicability of our findings by fabricating complete solar cells whose PCE can exceed 21%. Open circuit voltages in the enhanced devices reach 1.18V, indicating very low voltage losses. Finally, the stability tests under continuous illumination show outstanding improvement in the stability of the tetracene-Spiro devices. Our study paves the way towards minimization of interfacial losses and stabilization of high efficiency perovskite solar cells.

Chapter 9

Conclusions and Future Work

This chapter would review on the general findings of this thesis and provide some possible directions for future research.

9.1 Conclusions

This thesis focussed on optoelectronic and structural properties of metal halide perovskites that are chemically modified, doped and passivated using different approaches and development of charge transport layers to enhance charge collections, stability and photovoltaic performance of perovskite solar cells. A wide range of material characterisations were used in this thesis to probe the key properties of the metal halide perovskite semiconductors and the interfaces with the charge contact layers upon the applied modifications such as doping and passivation. The general finding in this work is that hybrid organic-inorganic metal halide perovskite show remarkably high tolerant to additives and different passivation routes and their properties can be remarkably tuned towards an ideal semiconductor for optoelectronic applications. The other general conclusion form this work is that the interfaces in perovskite solar cells plays a very important role particularly at the charge collection layers which are the main quenchers of the luminescence in the devices. Therefore, development of effective passivation approaches to clean the interfaces form defects is essential in order to enable metal halide perovskites to reach their full potential in optoelectronic devices reaching their theoretical limits.

9.2 Outlook and Future Prospects

The new directions for continuing work into the further enhancement of semiconductor quality in metal halide perovskite materials for optoelectronic applications open up many avenues for a research in this field. Despite rapid progress in this field, perovskites are still far from their full potential in optoelectronic devices such as solar cells and light emitting diodes (LEDs). Particularly, in perovskite photovoltaic devices apart from the perovskite as the absorber layer, charge transport contacts and their interfaces with the active layer are equally important to achieved highly stable and efficient perovskite solar cells. Below, I summarise a number of future prospects on the main topics of thesis.

9.2.1 Development of alternative electron transport layer

In Chapter 2, we applied a chemical treatment and a modification in the nanostructured of TiO_2 to enhance the collection efficiency of electrons and therefore the photovoltaic performance of the subsequent devices. However, utilizing titania needs a high temperature annealing step (e.g. 500 ^{o}C) and the developed chemical treatment add an extra annealing step to the device fabrication routs. Therefore, this not only limits the application of the resulting devices on the

rigid substrates, but also is substantially increase the manufacturing cost of perovskite solar cells.

There are several alternative to titania that can be processed at lower temperatures and in particular SnO_2 is a favourable candidate due to energy matching with various perovskites as well as the flexibility in fabrication routes. The other possible solution is to use the planar architecture (e.g. p-i-n or n-i-p geometry) which opens up many options including organic electron transport layers such as C60, PCBM as it does not need to be mesostructured.

9.2.2 Incorporation of monovalent cation additives in complex perovskite compositions and tracking their location

As we show in Chapter 5, monovalent cation additives with similar ionic radii to lead (i.e. Na, Cu and Ag) can significantly enhance the structural and optoelectronic properties of the $CH_3NH_3PbI_3$ and therefore increase the photovoltaic parameters of the resulting solar cells. Recently, we and others show that more complex composition of perovskite materials (e.g. mixed cation lead mixed halide) have superior stability and semiconductor quality. It would be indeed very interesting to explore the effect of these monovalent cations in other perovskite compositions to further improve their crystallinity and optoelectronic properties.

In the second part of Chapter 5, we utilize several advanced material characterisation techniques as well as modelling to understand the chemical distribution of these monovalent cations and their impact on the band structure of the $CH_3NH_3PbI_3$ perovskite. Although we could detect experimentally all the additives besides their low quantity, their location in the film, the doping efficiency and exact nature of doping is not clear. Further experimental studies in particular solid states Nuclear Magnetic Resonance (NMR) spectroscopy is required to address the remaining mysteries in this system.

9.2.3 Potassium passivation approach in other perovskite compositions, tandem solar cells and coloured-light-emitting diodes

In Chapter 6, we demonstrate a novel passivation approach using potassium halide passivating the non-radiative recombination pathways and leading to high luminescence efficiencies in the perovskite films. We show the flow of excess halides are immobilized in the form of benign, potassium-rich, halide-sequestering species at the grain boundaries and surfaces, thereby inhibiting halide migration and suppressing any additional non-radiative decay arising from

interstitial halides. Further investigation into potassium-based passivation will be required, including its efficacy in different perovskite compositions, deposition methods and contacts, and how it could be ultimately exploited (or even mimicked, using other halide-sequestering species) to eliminate interfacial non-radiative losses and ionic migration. The combination of high radiative efficiency, excellent charge transport and photostable bandgaps makes these passivation approaches extremely promising in taking perovskite devices to their efficiency limits across a range of bandgaps.

An obvious next step is to use the stabilised large bandgap perovskite (e.g. 1.7 eV) with potassium passivation in a tandem solar cell architecture (both perovskite-perovskite tandem and silicon-perovskite tandem) investigating the operation stability of the subsequent devices, which in principle should significantly be improved. Furthermore, the remarkable enhancement in the radiative recombination in perovskite thin-films via potassium passivation opens up a promising way to not only enhance the external quantum efficiency of the coloured-LEDs, but also improve their operation stabilities. Our preliminary results on this front further validate the viability of potassium passivation approach.

9.2.4 Elimination of unwanted side-products from the monovalent cation passivation routs combined with grain coalescence

As we systematically studied the optoelectronic properties of the passivated multiple cation based perovskite with potassium and rubidium in Chapter 7, we found the alloyed perovskite are tolerant towards higher loadings of potassium than rubidium. However, in both of these passivation approaches, we observe formation of non-perovskite species particularly upon humidity exposure. Although the potassium passivation route shows higher stability towards ambient moisture, after treatment of passivated perovskite at higher humidity, we observe phase segregation and significant grain coalescence for all compositions. This ageing process in humid environment can be beneficial in one hand as the grain sizes significantly increased correlating with further enhancements in photoluminescence quantum efficiency. However, formation of potassium or rubidium species at the perovskite film surfaces can indeed perturb the charge transport. We think this controlled humidity treatment of the passivated film is a way to supress the side products form these passivation routs as all the unwanted species are accumulating at the top surfaces and it is feasible to eliminate them via choosing a relevant solvent. The resulting films will be indeed highly crystalline with large grains and enhanced

optoelectronic properties that can be used for fabrication of highly efficient and stable perovskite solar cells.

9.2.5 Demonstration of singlet exciton fission process in bilayer of tetracene and metal halide perovskite

As a continuing work to our study on the possibility of energy transfer between low-bandgap perovskite films and tetracene as a well-known down-converter that we summarised in the first part of Chapter 8, further investigations on both the perovskite layer and the interface with the fission material will be required. We show one of the first preliminary study on the possibility of singlet exciton fission process in metal halide perovskite with tetracene in this chapter and the initial results exhibit no energy transfer referring to either poor quality of interface or misalignment in the energy levels between these two materials. To address the first challenge, using deposition techniques such as hot-casting or anti-solvent treatment can significantly improve the film formation quality of the low-bandgap perovskite. For the latter challenge of energy misalignment, it is well known that by tuning the composition of the perovskite, we can tune the perovskite conduction band energy level while maintaining a constant band-gap energy, which should allow for aligning its energy levels with those in tetracene.

In the second part of Chapter 8, we show that thermally evaporated, dopant free tetracene can act as an efficient hole transport layer in perovskite solar cells while maintaining high luminesce yield of perovskite in the device architecture. However, due to the poor ohmic contact between tetracene and metal electrode, we found that depositing a capping layer of Spiro-OMeTAD is not only beneficial to make a superior interface with top contact, but also facilitate the hole injection from perovskite into the external circuit via gradated energy levels. Therefore, it is required to have an efficient dopant free hole-extraction layer between perovskite and doped-Spiro and the top contact electrode not only to prevent the extrinsic ion migration in the device architecture, but also provide a very clean interface with perovskite active layer. In order to validate and generalise this approach, further investigations on the alternative materials with similar energy levels are required.

List of Publications

1. **Mojtaba Abdi-Jalebi,** Zahra Andaji-Garmaroudi, Stefania Cacovich, Camille Stavrakas, Bertrand Philippe, Johannes M. Richter1, Mejd Alsari, Edward P. Booker, Eline M. Hutter, Andrew J. Pearson, Samuele Lilliu, Tom J Savenije, Håkan Rensmo, Giorgio Divitini, Caterina Ducati, Richard H. Friend, Samuel D. Stranks; "*Maximising and Stabilising Luminescence in Metal Halide Perovskite Device*", ***Nature***, 555, 497-501 (2018). DOI: 10.1038/nature25989.

2. **Mojtaba Abdi-Jalebi**, Zahra Andaji-Garmaroudi, Andrew J. Pearson, Giorgio Divitini, Stefania Cacovich, Caterina Ducati, Richard H. Friend, Samuel D. Stranks, "*Potassium- and Rubidium-Passivated Perovskite Films: Optoelectronic Properties and Moisture Stability*", Accepted in ***ACS Energy Lett.*** (2018).

3. **Mojtaba Abdi-Jalebi**, Meysam Pazoki, Bertrand Philippe, M. Ibrahim Dar, Mejd Alsari, Aditya Sadhanala, Giorgio Divitini, Roghayeh Imani, Samuele Lilliu, Jolla Kullgren, Håkan Rensmo, Michael Grätzel, Richard H. Friend; "*Dedoping of Lead Halide Perovskites Incorporating Monovalent Cations*", ***ACS Nano***, 12 (7), pp 7301–7311 (2018). DOI: 10.1021/acsnano.8b03586.

4. **Mojtaba Abdi-Jalebi**, M. Ibrahim Dar, Satyaprasad P. Senanayak, Aditya Sadhanala, Zahra Andaji-Garmaroudi, Luis M Pazos-Outón, Johannes M. Richter, Andrew J. Pearson, Henning Sirringhaus, Michael Grätzel, Richard H. Friend; "*Charge Extraction via Graded Doping of Hole Transport Layers Gives Highly Luminescent and Stable Metal Halide Perovskite Devices*", Submitted to ***Science Advances***, (2018).

5. Guangjun Nan, Xu Zhang, **Mojtaba Abdi-Jalebi**, Zahra Andaji-Garmaroudi, Samuel D. Stranks, Gang Lu, David Beljonne; "*How Methylammonium Cations and Chlorine Dopants Heal Defects in Lead Iodide Perovskites*", ***Adv. Energy Mater***., 1702754, (2018). DOI: 10.1002/aenm.201702754.

6. Mejd Alsari, Oier Bikondoa, James Bishop, **Mojtaba Abdi-Jalebi**, Lütfiye Y. Ozer, Mark Hampton, Paul Thompson, Maximilian Hoerantner, Suhas Mahesh, Claire Greenland, J.

Emyr Macdonald, Giovanni Palmisano, Henry J. Snaith, David G. Lidzey, Samuel D. Stranks, Richard H. Friend, Samuele Lilliu; "*In-situ Simultaneous Photovoltaic and Structural Evolution of Perovskite Solar Cells During Film Formation*", ***Energy Environ. Sci.,*** 11, pp. 383-393 (2018). DOI: 10.1039/C7EE03013D.

7. Ka Kan Wong, Azhar Fakharuddin, Philipp Ehrenreich, Thomas Deckert, **Mojtaba Abdi-Jalebi**, Richard H Friend, Lukas Schmidt-Mende, "Interface-Dependent Radiative and Nonradiative Recombination in Perovskite Solar Cells", ***J. Phys. Chem. C,*** 122 (20), pp 10691–10698, (2018). DOI: 10.1021/acs.jpcc.8b00998.

8. **Mojtaba Abdi-Jalebi,** M. Ibrahim Dar, Aditya Sadhanala, Satyaprasad P. Senanayak, Michael Grätzel, Richard H. Friend; "*Monovalent Cation Doping of $CH_3NH_3PbI_3$ for Efficient Perovskite Solar Cells*", ***JoVE***, 10.3791/55307 (2017). DOI: 10.3791/55307.

9. Baodan Zhao, **Mojtaba Abdi-Jalebi**, Maxim Tabachnyk, Hugh Glass, Varun S Kamboj, Wanyi Nie, Andrew J Pearson, Yuttapoom Puttisong, Karl C Gödel, Harvey E Beere, David A Ritchie, Aditya D Mohite, Siân E Dutton, Richard H Friend, Aditya Sadhanala; "*High Open-Circuit Voltages in Tin-Rich Low-Bandgap Perovskite-Based Planar Heterojunction Photovoltaics*", ***Adv. Mater.***, 29, 1604744, (2017). DOI: 10.1002/adma.201604744.

10. Dawei Di, Alexander S Romanov, Le Yang, Johannes M Richter, Jasmine PH Rivett, Saul Jones, Tudor H Thomas, **Mojtaba Abdi-Jalebi**, Richard H Friend, Mikko Linnolahti, Manfred Bochmann, Dan Credgington; "*High-performance light-emitting diodes based on carbene-metal-amides*", ***Science***, 356 (6334), pp. 159-163 (2017). DOI: 10.1126/science.aah4345.

11. Eline M Hutter, Rebecca J Sutton, Sanjana Chandrashekar, **Mojtaba Abdi-Jalebi**, Samuel D Stranks, Henry J Snaith, Tom J Savenije; "*Vapour-Deposited Cesium Lead Iodide Perovskites: Microsecond Charge Carrier Lifetimes and Enhanced Photovoltaic Performance*", ***ACS Energy Lett.***, 2, pp. 1901–1908, (2017). DOI: 10.1021/acsenergylett.7b00591.

12. Hu Chen, Michael Hurhangee, Mark Nikolka, Weimin Zhang, Mindaugas Kirkus, Marios Neophytou, Samuel J Cryer, David Harkin, Pascal Hayoz, **Mojtaba Abdi-Jalebi**, Christopher R McNeill, Henning Sirringhaus, Iain McCulloch; "*Dithiopheneindenofluorene (TIF) Semiconducting Polymers with Very High Mobility in Field-Effect Transistors*", ***Adv. Mater.***, 1702523, (2017). DOI: 10.1002/adma.201702523.

13. Arman Mahboubi Soufiani, Zhuo Yang, Trevor Young, Atsuhiko Miyata, Alessandro Surrente, Alexander Pascoe, Krzysztof Galkowski, **Mojtaba Abdi-Jalebi**, Roberto Brenes, Joanna Urban, Nan Zhang, Vladimir Bulović, Oliver Portugall, Yi-Bing Cheng, Robin J Nicholas, Anita Ho-Baillie, Martin A Green, Paulina Plochocka, Samuel D Stranks; "*Impact of Microstructure on the Electron-hole Interaction in Metal Halide Perovskites*", ***Energy Environ. Sci***., 10, 1358-1366, (2017). DOI: 10.1039/C7EE00685C.

14. **Mojtaba Abdi-Jalebi**, M. Ibrahim Dar, Aditya Sadhanala, Satyaprasad P. Senanayak, Marius Franckevičius, Neha Arora, Yuanyuan Hu, Mohammad K. Nazeeruddin, Shaik M. Zakeeruddin, Michael Grätzel, Richard H. Friend; "*Impact of Monovalent Cation Halide Additives on the Structural and Optoelectronic Properties of CH3NH3PbI3 Perovskite*" ***Adv. Energy Mater***., 6, 1502472 (2016). DOI: 10.1002/aenm.201502472.

15. **Mojtaba Abdi-Jalebi,** M. Ibrahim Dar, Aditya Sadhanala, Satyaprasad P. Senanayak, Fabrizio Giordano, Shaik Mohammed Zakeeruddin, Michael Grätzel, and Richard H. Friend; "*Impact of a Mesoporous Titania–Perovskite Interface on the Performance of Hybrid Organic–Inorganic Perovskite Solar Cells*" ***J. Phys. Chem. Lett.***, 7 (16), pp 3264–3269 (2016). DOI: 10.1021/acs.jpclett.6b01617.

16. Johannes M Richter, **Mojtaba Abdi-Jalebi**, Aditya Sadhanala, Maxim Tabachnyk, Jasmine PH Rivett, Luis M Pazos-Outón, Karl C Gödel, Michael Price, Felix Deschler, Richard H Friend; "*Enhancing photoluminescence yields in lead halide perovskites by photon recycling and light out-coupling*" ***Nat. Commun***., 7, 13941 (2016). DOI: 10.1038/ncomms13941.

17. M Ibrahim Dar, **Mojtaba Abdi-Jalebi**, Neha Arora, Michael Grätzel, Mohammad Khaja Nazeeruddin; "*Growth Engineering of $CH_3NH_3PbI_3$ Structures for High- Efficiency Solar Cells*" ***Adv. Energy Mater.*** 6, 1501358 (2016). DOI: 10.1002/aenm.201501358.

18. Zahra Andaji Garmaroudi, **Mojtaba Abdi-Jalebi**, Mohammad-Reza Mohammadi, Richard H. Friend; "*A facile low temperature route to deposit TiO2 scattering layer for efficient dye-sensitized solar cells*" ***RSC Adv***., 6, 70895-70901, (2016).
DOI: 10.1039/C6RA13273A.

19. Luis M. Pazos-Outón, Monika Szumilo, Robin Lamboll, Johannes M. Richter, **Mojtaba Abdi-Jalebi**, Micaela Crespo-Quesada, Harry J. Beeson, Milan Vrućinić, Mejd Alsari, Henry J. Snaith, Bruno Ehrler, Richard H. Friend, Felix Deschler; "*Photon recycling in lead iodide perovskite solar cells*" ***Science,*** 351, 1430-1433 (2016).
DOI: 10.1126/science.aaf1168.

20. Neha Arora, M Ibrahim Dar, **Mojtaba Abdi-Jalebi**, Fabrizio Giordano, Norman Pellet, Gwénolé Jacopin, Richard H Friend, Shaik Mohammed Zakeeruddin, Michael Grätzel; "*Intrinsic and Extrinsic Stability of Formamidinium Lead Bromide Perovskite Solar Cells Yielding High Photovoltage*" ***Nano Lett***., 16 (11), pp 7155–7162, (2016).
DOI: 10.1021/acs.nanolett.6b03455.

21. Andrew J Pearson, Paul E Hopkinson, Elsa Couderc, Konrad Domanski, **Mojtaba Abdi-Jalebi**, Neil C Greenham; "*Critical light instability in CB/DIO processed PBDTTT-EFT: PC_71 BM organic photovoltaic devices*" ***Organic Electronics***, 30 225**e**236, (2016).
DOI: 10.1016/j.orgel.2015.12.024.

22. M Ibrahim Dar, **Mojtaba Abdi-Jalebi**, Neha Arora, Thomas Moehl, Michael Grätzel, Mohammad Khaja Nazeeruddin; "*Understanding the impact of bromide on the photovoltaic performance of $CH_3NH_3PbI_3$ solar cells*" ***Adv. Mater.*** 27, 7221-7228 (2015).
DOI: 10.1002/adma.201503124.

23. Claire L Armstrong, Michael B Price, David Munoz-Rojas, Nathaniel JKL Davis, **Mojtaba Abdi-Jalebi**, Richard H Friend, Neil C Greenham, Judith L MacManus-Driscoll, Marcus

L Böhm, Kevin P Musselman; "*Influence of an inorganic interlayer on exciton separation in hybrid solar cells*", ***ACS Nano***, 9 (12), pp 11863–11871, (2015). DOI: 10.1021/acsnano.5b05934.

References

1. Owusu, P. A. & Asumadu-Sarkodie, S. A review of renewable energy sources, sustainability issues and climate change mitigation. *Cogent Engineering* **3,** (2016).

2. Liu, J., Yao, Y. & Xiao, S. Review of status developments of high-efficiency crystalline silicon solar cells. *J. Phys D appl. Phys.* **51,** 123001 (2018).

3. Snaith, H. H. J. Perovskites: The Emergence of a New Era for Low-Cost, High-Efficiency Solar Cells. *J. Phys. Chem. Lett.* **4,** 3623–3630 (2013).

4. Grätzel, M. The light and shade of perovskite solar cells. *Nat. Mater.* **13,** 838–842 (2014).

5. Kojima, A., Teshima, K., Shirai, Y. & Miyasaka, T. Organometal Halide Perovskites as Visible-Light Sensitizers for Photovoltaic Cells. *J. Am. Chem. Soc.* **131,** 6050–6051 (2009).

6. Kim, H. S. *et al.* Lead iodide perovskite sensitized all-solid-state submicron thin film mesoscopic solar cell with efficiency exceeding 9%. *Sci. Rep.* **2,** (2012).

7. Lee, M. M., Teuscher, J., Miyasaka, T., Murakami, T. N. & Snaith, H. J. Efficient Hybrid Solar Cells Based on Meso-Superstructured Organometal Halide Perovskites. *Science* **338,** 643–647 (2012).

8. Yang, W. S. *et al.* Iodide management in formamidinium-lead-halide–based perovskite layers for efficient solar cells. *Science* **356,** 1376–1379 (2017).

9. Polman, A., Knight, M., Garnett, E. C., Ehrler, B. & Sinke, W. C. Photovoltaic materials: Present efficiencies and future challenges. *Science* **352,** (2016).

10. Tariq Khokhar. Over 1 Billion People Lack Access to Electricity | The Data Blog. Available at: https://blogs.worldbank.org/opendata/chart-globally-over-1-billion-people-lack-access-electricity. (Accessed: 12th April 2018)

11. *Global Market Outlook 2017–2021*. (SolarPower Europe, 2017).

12. Green, M. A., Ho-Baillie, A. & Snaith, H. J. The emergence of perovskite solar cells. *Nat. Photonics* **8,** 506–514 (2014).

13. Jung, H. S. & Lee, J.-K. Dye Sensitized Solar Cells for Economically Viable Photovoltaic Systems. *J. Phys. Chem. Lett.* **4,** 1682–1693 (2013).

14. Green, M. A. Commercial progress and challenges for photovoltaics. *Nature Energy* **1,** (2016).

15. Becquerel, A. E. Memoire sur les effects d´electriques produits sous l´influence des rayons solaires. *Acad. des Sci.* **9,** 561–567 (1839).

16. Chapin, D. M., Fuller, C. S. & Pearson, G. L. A new silicon p-n junction photocell for converting solar radiation into electrical power [3]. *Journal of Applied Physics* **25,** 676–677 (1954).

17. Green, M. A. The path to 25% silicon solar cell efficiency: History of silicon cell evolution. *Prog. Photovoltaics Res. Appl.* **17,** 183–189 (2009).

18. Green, M. A., Emery, K., Hishikawa, Y., Warta, W. & Dunlop, E. D. Solar cell efficiency tables (Version 45). *Prog. Photovoltaics Res. Appl.* **23,** 1–9 (2015).

19. Green, M. A. *et al.* Solar cell efficiency tables (version 50). *Prog. Photovoltaics Res. Appl.* **25,** 668–676 (2017).

20. Xu, Y., Gong, T. & Munday, J. N. The generalized Shockley-Queisser limit for nanostructured solar cells. *Sci. Rep.* **5,** (2015).

21. Shockley, W. & Queisser, H. J. Detailed balance limit of efficiency of p-n junction solar cells. *J. Appl. Phys.* **32,** 510–519 (1961).

22. Tiedje, T. Band tail recombination limit to the output voltage of amorphous silicon solar cells. *Appl. Phys. Lett.* **40,** 627–629 (1982).

23. Rau, U. & Werner, J. H. Radiative efficiency limits of solar cells with lateral band-gap fluctuations. *Appl. Phys. Lett.* **84,** 3735–3737 (2004).

24. Rau, U., Paetzold, U. W. & Kirchartz, T. Thermodynamics of light management in photovoltaic devices. *Phys. Rev. B - Condens. Matter Mater. Phys.* **90,** (2014).

25. Pazos-Outón, L. M., Xiao, T. P. & Yablonovitch, E. Fundamental Efficiency Limit of Lead Iodide Perovskite Solar Cells. *J. Phys. Chem. Lett.* 1703–1711 (2018). doi:10.1021/acs.jpclett.7b03054

26. Tabachnyk, M. *et al.* Resonant energy transfer of triplet excitons from pentacene to PbSe nanocrystals. *Nat. Mater.* **13,** 1033–1038 (2014).

27. Asahi, S., Teranishi, H., Kusaki, K., Kaizu, T. & Kita, T. Two-step photon up-conversion solar cells. *Nat. Commun.* **8,** (2017).

28. Smith, M. B. & Michl, J. Singlet fission. *Chem. Rev.* **110,** 6891–6936 (2010).

29. Rao, A., Wilson, M. W. B., Albert-Seifried, S., Di Pietro, R. & Friend, R. H. Photophysics of pentacene thin films: The role of exciton fission and heating effects. *Phys. Rev. B - Condens. Matter Mater. Phys.* **84,** (2011).

30. Wilson, M. W. B. *et al.* Ultrafast dynamics of exciton fission in polycrystalline pentacene. *J. Am. Chem. Soc.* **133,** 11830–11833 (2011).

31. Tabachnyk, M. Spin Triplet Excitons in Solar Energy Harvesting Devices. *Thesis* (2016).

32. Tanabe, K. A review of ultrahigh efficiency III-V semiconductor compound solar cells: Multijunction tandem, lower dimensional, photonic up/down conversion and plasmonic nanometallic structures. *Energies* **2,** 504–530 (2009).

33. Green, M. a. *Third generation photovoltaics: advanced solar energy conversion*. *Energy Conversion* **10,** (2006).

34. Imenes, A. G. & Mills, D. R. Spectral beam splitting technology for increased conversion efficiency in solar concentrating systems: A review. in *Solar Energy Materials and Solar Cells* **84,** 19–69 (2004).

35. Polman, A. & Atwater, H. A. Photonic design principles for ultrahigh-efficiency photovoltaics. *Nature Materials* **11,** 174–177 (2012).

36. Baig, H., Heasman, K. C., Sarmah, N. & Mallick, T. Solar cells design for low and medium concentrating photovoltaic systems. in *AIP Conference Proceedings* **1477,**

98–101 (2012).

37. Yamaguchi, M., Takamoto, T. & Araki, K. Super high-efficiency multi-junction and concentrator solar cells. *Sol. Energy Mater. Sol. Cells* **90,** 3068–3077 (2006).

38. Hayashi, N. *et al.* High-efficiency thin and compact concentrator photovoltaics with micro-solar cells directly attached to a lens array. *Opt. Express* **23,** A594 (2015).

39. Cheng, Z. & Lin, J. Layered organic–inorganic hybrid perovskites: structure, optical properties, film preparation, patterning and templating engineering. *CrystEngComm* **12,** 2646 (2010).

40. Mitzi, D. B., Chondroudis, K. & Kagan, C. R. Organic-inorganic electronics. *IBM J. Res. Dev.* **45,** 29–45 (2001).

41. Mitzi, D. B. Organic-inorganic perovskites containing trivalent metal halide layers: The templating influence of the organic cation layer. *Inorg. Chem.* **39,** 6107–6113 (2000).

42. Mitzi, D. B., Wang, S., Feild, C. A., Chess, C. A. & Guloy, A. M. Conducting layered organic-inorganic halides containing 〈110〉-oriented perovskite sheets. *Science* **267,** 1473–1476 (1995).

43. Im, J.-H., Lee, C.-R., Lee, J.-W., Park, S.-W. & Park, N.-G. 6.5% efficient perovskite quantum-dot-sensitized solar cell. *Nanoscale* **3,** 4088 (2011).

44. Park, N. G. Perovskite solar cells: An emerging photovoltaic technology. *Materials Today* **18,** 65–72 (2015).

45. Kim, H.-S. *et al.* Lead Iodide Perovskite Sensitized All-Solid-State Submicron Thin Film Mesoscopic Solar Cell with Efficiency Exceeding 9%. *Sci. Rep.* **2,** 591 (2012).

46. Salbeck, J., Yu, N., Bauer, J., Weissörtel, F. & Bestgen, H. Low molecular organic glasses for blue electroluminescence. *Synth. Met.* **91,** 209–215 (1997).

47. Bach, U. *et al.* Solid-state dye-sensitized mesoporous TiO2 solar cells with high photon-to-electron conversion efficiencies. *Nature* **395,** 583–585 (1998).

48. Stranks, S. D. *et al.* Electron-Hole Diffusion Lengths Exceeding 1 Micrometer in an Organometal Trihalide Perovskite Absorber. *Science* **342,** 341–344 (2013).

49. Burschka, J. *et al.* Sequential deposition as a route to high-performance perovskite-sensitized solar cells. *Nature* **499,** 316–319 (2013).

50. Liu, M., Johnston, M. B. & Snaith, H. J. Efficient planar heterojunction perovskite solar cells by vapour deposition. *Nature* **501,** 395–398 (2013).

51. Zhao, Y. & Zhu, K. Organic–inorganic hybrid lead halide perovskites for optoelectronic and electronic applications. *Chem. Soc. Rev.* **45,** 655–689 (2015).

52. Jeon, N. J. *et al.* Compositional engineering of perovskite materials for high-performance solar cells. *Nature* **517,** 476–480 (2015).

53. Jeon, N. J. *et al.* Solvent engineering for high-performance inorganic?organic hybrid perovskite solar cells. *Nat. Mater.* **13,** 897–903 (2014).

54. Pang, S. *et al.* NH2CH=NH2PbI3: An alternative organolead iodide perovskite sensitizer for mesoscopic solar cells. *Chem. Mater.* **26,** 1485–1491 (2014).

55. Koh, T. M. *et al.* Formamidinium-containing metal-halide: An alternative material for near-IR absorption perovskite solar cells. *J. Phys. Chem. C* **118,** 16458–16462 (2014).

56. Pellet, N. *et al.* Mixed-organic-cation perovskite photovoltaics for enhanced solar-light harvesting. *Angew. Chemie - Int. Ed.* **53,** 3151–3157 (2014).

57. Bi, D. *et al.* Polymer-templated nucleation and crystal growth of perovskite films for solar cells with efficiency greater than 21%. *Nat. Energy* **1,** (2016).

58. Saliba, M. *et al.* Incorporation of rubidium cations into perovskite solar cells improves photovoltaic performance. *Science* **354,** 206–209 (2016).

59. Saliba, M. *et al.* Cesium-containing Triple Cation Perovskite Solar Cells: Improved Stability, Reproducibility and High Efficiency. *Energy Environ. Sci.* **9,** (2016).

60. Yang, W. S. *et al.* Iodide management in formamidinium-lead-halide-based perovskite layers for efficient solar cells. *Science* **356,** 1376–1379 (2017).

61. Seo, J., Noh, J. H. & Seok, S. Il. Rational Strategies for Efficient Perovskite Solar Cells. *Accounts of Chemical Research* **49,** 562–572 (2016).

62. Abdi-Jalebi, M. *et al.* Maximising and Stabilising Luminescence in Metal Halide Perovskite Device Structures. *Nature* 1–21 (2018). doi:10.1038/nature25989

63. Protesescu, L. *et al.* Nanocrystals of Cesium Lead Halide Perovskites (CsPbX3, X = Cl, Br, and I): Novel Optoelectronic Materials Showing Bright Emission with Wide Color Gamut. *Nano Lett.* **15,** 3692–3696 (2015).

64. Kovalenko, M. V., Protesescu, L. & Bodnarchuk, M. I. Properties and potential optoelectronic applications of lead halide perovskite nanocrystals. *Science* **358,** 745–750 (2017).

65. Ravi, V. K., Markad, G. B. & Nag, A. Band Edge Energies and Excitonic Transition Probabilities of Colloidal CsPbX3(X = Cl, Br, I) Perovskite Nanocrystals. *ACS Energy Lett.* **1,** 665–671 (2016).

66. Zhang, D., Eaton, S. W., Yu, Y., Dou, L. & Yang, P. Solution-Phase Synthesis of Cesium Lead Halide Perovskite Nanowires. *J. Am. Chem. Soc.* **137,** 9230–9233 (2015).

67. Eperon, G. E. *et al.* Inorganic caesium lead iodide perovskite solar cells. *J. Mater. Chem. A* **3,** 19688–19695 (2015).

68. Schmidt, L. C. *et al.* Nontemplate synthesis of CH3NH3PbBr3 perovskite nanoparticles. *J. Am. Chem. Soc.* **136,** 850–853 (2014).

69. Zhang, Q., Ha, S. T., Liu, X., Sum, T. C. & Xiong, Q. Room-temperature near-infrared high-Q perovskite whispering-gallery planar nanolasers. *Nano Lett.* **14,** 5995–6001 (2014).

70. Sutherland, B. R., Hoogland, S., Adachi, M. M., Wong, C. T. O. & Sargent, E. H. Conformal organohalide perovskites enable lasing on spherical resonators. *ACS Nano* **8,** 10947–10952 (2014).

71. Wong, A. B. *et al.* Growth and Anion Exchange Conversion of CH3NH3PbX3 Nanorod Arrays for Light-Emitting Diodes. *Nano Lett.* **15,** 5519–5524 (2015).

72. Deng, Y. *et al.* Scalable fabrication of efficient organolead trihalide perovskite solar cells with doctor-bladed active layers. *Energy Environ. Sci.* **8,** 1544–1550 (2015).

73. Saidaminov, M. I. *et al.* High-quality bulk hybrid perovskite single crystals within minutes by inverse temperature crystallization. *Nat. Commun.* **6,** (2015).

74. Chen, Q. *et al.* Planar heterojunction perovskite solar cells via vapor-assisted solution process. *J. Am. Chem. Soc.* **136,** 622–625 (2014).

75. Yang, Z., Zhang, S., Li, L. & Chen, W. Research progress on large-area perovskite thin films and solar modules. *Journal of Materiomics* **3,** 231–244 (2017).

76. Stranks, S. D., Nayak, P. K., Zhang, W., Stergiopoulos, T. & Snaith, H. J. Formation of Thin Films of Organic-Inorganic Perovskites for High-Efficiency Solar Cells. *Angew. Chemie Int. Ed.* Advance (2015).

77. Sutherland, B. R. & Sargent, E. H. Perovskite photonic sources. *Nat. Photonics* **10,** 295–302 (2016).

78. de Quilettes, D. W. *et al.* Impact of microstructure on local carrier lifetime in perovskite solar cells. *Science* **348,** 683–686 (2015).

79. Stranks, S. D. Nonradiative Losses in Metal Halide Perovskites. *ACS Energy Lett.* **2,** 1515–1525 (2017).

80. Shi, D. *et al.* Low trap-state density and long carrier diffusion in organolead trihalide perovskite single crystals. *Science* **347,** 519–522 (2015).

81. Poglitsch, A. & Weber, D. Dynamic disorder in methylammoniumtrihalogenoplumbates (II) observed by millimeter-wave spectroscopy. *J. Chem. Phys.* **87,** 6373–6378 (1987).

82. Kadro, J. M., Nonomura, K., Gachet, D., Grätzel, M. & Hagfeldt, A. Facile route to freestanding CH3NH3PbI3 crystals using inverse solubility. *Sci. Rep.* **5,** 11654 (2015).

83. Fang, Y., Dong, Q., Shao, Y., Yuan, Y. & Huang, J. Highly narrowband perovskite single-crystal photodetectors enabled by surface-charge recombination. *Nat. Photonics* **9,** 679–686 (2015).

84. Dong, Q. *et al.* Electron-Hole Diffusion Lengths > 175 uM in Solution-Grown CH3NH3PbI3 Single Crystals. *Science* **347,** 967–970 (2015).

85. Zhang, W., Eperon, G. E. & Snaith, H. J. Metal halide perovskites for energy applications. *Nature Energy* **1,** (2016).

86. Umari, P., Mosconi, E. & De Angelis, F. Relativistic GW calculations on CH3NH3PbI3 and CH3NH3SnI3 Perovskites for Solar Cell Applications. *Sci. Rep.* **4,** 4467 (2015).

87. Even, J., Pedesseau, L., Jancu, J. M. & Katan, C. Importance of spin-orbit coupling in hybrid organic/inorganic perovskites for photovoltaic applications. *J. Phys. Chem. Lett.* **4,** 2999–3005 (2013).

88. Sell, D. D. & Lawaetz, P. New analysis of direct exciton transitions: Application to GaP. *Phys. Rev. Lett.* **26,** 311–314 (1971).

89. Even, J., Pedesseau, L., Dupertuis, M. A., Jancu, J. M. & Katan, C. Electronic model for self-assembled hybrid organic/perovskite semiconductors: Reverse band edge electronic states ordering and spin-orbit coupling. *Phys. Rev. B - Condens. Matter Mater. Phys.* **86,** (2012).

90. Ishihara, T. Optical properties of PbI-based perovskite structures. *J. Lumin.* **60–61,** 269–274 (1994).

91. D'Innocenzo, V. *et al.* Excitons versus free charges in organo-lead tri-halide perovskites. *Nat. Commun.* **5,** (2014).

92. Tauc, J. Optical properties and electronic structure of amorphous Ge and Si. *Mater. Res. Bull.* **3,** 37–46 (1968).

93. Elliott, R. J. Intensity of optical absorption by excitons. *Phys. Rev.* **108,** 1384–1389 (1957).

94. Tanaka, K. *et al.* Comparative Study in the Excitons in Lead- Halide based Perovskite-type Crystals CH3NH3PbBr3 CH3NH3PbI3. *Solid State Commun.* **127,** 619–623 (2003).

95. Pankove, J. I. & Kiewit, D. A. Optical Processes in Semiconductors. *J. Electrochem. Soc.* **119,** 156C (1972).

96. Urbach, F. The Long-Wavelength Edge of Photographic Sensitivity and of the Electronic Absorption of Solids. *Phys. Rev.* **92,** 1324–1324 (1953).

97. Sadhanala, A. *et al.* Preparation of Single-Phase Films of CH 3 NH 3 Pb(I 1– x Br x) 3 with Sharp Optical Band Edges. *J. Phys. Chem. Lett.* **5,** 2501–2505 (2014).

98. De Wolf, S. *et al.* Organometallic Halide Perovskites: Sharp Optical Absorption Edge and its Relation to Photovoltaic Performance. *J. Phys. Chem. Lett.* **In Press,** 140305122150008 (2014).

99. Eperon, G. E. *et al.* Formamidinium lead trihalide: a broadly tunable perovskite for efficient planar heterojunction solar cells. *Energy Environ. Sci.* **7,** 982 (2014).

100. Rau, U. Reciprocity relation between photovoltaic quantum efficiency and electroluminescent emission of solar cells. *Phys. Rev. B - Condens. Matter Mater. Phys.* **76,** (2007).

101. Tvingstedt, K. *et al.* Radiative efficiency of lead iodide based perovskite solar cells. *Sci. Rep.* **4,** (2014).

102. Soref, R. A. Silicon-Based Optoelectronics. *Proc. IEEE* **81,** 1687–1706 (1993).

103. Sze, S. M. & Ng, K. K. *Physics of Semiconductor Devices*. *Physics of semiconductor device* (2006). doi:10.1049/ep.1970.0039

104. Heo, J. H. *et al.* Planar CH3NH3PbI3perovskite solar cells with constant 17.2% average power conversion efficiency irrespective of the scan rate. *Adv. Mater.* **27,** 3424–3430 (2015).

105. Hutter, E. M., Eperon, G. E., Stranks, S. D. & Savenije, T. J. Charge Carriers in Planar and Meso-Structured Organic–Inorganic Perovskites: Mobilities, Lifetimes, and Concentrations of Trap States. *J. Phys. Chem. Lett.* **6,** 3082–3090 (2015).

106. Xing, G. *et al.* Long-Range Balanced Electron- and Hole-Transport Lengths in Organic-Inorganic CH3NH3PbI3. *Science* **342,** 344–347 (2013).

107. Saidaminov, M. I. *et al.* Planar-integrated single-crystalline perovskite photodetectors. *Nat. Commun.* **6,** (2015).

108. Dong, Q. *et al.* Solar cells. Electron-hole diffusion lengths > 175 μm in solution-grown CH3NH3PbI3 single crystals. *Science* **347,** 967–70 (2015).

109. Zhumekenov, A. A. *et al.* Formamidinium Lead Halide Perovskite Crystals with Unprecedented Long Carrier Dynamics and Diffusion Length. *ACS Energy Lett.* **1,** 32–37 (2016).

110. Oga, H., Saeki, A., Ogomi, Y., Hayase, S. & Seki, S. Improved understanding of the electronic and energetic landscapes of perovskite solar cells: High local charge carrier mobility, reduced recombination, and extremely shallow traps. *J. Am. Chem. Soc.* **136,** 13818–13825 (2014).

111. Wang, G. *et al.* Wafer-scale growth of large arrays of perovskite microplate crystals for functional electronics and optoelectronics. *Sci. Adv.* **1,** (2015).

112. Herz, L. M. Charge-Carrier Mobilities in Metal Halide Perovskites: Fundamental Mechanisms and Limits. *ACS Energy Letters* **2,** 1539–1548 (2017).

113. Miyata, K., Atallah, T. L. & Zhu, X. Y. Lead halide perovskites: Crystal-liquid duality, phonon glass electron crystals, and large polaron formation. *Science Advances* **3,** (2017).

114. Chin, X. Y., Cortecchia, D., Yin, J., Bruno, A. & Soci, C. Lead Iodide Perovskite Light-Emitting Field-Effect Transistor. *Arxiv* **6,** Advance (2015).

115. Hsiao, Y.-C. *et al.* Fundamental Physics behind High-Efficiency Organo-Metal Halide Perovskite Solar Cells. *J. Mater. Chem. A* **0,** 1–14 (2015).

116. DeQuilettes, D. W. *et al.* Impact of microstructure on local carrier lifetime in perovskite solar cells. *Science* **348,** 683–686 (2015).

117. Wehrenfennig, C., Liu, M., Snaith, H. J., Johnston, M. B. & Herz, L. M. Homogeneous Emission Line Broadening in the Organo Lead Halide Perovskite CH3NH3PbI3-xClx. *J. Phys. Chem. Lett.* **5,** 1300–6 (2014).

118. Wehrenfennig, C., Liu, M., Snaith, H. J., Johnston, M. B. & Herz, L. M. Homogeneous emission line broadening in the organo lead halide perovskite CH3NH3PbI3- xClx. *J. Phys. Chem. Lett.* **5,** 1300–1306 (2014).

119. Diab, H. *et al.* Narrow Linewidth Excitonic Emission in Organic-Inorganic Lead Iodide Perovskite Single Crystals. *J. Phys. Chem. Lett.* **7,** 5093–5100 (2016).

120. Wu, K. *et al.* Temperature-dependent excitonic photoluminescence of hybrid organometal halide perovskite films. *Phys. Chem. Chem. Phys.* **16,** 22476–22481 (2014).

121. Albero, J. & García, H. Luminescence control in hybrid perovskites and their applications. *J. Mater. Chem. C* **5,** 4098–4110 (2017).

122. Zhang, M. *et al.* Composition-dependent photoluminescence intensity and prolonged recombination lifetime of perovskite $CH_3NH_3PbBr_{3-x}Cl_x$ films. *Chem. Commun.* **50,** 11727–11730 (2014).

123. Albero, J., Malik, A. R. & Garcia, H. Influence of the Composition of Hybrid Perovskites on their Performance in Solar Cells. *J. Mater. Chem. A* 4353–4364 (2016). doi:10.1039/C6TA00334F

124. Li, L. *et al.* Precise Composition Tailoring of Mixed-Cation Hybrid Perovskites for Efficient Solar Cells by Mixture Design Methods. *ACS Nano* **11,** 8804–8813 (2017).

125. Abdi-Jalebi, M. *et al.* Maximizing and stabilizing luminescence from halide perovskites with potassium passivation. *Nature* **555,** (2018).

126. deQuilettes, D. W. *et al.* Photoluminescence Lifetimes Exceeding 8 μs and Quantum Yields Exceeding 30% in Hybrid Perovskite Thin Films by Ligand Passivation. *ACS Energy Lett.* 1–7 (2016). doi:10.1021/acsenergylett.6b00236

127. Hu, H., Salim, T., Chen, B. & Lam, Y. M. Molecularly Engineered Organic-Inorganic Hybrid Perovskite with Multiple Quantum Well Structure for Multicolored Light-Emitting Diodes. *Sci. Rep.* **6,** (2016).

128. Quan, L. N. *et al.* Ligand-Stabilized Reduced-Dimensionality Perovskites. *J. Am. Chem. Soc.* **138,** 2649–2655 (2016).

129. Yang, X. *et al.* Efficient green light-emitting diodes based on quasi-two-dimensional composition and phase engineered perovskite with surface passivation. *Nat. Commun.* **9,** (2018).

130. Byun, J. *et al.* Efficient Visible Quasi-2D Perovskite Light-Emitting Diodes. *Adv. Mater.* 7515–7520 (2016). doi:10.1002/adma.201601369

131. Jagielski, J., Kumar, S., Yu, W.-Y. & Shih, C.-J. Layer-controlled two-dimensional perovskites: synthesis and optoelectronics. *J. Mater. Chem. C* **5,** 5610–5627 (2017).

132. Tress, W. Perovskite Solar Cells on the Way to Their Radiative Efficiency Limit – Insights Into a Success Story of High Open-Circuit Voltage and Low Recombination. *Adv. Energy Mater.* **7,** (2017).

133. Sherkar, T. S. *et al.* Recombination in Perovskite Solar Cells: Significance of Grain Boundaries, Interface Traps, and Defect Ions. *ACS Energy Lett.* **2,** 1214–1222 (2017).

134. Lee, J.-W. *et al.* The role of grain boundaries in perovskite solar cells. *Mater. Today Energy* **7,** 149–160 (2018).

135. Yin, W. J., Shi, T. & Yan, Y. Unique properties of halide perovskites as possible origins of the superior solar cell performance. *Adv. Mater.* **26,** 4653–4658 (2014).

136. Edri, E. *et al.* Elucidating the charge carrier separation and working mechanism of CH3NH3PbI3−xClx perovskite solar cells. *Nat. Commun.* **5,** (2014).

137. Yun, J. S. *et al.* Benefit of grain boundaries in organic-inorganic halide planar perovskite solar cells. *J. Phys. Chem. Lett.* **6,** 875–880 (2015).

138. Bi, C., Zheng, X., Chen, B., Wei, H. & Huang, J. Spontaneous Passivation of Hybrid Perovskite by Sodium Ions from Glass Substrates: Mysterious Enhancement of Device Efficiency Revealed. *ACS Energy Lett.* **2,** 1400–1406 (2017).

139. Dong, Q. *et al.* Abnormal crystal growth in $CH_3NH_3PbI_{3-x}Cl_x$ using a multi-cycle solution coating process. *Energy Environ. Sci.* **8,** 2464–2470 (2015).

140. Nie, W. *et al.* High-efficiency solution-processed perovskite solar cells with millimeter-scale grains. (2014).

141. Bi, C. *et al.* Non-wetting surface-driven high-aspect-ratio crystalline grain growth for efficient hybrid perovskite solar cells. *Nat. Commun.* **6,** (2015).

142. Li, W. *et al.* Montmorillonite as bifunctional buffer layer material for hybrid perovskite solar cells with protection from corrosion and retarding recombination. *J. Mater. Chem. A* **2,** 13587–13592 (2014).

143. Shao, Y., Xiao, Z., Bi, C., Yuan, Y. & Huang, J. Origin and elimination of photocurrent hysteresis by fullerene passivation in CH3NH3PbI3planar heterojunction solar cells. *Nat. Commun.* **5,** (2014).

144. Snaith, H. J. *et al.* Anomalous hysteresis in perovskite solar cells. *J. Phys. Chem. Lett.* **5,** 1511–1515 (2014).

145. Kim, H., Lim, K.-G. & Lee, T.-W. Planar heterojunction organometal halide perovskite solar cells: roles of interfacial layers. *Energy Environ. Sci.* **9,** 12–30 (2016).

146. Kim, J. H., Williams, S. T., Cho, N., Chueh, C. C. & Jen, A. K. Y. Enhanced Environmental Stability of Planar Heterojunction Perovskite Solar Cells Based on Blade-Coating. *Adv. Energy Mater.* **5,** (2015).

147. Zuo, L. *et al.* Enhanced photovoltaic performance of CH3NH3PbI3 perovskite solar cells through interfacial engineering using self-assembling monolayer Enhanced photovoltaic performance of CH 3 NH 3 PbI 3 perovskite solar cells through interfacial engineering using self -. (2015). doi:10.1021/ja512518r

148. Nie, W. *et al.* High-efficiency solution-processed perovskite solar cells with millimeter-scale grains. *Science* **347,** 522–525 (2015).

149. Deschler, F. *et al.* High Photoluminescence Efficiency and Optically Pumped Lasing in Solution-Processed Mixed Halide Perovskite Semiconductors. *J. Phys. Chem. Lett.* **5,** 1421–1426 (2014).

150. Stranks, S. D. *et al.* Recombination Kinetics in Organic-Inorganic Perovskites: Excitons, Free Charge, and Subgap States. *Phys. Rev. Appl.* **2,** 34007 (2014).

151. Sutter-Fella, C. M. *et al.* High Photoluminescence Quantum Yield in Band Gap Tunable Bromide Containing Mixed Halide Perovskites. *Nano Lett.* **16,** 800–806

(2016).

152. Sargent, E. H. *et al.* Structural, optical, and electronic studies of wide-bandgap lead halide perovskites. *J. Mater. Chem. C* **3,** 8839–8843 (2015).

153. Tress, W. *et al.* Predicting the open-circuit voltage of CH3NH3PbI3 perovskite solar cells using electroluminescence and photovoltaic quantum efficiency spectra: The role of radiative and non-radiative recombination. *Adv. Energy Mater.* **5,** (2015).

154. Miller, O. D., Yablonovitch, E. & Kurtz, S. R. Strong internal and external luminescence as solar cells approach the Shockley-Queisser limit. *IEEE J. Photovoltaics* **2,** 303–311 (2012).

155. Yao, J. *et al.* Quantifying losses in open-circuit voltage in solution-processable solar cells. *Phys. Rev. Appl.* **4,** (2015).

156. Momblona, C. *et al.* Efficient vacuum deposited p-i-n and n-i-p perovskite solar cells employing doped charge transport layers. *Energy Environ. Sci.* **9,** 3456–3463 (2016).

157. Abdi-Jalebi, M. *et al.* Impact of a Mesoporous Titania–Perovskite Interface on the Performance of Hybrid Organic–Inorganic Perovskite Solar Cells. *J. Phys. Chem. Lett.* **7,** 3264–3269 (2016).

158. Giordano, F. *et al.* Enhanced electronic properties in mesoporous TiO2 via lithium doping for high-efficiency perovskite solar cells. *Nat. Commun.* **7,** 1–6 (2016).

159. Abdi-Jalebi, M. *et al.* Monovalent Cation Doping of CH3NH3PbI3 for Efficient Perovskite Solar Cells. *J. Vis. Exp.* 1–9 (2017). doi:10.3791/55307

160. Jackson, W. B., Amer, N. M., Boccara, A. C. & Fournier, D. Photothermal deflection spectroscopy and detection. *Appl. Opt.* **20,** 1333 (1981).

161. Street, R. A. *Hydrogenated Amorphous Silicon*. (Cambridge University Press, 1991).

162. Stella, M. Study of Organic Semiconductors for Device Applications. (Universitat de Barcelona, 2009).

163. John C. de Mello, H. Felix Wittmann, R. H. F. An improved experimental determination of external photoluminescence quantum efficiency. *Adv. Mater.* **9,** 230–

232 (1997).

164. Pazoki, M., Jacobsson, T. J., Hagfeldt, A., Boschloo, G. & Edvinsson, T. Effect of metal cation replacement on the electronic structure of metalorganic halide perovskites: Replacement of lead with alkaline-earth metals. *Phys. Rev. B* **93,** (2016).

165. Perdew, J., Burke, K. & Ernzerhof, M. Generalized Gradient Approximation Made Simple. *Phys. Rev. Lett.* **77,** 3865–3868 (1996).

166. Giannozzi, P. *et al.* a modular and open-source software project for quantum simulations of materials. *Condens. Matter* 395502 (2009).

167. Mosconi, E., Amat, A., Nazeeruddin, M. K., Grätzel, M. & De Angelis, F. First-principles modeling of mixed halide organometal perovskites for photovoltaic applications. *J. Phys. Chem. C* **117,** 13902–13913 (2013).

168. Chandiran, A. K., Abdi-Jalebi, M., Nazeeruddin, M. K. & Grätzel, M. Analysis of electron transfer properties of ZnO and TiO2 photoanodes for dye-sensitized solar cells. *ACS Nano* **8,** 2261–2268 (2014).

169. Abdi-Jalebi, M., Mohammadi, M. R. & Fray, D. J. Double-Layer TiO2 Electrodes with Controlled Phase Composition and Morphology for Efficient Light Management in Dye-Sensitized Solar Cells. *J. Clust. Sci.* **25,** 1029–1045 (2014).

170. Lee, M. M., Teuscher, J., Miyasaka, T., Murakami, T. N. & Snaith, H. J. Efficient Hybrid Solar Cells Based on Meso-Superstructured Organometal Halide Perovskites. *Science* **338,** 643–647 (2012).

171. Kim, H.-S. & Park, N.-G. Parameters Affecting I – V Hysteresis of CH 3 NH 3 PbI 3 Perovskite Solar Cells: Effects of Perovskite Crystal Size and Mesoporous TiO 2 Layer. *J. Phys. Chem. Lett.* **5,** 2927–2934 (2014).

172. Chiang, C.-H. & Wu, C.-G. Bulk heterojunction perovskite–PCBM solar cells with high fill factor. *Nat. Photonics* **10,** 196–200 (2016).

173. You, J. *et al.* Improved air stability of perovskite solar cells via solution-processed metal oxide transport layers. *Nat. Nanotechnol.* **11,** 75–81 (2015).

174. Chandiran, A. K. *et al.* Quantum-confined ZnO nanoshell photoanodes for mesoscopic solar cells. *Nano Lett.* **14,** 1190–1195 (2014).

175. Abdi-jalebi, M., Chandiran, A. K., Nazeeruddin, M. K. & Gr, M. Low temperature dye-sensitized solar cells based on conformal thin zinc oxide overlayer on mesoporous insulating template by atomic layer deposition. *Sci. Iran. F* **21,** 2479–2484 (2014).

176. Bi, D. *et al.* Efficient luminescent solar cells based on tailored mixed-cation perovskites. *Sci. Adv.* **2,** e1501170–e1501170 (2016).

177. Giordano, F. *et al.* Enhanced electronic properties in mesoporous TiO2 via lithium doping for high-efficiency perovskite solar cells. *Nat. Commun.* **7,** 1–6 (2016).

178. Massihi, N., Mohammadi, M. R., Bakhshayesh, a. M. & Abdi-Jalebi, M. Controlling electron injection and electron transport of dye-sensitized solar cells aided by incorporating CNTs into a Cr-doped TiO2 photoanode. *Electrochim. Acta* **111,** 921–929 (2013).

179. Lee, S. W., Ahn, K. S., Zhu, K., Neale, N. R. & Frank, a J. Effects of TiCl4 Treatment of Nanoporous TiO2 Films on Morphology, Light Harvesting, and Charge-Carrier Dynamics in Dye-Sensitized Solar Cells. *J. Phys. Chem. C* **116,** 21285–21290 (2012).

180. Choi, H. *et al.* The effect of TiCl4-treated TiO2 compact layer on the performance of dye-sensitized solar cell. *Curr. Appl. Phys.* **12,** 737–741 (2012).

181. Snaith, H. J. *et al.* Efficiency Enhancements in Solid-State Hybrid Solar Cells via Reduced Charge Recombination and Increased Light Capture. *Nano Lett.* **7,** 3372–3376 (2007).

182. Garmaroudi, Z. A., Abdi-Jalebi, M., Mohammadi, M. R. & Friend, R. H. A facile low temperature route to deposit a TiO 2 scattering layer for efficient dye-sensitized solar cells. *RSC Adv.* **6,** 70895–70901 (2016).

183. John, S., Soukoulis, C., Cohen, M. H. & Economou, E. N. Theory of electron band tails and the urbach optical-absorption edge. *Phys. Rev. Lett.* **57,** 1777–1780 (1986).

184. Jackson, W. B., Amer, N. M., Boccara, a C. & Fournier, D. Photothermal deflection spectroscopy and detection. *Appl. Opt.* **20,** 1333–44 (1981).

185. Zhao, Y., Nardes, A. & Zhu, K. Mesoporous Perovskite Solar Cells: Material Composition, Charge-Carrier Dynamics, and Device Characteristics. *Faraday Discuss.* **176,** Ahead of Print (2014).

186. Bach, U. *et al.* Solid-state dye-sensitized mesoporous TiO2 solar cells with high photon-to-electron conversion efficiencies. *Nature* **395,** 583–585 (1998).

187. Dar, M. I., Abdi-Jalebi, M., Arora, N., Grätzel, M. & Nazeeruddin, M. K. Growth Engineering of CH 3 NH 3 PbI 3 Structures for High-Efficiency Solar Cells. *Adv. Energy Mater.* **6,** 1501358 (2016).

188. Ibrahim Dar, M. *et al.* Understanding the Impact of Bromide on the Photovoltaic Performance of CH 3 NH 3 PbI 3 Solar Cells. *Adv. Mater.* **27,** 7221–7228 (2015).

189. Listorti, A. *et al.* Effect of Mesostructured Layer upon Crystalline Properties and Device Performance on Perovskite Solar Cells. *J. Phys. Chem. Lett.* **6,** 1628–1637 (2015).

190. Peng, W. *et al.* Influence of growth temperature on bulk and surface defects in hybrid lead halide perovskite films. *Nanoscale* 1627–1634 (2015). doi:10.1039/C5NR06222E

191. Senanayak, S. P., Ashar, a Z., Kanimozhi, C., Patil, S. & Narayan, K. S. Room-temperature bandlike transport and Hall effect in a high-mobility ambipolar polymer. *Phys. Rev. B* **91,** 115302 (2015).

192. Grancini, G. *et al.* The impact of the crystallization processes on the structural and optical properties of hybrid perovskite films for photovoltaics. *J. Phys. Chem. Lett.* **5,** 3836–3842 (2014).

193. Graetzel, M., Janssen, R. a J., Mitzi, D. B. & Sargent, E. H. Materials interface engineering for solution-processed photovoltaics. *Nature* **488,** 304–12 (2012).

194. Abdi-Jalebi, M. *et al.* Impact of Monovalent Cation Halide Additives on the Structural and Optoelectronic Properties of CH 3 NH 3 PbI 3 Perovskite. *Adv. Energy Mater.* **6,** 1502472 (2016).

195. Carnie, M. J. *et al.* A one-step low temperature processing route for organolead halide perovskite solar cells. *Chem. Commun. (Camb).* **49,** 7893–5 (2013).

196. Im, J.-H., Jang, I.-H., Pellet, N., Grätzel, M. & Park, N.-G. Growth of CH3NH3PbI3 cuboids with controlled size for high-efficiency perovskite solar cells. *Nat. Nanotechnol.* **9,** 927–932 (2014).

197. Cheng, Z. & Lin, J. Layered organic–inorganic hybrid perovskites: structure, optical properties, film preparation, patterning and templating engineering. *CrystEngComm* **12,** 2646 (2010).

198. Stranks, S. D. *et al.* Electron-Hole Diffusion Lengths Exceeding 1 Micrometer in an Organometal Trihalide Perovskite Absorber. *Science* **342,** 341–344 (2013).

199. Umari, P., Mosconi, E. & De Angelis, F. Relativistic GW calculations on CH3NH3PbI3 and CH3NH3SnI3 Perovskites for Solar Cell Applications. *Sci. Rep.* **4,** 4467 (2015).

200. Dar, M. I. *et al.* Origin of unusual bandgap shift and dual emission in organic-inorganic lead halide perovskites. *Sci. Adv.* **2,** e1601156–e1601156 (2016).

201. Filip, M. R., Eperon, G. E., Snaith, H. J. & Giustino, F. Steric Engineering of Metal-halide Perovskites with Tunable Optical Band Gaps. *Nat. Commun.* **5,** 5757 (2014).

202. Pazoki, M., Wolf, M. J., Edvinsson, T. & Kullgren, J. Vacancy dipole interactions and the correlation with monovalent cation dependent ion movement in lead halide perovskite solar cell materials. *Nano Energy* **38,** 537–543 (2017).

203. Hao, F., Stoumpos, C. C., Chang, R. P. H. & Kanatzidis, M. G. Anomalous band gap behavior in mixed Sn and Pb perovskites enables broadening of absorption spectrum in solar cells. 1–5

204. Navas, J. *et al.* New insights into organic-inorganic hybrid perovskite $CH_3NH_3PbI_3$ nanoparticles. An experimental and theoretical study of doping in Pb^{2+} sites with Sn^{2+}, Sr^{2+}, Cd^{2+} and Ca^{2+}. *Nanoscale* **7,** 6216–29 (2015).

205. Zhao, B. *et al.* High Open-Circuit Voltages in Tin-Rich Low-Bandgap Perovskite-Based Planar Heterojunction Photovoltaics. *Adv. Mater.* **29,** 1604744 (2017).

206. Abdi-jalebi, M. *et al.* Monovalent Cation Doping of CH 3 NH 3 PbI 3 for Efficient Perovskite Solar Cells. **J. Vis. Ex,** (2017).

207. Abdelhady, A. L. *et al.* Heterovalent Dopant Incorporation for Bandgap and Type Engineering of Perovskite Crystals. *J. Phys. Chem. Lett.* **7,** 295–301 (2016).

208. Wang, L. *et al.* Alkali metal halide salts as interface additives to fabricate hysteresis-free hybrid perovskite-based photovoltaic devices. *ACS Appl. Mater. Interfaces* **8,** 23086–23094 (2016).

209. Chang, J. *et al.* Enhancing the photovoltaic performance of planar heterojunction perovskite solar cells by doping the perovskite layer with alkali metal ions. *J. Mater. Chem. A* **4,** 16546–16552 (2016).

210. Bag, S. & Durstock, M. F. Large Perovskite Grain Growth in Low-Temperature Solution-Processed Planar p-i-n Solar Cells by Sodium Addition. *ACS Appl. Mater. Interfaces* **8,** 5053–5057 (2016).

211. Jahandar, M. *et al.* Highly efficient metal halide substituted CH3NH3I(PbI2)1???X(CuBr2)X planar perovskite solar cells. *Nano Energy* **27,** 330–339 (2016).

212. Chen, Q. *et al.* Ag-Incorporated Organic-Inorganic Perovskite Films and Planar Heterojunction Solar Cells. *Nano Lett.* **17,** 3231–3237 (2017).

213. Shahbazi, S. *et al.* Ag Doping of Organometal Lead Halide Perovskites: Morphology Modification and p-Type Character. *J. Phys. Chem. C* **121,** 3673–3679 (2017).

214. Liang, K., Mitzi, D. & Prikas, M. Synthesis and characterization of organic-inorganic perovskite thin films prepared using a versatile two-step dipping technique. *Chem. Mater.* **4756,** 403–411 (1998).

215. Niu, G., Guo, X. & Wang, L. Review of Recent Progress in Chemical Stability of Perovskite Solar Cells. *J. Mater. Chem. A* Advance (2015).

216. Baikie, T. *et al.* Synthesis and crystal chemistry of the hybrid perovskite (CH3NH3)PbI3 for solid-state sensitised solar cell applications. *J. Mater. Chem. A* **1,** 5628 (2013).

217. Patterson, a. L. The scherrer formula for X-ray particle size determination. *Phys. Rev.* **56,** 978–982 (1939).

218. Wehrenfennig, C., Liu, M., Snaith, H. J., Johnston, M. B. & Herz, L. M. Homogeneous Emission Line Broadening in the Organo Lead Halide Perovskite CH3NH3Pb3-xClx. *J. Phys. Chem. Lett.* **5,** 1300–1306 (2014).

219. Sadhanala, A. *et al.* Preparation of Single-Phase Films of CH 3 NH 3 Pb(I 1 −. 1–5 (2014).

220. Kim, J., Lee, S. H., Lee, J. H. & Hong, K. H. The role of intrinsic defects in methylammonium lead iodide perovskite. *J. Phys. Chem. Lett.* **5,** 1312–1317 (2014).

221. Nonnenmacher, M., O'Boyle, M. P. & Wickramasinghe, H. K. Kelvin probe force microscopy. *Appl. Phys. Lett.* **58,** 2921–2923 (1991).

222. Elias, G. *et al.* The role of the cantilever in Kelvin probe force: Microscopy measurements. *Beilstein J. Nanotechnol.* **2,** 252–260 (2011).

223. Visoly-Fisher, I., Cohen, S. R., Cahen, D. & Ferekides, C. S. Electronically active layers and interfaces in polycrystalline devices: Cross-section mapping of CdS/CdTe solar cells. *Appl. Phys. Lett.* **83,** 4924–4926 (2003).

224. Jiang, C. S. *et al.* Direct evidence of a buried homojunction in Cu(In,Ga)Se2 solar cells. *Appl. Phys. Lett.* **82,** 127–129 (2003).

225. Edri, E. *et al.* Why Lead Methylammonium Tri-Iodide Perovskite-Based Solar Cells Require a Mesoporous Electron Transporting Scaffold (but Not Necessarily a Hole Conductor). *Nano Lett.* **14,** 1000–4 (2014).

226. Qin, P. *et al.* Yttrium-substituted nanocrystalline TiO_2 photoanodes for perovskite based heterojunction solar cells. *Nanoscale* **6,** 1508–14 (2014).

227. Bergmann, V. W. *et al.* Real-space observation of unbalanced charge distribution inside a perovskite-sensitized solar cell. *Nat. Commun.* **5,** 5001 (2014).

228. Dymshits, A., Henning, A., Segev, G., Rosenwaks, Y. & Etgar, L. The electronic structure of metal oxide/organo metal halide perovskite junctions in perovskite based solar cells. *Sci. Rep.* **5,** 8704 (2015).

229. Cargnello, M. *et al.* Substitutional doping in nanocrystal superlattices. *Nature* **524,**

450–453 (2015).

230. Shi, D. *et al.* Low trap-state density and long carrier diffusion in organolead trihalide perovskite single crystals. **347,** 519–522 (2015).

231. Son, D.-Y. *et al.* Universal Approach toward Hysteresis−Free Perovskite Solar Cell via Defect Engineering. *J. Am. Chem. Soc.* jacs.7b10430 (2018). doi:10.1021/jacs.7b10430

232. Lilliu, S. *et al.* Grain rotation and lattice deformation during perovskite spray coating and annealing probed *in situ* by GI-WAXS. *CrystEngComm* **18,** 5448–5455 (2016).

233. Lilliu, S. *et al.* Dynamics of crystallization and disorder during annealing of P3HT/PCBM bulk heterojunctions. *Macromolecules* **44,** 2725–2734 (2011).

234. Philippe, B. *et al.* Chemical Distribution of Multiple Cation (Rb + , Cs + , MA + , and FA +) Perovskite Materials by Photoelectron Spectroscopy. *Chem. Mater.* **29,** 3589–3596 (2017).

235. Barker, A. J. *et al.* Defect-Assisted Photoinduced Halide Segregation in Mixed-Halide Perovskite Thin Films. *ACS Energy Lett.* **2,** 1416–1424 (2017).

236. Dar, M. I. *et al.* Investigation Regarding the Role of Chloride in Organic − Inorganic Halide Perovskites Obtained from Chloride Containing Precursors. *Nano Lett.* (2014).

237. Pauca, V. P., Piper, J. & Plemmons, R. J. Nonnegative matrix factorization for spectral data analysis. *Linear Algebra Appl.* **416,** 29–47 (2006).

238. Pazoki, M. *et al.* Photoinduced Stark Effects and Mechanism of Ion Displacement in Perovskite Solar Cell Materials. *ACS Nano* **11,** 2823–2834 (2017).

239. Stranks, S. D. & Snaith, H. J. Metal-halide perovskites for photovoltaic and light-emitting devices. *Nat. Nanotechnol.* **10,** 391–402 (2015).

240. Eperon, G. E. *et al.* Perovskite-perovskite tandem photovoltaics with optimized band gaps. *Science* **354,** 861–865 (2016).

241. McMeekin, D. P. *et al.* A mixed-cation lead mixed-halide perovskite absorber for tandem solar cells. *Science* **351,** 151–155 (2016).

242. Bush, K. A. *et al.* 23.6%-efficient monolithic perovskite/silicon tandem solar cells with improved stability. *Nat. Energy* **2,** 17009 (2017).

243. Hoke, E. T. *et al.* Reversible photo-induced trap formation in mixed-halide hybrid perovskites for photovoltaics. *Chem. Sci.* **6,** 613–617 (2015).

244. Stoddard, R. J., Eickemeyer, F. T., Katahara, J. K. & Hillhouse, H. W. Correlation between Photoluminescence and Carrier Transport and a Simple in Situ Passivation Method for High-Bandgap Hybrid Perovskites. *J. Phys. Chem. Lett.* **8,** 3289–3298 (2017).

245. Saliba, M. *et al.* Cesium-containing triple cation perovskite solar cells: improved stability, reproducibility and high efficiency. *Energy Environ. Sci.* **9,** 1989–1997 (2016).

246. Park, B. *et al.* Chemical engineering of methylammonium lead iodide/bromide perovskites: tuning of opto-electronic properties and photovoltaic performance. *J. Mater. Chem. A* **3,** 21760–21771 (2015).

247. Miller, O. D., Yablonovitch, E. & Kurtz, S. R. Strong Internal and External Luminescence as Solar Cells Approach the Shockley–Queisser Limit. *IEEE J. Photovoltaics* **2,** 303–311 (2012).

248. Agiorgousis, M. L., Sun, Y.-Y., Zeng, H. & Zhang, S. Strong Covalency-Induced Recombination Centers in Perovskite Solar Cell Material CH 3 NH 3 PbI 3. *J. Am. Chem. Soc.* **136,** 14570–14575 (2014).

249. Richter, J. M. *et al.* Enhancing photoluminescence yields in lead halide perovskites by photon recycling and light out-coupling. *Nat. Commun.* **7,** 13941 (2016).

250. Deschler, F. *et al.* High Photoluminescence Efficiency and Optically Pumped Lasing in Solution-Processed Mixed Halide Perovskite Semiconductors. *J. Phys. Chem. Lett.* **5,** 1421–1426 (2014).

251. Hutter, E. M. *et al.* Direct-indirect character of the bandgap in methylammonium lead iodide perovskite. *Nat. Mater.* **16,** 115–120 (2017).

252. Reid, O. G., Yang, M., Kopidakis, N., Zhu, K. & Rumbles, G. Grain-Size-Limited

Mobility in Methylammonium Lead Iodide Perovskite Thin Films. *ACS Energy Lett.* **1,** 561–565 (2016).

253. deQuilettes, D. W. *et al.* Photo-induced halide redistribution in organic–inorganic perovskite films. *Nat. Commun.* **7,** 11683 (2016).

254. Zhao, P. *et al.* Improved carriers injection capacity in perovskite solar cells by introducing A-site interstitial defects. *J. Mater. Chem. A* **5,** 7905–7911 (2017).

255. Tang, Z. *et al.* Hysteresis-free perovskite solar cells made of potassium-doped organometal halide perovskite. *Sci. Rep.* **7,** 12183 (2017).

256. Nam, J. K. *et al.* Potassium Incorporation for Enhanced Performance and Stability of Fully Inorganic Cesium Lead Halide Perovskite Solar Cells. *Nano Lett.* **17,** 2028–2033 (2017).

257. Kubicki, D. J. *et al.* Phase Segregation in Cs-, Rb- and K-Doped Mixed-Cation (MA) x (FA) 1– x PbI 3 Hybrid Perovskites from Solid-State NMR. *J. Am. Chem. Soc.* **139,** 14173–14180 (2017).

258. Yablonovitch, E. & Miller, O. D. The Opto-Electronics which Broke the Efficiency Record in Solar Cells. *Conf. Lasers Electro-Optics 2012* **2,** CF2J.1 (2012).

259. Pazos-Outon, L. M. *et al.* Photon recycling in lead iodide perovskite solar cells. *Science* **351,** 1430–1433 (2016).

260. Kubicki, D. J. *et al.* Phase Segregation in Cs-, Rb- and K-Doped Mixed-Cation (MA) x (FA) 1– x PbI 3 Hybrid Perovskites from Solid-State NMR. *J. Am. Chem. Soc.* **139,** 14173–14180 (2017).

261. Li, Z. *et al.* Stabilizing Perovskite Structures by Tuning Tolerance Factor: Formation of Formamidinium and Cesium Lead Iodide Solid-State Alloys. *Chem. Mater.* **28,** 284–292 (2016).

262. Wang, Z. *et al.* Efficient and Air-Stable Mixed-Cation Lead Mixed-Halide Perovskite Solar Cells with n-Doped Organic Electron Extraction Layers. *Adv. Mater.* **29,** (2017).

263. Hu, Y., Aygüler, M. F., Petrus, M. L., Bein, T. & Docampo, P. Impact of Rubidium

and Cesium Cations on the Moisture Stability of Multiple-Cation Mixed-Halide Perovskites. *ACS Energy Lett.* **2,** 2212–2218 (2017).

264. Saliba, M. *et al.* Incorporation of rubidium cations into perovskite solar cells improves photovoltaic performance. *Science* **354,** 206–209 (2016).

265. Zhang, M. *et al.* High-Efficiency Rubidium-Incorporated Perovskite Solar Cells by Gas Quenching. *ACS Energy Letters* **2,** 438–444 (2017).

266. Kubicki, D. J. *et al.* Phase Segregation in Cs-, Rb- and K-Doped Mixed-Cation (MA)x(FA)1-xPbI3 Hybrid Perovskites from Solid-State NMR. *J. Am. Chem. Soc.* **139,** 14173–14180 (2017).

267. Yadav, P. *et al.* The Role of Rubidium in Multiple-Cation-Based High-Efficiency Perovskite Solar Cells. *Adv. Mater.* **29,** (2017).

268. Kaye, G. W. C. & Laby, T. H. Tables of Physical and Chemical Constants. *Zeitschrift fur Krist. - New Cryst. Struct.* **212,** 400 (1997).

269. Cohen, E. R. & Taylor, B. N. The 1986 CODATA Recommended Values of the Fundamental Physical Constants. *J. Phys. Chem. Ref. Data* **17,** 1795–1803 (1988).

270. Wright, A. D. *et al.* Electron-phonon coupling in hybrid lead halide perovskites. *Nat. Commun.* **7,** (2016).

271. Wang, Q. *et al.* Scaling behavior of moisture-induced grain degradation in polycrystalline hybrid perovskite thin films. *Energy Environ. Sci.* **10,** 516–522 (2017).

272. Roose, B. *et al.* Spontaneous crystal coalescence enables highly efficient perovskite solar cells. *Nano Energy* **39,** 24–29 (2017).

273. Osherov, A. *et al.* The Impact of Phase Retention on the Structural and Optoelectronic Properties of Metal Halide Perovskites. *Adv. Mater.* **28,** 10757–10763 (2016).

274. Brenes, R. *et al.* Metal Halide Perovskite Polycrystalline Films Exhibiting Properties of Single Crystals. *Joule* **1,** 155–167 (2017).

275. Eperon, G. E., Moerman, D. & Ginger, D. S. Anticorrelation between Local Photoluminescence and Photocurrent Suggests Variability in Contact to Active Layer

in Perovskite Solar Cells. *ACS Nano* **10,** 10258–10266 (2016).

276. Rehman, W. *et al.* Photovoltaic mixed-cation lead mixed-halide perovskites: links between crystallinity, photo-stability and electronic properties. *Energy Environ. Sci.* **10,** 361–369 (2017).

277. Keller, H. L. & Jess, I. Darstellung und kristallstrukturuntersuchung von KPbBr3· H20. *J. Less-Common Met.* **125,** 215–221 (1986).

278. COOK, A. P., BOWMAN, L. E. & WADE, A. P. Study of KBr/Pb(NO3)2 growth and crystal morphologies by acoustic-emission and photomicrographic techniques. *J. Cryst. Growth* **131,** 395–412 (1993).

279. Hanna, M. C. & Nozik, A. J. Solar conversion efficiency of photovoltaic and photoelectrolysis cells with carrier multiplication absorbers. *J. Appl. Phys.* **100,** (2006).

280. Ehrler, B., Wilson, M. W. B., Rao, A., Friend, R. H. & Greenham, N. C. Singlet Exciton Fission-Sensitized Infrared Quantum Dot Solar Cells. *Nano Lett.* **12,** 1053–1057 (2012).

281. Ehrler, B., Musselman, K. P., Böhm, M. L., Friend, R. H. & Greenham, N. C. Hybrid pentacene/a-silicon solar cells utilizing multiple carrier generation via singlet exciton fission. *Appl. Phys. Lett.* **101,** (2012).

282. Thompson, N. J. *et al.* Energy harvesting of non-emissive triplet excitons in tetracene by emissive PbS nanocrystals. *Nat. Mater.* **13,** 1039–1043 (2014).

283. Tabachnyk, M., Ehrler, B., Bayliss, S., Friend, R. H. & Greenham, N. C. Triplet diffusion in singlet exciton fission sensitized pentacene solar cells. *Appl. Phys. Lett.* **103,** (2013).

284. Ogomi, Y. *et al.* CH3NH3SnxPb(1-x)I3perovskite solar cells covering up to 1060 nm. *J. Phys. Chem. Lett.* **5,** 1004–1011 (2014).

285. Stoumpos, C. C., Malliakas, C. D. & Kanatzidis, M. G. Semiconducting tin and lead iodide perovskites with organic cations: phase transitions, high mobilities, and near-infrared photoluminescent properties. *Inorg. Chem.* **52,** 9019–38 (2013).

286. Meillaud, F., Shah, A., Droz, C., Vallat-Sauvain, E. & Miazza, C. Efficiency limits for single-junction and tandem solar cells. *Sol. Energy Mater. Sol. Cells* **90,** 2952–2959 (2006).

287. Chang, W. *et al.* Spin-dependent charge transfer state design rules in organic photovoltaics. *Nat. Commun.* **6,** (2015).

288. Peng, J. *et al.* Interface passivation using ultrathin polymer–fullerene films for high-efficiency perovskite solar cells with negligible hysteresis. *Energy Environ. Sci.* **10,** 1792–1800 (2017).

289. Su, P.-Y. *et al.* A multifunctional poly-N-vinylcarbazole interlayer in perovskite solar cells for high stability and efficiency: a test with new triazatruxene-based hole transporting materials. *J. Mater. Chem. A* **5,** 1913–1918 (2017).

290. Ji, G. *et al.* Interfacial electronic structures revealed at the rubrene/CH3NH3PbI3 interface. *Phys. Chem. Chem. Phys.* **19,** 6546–6553 (2017).

291. Abdi-Jalebi, M. *et al.* Impact of a Mesoporous Titania-Perovskite Interface on the Performance of Hybrid Organic-Inorganic Perovskite Solar Cells. *J. Phys. Chem. Lett.* **7,** (2016).

292. Zhou, H. *et al.* Interface engineering of highly efficient perovskite solar cells. *Science* **345,** 542–546 (2014).

293. Arora, N. *et al.* Intrinsic and Extrinsic Stability of Formamidinium Lead Bromide Perovskite Solar Cells Yielding High Photovoltage. *Nano Lett.* **16,** (2016).

294. Salado, M. *et al.* Interface Play between Perovskite and Hole Selective Layer on the Performance and Stability of Perovskite Solar Cells. *ACS Appl. Mater. Interfaces* **8,** 34414–34421 (2016).

295. Pandey, R. & Holmes, R. J. Graded donor-acceptor heterojunctions for efficient organic photovoltaic cells. *Adv. Mater.* **22,** 5301–5305 (2010).

296. Cho, K. T. *et al.* Highly efficient perovskite solar cells with a compositionally engineered perovskite/hole transporting material interface. *Energy Environ. Sci.* **10,** 621–627 (2017).

297. Christians, J. A. *et al.* Tailored interfaces of unencapsulated perovskite solar cells for >1,000 hour operational stability. *Nat. Energy* **3,** 68–74 (2018).

298. Li, X. *et al.* Improved performance and stability of perovskite solar cells by crystal crosslinking with alkylphosphonic acid ω -ammonium chlorides. *Nat. Chem.* **7,** 703–711 (2015).

299. Wei, D. *et al.* Photo-induced degradation of lead halide perovskite solar cells caused by the hole transport layer/metal electrode interface. *J. Mater. Chem. A* **4,** 1991–1998 (2016).

300. Zhang, H. *et al.* Pinhole-free and surface-nanostructured niox film by room-Temperature solution process for high-performance flexible perovskite solar cells with good stability and reproducibility. *ACS Nano* **10,** 1503–1511 (2016).

301. Guerrero, A. *et al.* Interfacial degradation of planar lead halide perovskite solar cells. *ACS Nano* **10,** 218–224 (2016).

302. Li, W. *et al.* Enhanced UV-light stability of planar heterojunction perovskite solar cells with caesium bromide interface modification. *Energy Environ. Sci.* **9,** 490–498 (2016).

303. Marshall, K. P., Walker, M., Walton, R. I. & Hatton, R. A. Enhanced stability and efficiency in hole-transport-layer-free CsSnI 3 perovskite photovoltaics. *Nat. Energy* **1,** (2016).

304. Grancini, G. *et al.* One-Year stable perovskite solar cells by 2D/3D interface engineering. *Nat. Commun.* **8,** (2017).

305. Chen, W. *et al.* Efficient and stable large-area perovskite solar cells with inorganic charge extraction layers. *Science* **350,** 944–948 (2015).

306. You, J. *et al.* Improved air stability of perovskite solar cells via solution-processed metal oxide transport layers. *Nat. Nanotechnol.* **11,** 75–81 (2016).

307. Arora, N. *et al.* Perovskite solar cells with CuSCN hole extraction layers yield stabilized efficiencies greater than 20%. *Science* **358,** 768–771 (2017).

308. Li, Z. *et al.* Extrinsic ion migration in perovskite solar cells. *Energy Environ. Sci.* **10,**

1234–1242 (2017).

309. Domanski, K. *et al.* Not All That Glitters Is Gold: Metal-Migration-Induced Degradation in Perovskite Solar Cells. *ACS Nano* **10,** 6306–6314 (2016).

310. Abate, A. *et al.* Protic ionic liquids as p-dopant for organic hole transporting materials and their application in high efficiency hybrid solar cells. *J. Am. Chem. Soc.* **135,** 13538–13548 (2013).

311. Armstrong, C. L. *et al.* Influence of an Inorganic Interlayer on Exciton Separation in Hybrid Solar Cells. *ACS Nano* **9,** 11863–11871 (2015).

312. Bi, D., Yang, L., Boschloo, G., Hagfeldt, A. & Johansson, E. M. J. Effect of Different Hole Transport Materials on Recombination in CH3NH3PbI3 Perovskite-Sensitized Mesoscopic Solar Cells. *J. Phys. Chem. Lett.* **4,** 1532–6 (2013).

313. Koster, L. J. A., Mihailetchi, V. D., Ramaker, R. & Blom, P. W. M. Light intensity dependence of open-circuit voltage of polymer:fullerene solar cells. *Appl. Phys. Lett.* **86,** 123509 (2005).

314. Zhao, B. *et al.* High Open-Circuit Voltages in Tin-Rich Low-Bandgap Perovskite-Based Planar Heterojunction Photovoltaics. *Adv. Mater.* **29,** (2017).